

Action Space Diffusion Resonances for an Atom Optics Kicked Rotor with Decoherence and Amplitude Noise

Andrew John Daley

A thesis
submitted in partial fulfilment
of the requirements for the degree
of
Master of Science
at the
University of Auckland



University of Auckland
2002

*To my parents, Paul and Robyn Daley,
for all of their love and support over the last $23\frac{1}{2}$ years,
without which I would not be doing what I am today.*

Abstract

In this thesis the atom optics kicked rotor with spontaneous emission noise is studied as a specific experimental instance of the quantum kicked rotor with decoherence. The momentum diffusion rates of this system are investigated as we fix the level of decoherence and make the system more macroscopic or less macroscopic by varying the total system action. We find dramatic structure in the initial quantum diffusion rates and also the late time momentum diffusion rates, which are generated when dynamical localisation is disturbed by the introduction of decoherence. This structure includes peaks around quantum resonances and enhanced diffusion peaks which arise from uniquely quantum mechanical correlations. We also investigate the effects of adding amplitude noise to our system and the dependence of early time diffusion rates on the width of the initial momentum distribution.

Our study is primarily numerical, but is performed using experimentally realistic parameters and takes into account effects such as a finite pulse duration. We also look at an alternative characterisation of the system which makes experiments more simple to perform, and which has been realised by two research groups including our own. All of our numerical results are related to a combination of well known analytical results for the δ -kicked rotor and our own analytical work which is presented in this thesis.

Acknowledgments

There are several people without whom this research would not have been possible, and many more whose friendship and support has been important in making this year and this work a pleasant and rewarding experience. There are far too many to thank in a short section like this one, but there are some specific people I would like to mention who have either worked on this research project or supported me in its completion.

Firstly I would like to thank Scott Parkins, who has been a wonderful supervisor over the last year. His door has always been open, and regardless of how busy he has been he has always had time to discuss our work. It has been a real privilege to work under someone who has his level of physical insight into atom optics, his impressive ability to generate fruitful ideas for areas to investigate, his clarity of thought in discussions, and his unwavering commitment to the work of his students.

In addition, I would like to thank my co-supervisor, Rainer Leonhardt, for his constant encouragement, and for keeping me in touch with the reality of the experiments (yes, he actually let a theoretical student into the lab!). I especially appreciated his many pertinent and motivating questions about the meaning of my results and their relationship to measurements made in the lab.

Special thanks on many fronts must go to Sze Tan, whose insightful discussions on many areas of physics, not just related to the work in this thesis, have been a highlight of my time in the Physics Department here over the last five years. His help with the numerical simulations in this thesis and the extraction of data therefrom was invaluable, as were his many stimulating conversations on all of the different aspects of this work.

In direct connection with this work I would also like to thank Kurt Jacobs, whose interesting discussions on the work in reference [1] helped to provide the basis for the initial ideas of our research, as well as Andrew Doherty, who provided the MATLAB source code of reference [46] which formed the basis for our quantum simulations.

Mark Sadgrove was my office-mate for the second half of the year, but I pestered him throughout almost the entire year with early morning discussions while he was trying to do work in the lab (sorry, Leo!). These conversations often helped to clarify many points of our work, and I am very grateful to Mark for his constant enthusiasm, and for his willingness to keep me in touch with the experiments.

I am also grateful to Mary Williams and Richard Gray for their discussions on many aspects of our group's experiments and experimental results, and to Maarten Hoogerland for his stimulating discussions on this work after his arrival in January.

Thank you to the other members of the Quantum Optics group for their very useful discussions. Particular thanks go to Matthew Collett and Lev Plimak for their insight at group meetings (and especially to Lev for teaching me how to pronounce “Shepelyansky”), to Stojan Rebic and Steve Clark for their morning discussions on a variety of matters, and to Ashton Bradley and Steve Kurzeja for being wonderful office-mates for the first half of the year.

My thanks go to the many members of the Department of Physics here at the University of Auckland, who have made this year a wonderfully enjoyable experience through their friendship and encouragement, and for their stimulating lunchtime conversations on all topics, which have been a highlight of this year. I am especially grateful to Lionel Watkins and Ruth Lyons for giving me the opportunity to take on teaching duties in various capacities, which has enhanced my enthusiasm for physics in all of its forms. Thank you also to Keith Smith, who along with Sze Tan convinced me to convert to Linux as my operating system, and then helped me to become acquainted with it. I have found it to be considerably more stable and powerful for the tasks that I want to perform than any other operating system I had previously used.

I have many friends outside of physics who have shown me enormous amounts of encouragement and who have given me a life outside my studies, some of them over a long period of time. There are too many to name individually, but I would particularly like to thank Andrew, Stuart, Paul and Chris Sweetman, Mike Elmsly and Russell Browning for their friendship over a long period of time. My thanks also go to Stephanie Wayper, for her constant encouragement and for keeping me sane during the thesis writing period.

I am very grateful to Rodger Fox for giving me a significant interest outside of physics over the last five years through the Rodger Fox Big Band, and to the other members of the band for all of the fun we have on tour. Similarly, I would like to thank all of the members of the two indoor cricket teams I have played for over the last three years - for distracting me from my studies and in so doing helping me to appreciate physics more.

I would like to finish this section with two very special acknowledgments.

Firstly, I would like to thank all of those people whose passion for physics and interest in me as a student when I was an undergraduate encouraged me to pursue physics to this level. Particularly I would like to thank Gary Bold, Sze Tan, Dave Wardle, Tom Barnes, Peter Wills, Steve Buckman, and the late Tom Rhymes. Without them, I might not be studying physics today.

And, secondly I would like to thank my family - my parents Paul and Robyn, to whom this thesis is dedicated, and my brothers, Chris and Nick. They have been a source of endless strength and support over the last $23\frac{1}{2}$ years, and I would not be the person I am without them. They are the best family anyone could ever have.

Andrew Daley
February 22, 2002

Contents

Abstract	v
Acknowledgments	vii
Contents	ix
List of Figures	xiii
List of Tables	xix
1 Overview	1
1.1 Introduction	1
1.2 Outline of Thesis	3
2 The Classical Kicked Rotor	5
2.1 Introduction to Classical Dynamics	5
2.1.1 The Action Principle and Hamiltonian Mechanics	5
2.1.2 Canonical Transformations	6
2.1.3 Integrability	7
2.1.4 Poincaré Sections	8
2.1.5 Time - Dependent Systems	8
2.1.6 Periodic Systems and Action-Angle Variables	9
2.1.7 Near-Integrable Systems and the KAM Theorem	10
2.2 The Classical Rotor	11
2.3 The Classical Kicked Rotor	14
2.3.1 The δ -Kicked Rotor	14
2.3.2 The Pulse-Kicked Rotor	19
2.4 Momentum Diffusion in the Classical δ -Kicked Rotor	25
2.4.1 Momentum Diffusion Rates	25
2.4.2 Correlation Functions and Quasilinear Diffusion	25
2.4.3 Long Time Classical Diffusion Rates	27

3	The Quantum Kicked Rotor	31
3.1	Quantum Dynamics	31
3.1.1	Basic Quantum Mechanics	31
3.1.2	The Parameter k	32
3.1.3	Quantum Chaos	32
3.2	The Quantum Kicked Rotor	33
3.2.1	The Quantum δ -Kicked Rotor	34
3.2.2	The Quantum Pulse-Kicked Rotor	34
3.2.3	Angular Momentum and Floquet State Representations	35
3.2.4	Dynamical Localisation	36
3.2.5	Quantum Resonances	37
3.3	Momentum Diffusion in the Quantum δ -Kicked Rotor	40
3.3.1	Definitions	40
3.3.2	Quasilinear Behaviour	40
3.3.3	Initial Quantum Diffusion	41
3.3.4	The Quantum Break Time	43
4	The Atom Optics Kicked Rotor	45
4.1	Introduction	45
4.2	Theory	45
4.3	Experiments at the University of Auckland	47
4.3.1	The Atom Trapping Laboratory	47
4.3.2	Structure of Caesium	50
4.3.3	Theory and Experiment	51
4.4	Decoherence and Spontaneous Emission Noise	52
4.4.1	Measurement and Decoherence in Quantum Mechanics	53
4.4.2	Spontaneous Emission rate for a Two-Level Atom	54
4.4.3	Spontaneous Emission Noise in the Atom Optics Kicked Rotor	56
4.4.4	Decoherence and the Kicked Rotor	57
4.5	Amplitude Noise	58
4.6	The Classical Limit of the Atom Optics Kicked Rotor	59
5	Techniques for Simulation of the Kicked Rotor	61
5.1	Introduction	61
5.2	Classical Simulations	61
5.2.1	General Method	61
5.2.2	Addition of Amplitude and Spontaneous Emission Noise	62
5.3	Quantum Simulations	63
5.3.1	The Monte-Carlo Wavefunction Method	63
5.3.2	The Atom Optics Kicked Rotor with Spontaneous Emission Noise	66
5.3.3	Amplitude Noise	71
5.3.4	Estimation of Errors	71

6	Diffusion in the QKR with Decoherence	73
6.1	Introduction	73
6.2	Early Time Diffusion Rates	74
6.3	The Initial Quantum Diffusion Period	74
6.3.1	The Effects of Varying κ	77
6.3.2	Comparison with Shepelyansky's Formula	80
6.3.3	Varying Levels of Spontaneous Emission Noise	82
6.3.4	Momentum Diffusion from Spontaneous Emission Recoils - Classical Results	84
6.3.5	Results for high values of $\hbar k$	85
6.4	Simulation Results in the Late Time Diffusion Regime	85
6.4.1	Results for Varying κ	85
6.4.2	Varying levels of Decoherence	87
6.4.3	Results for high values of $\hbar k$	87
6.5	Analytical Results for Late Time Diffusion Rates	94
6.5.1	Relationship with Early Time Diffusion Rates	94
6.5.2	A Fully Analytical Result	98
6.6	Austin Method for generating Spontaneous Emissions	103
6.7	The Effects of Varying α	107
6.8	Varying Widths of the Initial Momentum Distribution	108
7	Diffusion in the QKR with Amplitude Noise	109
7.1	Introduction	109
7.2	Amplitude Noise in the CKR	110
7.3	Initial Quantum Diffusion Rates	112
7.3.1	The Generalised Shepelyansky Formula	112
7.3.2	Simulation Results	114
7.4	Late Time Diffusion Rates	117
7.4.1	Simulation Results	117
7.4.2	Towards an Analytical Theory	117
7.5	Mixtures of Two Types of Noise	121
8	Diffusion Structures in Physical Units	125
8.1	Introduction	125
8.2	Physical Units vs. Scaled Units	126
8.3	Initial Diffusion Rates	127
8.4	Classical Comparison	130
8.5	Late Time Diffusion Structures with Decoherence	132
8.6	Late Time Diffusion Structures with Amplitude Noise	138
9	Narrow Initial Momentum Distributions	139
9.1	Introduction	139
9.2	Early Time Classical Diffusion Results	139

9.3	Early Time Quantum Diffusion Results	141
9.3.1	An Alternative Standard Map	141
9.3.2	Analytical Results for the Second Kick	143
9.3.3	Higher Kick Numbers	152
9.4	Quantum Superpositions in Initial States	152
10	Conclusion and Future Directions	161
10.1	Conclusions	161
10.1.1	Spontaneous Emission Decoherence	161
10.1.2	Amplitude Noise	162
10.1.3	Combination of Spontaneous Emissions and Amplitude Noise . .	163
10.1.4	Unscaled Units	164
10.1.5	Narrow Initial Momentum Distributions	164
10.2	Future Directions	165
A	Bessel Functions	167
A.1	The Bessel Differential Equation	167
A.2	Relationships between solutions	168
A.3	Series Expansions	169
A.4	Integral Expressions	169
A.5	Recurrence Relationships	170
A.6	Bessel Functions of Large Order	170
A.7	Generating Function and Related Series	170
A.8	Neumann's Addition Theorem	171
B	Calculation of Correlations	173
B.1	Introduction	173
B.2	Classical Correlations	173
B.3	Quantum Correlations	175
C	Source Code	177
C.1	Poincaré Sections: poin.m	177
C.2	Simulation of the Pulse - Kicked Rotor	178
C.2.1	Integration of Differential Equations: ckr.c	178
C.2.2	Use of Jacobi Elliptic Functions: pulseclass.m	181
C.2.3	Spontaneous Emission recoils in the CKR: spemclass.m	183
C.3	Simulation of the QKR with Decoherence: mcwfspem.m	185
C.4	QKR with Decoherence and Amplitude Noise: ampspem.m	188
	Bibliography	191

List of Figures

2.1	The Classical Rotor	12
2.2	Trajectories in phase space for a classical rotor with $I = 1$ and $K = 1$	13
2.3	A train of δ functions	15
2.4	Poincaré Section for the classical kicked rotor with $\kappa = 0.5$	16
2.5	Poincaré Section for the classical kicked rotor with $\kappa = 0.8$	16
2.6	Poincaré Section for the classical kicked rotor with $\kappa = 1.0$	17
2.7	Poincaré Section for the classical kicked rotor with $\kappa = 1.5$	17
2.8	Poincaré Section for the classical kicked rotor with $\kappa = 2.0$	18
2.9	Poincaré Section for the classical kicked rotor with $\kappa = 7.0$	18
2.10	Square Wave Pulses	20
2.11	The dependence of κ_{eff} on ρ for the classical pulse-kicked rotor.	23
2.12	Poincaré Section for a classical pulse-kicked rotor with $\kappa = 8$, $\alpha = 0.1$	24
2.13	Simulation values of mean kinetic energy as a function of n for a classical δ -kicked rotor, showing the transition from quasilinear diffusion to classical diffusion.	27
2.14	Simulation results for mean kinetic energy as a function of n in the classical δ -kicked rotor, showing the steady state diffusion regime.	28
2.15	Steady state momentum diffusion rates for the classical δ -kicked rotor, as a function of κ	30
2.16	Average momentum diffusion rates over the first 50 kicks for the classical kicked rotor with rectangular pulses and $\alpha=0.005$, as a function of $\kappa = k\alpha$	30
3.1	Momentum probability distributions after N kicks for $\kappa = 20$ and $\hbar k = 4\pi$, showing ballistic motion at a quantum resonance.	39
3.2	Initial quantum diffusion rates as a function of $\hbar k$ from Shepelyansky's formula.	42
3.3	Simulation result for mean energy as a function of kick number for the quantum kicked rotor with $\alpha = 0.005$, $\kappa = 12$, $\hbar k = 3$	43
4.1	The Atom Trapping Laboratory, Department of Physics, University of Auckland	48
4.2	The main cell of the Atom Trapping Laboratory	49
4.3	Hyperfine structure of the D_2 transition for Caesium.	50

5.1	Plot of $\sin[\pi(r-0.5)]/\sin[\pi(r-0.5)/30]$ against r , showing the smearing of a single component of a DFT into adjacent components.	69
5.2	Simulation momentum distribution after 200 kicks for $\kappa = 10$, $\eta = 0.1$, $\alpha = 0.005$, $\bar{k} = 4.0$, with a basis spacing of \bar{k} , showing the effects of spectral leakage in the DFT.	70
5.3	Simulation momentum distribution after 200 kicks for $\kappa = 10$, $\eta = 0.1$, $\alpha = 0.005$, $\bar{k} = 4.0$, with a basis spacing of $\bar{k}/2$, showing the expected momentum distribution without spectral leakage in the DFT.	70
6.1	Diffusion Rates, $D(n)$, for the quantum kicked rotor with $\alpha = 0.005$, $\kappa = 10$, $\eta = 10\%$ and $\sigma_\rho = 4$, plotted as a function of \bar{k} for $n = 0, 1, 2, 3, 4$	75
6.2	Diffusion Rates, $D(n)$, for the quantum kicked rotor with $\alpha = 0.005$, $\kappa = 12$, $\eta = 1\%$ and $\sigma_\rho = 4$, plotted as a function of \bar{k} for $n = 0, 1, 2, 3, 4$	76
6.3	Simulation results for initial quantum diffusion rates for the QKR with $\alpha = 0.005$ and $\eta = 10\%$. $\kappa = 9, 10, 11, 12$	77
6.4	Simulation results for initial quantum diffusion rates for the QKR with $\alpha = 0.005$ and $\eta = 10\%$. $\kappa = 13, 14, 15, 16$	78
6.5	Simulation results for initial quantum diffusion rates for the QKR with $\alpha = 0.005$ and $\eta = 10\%$. $\kappa = 17, 18, 19, 20$	79
6.6	Comparison of simulation results for initial quantum diffusion rates with results from Shepelyansky's formula for the QKR with $\alpha = 0.005$ and $\eta = 10\%$. $\kappa = 9, 11$	80
6.7	Comparison of simulation results for initial quantum diffusion rates with results from Shepelyansky's formula for the QKR with $\alpha = 0.005$ and $\eta = 10\%$. $\kappa = 10, 12$	81
6.8	Simulation results for the initial quantum diffusion rates of the QKR with $\alpha = 0.005$ and $\kappa = 9$, showing the behaviour as we vary η	83
6.9	Simulation results for initial quantum diffusion rates of the QKR with $\alpha = 0.005$ and $\kappa = 11$, showing the behaviour as we vary η	83
6.10	Simulation results for initial quantum diffusion rates of the QKR with $\alpha = 0.005$, $\kappa = 12$ and $\eta = 10\%$, showing the behaviour for high values of \bar{k} and a comparison of this with Shepelyansky's formula.	86
6.11	Simulation results for late time quantum diffusion rates for the QKR with $\alpha = 0.005$ and $\eta = 10\%$. $\kappa = 9, 10, 11, 12$	88
6.12	Simulation results for late time quantum diffusion rates for the QKR with $\alpha = 0.005$ and $\eta = 10\%$. $\kappa = 13, 14, 15, 16$	89
6.13	Simulation results for late time quantum diffusion rates for the QKR with $\alpha = 0.005$ and $\eta = 10\%$. $\kappa = 17, 18, 19, 20$	90
6.14	Simulation results of late time quantum diffusion rates for the QKR with $\alpha = 0.005$ and $\kappa = 9$, showing the variation with η	91
6.15	Simulation results of late time quantum diffusion rates for the QKR with $\alpha = 0.005$ and $\kappa = 11$, showing the variation with η	92

6.16	Simulation results of late time quantum diffusion rates for the QKR with $\alpha = 0.005$, $\kappa = 12$ and $\eta = 10\%$, showing the behaviour at large values of $\hbar k$	93
6.17	Comparison of simulation results for late time quantum diffusion rates and results from the right hand side of (6.10) for the QKR with $\alpha = 0.005$ and $\eta = 10\%$. $\kappa = 9, 11$	96
6.18	Comparison of simulation results for late time quantum diffusion rates and results from the right hand side of (6.10) for the QKR with $\alpha = 0.005$ and $\eta = 10\%$. $\kappa = 10, 12$	97
6.19	Comparison of simulation results for late time quantum diffusion rates with the analytical expression of Ammann <i>et al.</i> [30], (6.11), for the QKR with $\alpha = 0.005$ and $\eta = 10\%$	99
6.20	Comparison of simulation results for late time quantum diffusion rates with the analytical expression from (6.12), for the QKR with $\alpha = 0.005$, $\eta = 10\%$, and $\kappa = 9, 11$	100
6.21	Comparison of simulation results for late time quantum diffusion rates with the analytical expression from (6.12), for the QKR with $\alpha = 0.005$, $\eta = 10\%$, and $\kappa = 10, 12$	101
6.22	Comparison of simulation results for late time quantum diffusion rates with the analytical expression from (6.12), for the QKR with $\alpha = 0.005$ and $\kappa = 10$, showing variation with changing η	102
6.23	Diffusion rates, $D_0(n)$, for the quantum kicked rotor without noise, shown as a function of kick number and demonstrating the variation in behaviour with changing $\hbar k$ for $\hbar k \leq 5.5$	104
6.24	Diffusion rates, $D_0(n)$, for the quantum kicked rotor without noise, shown as a function of kick number and demonstrating the variation in behaviour with changing $\hbar k$ for values around the quantum resonance at $\hbar k = 2\pi$	105
6.25	Simulation results for late time quantum diffusion rates for the QKR with $\alpha = 0.005$ and $\eta = 10\%$. Spontaneous emission noise is implemented in the Austin style.	106
6.26	Comparison of simulation results for late time quantum diffusion rates with Austin-style spontaneous emission noise and results from the right hand side of (6.10) for the QKR with $\alpha = 0.005$ and $\eta = 10\%$. $\kappa = 10, 12$	106
6.27	Simulation results of initial quantum diffusion rates for the QKR with $\kappa = 12$ and $\eta = 10\%$, showing the effects of varying α	107
6.28	Simulation results of late time quantum diffusion rates for the QKR with $\kappa = 12$ and $\eta = 10\%$, showing the effects of varying α	108
7.1	Classical diffusion rates for the CKR with amplitude noise, from (7.1), plotted as a function of κ for different levels of noise.	111

7.2	Initial quantum diffusion rates as predicted by the modified Shepelyansky formula with the inclusion of amplitude noise, (7.3), for the quantum δ -kicked rotor with $\kappa = 10$	113
7.3	Initial quantum diffusion rates as predicted by the modified Shepelyansky formula with the inclusion of amplitude noise, (7.3), for the quantum δ -kicked rotor with $\kappa = 13$	114
7.4	Comparison of initial quantum diffusion rates computed from simulation results with those predicted by the modified Shepelyansky formula with the inclusion of amplitude noise, (7.3), for the quantum δ -kicked rotor with $\kappa = 10$	115
7.5	Comparison of initial quantum diffusion rates computed from simulation results with those predicted by the modified Shepelyansky formula with the inclusion of amplitude noise, (7.3), for the quantum δ -kicked rotor with noise=50%.	116
7.6	Late time diffusion rates from simulation results for the quantum kicked rotor with $\kappa = 10$, $\alpha = 0.005$, and varying levels of amplitude noise. . .	118
7.7	Late time diffusion rates from simulation results for the quantum kicked rotor with amplitude noise=50%, $\alpha = 0.005$, and varying values of κ . .	119
7.8	Simulation results of late time diffusion rates with a combination of spontaneous emission noise and amplitude noise, for the quantum kicked rotor with $\alpha = 0.005$, $\kappa = 11$, and amplitude noise=50%, with varying values of η	123
7.9	Simulation results of late time diffusion rates with a combination of spontaneous emission noise and amplitude noise, for the quantum kicked rotor with $\alpha = 0.005$, $\kappa = 11$, and $\eta=10\%$, with varying levels of amplitude noise.	124
8.1	Initial quantum diffusion rates as a function of pulse separation, T , as predicted for physical units by Shepelyansky's formula (8.1) for the δ -kicked rotor. We use ω_R from the Caesium D2 transition, so that the first quantum resonance occurs at $T = 60.4\mu s$, and $\phi_d \in [0.75\pi, 2.25\pi]$.	128
8.2	Initial quantum diffusion rates as a function of pulse separation, T , as predicted for physical units by Shepelyansky's formula (8.1) for the δ -kicked rotor. We use ω_R from the Caesium D2 transition, so that the first quantum resonance occurs at $T = 60.4\mu s$, and $\phi_d \in [2.5\pi, 4\pi]$. . .	129
8.3	Diffusion rates for the δ -kicked rotor in physical momentum units, showing variation with T for the initial quantum diffusion rate and the classical diffusion rate, as predicted by (8.1) and (8.2) respectively.	131
8.4	Experimental results from the group at the university of Oxford, showing mean energy of the cloud in physical units after 30 kicks for the quantum kicked rotor with $\phi_d \sim \pi$ and $\tau_p = 0.5\mu s$	134

8.5	Simulation results for the mean energy of the cloud in physical units after 30 kicks for the quantum kicked rotor with $\phi_d = \pi$ and $\tau_p = 0.5\mu\text{s}$. Amplitude noise at the 10% level is included to model fluctuations in the power and detuning of the kicking beam.	135
8.6	Experimental results for the mean energy of the cloud in physical units after 30 kicks for the quantum kicked rotor with $\eta = 1.2\%$ and $\tau_p = 0.52\mu\text{s}$, showing variation with changing ϕ_d	136
8.7	Simulation results for the mean energy of the cloud in physical units after 30 kicks for the quantum kicked rotor with $\eta = 1.2\%$ and $\tau_p = 0.52\mu\text{s}$. Amplitude noise at the 10% level is included to model fluctuations in the power and detuning of the kicking beam.	137
8.8	Experimental results for the mean energy of the cloud in physical units after 20 kicks for the quantum kicked rotor with $\phi_d = 4$, $\eta = 1\%$ and $\tau_p = 0.2\mu\text{s}$, showing variation with changing levels of amplitude noise. .	138
9.1	Diffusion rates, $D(1)$, in the second kick for the classical δ -kicked rotor for varying widths of the initial momentum distribution, as given by equation (9.3).	142
9.2	Diffusion rates in the second kick, $D(1)$, for the quantum δ -kicked rotor as a function of $\hbar k$ plotted for various values of $\sigma_n = \sigma_p/(2\hbar k_l)$, as predicted by (9.27).	150
9.3	Comparison of simulated diffusion rates in the second kick, $D(1)$, for the quantum kicked rotor ($\alpha = 0.005$, $\eta = 10\%$) with analytical values predicted from (9.27).	151
9.4	Diffusion rates in the second kick, $D(1)$, for the quantum δ -kicked rotor with $\sigma_n = 0.01$, plotted as a function of $\hbar k$ for various values of $\rho_0 = p_0/(2\hbar k_l)$, as predicted by (9.29).	153
9.5	Simulated diffusion rates in the third kick, $D(2)$, for the quantum kicked rotor with $\alpha = 0.005$, and $\eta = 10\%$ plotted as a function of $\hbar k$ for various values of σ_n	154
9.6	Simulated diffusion rates in the fourth kick, $D(3)$ for the quantum kicked rotor with $\alpha = 0.005$, and $\eta = 10\%$ plotted as a function of $\hbar k$ for various values of σ_n	155
9.7	Simulated diffusion rates in the fifth kick, $D(4)$, for the quantum kicked rotor with $\alpha = 0.005$, and $\eta = 10\%$ plotted as a function of $\hbar k$ for various values of σ_n	156
9.8	Simulated diffusion rates (points) and analytical predictions (lines) for the second kick in the quantum kicked rotor with $\alpha = 0.005$ and $\eta = 10\%$. The initial momentum distribution used is a coherent superposition of states separated by $2\hbar k_l$, which are sampled from a Gaussian distribution centred on $p_0 = 0$ with various values of σ_n	158

9.9	Comparison of analytical prediction from (9.31) with simulated diffusion rates in the second kick for the quantum kicked rotor with $\alpha = 0.005$, $\kappa = 12$ and $\eta = 10\%$, and with an initial coherent superposition of states separated by $2\hbar k_l$, and initially sampled from a Gaussian distribution centred on $\rho_0 = 0$ with $\sigma_n = 4$	159
A.1	Ordinary Bessel functions of the first kind, $J_\nu(z)$ for $\nu = 0, 1, 2$	168
A.2	Ordinary Bessel functions of the second kind, $Y_\nu(z)$ for $\nu = 0, 1, 2$	169

List of Tables

6.1	Simulation results for momentum diffusion rates in the classical kicked rotor with $\alpha = 0.005$, including spontaneous emission recoils for varying η	84
7.1	Table showing classical diffusion rates for varying κ and varying levels of noise, both from numerical simulations of the classical kicked rotor with $\alpha = 0.005$ and from the analytical result (7.1).	111
8.1	Comparison of and conversions between quantities in scaled units and physical units.	126

Chapter 1

Overview

1.1 Introduction

At the end of the nineteenth century, classical mechanics, as formulated by Newton and Hamilton, was seen to be a complete description of motion in the universe. This description was deterministic - if you knew the initial conditions of a system, you could predict its motion for all time. The wide application of these theories to most known phenomena led many physicists to believe that the whole universe was “mechanistic”.

However, this view was about to change. The advent of quantum mechanics in the early part of the twentieth century brought about a belief in a lack of determinism for physics on small scales. The predictability of classical mechanics became seen as an approximation, valid for large scale systems with a high value for their classical action (or high quantum numbers). This relationship was encompassed in Bohr’s correspondence principle, which states that classical mechanics should be obtained in the limit that $\hbar \rightarrow 0$. Classical mechanics as a philosophy for describing the universe became a useful limiting case, employed to test the viability of a new quantum theory.

By the 1960s, this situation had begun to change again. An increased understanding of classical systems had led to the understanding that classical systems were not always predictable. In fact, for a vast class of systems, sensitive dependence on initial conditions caused the complete failure of classical perturbation theory. These systems were referred to as “chaotic”, and amongst many other contributions to physics, they brought about a new challenge for the correspondence principle. Quantum systems cannot exhibit such a sensitive dependence on initial conditions, ultimately because Schrödinger’s equation is linear. This has led us to ask many questions about the behaviour of quantum systems which correspond to chaotic classical systems. Over the last thirty years, a whole new field has opened up, and is known as “Quantum Chaos”. Because there is really no such phenomenon, many critics suggest that it should probably be called “The quantum mechanics of systems that have chaotic classical analogues”. However, for obvious reasons this title has not become widely accepted.

Quantum chaos has become a large scale testing ground for our understanding of the relationship between classical systems and quantum systems. We want to know

what properties of the dynamics in a chaotic classical system are also observed in its quantum analogue, and we want to know what phenomena in quantum mechanics inhibit the stochastic nature of the classical dynamics. Most importantly, we want to know what happens as we make the quantum system behave more classically, and in what sense and under what conditions we can generate correspondence with the chaotic classical dynamics. The largest question facing this area of study is that of how to deal in the classical regime with the paradox of Schrödinger's cat - the macroscopic system which is supposed to exist in a coherent quantum superposition of macroscopically distinguishable states. Recently there has been a lot of emphasis placed on our understanding of decoherence in quantum systems in order to resolve this paradox. It is widely believed that the reason why quantum superpositions are not observed in macroscopic systems is related to the coupling of these systems to their environment.

Several systems in the field of quantum chaos have been used to test this, but one of the more successful systems has been the atom optics kicked rotor. The atom optics kicked rotor is an implementation of the quantum kicked rotor created using a cloud of ultra-cold atoms which interact with a pulsed standing wave of laser light. The quantum kicked rotor is the quantum analogue of the classical kicked rotor, which essentially is a rotor system in a standard pendulum potential, where the potential is pulsed on and off in time. Each pulse is referred to as a "kick" (hence the term "kicked rotor"), and for analytical purposes we often consider the case of the δ -kicked rotor, in which the kicks have an infinitesimally short duration. For experimental purposes we usually choose short but finite length rectangular pulses, and the resulting system is referred to as the (rectangular) pulse-kicked rotor. The classical kicked rotor is a well studied example of a chaotic system, which makes the atom optics kicked rotor ideal for studies in quantum chaos. The chaotic classical dynamics turn out to be completely suppressed in the quantum system. After a short time, a phenomenon known as dynamical localisation sets in, and the kinetic energy stops increasing as the system continues to be kicked. Two primary experimental groups have worked on this system over the past decade (see chapter 4), and have investigated this phenomenon of dynamical localisation, the effects of decoherence and various other forms of noise on the dynamics of the quantum system, and the effects of classical phase space structures on the quantum dynamics.

One of the most useful parameters to calculate or measure for the kicked rotor is the momentum diffusion rate, i.e., the increase in mean kinetic energy for the system during one kick. Many investigations have looked at what happens to this rate when most system parameters are fixed and the level of decoherence or noise is increased, in order to drive the quantum system back to classical behaviour. In this thesis, we follow the lead of a recent investigation by Bhattacharya *et al.* [1] in that we investigate the momentum diffusion rates obtained when we fix the level of noise or decoherence and make the system more macroscopic or less macroscopic by varying its action. Under various diffusion regimes and considering both decoherence through spontaneous emissions and amplitude noise on the kicking potential, we find dramatic resonance structures in the diffusion rates when the classical action is of the order of

\hbar , i.e., when the quantum system is on the threshold of classical-like behaviour. Our main results for the atom optics kicked rotor with spontaneous emission noise have been published in reference [2], and these are presented along with many other related investigations in this thesis.

1.2 Outline of Thesis

The structure of this thesis is essentially broken into a collection of chapters outlining the background theory of our system, and a collection of chapters which describe in detail the results of our investigation. It was intended that this thesis should be reasonably self-contained, and so a lot of background material is included in chapters 2-5 that will be familiar to many readers.

Chapter 2 serves as an introduction to the classical kicked rotor, its chaotic nature, and the resulting momentum diffusion rates. Most of the information contained there is classical theory, although section 2.4 on momentum diffusion rates in the kicked rotor is presented in an original way in order to better clarify the comparison of these diffusion rates with the corresponding results for the quantum system.

Chapter 3 introduces the quantum kicked rotor and its properties, including the phenomenon of dynamical localisation (where quantum coherences halt momentum diffusion in the system), and the early and late time diffusion regimes exhibited by that system.

Chapter 4 introduces the atom optics implementation of the quantum kicked rotor system. The standard experimental setup is described, as this is what we model numerically. There is a discussion of decoherence in quantum mechanics and specifically decoherence created through spontaneous emission noise in the atom optics kicked rotor. Amplitude noise is introduced, as is the limiting case of the atom optics kicked rotor as the effective Planck's constant is reduced to zero.

Chapter 5 describes the methods used to perform the numerical simulations from which we take the majority of the results presented in this thesis. Most of this chapter is well established theory, but there are several considerations taken into account in section 5.3.2, especially adjustments to the momentum state basis to prevent spectral leakage effects from discrete Fourier transforms, which were new adaptations specific to our research.

Chapter 6 presents all of our results for the atom optics kicked rotor with spontaneous emission noise. Some of these have been published in reference [2], and others are yet to be published. We relate our work to earlier theoretical considerations by Cohen [3], adapting his theory and giving a great deal of physical insight into the origins of the diffusion resonances found under various regimes from the numerical simulations.

Chapter 7 presents similar results, but for the quantum kicked rotor with amplitude noise. The last part of this chapter looks at the effects of including a combination of decoherence through spontaneous emissions and amplitude noise.

It is common practice to express the atom optics kicked rotor in a system of scaled

units in order to make its Hamiltonian exactly equivalent to that of the standard quantum kicked rotor. Chapter 8 looks at the diffusion resonances occurring in the atom optics kicked rotor in unscaled, or “physical” units, which is an easier description to work with experimentally. Results from our simulations are also compared in this chapter with some recent experimental results in this field.

Chapter 9 presents results from an investigation of the early time momentum diffusion rates in the atom optics kicked rotor when we begin with a very narrow initial momentum distribution. In addition to simulation results we present an analytical theory for the diffusion rate in the second kick, based on operator expectation values originally calculated by Scott Parkins. These results are extended (both analytically and in simulations) to quantum superpositions of initial momentum eigenstates.

The thesis is completed by three appendices. Appendix A provides some useful facts on Bessel functions, which occur commonly throughout the body of this thesis. Appendix B presents an outline calculation of some classical and quantum correlations that are important in the calculation of diffusion rates quoted throughout this thesis. Example source code related to the simulations discussed in chapter 5, which form the basis for many of our results, is included in Appendix C.

Chapter 2

The Classical Kicked Rotor

2.1 Introduction to Classical Dynamics

2.1.1 The Action Principle and Hamiltonian Mechanics

For an N -dimensional system with generalised coordinates q_1, q_2, \dots, q_N , we define the action associated with a trajectory over time $[t_1, t_2]$ to be

$$\mathcal{S}(q_1, q_2, \dots, q_n) = \int_{t_1}^{t_2} \mathcal{L}(q_1, q_2, \dots, q_n, \dot{q}_1, \dot{q}_2, \dots, \dot{q}_n, t) dt, \quad (2.1)$$

where \mathcal{L} is the Lagrangian of the system, i.e., $\mathcal{L} = \mathcal{T} - \mathcal{V}$ with \mathcal{T} the total kinetic energy of the system and \mathcal{V} the total potential energy of the system. We write $\dot{q}_i = dq_i/dt$. The motion of the system obeys the Action Principle (also known as Hamilton's Principle of Least Action), which states that of all the permitted trajectories a system may take between particular initial and final configurations, it will take the path(s) for which the action \mathcal{S} has an extreme value.

We define $p_j = \partial\mathcal{L}/\partial\dot{q}_j$ to be the conjugate momentum to the coordinate q_j , and we define the Hamiltonian of the system, $\mathcal{H}(q_1, q_2, \dots, q_n, p_1, p_2, \dots, p_n, t) \equiv \mathcal{H}(q_i, p_i, t)$, by the Legendre transformation

$$\mathcal{H} = \sum_{j=1}^N p_j \dot{q}_j - \mathcal{L}. \quad (2.2)$$

We can then re-express the Action Principle in the Hamiltonian formalism using Hamilton's equations of motion,

$$\dot{q}_i = \frac{\partial\mathcal{H}}{\partial p_i}, \quad (2.3a)$$

$$\dot{p}_i = -\frac{\partial\mathcal{H}}{\partial q_i}. \quad (2.3b)$$

In this formalism, a point in the system's $2N$ dimensional phase space is characterised by the co-ordinate values and the values of their conjugate momenta. If we have a conservative system (where \mathcal{V} depends only on q_j and t), and if there exist transformations from generalised co-ordinates to inertial Cartesian co-ordinates $x_i(q_1, \dots, q_N)$ which are not explicitly time dependent, then the Hamiltonian, \mathcal{H} , is the total energy function of the system. This is also true for some systems with velocity dependent potentials \mathcal{V} . If \mathcal{H} is independent of a particular co-ordinate q_j then $\dot{p}_j = 0$ and p_j is said to be conserved.

2.1.2 Canonical Transformations

It is often useful to change from one set of generalised co-ordinates to another in order to simplify the equations of motion. Such transformations are known as canonical transformations. In order for a new set of co-ordinates Q_1, \dots, Q_N and their conjugate momenta P_1, \dots, P_N to specify the same dynamics as the original co-ordinates q_1, \dots, q_N and their conjugate momenta p_1, \dots, p_N we need not require that the action, \mathcal{S} , along any path is the same in each system of co-ordinates. It is sufficient that the variation in the action along any path due to a given perturbation is the same in each system of co-ordinates. The Action Principle can be written as [4]

$$\delta \int_{t_1}^{t_2} \mathcal{L}(q_i, p_i, t) dt = \delta \int_{t_1}^{t_2} \left(\sum_{i=1}^N p_i \dot{q}_i - \mathcal{H}(q_i, p_i, t) \right) dt = 0, \quad (2.4)$$

where δ implies a variation in the integral expression to which it is applied based on any small perturbation about the trajectory forming the path of integration. In the new coordinates this may be written as

$$\delta \int_{t_1}^{t_2} \left(\sum_{i=1}^N P_i \dot{Q}_i - \bar{\mathcal{H}}(Q_i, P_i, t) \right) dt = 0. \quad (2.5)$$

So, if we choose new coordinates such that

$$\sum_{i=1}^N p_i \dot{q}_i - \mathcal{H}(p_i, q_i, t) = \sum_{i=1}^N P_i \dot{Q}_i - \bar{\mathcal{H}}(P_i, Q_i, t) + \frac{dF}{dt} \quad (2.6)$$

for some function F , then the new coordinates will describe the same dynamics as the original coordinates because for trajectories with fixed endpoints,

$$\delta \int_{t_1}^{t_2} \frac{dF}{dt} dt = 0. \quad (2.7)$$

F is called a generating function for the transformation, and can be any function of time t , either the old coordinates q_i or the old conjugate momenta p_i , and either the

new coordinates Q_i or the new conjugate momenta P_i . For example, if we choose $F = F_1(q_1, \dots, q_N, Q_1, \dots, Q_N, t)$ then

$$\frac{d}{dt}F_1(q_i, Q_i, t) = \sum_{i=1}^N \frac{\partial F_1}{\partial q_i} \dot{q}_i + \sum_{i=1}^N \frac{\partial F_1}{\partial Q_i} \dot{Q}_i + \frac{\partial F_1}{\partial t}. \quad (2.8)$$

Combining (2.6) and (2.8) and comparing terms gives the resulting transformation

$$p_i = \frac{\partial F_1}{\partial q_i}, \quad (2.9a)$$

$$P_i = -\frac{\partial F_1}{\partial Q_i}, \quad (2.9b)$$

$$\bar{\mathcal{H}}(P_i, Q_i, t) = \mathcal{H}(p_i, q_i, t) + \frac{\partial}{\partial t} F_1(q_i, Q_i, t). \quad (2.9c)$$

Generating functions of other variables may be produced from F_1 by way of a Legendre transformation. For example,

$$F_2(q_i, P_i, t) = F_1(q_i, Q_i, t) + \sum_{j=1}^N Q_j P_j. \quad (2.10)$$

The resulting transformation equations from this generating function are given by

$$p_i = \frac{\partial F_2}{\partial q_i}, \quad (2.11a)$$

$$Q_i = \frac{\partial F_2}{\partial P_i}, \quad (2.11b)$$

$$\bar{\mathcal{H}}(P_i, Q_i, t) = \mathcal{H}(p_i, q_i, t) + \frac{\partial}{\partial t} F_2(q_i, P_i, t). \quad (2.11c)$$

2.1.3 Integrability

If some canonical co-ordinate system exists such that Hamilton's equations of motion become independent, i.e.,

$$\dot{q}_i = \frac{\partial \mathcal{H}}{\partial p_i} = f_i(q_i), \quad (2.12)$$

then the system is said to be integrable [4, 5]. This requires there to exist N isolating integrals of the motion, each associated with some conserved quantity - a global invariant of the system. Such systems are predictable for all time with any set of initial conditions.

For a one dimensional system in which \mathcal{H} is explicitly independent of time, the one isolating integral required is provided by the Hamiltonian, and so all such systems are integrable. For higher dimensional systems, there is no general test for integrability, and instead, the individual isolating integrals must be discovered. Sometimes they are

associated with obvious symmetries in the dynamical system - for example, invariance of \mathcal{L} under rotations leads to conservation of angular momentum. However, numerical simulations are often required to discover the existence of “hidden” symmetries and associated isolating integrals.

2.1.4 Poincaré Sections

For an N dimensional system with a time independent Hamiltonian, the trajectories of the motion in phase space lie on a $2N - 1$ dimensional subspace (or “energy surface”) defined by the equation

$$H(q_1, \dots, q_N, p_1, \dots, p_N) = E_0. \quad (2.13)$$

Integrability of such systems is often studied using a Poincaré Section (or Surface of Section) [4, 5], in which we consider the intersection of trajectories of the motion with a $2N - 2$ dimensional subspace, chosen by projecting out a co-ordinate from the $2N - 1$ dimensional energy surface (i.e. setting $q_k = \text{const.}$ or $p_k = \text{const.}$ for some k). If additional integrals exist, then we expect the intersections of the trajectories with our $2N - 2$ dimensional subspace to lie on a surface of dimensionality less than $2N - 2$.

This is particularly useful for an autonomous two dimensional system. The conserved Hamiltonian confines trajectories to a three dimensional subspace, in which we may write, for example,

$$p_2 = p_2(p_1, q_1, q_2). \quad (2.14)$$

If in addition we have a second isolating integral,

$$I(q_1, q_2, p_1, p_2) = C, \quad (2.15)$$

for some constant C , then this confines the motion to a two dimensional subspace, and we can combine (2.14) and (2.15) to give

$$p_1 = p_1(q_1, q_2). \quad (2.16)$$

If we consider the intersection of the phase space trajectories with the subspace defined by $q_2 = \text{const.}$, then we see that they lie on a line defined by (2.16). We should thus see points which lie on a line if we plot the values of q_1 and p_1 for the system whenever $q_2 = 0$. If the points on the plot do not lie on a line, but are instead scattered over a finite area (their positions are still limited by energy conservation), we know that the isolating integral (2.15) does not exist, and the system is not integrable.

2.1.5 Time - Dependent Systems

So far we have mainly discussed autonomous systems - those for which the Hamiltonian is explicitly independent of time. We can easily generalise to the case of a nonautonomous system using the concept of an extended phase space [4].

We are free to parameterise the path integral in (2.4) using any variable which is independent of the variation implied by δ . For example, any differentiable function of t is a suitable choice. Choosing such a variable, ξ , we can write

$$\delta \int_{\xi_1}^{\xi_2} \left(\sum_{i=1}^N p_i \frac{dq_i}{d\xi} - \mathcal{H} \frac{dt}{d\xi} \right) d\xi = 0. \quad (2.17)$$

If we then increase the dimensionality of the system by choosing a new co-ordinate Q_{N+1} such that $Q_{N+1} = t$ and $P_{N+1} = -\mathcal{H}$, we can write the path integral as

$$\delta \int_{\xi_1}^{\xi_2} \sum_{i=1}^{N+1} P_i \frac{dQ_i}{d\xi} d\xi = 0, \quad (2.18)$$

where we now consider trajectories in an extended phase space with $2N+2$ dimensions. This is essentially a canonical transformation with $Q_i = q_i$ and $P_i = p_i$ for $i = 1, \dots, N$. The corresponding generating function is

$$F_2(q_j, P_j, t) = \sum_{i=1}^N P_i q_i + P_{N+1} t \quad (2.19)$$

and so from (2.11c) the transformed Hamiltonian is given by

$$\begin{aligned} \bar{\mathcal{H}}(Q_i, P_i) &= \mathcal{H}(q_i, p_i, t) - P_{N+1} \\ &= \mathcal{H}(q_i, p_i) - \mathcal{H}. \end{aligned} \quad (2.20)$$

For our choice of transformation, we also find that $t(\xi) = \xi$ provided we set $t(0) = 0$. Note that whilst $\bar{\mathcal{H}}$ evaluates numerically to zero, it is the non-trivial dependence on of the Hamiltonian on Q_i and P_i that describes the motion.

Our Hamiltonian for our $N+1$ dimensional system is now explicitly independent of our parameter, ξ . We have essentially used an extra dimension to decouple the dynamics of our system from the system clock. In this way, we can transform any time dependent system into an autonomous system with one higher dimension.

One of the simplest examples in which this technique is useful is the sinusoidally driven pendulum system. The Hamiltonian for such a system is dependent on time, because the potential created by the driving field is time dependent. By extending the phase space and re-parameterising the system we create an extra dimension which could be seen as specifying the phase of the driving field. The new Hamiltonian then represents the coupling of the system to that phase through the new dimension, rather than including an explicit time dependence.

2.1.6 Periodic Systems and Action-Angle Variables

A periodic system is a system in which for every generalised coordinate, q_i , either q_i is bounded or \mathcal{H} is a periodic function of q_i . The motion of an integrable periodic

system may be categorised into two cases. Either (1) q_i and p_i are periodic functions of time with the same period for each i or (2) p_i is a periodic function of q_i . Case (1) is known as libration and case (2) is known as rotation. In case (1), the periods need not be the same for all degrees of freedom. If the ratio of periods is not rational for all combinations of different degrees of freedom then the system is referred to as being conditionally periodic.

For integrable periodic systems there is a particularly convenient choice of coordinate variables and their conjugate momenta known as the action-angle variables. We consider the action integral

$$J_i = \frac{1}{2\pi} \oint p_i dq_i, \quad (2.21)$$

where the integral is taken over one full cycle of a periodic trajectory. It is seen readily that J_i is conserved, because the definition gives the same value for all points on the trajectory. We then define the angle variable θ_i to be the dimensionless coordinate variable with conjugate momentum J_i . Because J_i is conserved, the Hamiltonian is independent of θ_i , and we write $\mathcal{H}(\theta_j, J_j) = \mathcal{H}(J_j)$. We also see that $\theta_i = \omega_i t + \theta_i(0)$ where $\omega_i = \omega_i(J_1, \dots, J_N) = \partial\mathcal{H}/\partial J_i$.

We can express transformation to action-angle variables using a canonical transformation with a generating function $F_2(q_i, J_i)$. The transformation equations are given by (2.11a) and (2.11b) with $Q_i = \theta_i$ and $P_i = J_i$.

2.1.7 Near-Integrable Systems and the KAM Theorem

In general the dynamics of non-integrable systems is very difficult to predict. For appropriate regimes of initial conditions these systems exhibit chaotic motion, which follows from their sensitive dependence on initial conditions and leads to motion which is essentially stochastic in nature.

We are able to make some predictions about the class of systems known as near-integrable systems, based primarily on the work of Kolmogorov, Arnold and Moser [6, 7, 8] (the main results of which are encompassed in the KAM Theorem [4]). Near-integrable systems are those systems which can be expressed as a perturbation of integrable systems, and their phase space is characterised by regions of stochasticity separated by regular trajectories. The Hamiltonian for such systems has the form

$$\mathcal{H}(J_1, \dots, J_N, \theta_1, \dots, \theta_N) = \mathcal{H}_0(J_1, \dots, J_N) + \epsilon\mathcal{H}_1(J_1, \dots, J_N, \theta_1, \dots, \theta_N) \quad (2.22)$$

where \mathcal{H}_0 is the Hamiltonian for an integrable system, J_i and θ_i are the action-angle variables for such a system and ϵ is a small constant. We are mainly interested in periodic two dimensional systems, which we assume to be autonomous.

The KAM theorem states that the phase space of these systems is filled with a finite fraction of regular trajectories (resulting from the unperturbed Hamiltonian), which occur discontinuously as a function of initial conditions. For a two dimensional

periodic system these trajectories have the same topology as the surface of a torus in the four dimensional phase space (the periodic motion in each dimension has a circular topology, and the product space of two circles has the topology of a toroidal surface).

Regular trajectories are periodic in θ_1 with an angular frequency $\omega_1(J_1)$ and periodic in θ_2 with an angular frequency $\omega_2(J_2)$. Those with a rational ratio of angular frequencies, $\omega_1(J_1)/\omega_2(J_2)$, which are closed periodic trajectories of the unperturbed Hamiltonian, are called primary resonances. These resonances provide structures in phase space which interact to form secondary resonances, and thus create more complicated structures. Regular trajectories with an irrational ratio of angular frequencies (i.e. conditionally periodic trajectories) are interesting because they form an invariant curve which densely covers a toroidal surface. The resulting invariant torus is called a KAM torus, and acts as a barrier through which stochastic trajectories may not pass. For this reason, these tori are also known as KAM boundaries.

Systems to which the KAM theorem may be applied have perturbation Hamiltonians which may be written in the form

$$\mathcal{H}_1 = \sum_{n_1=-\infty}^{\infty} \dots \sum_{n_N=-\infty}^{\infty} \mathcal{H}_{n_1, \dots, n_N}(J_1, \dots, J_N) \exp[i(n_1\theta_1 + \dots + n_N\theta_N)]. \quad (2.23)$$

Each term in the summation is a primary non-linear resonance. As ϵ increases, the topological defects in phase space created by the non-linear resonances increase in size. For some finite ϵ particular KAM tori will be breached and destroyed by the resonances, and for some critical perturbation strength $\epsilon = \epsilon^*$ all KAM tori will be destroyed. At this point the system is said to be globally chaotic (as opposed to locally chaotic), because the path of chaotic trajectories is now restricted only by the total energy available in the system, and not by KAM boundaries. The most simple way to obtain an estimate for the value of ϵ^* is by way of the Chirikov overlap criterion, which assumes that all KAM tori are destroyed when all adjacent resonances overlap, so that the region between them can no longer contain any KAM tori.

2.2 The Classical Rotor

We now discuss the motion of the Classical Rotor (also known as the simple pendulum), illustrated in figure 2.1, which is the simple system upon which the kicked rotor is based. The Lagrangian for this system is

$$\mathcal{L} = \frac{1}{2}ml^2\dot{\theta}^2 + mgl \cos(\theta) \quad (2.24)$$

and the momentum conjugate to θ is given by

$$L = ml^2\dot{\theta}. \quad (2.25)$$

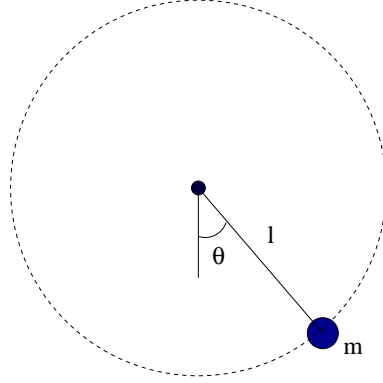


Figure 2.1: The Classical Rotor, a mass m rotating on a massless rod of length l in a gravitational field with acceleration due to gravity g .

Thus the Hamiltonian for the system is given by

$$\begin{aligned}\mathcal{H} &= \frac{L^2}{2ml^2} - mgl \cos(\theta) \\ &= \frac{L^2}{2I} - K \cos(\theta)\end{aligned}\quad (2.26)$$

where $I = ml^2$ and $K = mgl$. From this we can obtain Hamilton's equations of motion for the system,

$$\dot{L} = -K \sin(\theta), \quad (2.27a)$$

$$\dot{\theta} = \frac{L}{I}. \quad (2.27b)$$

The classical rotor is a one dimensional system with a conserved Hamiltonian ($H(\theta, L) = E_0$), and hence is integrable. It exhibits periodic motion, as described in section 2.1.6, either in the form of oscillations about $\theta = 0$ (libration), or in the form of full rotations. A plot of several trajectories in the phase space of this system is shown in Figure 2.2. Closed trajectories represent libration of the rotor, and open trajectories give examples of rotations. The curves passing through $(\theta = \pi, L = 0)$ are the separatrix trajectories, and mark the boundary between the two modes of periodic behaviour. Motion on the separatrix curves is not periodic, although it is the limiting case of both modes of periodic behaviour.

An analytical solution for θ and L may be found as a function of time, t , in terms of Jacobi elliptic functions. The derivation of this result may be found in many textbooks, including references [5, 4]. We define the inverse function $\text{sn}^{-1}(x)$ as

$$\text{sn}^{-1}(x) = \int_0^x \frac{dt}{\sqrt{1-t^2}\sqrt{1-k^2t^2}} \quad (2.28a)$$

$$= \int_0^{\text{sn}^{-1}(x)} \frac{d\psi}{\sqrt{1-k^2\sin^2(\psi)}}. \quad (2.28b)$$

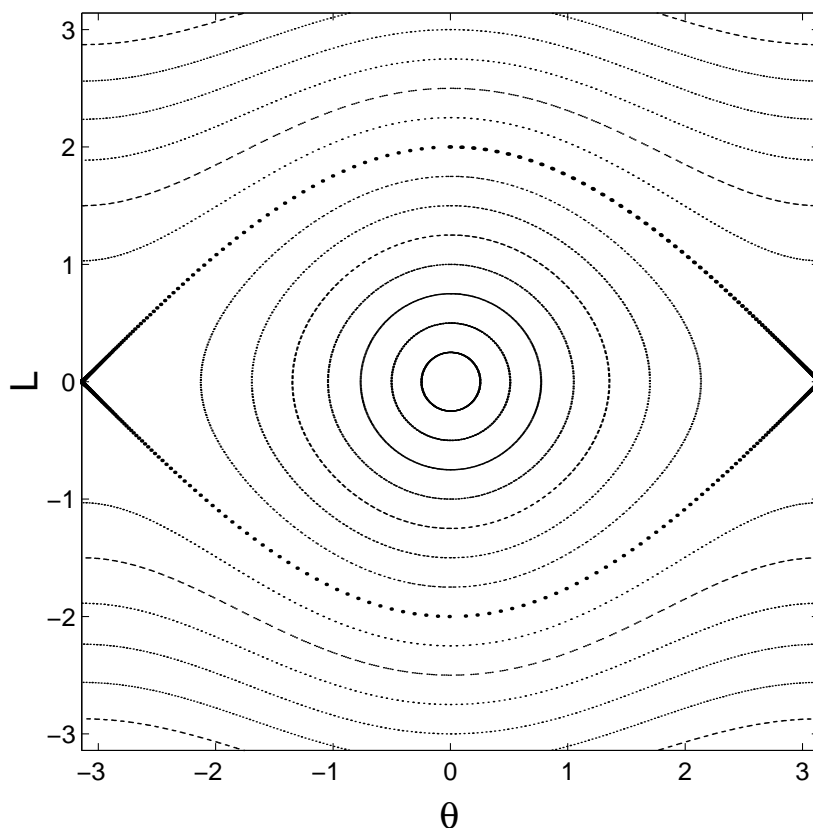


Figure 2.2: Dotted Lines showing trajectories in phase space for a classical rotor with $I = 1$ and $K = 1$. The angle variable θ has been wrapped into the range $[-\pi, \pi]$.

Then, if $y = \text{sn}^{-1}(x)$, we say $x = \text{sn}(y)$, and we also define

$$\text{cn}(y) = \sqrt{1 - \text{sn}^2(y)}, \quad (2.29)$$

$$\text{dn}(y) = \sqrt{1 - k^2 \text{sn}^2(y)}. \quad (2.30)$$

Making use of the signum function, which is defined by

$$\text{sgn}(x) = \begin{cases} 1 & x > 0 \\ -1 & x < 0 \\ 0 & x = 0, \end{cases} \quad (2.31)$$

we have, in the case of libration,

$$k = \sqrt{\frac{1}{2} \left(1 + \frac{E_0}{K} \right)}, \quad (2.32a)$$

$$\theta = 2 \text{sgn}(L_0) \sin^{-1}[k \text{sn}(\sqrt{K}t + u_0)], \quad (2.32b)$$

$$L = 2 \text{sgn}(L_0) \sqrt{K} k \text{cn}(\sqrt{K}t + u_0), \quad (2.32c)$$

where $u_0 = \text{sn}^{-1}(\text{sgn}(L_0) \sin^{-1}(\sin(\theta_0/2)/k))$. For rotation, we have

$$k = 1/\sqrt{\frac{1}{2} \left(1 + \frac{E_0}{K}\right)}, \quad (2.33a)$$

$$\theta = 2 \text{sgn}(L_0) \sin^{-1}[\text{sgn}[\text{cn}(\sqrt{K}t/k + u_0)] \text{sn}(\sqrt{K}t/k + u_0)], \quad (2.33b)$$

$$L = 2 \text{sgn}(L_0) \sqrt{K}/k \text{dn}(\sqrt{K}t/k + u_0), \quad (2.33c)$$

where $u_0 = \text{sn}^{-1}(\text{sgn}(L_0)\theta_0/2)$. L_0 is defined throughout as $L(t=0)$.

2.3 The Classical Kicked Rotor

We now turn our attention to the primary system of interest in this thesis - the kicked rotor. Essentially the kicked rotor consists of a classical rotor for which the potential field (due to gravity in the case of a simple pendulum) is pulsed on for short periods and at other times the rotor is left to evolve freely.

The Hamiltonian for the kicked rotor system is given by

$$\mathcal{H} = \frac{\rho^2}{2} + k \cos(\phi) \sum_{n=0}^{\infty} f(t - nT), \quad (2.34)$$

where $f(t)$ is some pulse profile function defined on the interval $[0, T]$, T is the pulse period, and we have chosen to write the momentum and displacement variables as ρ and ϕ respectively. This system is one dimensional and nonautonomous, but may be treated as an effective two dimensional autonomous system.

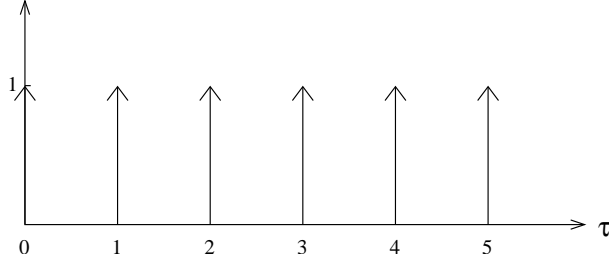
2.3.1 The δ -Kicked Rotor

The δ -Kicked Rotor is the system that arises when we choose the pulse profile function $f(t)$ in such a way that the pulse length is infinitesimal, but the area under the pulse is finite. Conventionally, we also scale the time axis as $\tau = t/T$ so that the period is set to 1. The Hamiltonian for the δ -kicked rotor is thus

$$\mathcal{H} = \frac{\rho^2}{2} + \kappa \cos(\phi) \sum_{n=0}^{\infty} \delta(\tau - n), \quad (2.35)$$

where κ is a parameter known as the classical stochasticity, and adjusts the total area under each δ function pulse. The summation $\sum_{n=0}^{\infty} \delta(\tau - n)$ essentially provides us with a train of infinitesimal length pulses of unit area, as illustrated in figure 2.3. In its most versatile and well defined form, the δ function, $\delta(x)$, is defined as a generalised function in the context of distribution theory [9]. It is often useful, though, to think of it as the limit of a series of square wave pulses, i.e.,

$$\delta(x) = \lim_{a \rightarrow 0} \begin{cases} 1/a & |x| < \frac{a}{2} \\ 0 & |x| \geq \frac{a}{2} \end{cases}. \quad (2.36)$$

Figure 2.3: A train of δ functions

Hamilton's equations of motion for the δ -kicked rotor are given by

$$\dot{\phi} = \rho, \quad (2.37a)$$

$$\dot{\rho} = \kappa \sin(\phi) \sum_{n=0}^{\infty} \delta(\tau - n), \quad (2.37b)$$

where $\dot{\phi}$ represents the total derivative of ϕ with respect to τ , rather than t . From these equations, we can see that changes in ρ occur discontinuously wherever $\tau = n$ for positive integer values of n , i.e., whenever the system is “kicked”. At those kicks, ρ jumps in value by $-\kappa \sin(\phi)$, whilst ϕ remains constant. Between kicks, when $\dot{\rho} = 0$, ϕ changes at a rate equal to the current value of ρ . Thus, we can rewrite the equations of motion for the δ -kicked rotor as a mapping. If we denote the values of ϕ and ρ immediately before the kick at $\tau = n$ by ϕ_n and ρ_n respectively, then we can write

$$\rho_{n+1} = \rho_n + \kappa \sin(\phi_n), \quad (2.38a)$$

$$\phi_{n+1} = \phi_n + \rho_{n+1}. \quad (2.38b)$$

This mapping is known as the standard map, and has been studied extensively in terms of the transition to global chaos, which occurs as κ (hence known as the stochasticity parameter) is increased. It is reasonably simple to simulate this mapping numerically, and as described in section 2.1.4, one of the best ways to analyse the system is by way of Poincaré sections. We take “snapshots” of the phase space of our effective two dimensional system at a particular instant in each cycle of the system. To clarify symmetries in the system, we choose to plot points in the (ϕ, ρ) subspace when $\tau = n + \frac{1}{2}$ for integer values of n . The pulse train is then somewhat symmetric above and below the “snapshot” times, and we observe reflection symmetries in the ϕ and ρ axes of the Poincaré section as a result. (The same would be true if we chose $\tau = n$ for integer values of n as the snapshot time, but either choice is equally convenient.)

Figures 2.4-2.9 show Poincaré sections for various values of κ . The reflection symmetry in the $\phi = 0$ axis is clearly displayed, and this same symmetry occurs in the $\rho = 0$ axis, although this is not shown in the figures. The structure shown is periodic in ρ with a period of 4π , which arises from our choice of “snapshot” times.

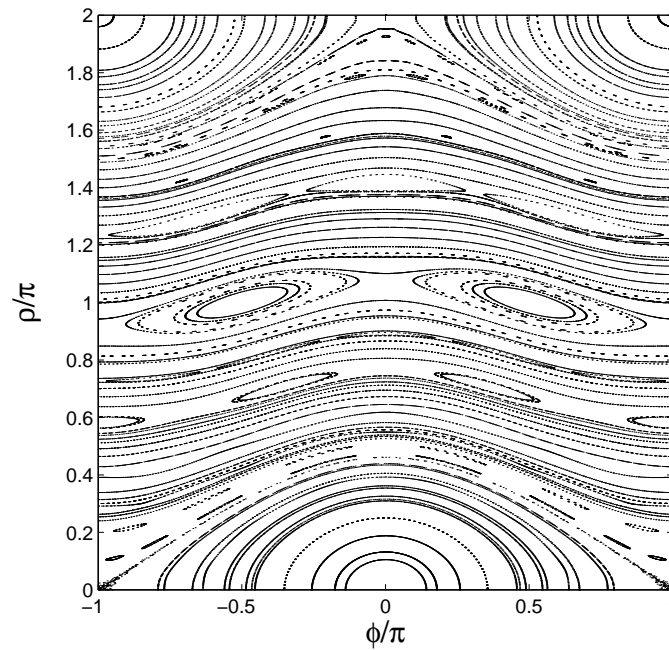


Figure 2.4: Poincaré Section for the classical kicked rotor with $\kappa = 0.5$

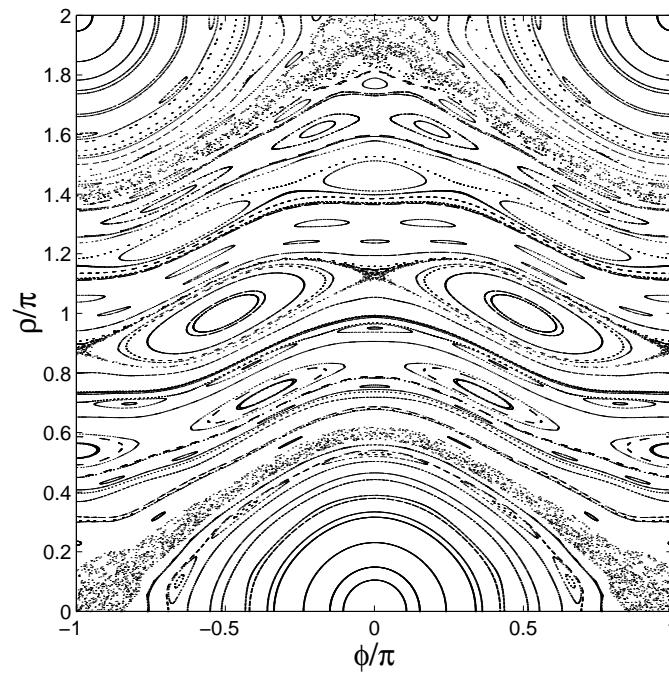
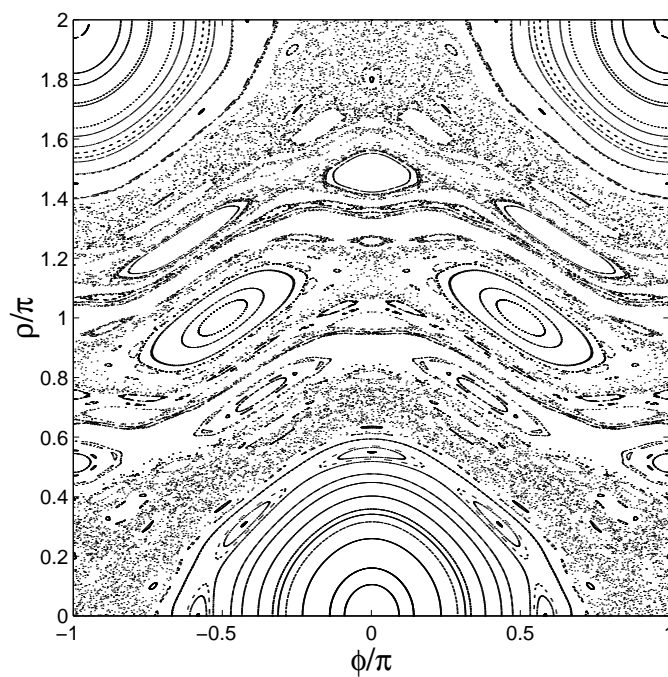
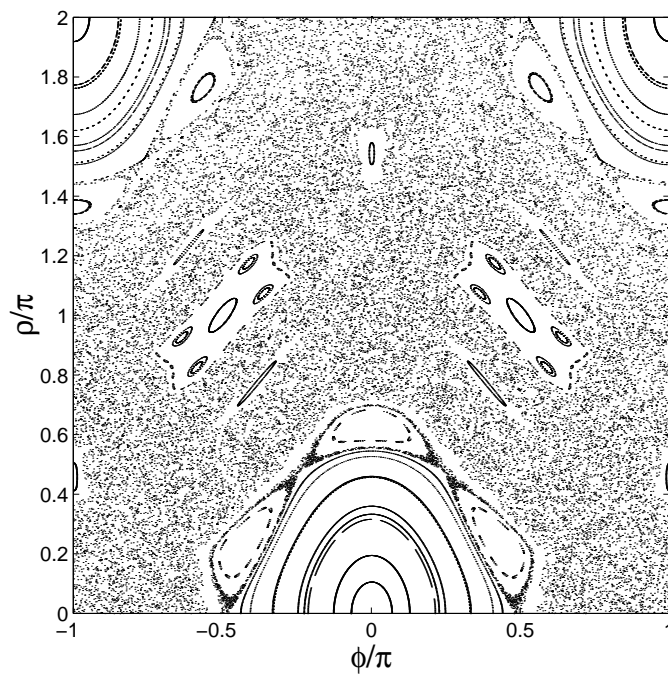


Figure 2.5: Poincaré Section for the classical kicked rotor with $\kappa = 0.8$

Figure 2.6: Poincaré Section for the classical kicked rotor with $\kappa = 1.0$ Figure 2.7: Poincaré Section for the classical kicked rotor with $\kappa = 1.5$

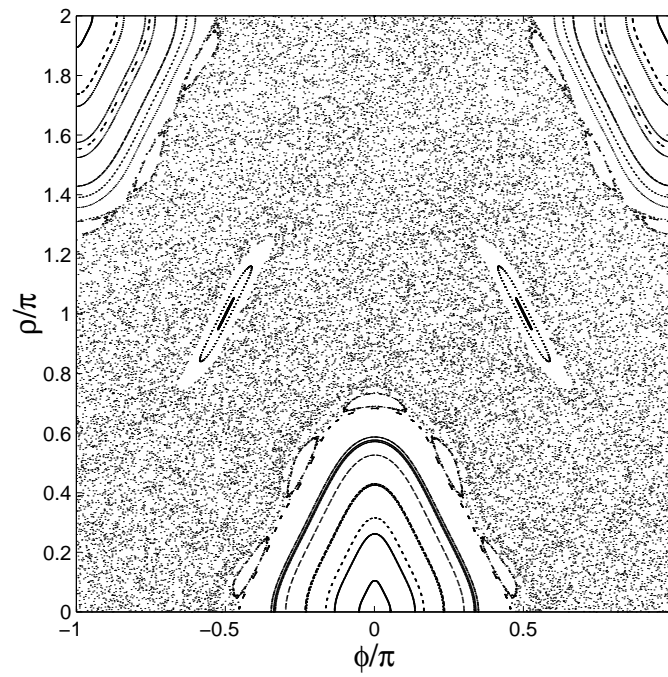


Figure 2.8: Poincaré Section for the classical kicked rotor with $\kappa = 2.0$

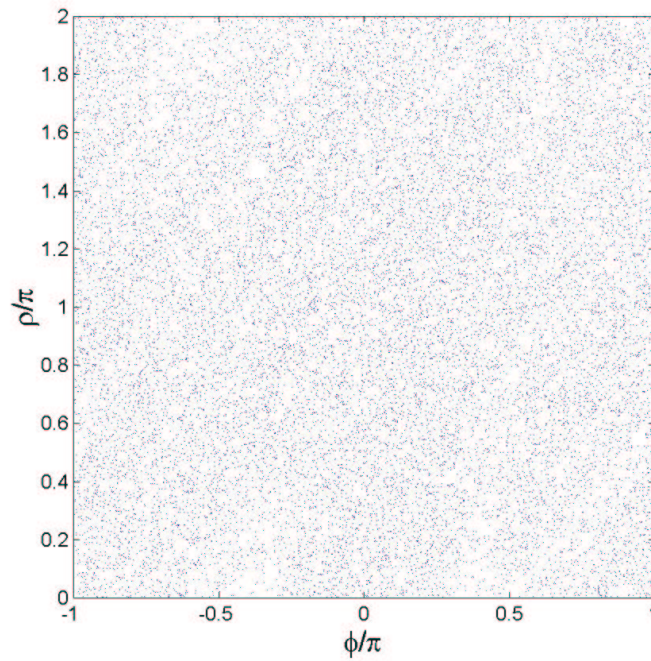


Figure 2.9: Poincaré Section for the classical kicked rotor with $\kappa = 7.0$

For $\kappa = 0.5$ we can see (figure 2.4) that there are large regions of regular behaviour, with the only significant chaotic region being the trajectories close to the separatrix between rotation and libration modes. These regions grow significantly as we move to $\kappa = 0.8$ in figure 2.5, but regular trajectories still dominate the section, and phase space is still partitioned by KAM tori which have not yet been destroyed.

For $\kappa = 1.0$ we see in figure 2.6 that the chaotic regions have grown and overlapped and the last remaining KAM tori have been destroyed. While there are still some regions containing only regular trajectories, chaotic trajectories throughout the rest of phase space are not bounded, and so we have observed the onset of global chaos. As we increase κ to $\kappa = 1.5$ (figure 2.7), $\kappa = 2.0$ (figure 2.8) and then $\kappa = 7.0$ (figure 2.9) we observe the destruction of the regions of regular behaviour. For $\kappa = 7$, the phase space is filled entirely with chaotic trajectories, and we observe no structure at all in the corresponding Poincaré section.

From a resonance analysis of the Hamiltonian for the δ -kicked rotor, it can be shown (see section 2.3.2) that the primary resonances in this system are separated by $\Delta\rho = 2\pi$ and that the width of each primary resonance is $4\sqrt{\kappa}$. Thus, if we apply the Chirikov overlap criterion described in section 2.1.7, we obtain an estimate of $\kappa^* = 2.47$ for the overlap of all primary resonances, and hence for the onset of global chaos. However, this turns out to be a much overestimated upper bound, mainly because the criterion ignores the overlap of the structures produced by the coupling of different resonances. A much more sensitive criterion for stochasticity is described by Lichtenberg and Lieberman [4], and gives $\kappa^* = 0.9716$. This agrees well with what we observe qualitatively from our Poincaré sections for $\kappa = 0.8$ and $\kappa = 1.0$.

2.3.2 The Pulse-Kicked Rotor

The δ -kicked rotor is an idealised system, and in practice we can only realise it approximately experimentally. In order to do this we usually choose to use rectangular kicks, which have a finite width in time, α , and a height k , as shown in figure 2.10. The major difference between the δ -kicked rotor and a kicked rotor with rectangular pulses is that for the latter system, the effective “strength” of each kick (given by the stochasticity parameter κ for the δ -kicked rotor) varies as the momentum, ρ , of the rotor changes. For example, it is possible to have an effective kick strength of zero in the pulse-kicked rotor system for particular values of ρ because of the existence of KAM boundaries, which occur even for large values of k . In the Poincaré section, these exist along lines of approximately constant ρ , but can become somewhat distorted for large kick strengths. Physically, we may think of these momentum values as the momenta at which the rotor will pass through an integer number of rotations in the time α , thus experiencing a time averaged net force of zero from a particular kick regardless of the initial value of ϕ . This will occur whenever $\rho = 2\pi m/\alpha$ for some integer m .

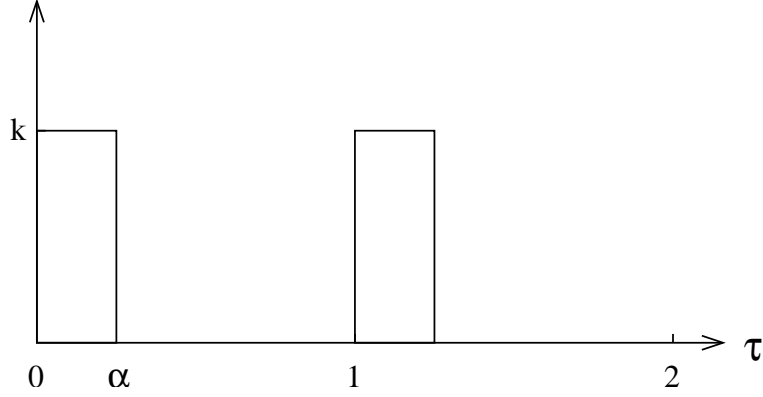


Figure 2.10: Square Wave Pulses

To see how this modification of kick strength with changing momentum value comes about, we need to look at how rectangular pulses modify the resonances in the Hamiltonian. To simplify our calculations, we rewrite the Hamiltonian for the kicked rotor as

$$\mathcal{H} = \frac{\rho^2}{2} + k \cos(\phi) \sum_{n=-\infty}^{\infty} f(t - nT). \quad (2.39)$$

In the case of δ -kicks, we can then make use of the identity [9, 10]

$$\sum_{n=-\infty}^{\infty} \delta(\tau - n) = \sum_{m=-\infty}^{\infty} \cos(2\pi m\tau) \quad (2.40)$$

and we see that

$$\begin{aligned} \cos(\phi) \sum_{n=-\infty}^{\infty} \delta(\tau - n) &= \cos(\phi) \sum_{m=-\infty}^{\infty} \cos(2\pi m\tau) \\ &= \frac{1}{2} \left(\sum_{m=-\infty}^{\infty} \cos(\phi - 2\pi m\tau) + \sum_{m=-\infty}^{\infty} \cos(\phi + 2\pi m\tau) \right) \\ &= \sum_{m=-\infty}^{\infty} \cos(\phi - 2\pi m\tau). \end{aligned} \quad (2.41)$$

Thus, we may express the Hamiltonian for the δ -kicked rotor as a sum over non-linear resonances in the form

$$\mathcal{H} = \frac{\rho^2}{2} + \kappa \sum_{n=-\infty}^{\infty} \cos(\phi - 2\pi n\tau). \quad (2.42)$$

To obtain a similar expression for the kicked rotor with rectangular kicks we use Fourier transform techniques and make use of the properties of the generalised function $\delta(x)$ [9]. We define the Fourier transform of a function $f(t)$ to be

$$F(\nu) = \frac{1}{2\pi} \int_{-\infty}^{\infty} f(t)e^{-i2\pi\nu t} dt. \quad (2.43)$$

The inverse transform is then given by

$$f(t) = \int_{-\infty}^{\infty} F(\nu)e^{i2\pi\nu t} d\nu. \quad (2.44)$$

We denote the rectangular pulse of width α by

$$\Pi(t/\alpha) = \begin{cases} 1 & |t| < \alpha/2 \\ 0 & |t| \geq \alpha/2, \end{cases} \quad (2.45)$$

and the Fourier transform of this rectangular pulse is $\alpha \text{sinc}(\alpha\nu)$ where the sinc function is given by

$$\text{sinc}(x) = \begin{cases} \sin(\pi x)/(\pi x) & x \neq 0 \\ 1 & x = 0. \end{cases} \quad (2.46)$$

Now, we can write the train of rectangular pulses as a convolution of one rectangular pulse with a train of δ functions [9],

$$\sum_{n=-\infty}^{\infty} \Pi[(\tau - n)/\alpha] = \Pi(\tau/\alpha) * \sum_{n=-\infty}^{\infty} \delta(\tau - n), \quad (2.47)$$

where the convolution of two functions is defined as

$$(f * g)(t) = \int_{-\infty}^{\infty} f(\tau)g(t - \tau) d\tau. \quad (2.48)$$

We also know that the Fourier transform of the convolution of two functions is the product of the Fourier transforms of the functions, i.e.,

$$(f * g)(t) \leftrightarrow F(\nu)G(\nu) \quad (2.49)$$

where $f(t) \leftrightarrow F(\nu)$ and $g(t) \leftrightarrow G(\nu)$. Then, using the Fourier transform pair [9]

$$\sum_{n=-\infty}^{\infty} \delta(\tau - n) \leftrightarrow \sum_{m=-\infty}^{\infty} \delta(\nu - m), \quad (2.50)$$

we can write

$$\begin{aligned} \Pi(\tau/\alpha) * \sum_{n=-\infty}^{\infty} \delta(\tau - n) &= \int_{-\infty}^{\infty} \alpha \text{sinc}(\alpha\nu) \sum_{m=-\infty}^{\infty} \delta(\nu - m) e^{i2\pi\nu\tau} d\nu \\ &= \sum_{m=-\infty}^{\infty} \alpha \text{sinc}(\alpha m) e^{i2\pi m\tau} \\ &= \sum_{m=-\infty}^{\infty} \alpha |\text{sinc}(\alpha m)| e^{i\gamma_m} e^{i2\pi m\tau}, \end{aligned} \quad (2.51)$$

where $\gamma_m = 0$ if $\text{sinc}(\alpha m) \geq 0$ and $\gamma_m = \pi$ if $\text{sinc}(\alpha m) < 0$. Using the fact that $\text{sinc}(x)$ is an even function, so that $\gamma_m = \gamma_{-m}$, and also the fact that $e^{i\pi} = e^{-i\pi}$, we can then write

$$\begin{aligned} \prod (\tau/\alpha) * \sum_{n=-\infty}^{\infty} \delta(\tau - n) &= \frac{1}{2} \sum_{m=-\infty}^{\infty} \alpha |\text{sinc}(\alpha m)| [e^{i\gamma_m} e^{i2\pi m\tau} + e^{-i\gamma_m} e^{-i2\pi m\tau}] \\ &= \sum_{m=-\infty}^{\infty} \alpha |\text{sinc}(\alpha m)| \cos(2\pi m\tau + \gamma_m). \end{aligned} \quad (2.52)$$

Thus, the Hamiltonian for the kicked rotor with rectangular pulses may be written as

$$\mathcal{H} = \frac{\rho^2}{2} + k\alpha \sum_{n=-\infty}^{\infty} |\text{sinc}(\alpha n)| \cos(\phi - 2\pi n\tau). \quad (2.53)$$

The primary resonances of this Hamiltonian occur at $\rho = d\phi/dt = 2\pi n$, so if we evaluate the function $\text{sinc}(\alpha n)$ at $n = \rho/(2\pi)$ we see in comparison with (2.42) that the stochasticity parameter, κ , has been replaced by a function which depends on the value of ρ ,

$$\kappa_{\text{eff}} = k\alpha \left| \text{sinc} \left(\frac{\alpha\rho}{2\pi} \right) \right|. \quad (2.54)$$

This is the same result obtained by Klappauf *et al.* in reference [11], and is plotted in figure 2.11 for various values of α . For small α and ρ , the rectangular kicks approximate δ -kicks with kick strength $\kappa = \alpha k$. However, at higher values of ρ the kick strength is considerably smaller than this value. Thus, if we wish to approximate the δ -kicked rotor with rectangular pulses, we must use as small a value of α as possible, and, if possible, deal only with small values of ρ .

We now come back to the issue of remaining KAM tori. In terms of the KAM theorem, this phenomenon occurs because the non linear resonances produced by rectangular kicks have sizes which vary depending on the central momentum at which the resonance is located. For the δ -kicked rotor, the widths of the resonances are equal to $4\sqrt{\kappa}$ - a result which we applied in section 2.3.1 to derive the result for κ^* from the Chirikov overlap criterion (it is now also apparent where the separation of $\Delta\rho = 2\pi$ between the resonances comes from).

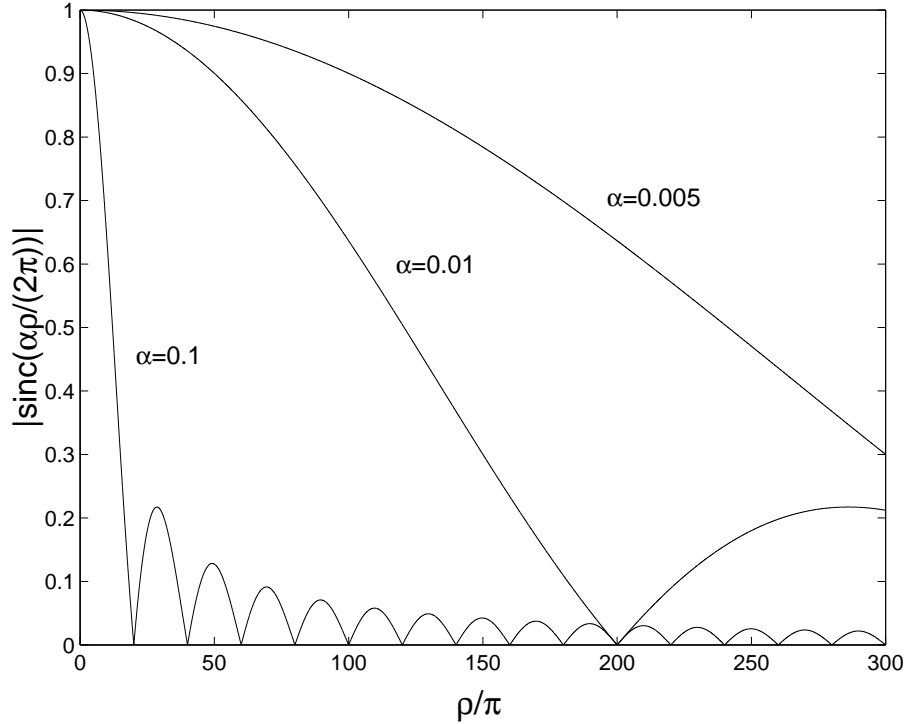


Figure 2.11: $|\text{sinc}(\alpha\rho/(2\pi))|$ for different values of α , showing the dependence on ρ of κ_{eff} .

In the same way, we find for rectangular kicks that the size of a resonance centred at the momentum value $\rho = 2\pi n$ for some integer n will be proportional to $\sqrt{\kappa}|\text{sinc}(\alpha n)|$. For some value of ρ , the resonance located at that value has zero size, and will be unable to breach the nearby KAM tori. This will result in some KAM tori remaining once all of the other resonances are already overlapping. The zeros of $|\text{sinc}(\alpha n)|$ are given by $\alpha n = m$ for some integer m , so that the values near which KAM boundaries will exist are again given by $\rho = 2\pi m/\alpha$. This is also sensible because it is at these values that $\kappa_{eff} \rightarrow 0$.

The KAM boundaries are clearly visible near values of $\rho = 20\pi m$ for integer m in figure 2.12, which shows a Poincaré section for a pulse-kicked rotor with $\kappa = 8$ and $\alpha = 0.1$. Furthermore, we see that as ρ approaches $\rho = 20\pi$ much more regular structure is visible in phase space and that regular structure also occurs for $\rho > 20$. This is exactly what we expect from the above analysis, as we observe the phase space structures normally associated with smaller values of the stochasticity parameter κ as our effective kick strength κ_{eff} decreases according to the factor $|\text{sinc}[\alpha\rho/(2\pi)]|$.

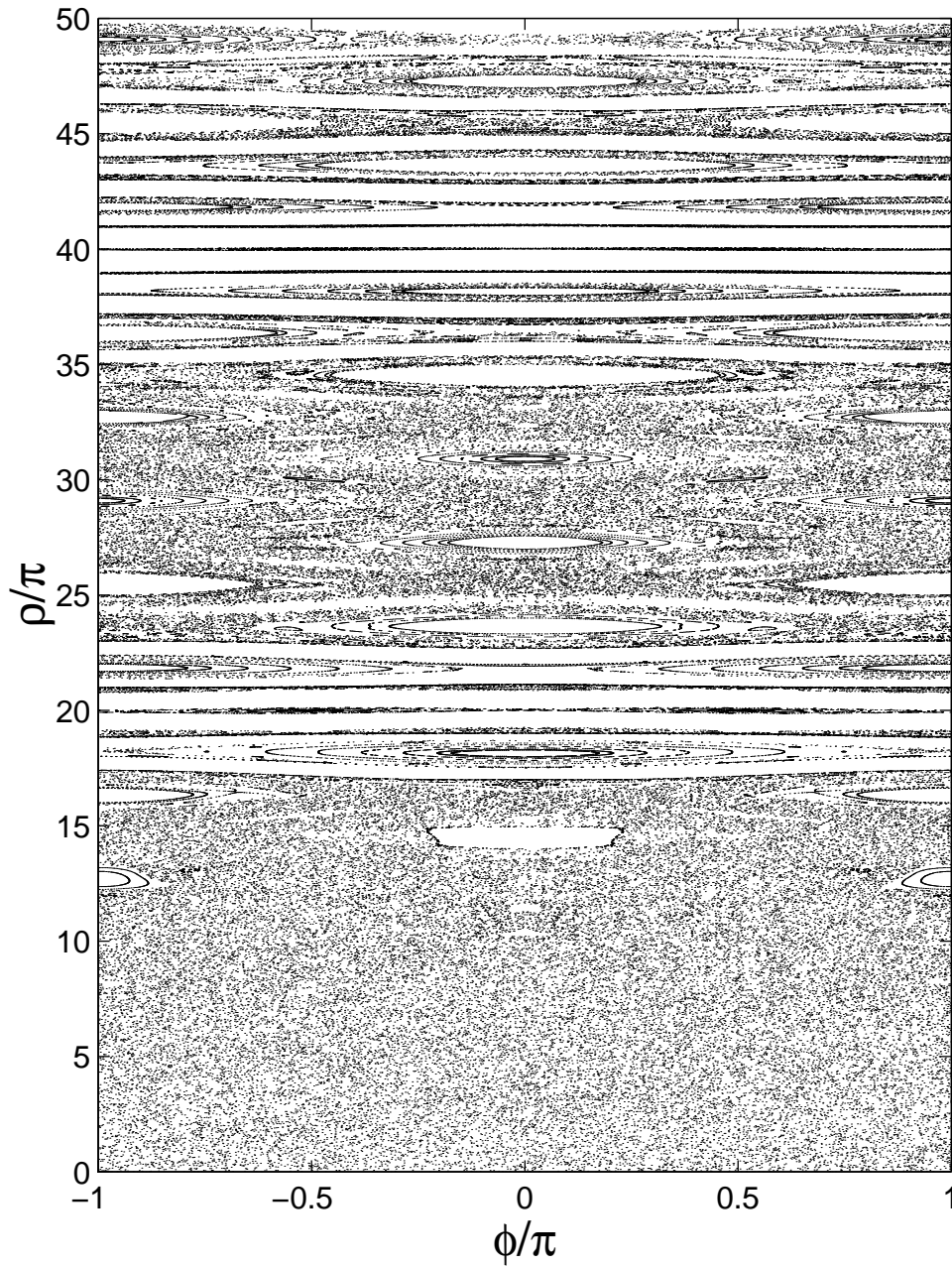


Figure 2.12: Poincaré Section for a classical pulse-kicked rotor with $\kappa = 8$, $\alpha = 0.1$

2.4 Momentum Diffusion in the Classical δ -Kicked Rotor

2.4.1 Momentum Diffusion Rates

The primary quantity which we will be interested in studying, for both the classical kicked rotor and the quantum kicked rotor, is the momentum diffusion rate, $D(n)$. For a collection of rotors, this is defined as the increase in the mean kinetic energy of the collection of rotors from one kick to the next. That is,

$$D(n) = \frac{\langle \rho_{n+1}^2 \rangle}{2} - \frac{\langle \rho_n^2 \rangle}{2}, \quad (2.55)$$

where we define $\rho_n = \rho(\tau = n)$, and $\langle A \rangle$ is the mean value or expectation value of A taken over all of the rotors in the system. Following a standard convention, we label the first kick, which occurs at $\tau = 0$, by the value $n = 0$, and **not** $n = 1$. The momentum diffusion rate for the first kick is then given by $2D(0) = \langle \rho_1^2 \rangle - \langle \rho_0^2 \rangle$.

It is sometimes convenient to use a different definition of the diffusion rate in order to simplify analytical computations. In particular, we can also define

$$\tilde{D}(n) = \frac{\langle (\rho_{n+1} - \rho_0)^2 \rangle}{2} - \frac{\langle (\rho_n - \rho_0)^2 \rangle}{2}. \quad (2.56)$$

These two definitions for $D(n)$ are equivalent if $\rho_0 = 0$, and for most cases dealt with in this thesis they are generally found to be numerically very similar. We are primarily interested in results from (2.55), as it is the difference in mean energies that is measured in atom optics kicked rotor experiments.

2.4.2 Correlation Functions and Quasilinear Diffusion

From the standard mapping (2.38) it follows that

$$\rho_n - \rho_0 = \kappa \sum_{m=0}^{n-1} \sin(\phi_m). \quad (2.57)$$

We can then write

$$E_n = \langle (\rho_n - \rho_0)^2 \rangle / 2 = \frac{\kappa^2}{2} \sum_{i=0}^{n-1} \sum_{j=0}^{n-1} \langle \sin(\phi_i) \sin(\phi_j) \rangle = \frac{\kappa^2}{2} \sum_{i=0}^{n-1} \sum_{j=0}^{n-1} C_s(i-j), \quad (2.58)$$

where we define $E_n = \langle (\rho_n - \rho_0)^2 \rangle / 2$, and

$$C_s(i-j) = \langle \sin(\phi_i) \sin(\phi_j) \rangle = \langle \sin(\phi_{i-j}) \sin(\phi_0) \rangle, \quad (2.59)$$

as the sine correlation function depends only on the absolute value of the time difference [3]. Then, using (2.56), we have

$$\begin{aligned}\tilde{D}(n) = E_{n+1} - E_n &= \frac{\kappa^2}{2} \sum_{i=0}^n \sum_{j=0}^n C_s(i-j) - \frac{\kappa^2}{2} \sum_{k=0}^{n-1} \sum_{l=0}^{n-1} C_s(k-l) \\ &= \frac{\kappa^2}{2} \sum_{i=-n}^n C_s(i).\end{aligned}\quad (2.60)$$

It is straight forward to evaluate this expression for the first kick ($n = 0$). We see that

$$\tilde{D}(0) = \frac{\kappa^2}{2} \langle \sin^2 \phi_0 \rangle = \frac{\kappa^2}{4} \quad (2.61)$$

provided that we have a uniform initial position distribution. We can obtain the same result from the definition in (2.55),

$$\begin{aligned}D(0) &= \frac{\langle \rho_1^2 \rangle}{2} - \frac{\langle \rho_0^2 \rangle}{2} = \frac{[\langle \rho_0 + \kappa \sin(\phi_0) \rangle^2]}{2} - \frac{\langle \rho_0^2 \rangle}{2} \\ &= \frac{\kappa^2}{2} \langle \sin^2(\phi_0) \rangle + \kappa \langle \rho_0 \sin(\phi_0) \rangle \\ &= \frac{\kappa^2}{4},\end{aligned}\quad (2.62)$$

again provided that we average over a uniform distribution of ϕ_0 values (and these are uncorrelated with the ρ_0 values. The diffusion rate, $\kappa^2/4$, that we observe here is called the quasilinear diffusion rate, or the random phase diffusion rate. For the second kick ($n = 1$), we also obtain the quasilinear diffusion rate, provided that the initial momentum distribution is sufficiently broad, as well as the initial position distribution being uniform. From (2.55),

$$\begin{aligned}D(1) &= \frac{\langle \rho_2^2 \rangle}{2} - \frac{\langle \rho_1^2 \rangle}{2} \\ &= \frac{\kappa^2}{2} \langle \sin^2(\phi_1) \rangle + \kappa \langle \rho_1 \sin(\phi_1) \rangle \\ &= \frac{\kappa^2}{2} \langle \sin^2(\rho_1 + \phi_0) \rangle + \kappa \langle \rho_1 \sin(\phi_0 + \rho_1) \rangle \\ &= \frac{\kappa^2}{2} \langle \sin^2[\phi_0 + \rho_0 + \kappa \sin(\phi_0)] \rangle \\ &\quad + \kappa \langle \rho_0 \sin[\phi_0 + \rho_0 + \kappa \sin(\phi_0)] \rangle \\ &\quad + \kappa^2 \langle \sin(\phi_0) \sin[\phi_0 + \rho_0 + \kappa \sin(\phi_0)] \rangle\end{aligned}\quad (2.63a)$$

$$= \frac{\kappa^2}{4}, \quad (2.63b)$$

where the condition of a broad initial momentum distribution is required in the last step, as we will see in chapter 9. If we begin with a very narrow initial momentum distribution we obtain different results, and these also will be dealt with in more detail in chapter 9.

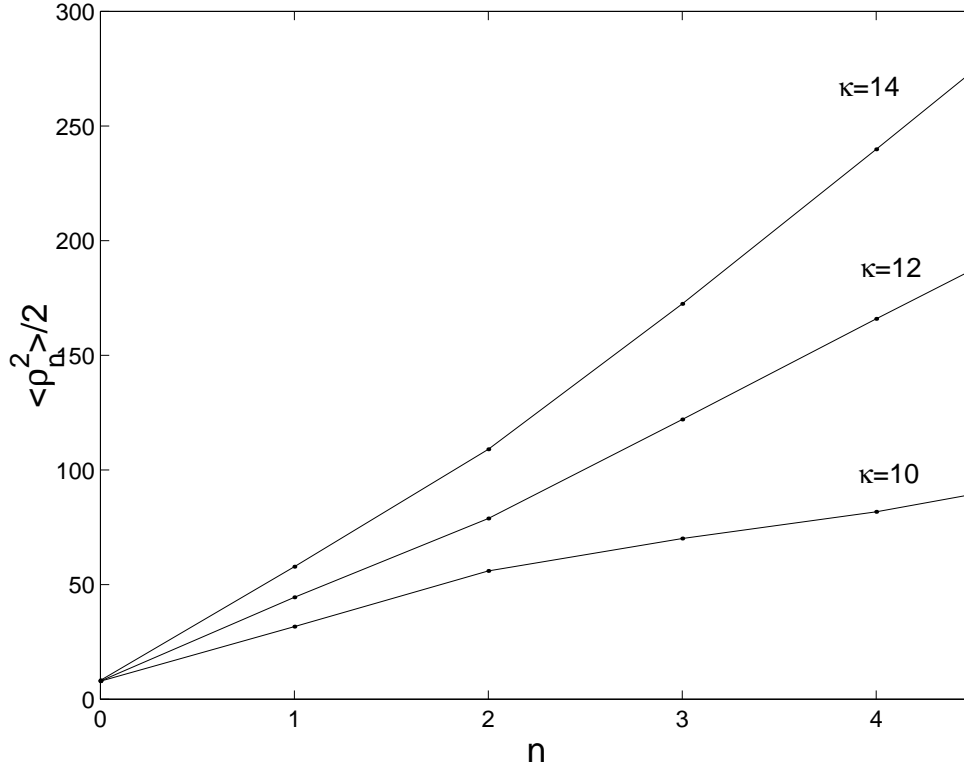


Figure 2.13: Simulation values of mean kinetic energy as a function of n for a classical δ -kicked rotor, showing the transition from quasilinear diffusion to classical diffusion.

2.4.3 Long Time Classical Diffusion Rates

We often refer to the diffusion period in which we observe the quasilinear diffusion rate of $\kappa^2/4$ as the quasilinear diffusion period, and this lasts for at most two kicks. After this period, there is a sharp transition away from this diffusion rate, and the system settles rapidly into a final steady state diffusion regime. In this regime, $\langle \rho^2 \rangle / 2$ increases linearly with kick number n , and so we have a constant diffusion rate, which we will refer to as the classical diffusion rate. The abrupt transition away from quasilinear behaviour after the second kick is shown in figure 2.13 for various values of κ , and the steady state diffusion behaviour is shown in figure 2.14. It can be seen from this figure that the classical diffusion rate has a non-trivial dependence on the kick strength, κ . This dependence was first evaluated for large κ by Rechester and White in 1980 [12], using Fourier transform methods, along with the addition of some external stochasticity. Rechester *et al.* performed a similar calculation valid for all values of κ in 1981 [13]. The calculation was first performed without introducing external noise into the problem by Abarbanel and Crawford [14] in 1981, and this result is reproduced in Lichtenberg and Lieberman [4]. Ultimately, all of these methods involve the calculation of the first few correlations appearing in equation (2.60). An example

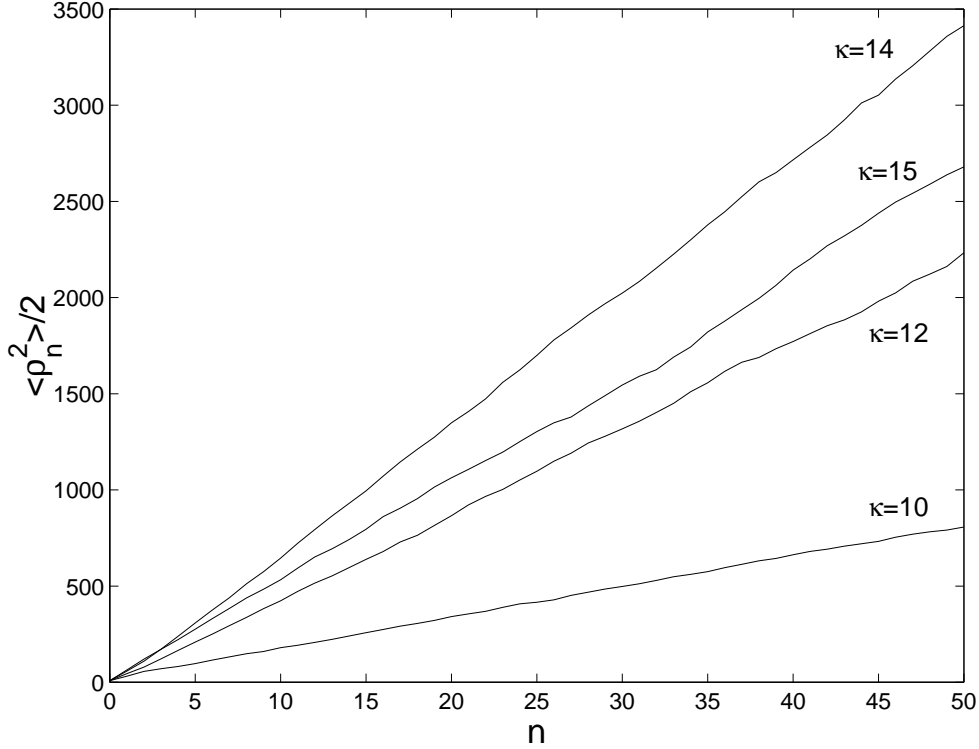


Figure 2.14: Simulation results for mean kinetic energy as a function of n in the classical δ -kicked rotor, showing the steady state diffusion regime.

of such a calculation is presented in appendix B, based on a summary in reference [15] of the direct method used by Shepelyansky [16].

To order κ^{-1} the final result is

$$D_{class} = \frac{\kappa^2}{2} \left(\frac{1}{2} - J_2(\kappa) - J_1^2(\kappa) + J_2^2(\kappa) + J_3^2(\kappa) \right) \quad (2.64)$$

where $J_n(z)$ denotes an ordinary Bessel function of order n (see appendix A for a discussion of these functions). This function is plotted along with simulation results for the classical diffusion rate as a function of κ in figure 2.15, and the two sets of values show very good agreement. The simulation results are averaged over 4000 particles with initial positions taken from a uniform distribution on $[-\pi, \pi]$, and initial momenta taken from a Gaussian distribution with centre $\rho_0 = 0$ and width $\sigma = 4$.

For large κ , we note that the diffusion rate is well approximated by $\kappa^2/4$. This is not surprising, because as κ is increased, the system becomes more chaotic, and the correlations between ϕ_i and ϕ_j for $i \neq j$ become weaker. It is also interesting to note from the correlation evaluations presented in appendix B, that the correlation function $C_s(2) = -J_2(\kappa)/2$, so that from (2.60) we have $\tilde{D}(2) = (\kappa^2/4)(1 - 2J_2(\kappa))$. For all of the κ values we deal with, the approximation $D_{class} \approx (\kappa^2/4)[1 - 2J_2(\kappa)]$ is a very

good one, and thus we see from (2.60) that the diffusion rate for the third kick ($n = 2$) has essentially reached the final steady state value immediately.

Simulation results for the momentum diffusion rates in the kicked rotor with rectangular pulses are shown in figure 2.16 along with values from (2.64), choosing $\kappa = k\alpha$, as we would do experimentally in order to approximate a delta kicked rotor with stochasticity parameter κ . Again these results are averaged over 4000 trajectories with initial positions taken from a uniform distribution, and initial momenta taken from a Gaussian distribution with centre $\rho_0 = 0$ and width $\sigma = 4$. We see that the agreement here is very good for $\kappa < 20$. However, as the average momentum increases, the effective kick strength decreases (see section 2.3.2). Thus, the momentum diffusion rate decreases as we reach sufficiently high momenta, which occurs in fewer kicks for higher values of $\kappa = k\alpha$. We thus observe discrepancies from (2.64) in the average momentum diffusion rates for the first 50 kicks in figure 2.16 for sufficiently large values of $\kappa = k\alpha$.

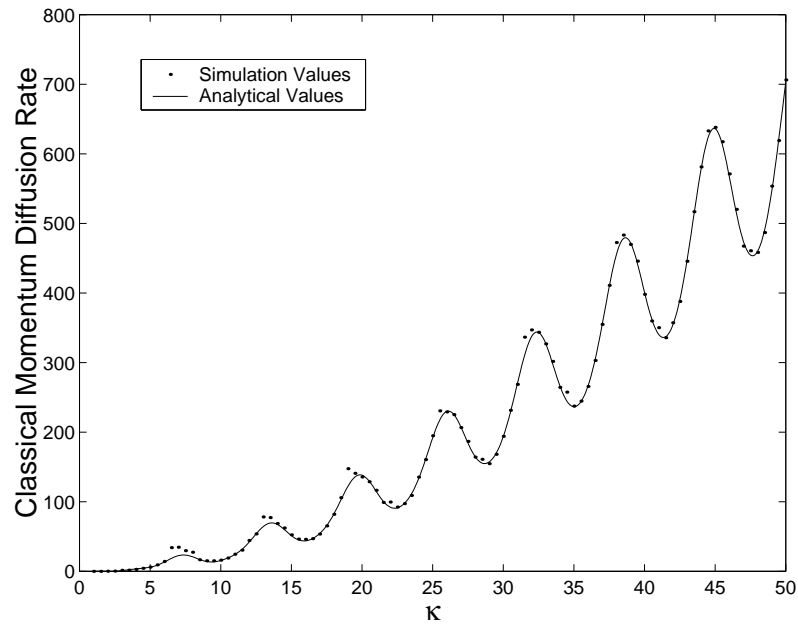


Figure 2.15: Steady state momentum diffusion rates for the classical δ -kicked rotor, as a function of κ .

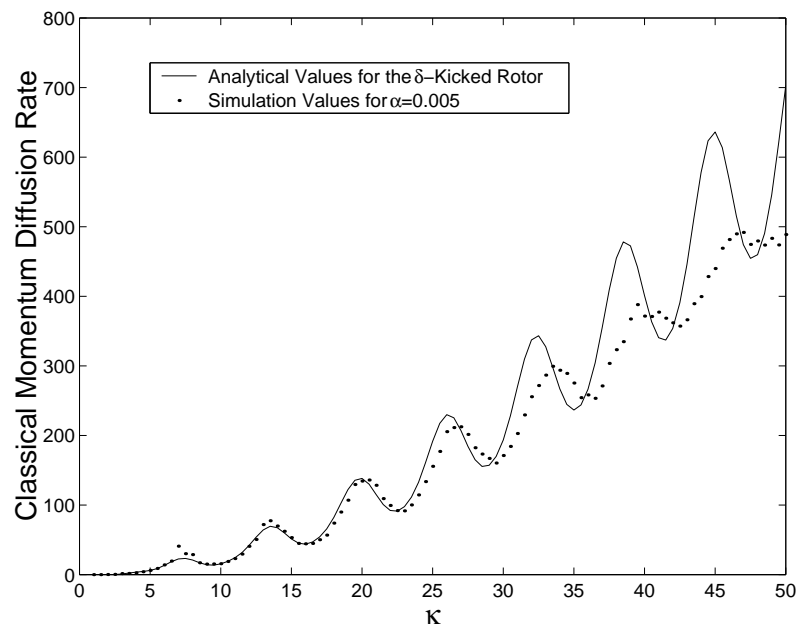


Figure 2.16: Average momentum diffusion rates over the first 50 kicks for the classical kicked rotor with rectangular pulses and $\alpha=0.005$, as a function of $\kappa = k\alpha$.

Chapter 3

The Quantum Kicked Rotor

3.1 Quantum Dynamics

3.1.1 Basic Quantum Mechanics

In quantum mechanics we represent the state of a system using a state ket, $|\psi\rangle$, which is normalised so that $\langle\psi|\psi\rangle = 1$, and we represent any observable A by an operator, \hat{A} , which acts on the state kets. In general, operators for two observables do not commute; for example in the case of position $\hat{\phi}$ and momentum $\hat{\rho}$, the commutator for the operators is given by

$$[\hat{\phi}, \hat{\rho}] = \hat{\phi}\hat{\rho} - \hat{\rho}\hat{\phi} = i\hbar, \quad (3.1)$$

where \hbar is Planck's constant divided by 2π . The expectation value of an operator \hat{A} for a given state of the system $|\psi\rangle$ is given by the inner product, $\langle\psi|\hat{A}|\psi\rangle$. For a mixed state, represented by a density operator \hat{w} , the expectation value of an observable A is given by $\text{Tr}\{\hat{A}\hat{w}\}$, where $\text{Tr}\{\dots\}$ represents the trace over any complete set of basis states. Note that the symbol \hat{w} is used for a density operator rather than the common notation $\hat{\rho}$ because of the possible confusion with the notation for the momentum operator.

The time evolution of the system is governed by the quantum Hamiltonian, \hat{H} , which itself is an operator. This time evolution may be expressed in two ways. Using the Schrödinger picture, we can express the time dependence as a time variation of the state ket $|\psi\rangle$,

$$i\hbar\frac{d}{dt}|\psi\rangle = \hat{H}\psi, \quad (3.2a)$$

$$|\psi(t)\rangle = \exp[-i\hat{H}t/\hbar]|\psi(0)\rangle = \hat{U}(t)|\psi(0)\rangle, \quad (3.2b)$$

where $\hat{U}(t) = \exp[-i\hat{H}t/\hbar]$ is the time evolution operator. For a mixed state, the density operator \hat{w} evolves in time according to

$$\hat{w}(t) = \hat{U}^\dagger(t)\hat{w}(0)\hat{U}(t), \quad (3.3)$$

where \hat{U}^\dagger denotes the adjoint operator of \hat{U} . Alternatively, we may express the time dependence of the system as a time variation in the operators by transforming the Schrödinger picture operators \hat{A}_S into the Heisenberg picture,

$$\hat{A}_H = \exp[i\hat{H}t/\hbar]\hat{A}_S \exp[-i\hat{H}t/\hbar] = \hat{U}^\dagger(t)\hat{A}_S\hat{U}(t). \quad (3.4)$$

Then, the state $|\psi\rangle$ is independent of time, and we see that

$$\frac{d}{dt}\hat{A} = \frac{i}{\hbar}[\hat{H}, \hat{A}]. \quad (3.5)$$

3.1.2 The Parameter \bar{k}

The distinction between quantum and classical systems is essentially one of the scale of the systems. The greater the action in a system, the more classically it behaves, and the smaller the total action in a system, the more significant quantum mechanical effects become in the evolution of the system. When we reduce our system to dimensionless units, this dependence is reflected in a scaling of the dimensionless Planck's constant with the total action in the system. We find that

$$[\hat{\phi}, \hat{\rho}] = i\bar{k} \quad (3.6)$$

for some dimensionless constant \bar{k} , which is related to \hbar by various system parameters. Some authors choose to write \hbar for the dimensionless Planck's constant, but here we use \bar{k} to make the distinction that it is the action in the system, not Planck's constant, which is physically being varied when we study the transition between quantum and classical regimes. In effect, \bar{k} is a measure of how classically the system is behaving. In terms of the classical action, we may write

$$\bar{k} \sim \frac{\hbar}{\text{Classical Action}}, \quad (3.7)$$

so that the system becomes more classical as the action becomes large, or $\bar{k} \rightarrow 0$.

3.1.3 Quantum Chaos

As was described in chapter 1, quantum mechanical systems do not exhibit stochastic behaviour in the way that classical systems do. This is a fundamental phenomenon, which ultimately arises from the fact that Schrödinger's Equation is linear [17]. The fact that chaotic motion does not occur in quantum mechanics has led to many interesting investigations, comparing and contrasting appropriate quantum mechanical systems with their chaotic classical analogues. This field has usually been given the rather misleading title "Quantum Chaos", and is now dominated by studies of how the transition from quantum behaviour to classical behaviour is achieved, and how this relates to principles of quantum - classical correspondence. It is interesting to note that there are still many similarities between the classical and quantum systems, including

the fact that KAM tori act as a barrier to diffusion in quantum systems. This property has been investigated both theoretically [18] and experimentally [19] using the kicked rotor system.

The lack of chaotic motion in quantum mechanics leads to a suppression of the unlimited energy growth observed in chaotic classical systems. In the case of the kicked rotor, we instead observe the striking phenomenon of dynamical localisation, which will be described in section 3.2.4. The resulting patterns of energy growth, and how the rates at which the growth occurs change as we vary the effective Planck's constant, \hbar , are the main topics of investigation in this thesis.

3.2 The Quantum Kicked Rotor

In general, the Hamiltonian for a quantum system may be found by replacing the observables in the Hamiltonian for the corresponding classical system with the appropriate quantum mechanical operators. In this way, the Hamiltonian for the quantum kicked rotor may be written as

$$\hat{H} = \frac{\hat{L}^2}{2I} + K \cos(\hat{\phi}) \sum_{n=0}^{\infty} f(t - nT), \quad (3.8)$$

where \hat{L} is the angular momentum operator, $\hat{\phi}$ is the angular displacement operator, $I = ml^2$ is the rotational moment of inertia for the rotor and all other symbols have the same meaning as for the classical kicked rotor.

We may rewrite this Hamiltonian using dimensionless momentum units ($\hat{\phi}$ is already dimensionless) by defining a new momentum operator $\hat{\rho} = \hat{L}T/I$, and choosing a scaled time parameter $\tau = t/T$. The rescaled Hamiltonian is then given by

$$\hat{H}' = \frac{\hat{\rho}^2}{2} + k \cos(\hat{\phi}) \sum_{n=0}^{\infty} f(\tau - n), \quad (3.9)$$

where $\hat{H}' = (T^2/I)\hat{H}$ and $k = (T^2/I)K$.

The scale of the system can be expressed in terms of the new dimensionless Planck's constant, which is given by $[\hat{\phi}, \hat{\rho}] = i\hbar k$, with $\hbar k = \hbar T/I$. We thus see that by varying the period between kicks, we can alter the scale of our quantum system so as to make it behave more classically. The classical limit is reached by letting $T \rightarrow 0$ so that $\hbar k \rightarrow 0$.

Note that from (2.21) the classical action for the kicked rotor is given by

$$J = \frac{1}{2\pi} \oint L d\phi.$$

If we reparameterise this integral using the relationship between $\Delta\phi$ for one cycle and

L , $\Delta\phi = LT/I$, we get

$$J = \frac{1}{2\pi} \frac{T}{I} \int_0^{\frac{2\pi I}{T}} L dL, \quad (3.10)$$

$$= \frac{\pi I}{T}, \quad (3.11)$$

and so $\bar{k} = \hbar T/I = \hbar\pi/J \sim \hbar/J$, as was described in section 3.1.2.

3.2.1 The Quantum δ -Kicked Rotor

As in the classical case, the quantum δ -kicked rotor is defined by choosing the function $f(\tau) = \delta(\tau)$. In dimensionless units, then, the Hamiltonian for the quantum δ -kicked rotor is given by

$$\hat{H} = \frac{\hat{\rho}^2}{2} + \kappa \cos(\hat{\phi}) \sum_{n=0}^{\infty} \delta(\tau - n). \quad (3.12)$$

The time evolution operator for one cycle of this system (the one step propagation operator) is then given by

$$\hat{U} = \exp[-i\hat{\rho}^2/(2\bar{k})] \exp[-i\kappa \cos(\hat{\phi})/\bar{k}], \quad (3.13)$$

and we can express the state of the system at time $\tau = n$ for positive integer n as

$$|\psi(\tau = n)\rangle = \hat{U}^n |\psi(0)\rangle. \quad (3.14)$$

We can also alternatively express this time evolution in the Heisenberg picture. This is given by the mapping

$$\hat{\rho}_{n+1} = \hat{\rho}_n + \kappa \sin(\hat{\phi}_n), \quad (3.15a)$$

$$\hat{\phi}_{n+1} = \hat{\phi}_n + \hat{\rho}_{n+1}, \quad (3.15b)$$

where we denote $\hat{\phi}_n = \hat{\phi}(\tau = n)$ and $\hat{\rho}_n = \hat{\rho}(\tau = n)$. This mapping is known as the quantum standard map and is the quantum mechanical analogue of the classical standard map (2.38).

3.2.2 The Quantum Pulse-Kicked Rotor

As we saw with the classical system in section 2.3.2, the quantum δ -kicked rotor is an idealised system, and experimentally we must approximate it with a pulse-kicked rotor. Once again we will use rectangular pulses of height k and time duration α , such that $\kappa = k\alpha$. The difficulties due to the dependence of the effective kick strength on ρ which were discussed in section 2.3.2 again apply here, and we must be careful to use

a small value for α , and to not let the momentum distributions diffuse to momentum values which are too large for a good approximation to the δ -kicked rotor to hold.

We may express the evolution of the pulse kicked rotor in two parts - the evolution during the kick, which is governed by \hat{H}_{kick} , and the free evolution at other times, which is governed by \hat{H}_{free} , where we define

$$\hat{H}_{kick} = \frac{\hat{\rho}^2}{2} + \kappa \cos(\hat{\phi}), \quad (3.16a)$$

$$\hat{H}_{free} = \frac{\hat{\rho}^2}{2}. \quad (3.16b)$$

The time evolution operators for the two parts can then be expressed as:

$$\hat{U}_{kick}(t) = \exp[-i\hat{H}_{kick}t/\hbar], \quad (3.17a)$$

$$\hat{U}_{free}(t) = \exp[-i\hat{H}_{free}t/\hbar]. \quad (3.17b)$$

Combining these two parts of the evolution together, we may write the one step propagation operator as

$$\hat{U} = \exp[-i\hat{H}_{free}(1 - \alpha)/\hbar] \exp[-i\hat{H}_{kick}\alpha/\hbar]. \quad (3.18)$$

3.2.3 Angular Momentum and Floquet State Representations

In the dimensionless quantum rotor, angular momentum is quantised in ladder states separated by \hbar . We can thus represent the system in a basis of angular momentum states $|n\rangle$ for integer n , with the properties

$$\hat{\rho}|n\rangle = n\hbar|n\rangle, \quad (3.19a)$$

$$\langle\phi|n\rangle = \frac{1}{\sqrt{2\pi}}e^{in\phi}. \quad (3.19b)$$

Another common representation for the quantum kicked rotor is in terms of Floquet states. These states are the eigenstates of the one step propagation operator, \hat{U} ,

$$\hat{U}|\alpha_j\rangle = e^{-iE_j/\hbar}|\alpha_j\rangle. \quad (3.20)$$

The eigenvalues of \hat{U} have the form $e^{-iE_j/\hbar}$, where E_j is known as a quasienergy, because \hat{U} is unitary. From the definition of \hat{U} we see that the states $|\alpha_j\rangle$ are periodic in time with period 1.

3.2.4 Dynamical Localisation

Unlike the classical δ -kicked rotor for $\kappa > \kappa^* = 0.9716$, the quantum δ -kicked rotor does not undergo unbounded diffusion. Instead, it passes through a period of initial diffusion and then undergoes dynamical localisation, in which the energy growth in the system ceases. This phenomenon has been investigated in many settings by many different authors, and the effects observed in the δ -kicked rotor [20, 21] have often been compared with Anderson localisation in Solid State Physics [22]. Dynamical localisation sets in on a timescale known as the quantum break time, and this is discussed in section 3.3.4.

In order to investigate the phenomenon of dynamical localisation, we consider the asymptotic, or long time average momentum distribution. This is defined by:

$$P(n|\hat{w}_0) = \lim_{N \rightarrow \infty} \frac{1}{N} \sum_{\tau=0}^{N-1} \langle n|\hat{w}_\tau|n \rangle, \quad (3.21)$$

where $\hat{w}_0 = \hat{w}(\tau = 0)$ is the initial density operator and $\hat{w}_\tau = \hat{w}(\tau)$. If we rewrite \hat{w}_τ in terms of the propagation operator \hat{U} , we can express this function in a Floquet state basis:

$$\begin{aligned} P(n|\hat{w}_0) &= \lim_{N \rightarrow \infty} \frac{1}{N} \sum_{\tau=0}^{N-1} \langle n|\hat{U}^\tau \hat{w}_0 \hat{U}^{\dagger\tau}|n \rangle \\ &= \lim_{N \rightarrow \infty} \frac{1}{N} \sum_{\tau=0}^{N-1} \sum_{i,j} \langle n|\hat{U}^\tau|\alpha_i \rangle \langle \alpha_i|\hat{w}_0|\alpha_j \rangle \langle \alpha_j|\hat{U}^{\dagger\tau}|n \rangle \\ &= \lim_{N \rightarrow \infty} \frac{1}{N} \sum_{\tau=0}^{N-1} \sum_{i,j} \langle n|\alpha_i \rangle \langle \alpha_i|\hat{w}_0|\alpha_j \rangle \langle \alpha_j|n \rangle e^{-i(E_i - E_j)\tau/\hbar} \\ &= \sum_{i,j} \langle n|\alpha_i \rangle \langle \alpha_i|\hat{w}_0|\alpha_j \rangle \langle \alpha_j|n \rangle \delta_{ij} \\ &= \sum_j \langle \alpha_j|\hat{w}_0|\alpha_j \rangle |\langle n|\alpha_j \rangle|^2. \end{aligned} \quad (3.22)$$

Now, if we write \hat{w}_0 in terms of the momentum states $|m\rangle$ as $\hat{w}_0 = \sum_i P_0(m_i)|m_i\rangle\langle m_i|$ then we have

$$P(n|\hat{w}_0) = \sum_i \sum_j P_0(m_i) |\langle m_i|\alpha_j \rangle|^2 |\langle n|\alpha_j \rangle|^2. \quad (3.23)$$

The Floquet states are eigenstates of the one step propagation operator, \hat{U} , which may be expressed in the momentum state representation [3] as

$$\langle m|\hat{U}|n \rangle = (-i)^{m-n} J_{m-n} \left(\frac{\kappa}{\hbar} \right) e^{-i\kappa n^2/2}. \quad (3.24)$$

For large order $m - n$ the Bessel function may be approximated by

$$J_{m-n} \left(\frac{\kappa}{\hbar} \right) \approx \frac{1}{\sqrt{2\pi(m-n)}} \left(\frac{e\kappa}{2\hbar(m-n)} \right)^{(m-n)}, \quad (3.25)$$

so that as $m - n$ becomes large, $\langle m | \hat{U} | n \rangle \rightarrow 0$. We thus assume [3] that the momentum representation of the Floquet states is of the same nature as the eigenstates of a generic banded matrix - that is, the Floquet states are exponentially localised in momentum space,

$$\langle m_i | \alpha_j \rangle \sim e^{-|m_i - \Lambda_j| / \xi_j}, \quad (3.26)$$

where Λ_j and ξ_j are the localisation centre and localisation length of the Floquet state $|\alpha_j\rangle$ respectively. This localisation has been extensively studied and verified numerically in various investigations, the first of which was by Fishman, Grempel and Prange [22, 23].

From (3.23) we can then write

$$P(n | \hat{w}_0) \sim \sum_i \sum_j P_0(m_i) e^{-2|m_i - \Lambda_j| / \xi_j} e^{-2|n - \Lambda_j| / \xi_j}. \quad (3.27)$$

We see that $P(n | \hat{w}_0)$ will only be large where n is close to the localisation centre Λ_j of a particular Floquet State $|\alpha_j\rangle$ for which Λ_j itself is close to a momentum value m_i with large $P_0(m_i)$ in the initial momentum distribution. In general, the long time average momentum distribution will decay exponentially about the states in the initial momentum distribution. Thus it becomes apparent that on some scale the energy growth will be restricted by this phenomenon of localisation. The width of the long time average momentum distribution will be restricted and determined by the localisation lengths ξ_j of the Floquet states with localisation centres Λ_j close to momentum values which contribute significantly to the initial momentum distribution.

3.2.5 Quantum Resonances

There is another possible motion for the quantum kicked rotor in which dynamical localisation does not occur. This is due to another uniquely quantum phenomenon known as quantum resonances. A quantum resonance occurs when the period between kicks is chosen so that the accumulated phase between kicks is exactly 1 or -1 . For appropriate plane wave initial conditions this results in ballistic motion, i.e., motion with a quadratic increase in energy [24].

We already know that between kicks a plane wave state $|\rho_0\rangle$ for the quantum δ -kicked rotor will accumulate a phase factor according to the evolution operator $\exp[-iH_{free}/\hbar]$, i.e., $\exp[-i\rho_0^2/(2\hbar)]$ (in dimensionless units). We also know that during each kick the system may couple to momentum states on a ladder $\rho_0 \pm n\hbar$ for integer n . Thus if we choose ρ_0 to be an integer multiple of \hbar then if \hbar is an even multiple of 2π , the total accumulated phase between kicks will be 1. This is known as a quantum resonance. If \hbar is instead an odd multiple of 2π then the total accumulated phase in this situation will be ± 1 . This is known as a quantum anti-resonance.

The ballistic motion which occurs at a quantum resonance for $\rho = n\hbar$ with integer n may be illustrated by considering $\rho_0 = 0$. From (3.24) we see that the probability

that the system is in a momentum state $|m\rangle$ after one kick is given by

$$P(m) = |\langle m|\hat{U}|0\rangle|^2 = \left|(-i)^m J_m\left(\frac{\kappa}{\hbar}\right)\right|^2 = J_m^2\left(\frac{\kappa}{\hbar}\right). \quad (3.28)$$

But, we know that if the quantum resonance condition is satisfied, then the total phase factor accumulated between kicks is 1. Thus, the free evolution is “collapsed” because the state immediately before a particular kick is identically the same state that the system was in immediately after the previous kick. Therefore, the momentum distribution after N kicks of effective strength κ is the same as the momentum distribution after a single pulse with effective strength $N\kappa$. The resulting distribution is then given by

$$P_N(m) = J_m^2\left(\frac{N\kappa}{\hbar}\right). \quad (3.29)$$

This function is plotted for particular values of κ and \hbar in figure 3.1. $J_n(x)$ peaks when $x \sim n$, and so we see that as N increases, the peaks in the distribution $P_N(m)$ move away from $m = 0$ at an approximately uniform rate. This linear increase in the peak momentum value leads to an approximately quadratic increase in the total energy, i.e., ballistic motion.

For an initial momentum distribution with a finite width, the evolution of the system near a quantum resonance is more complicated. Several investigations have been made of this evolution, including that by Oskay *et al.* [24]. They found that the system settles rapidly into a nearly static momentum distribution, with a smaller width than would normally be expected due to dynamical localisation on its own. We have found interesting behaviour in the momentum diffusion rates near the quantum anti-resonance at $\hbar = 2\pi$ for systems with initial momentum distributions of a finite width, and this is discussed in more detail in chapter 6.

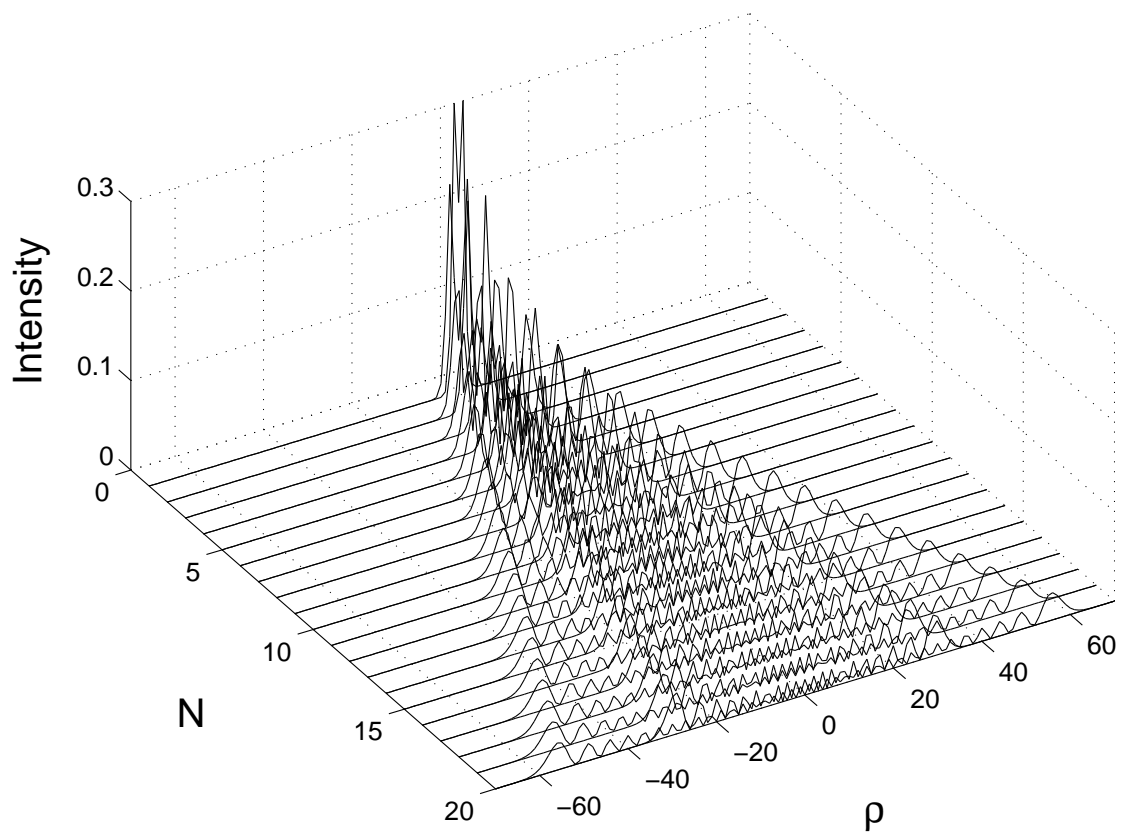


Figure 3.1: Momentum probability distributions after N kicks for $\kappa = 20$ and $\hbar k = 4\pi$, showing ballistic motion at a quantum resonance, with two clear peaks moving away from $\rho_0 = 0$ at a constant rate.

3.3 Momentum Diffusion in the Quantum δ -Kicked Rotor

3.3.1 Definitions

Momentum diffusion rates are defined for the quantum kicked rotor in the same fashion as they were for the classical kicked rotor in section 2.4.1, replacing the expectation values for momentum by the appropriate operator expressions. Note that it is usually more convenient to deal with operators in the Heisenberg picture when we consider these diffusion rates.

Thus, our standard definition for the quantum momentum diffusion rate, analogous to the classical definition (2.55), is

$$D(n) = \frac{\langle \hat{\rho}_{n+1}^2 \rangle}{2} - \frac{\langle \hat{\rho}_n^2 \rangle}{2}, \quad (3.30)$$

where we define $\hat{\rho}_n = \hat{\rho}(\tau = n)$, and $\langle \hat{A} \rangle$ is the expectation value of the operator \hat{A} . As in the classical case, we label the first kick, which occurs at $\tau = 0$, by the value $n = 0$.

Similarly to the classical momentum diffusion rate, it is sometimes convenient to use a different definition of the quantum diffusion rate in order to simplify analytical computations. The quantum definition analogous to (2.56) is

$$\tilde{D}(n) = \frac{\langle (\hat{\rho}_{n+1} - \hat{\rho}_0)^2 \rangle}{2} - \frac{\langle (\hat{\rho}_n - \hat{\rho}_0)^2 \rangle}{2}, \quad (3.31)$$

which may be written in terms of symmetrised correlation functions analogous to those in (2.60) as

$$\tilde{D}(n) = \frac{\kappa^2}{4} \sum_{i=-n}^n \langle \sin \hat{\phi}_i \sin \hat{\phi}_0 + \sin \hat{\phi}_0 \sin \hat{\phi}_i \rangle. \quad (3.32)$$

3.3.2 Quasilinear Behaviour

Using analogies between the quantum standard map (3.15) and the classical standard map (2.38) we can derive expressions for diffusion rates for the quantum δ -kicked rotor in a similar fashion to our calculations for the classical kicked rotor.

From (3.30), the diffusion rate for the first kick, $D(0)$, is given by

$$\begin{aligned} D(0) &= \frac{\langle \hat{\rho}_1^2 \rangle}{2} - \frac{\langle \hat{\rho}_0^2 \rangle}{2} = \frac{\langle [\hat{\rho}_0 + \kappa \sin(\hat{\phi}_0)]^2 \rangle}{2} - \frac{\langle \hat{\rho}_0^2 \rangle}{2} \\ &= \frac{\kappa^2}{2} \langle \sin^2(\hat{\phi}_0) \rangle + \frac{\kappa}{2} \left(\langle \hat{\rho}_0 \sin(\hat{\phi}_0) \rangle + \langle \sin(\hat{\phi}_0) \hat{\rho}_0 \rangle \right) \end{aligned} \quad (3.33a)$$

$$= \frac{\kappa^2}{4}, \quad (3.33b)$$

where the last step holds provided that our initial momentum distribution is an incoherent mixture of plane wave states. This assumption is essentially the quantum analogue to our classical assumption of a uniform initial position distribution, and the result (3.33b) may be proven by calculating the expectation values in (3.33a) for an arbitrary plane wave state. We see that for a quantum kicked rotor system, the diffusion rate for the first kick ($n = 0$) will be the same as for the classical system, that is, the quasilinear diffusion rate of $\kappa^2/4$.

The diffusion rate in the second kick, $D(1)$, is given by

$$\begin{aligned}
 D(1) &= \langle \hat{\rho}_2^2 \rangle / 2 - \langle \hat{\rho}_1^2 \rangle / 2 \\
 &= \frac{\kappa^2}{2} \langle \sin^2(\hat{\phi}_1) \rangle + \frac{\kappa}{2} \langle \hat{\rho}_1 \sin(\hat{\phi}_1) + \sin(\hat{\phi}_1) \hat{\rho}_1 \rangle \\
 &= \frac{\kappa^2}{2} \langle \sin^2(\hat{\rho}_1 + \hat{\phi}_0) \rangle + \frac{\kappa}{2} \langle \hat{\rho}_1 \sin(\hat{\phi}_0 + \hat{\rho}_1) + \sin(\hat{\phi}_0 + \hat{\rho}_1) \hat{\rho}_1 \rangle \\
 &= \frac{\kappa^2}{2} \langle \sin^2[\hat{\phi}_0 + \hat{\rho}_0 + \kappa \sin(\hat{\phi}_0)] \rangle \\
 &\quad + \frac{\kappa}{2} \langle \hat{\rho}_0 \sin[\hat{\phi}_0 + \hat{\rho}_0 + \kappa \sin(\hat{\phi}_0)] + \sin[\hat{\phi}_0 + \hat{\rho}_0 + \kappa \sin(\hat{\phi}_0)] \hat{\rho}_0 \rangle \\
 &\quad + \frac{\kappa^2}{2} \langle \sin(\hat{\phi}_0) \sin[\hat{\phi}_0 + \hat{\rho}_0 + \kappa \sin(\hat{\phi}_0)] \\
 &\quad + \sin[\hat{\phi}_0 + \hat{\rho}_0 + \kappa \sin(\hat{\phi}_0)] \sin(\hat{\phi}_0) \rangle. \tag{3.34}
 \end{aligned}$$

Further simplification and investigation of this expression is discussed in more detail in chapter 9. Essentially, we calculate the expectation values for an initial momentum eigenstate $|\rho_0\rangle$ and then we average over an incoherent Gaussian distribution of ρ_0 values. As in the classical case, we find that for a sufficiently broad initial momentum distribution the expression for $D(1)$ reduces to $\kappa^2/4$, meaning that under these initial conditions, a quantum δ -kicked rotor exhibits quasilinear diffusion for the first two kicks in the same way as the classical δ -kicked rotor does.

3.3.3 Initial Quantum Diffusion

After the initial quasilinear diffusion period, the quantum δ -kicked rotor moves abruptly to a different diffusion rate. This new diffusion regime, called the initial quantum diffusion period, lasts for only a small number of kicks before dynamical localisation begins to set in. The diffusion during this time is referred to as classical-like, because of the nearly linear increase in kinetic energy over the course of four or five kicks, but the initial quantum diffusion rate is often very different to the classical diffusion rate. The first few quantum correlations that appear in (3.32) were first calculated by Shepelyansky [25, 16, 3], giving an expression for the initial quantum diffusion rate, D_q . This expression is valid under the conditions $k \gtrsim 1$ and $\kappa \gg k$ and is given by

$$D_q = \frac{\kappa^2}{2} \left(\frac{1}{2} - J_2(K_q) - J_1^2(K_q) + J_2^2(K_q) + J_3^2(K_q) \right), \tag{3.35}$$

with $K_q = 2\kappa \sin(\bar{k}/2)/\bar{k}$. Note that this form is the same as the expression for the classical diffusion rate, but with κ replaced by K_q in the arguments of the Bessel functions. The evaluation of the quantum correlations and derivation of this expression is presented in appendix B, based on a summary of Shepelyansky's work given by Steck in reference [15].

The dependence of Shepelyansky's expression for D_q on \bar{k} is very striking and is shown in figure 3.2 for $\kappa = 10, 11, 12$ and 13 . We expect from (3.35) to observe peaks in the diffusion rate near the quantum anti-resonance at $\bar{k} = 2\pi$, as well as an enhanced diffusion peak at lower \bar{k} values that shifts and scales with changing κ . Note that only points with $\bar{k} < 7$ are plotted as the assumptions which lead to (3.35) break down at larger values (note that even near $\bar{k} \approx 5$ the formula predicts some negative values for the diffusion rate, which should not physically occur in this regime).

Most of the investigation in chapters 6, 7, and 8 will involve the study of structures similar to these which occur in various diffusion regimes under a multitude of system conditions. It is interesting that much of this non-trivial structure occurs near the threshold of the quantum-classical transition, where $\bar{k} \sim 1$, i.e., where the classical action is of the order of \hbar .

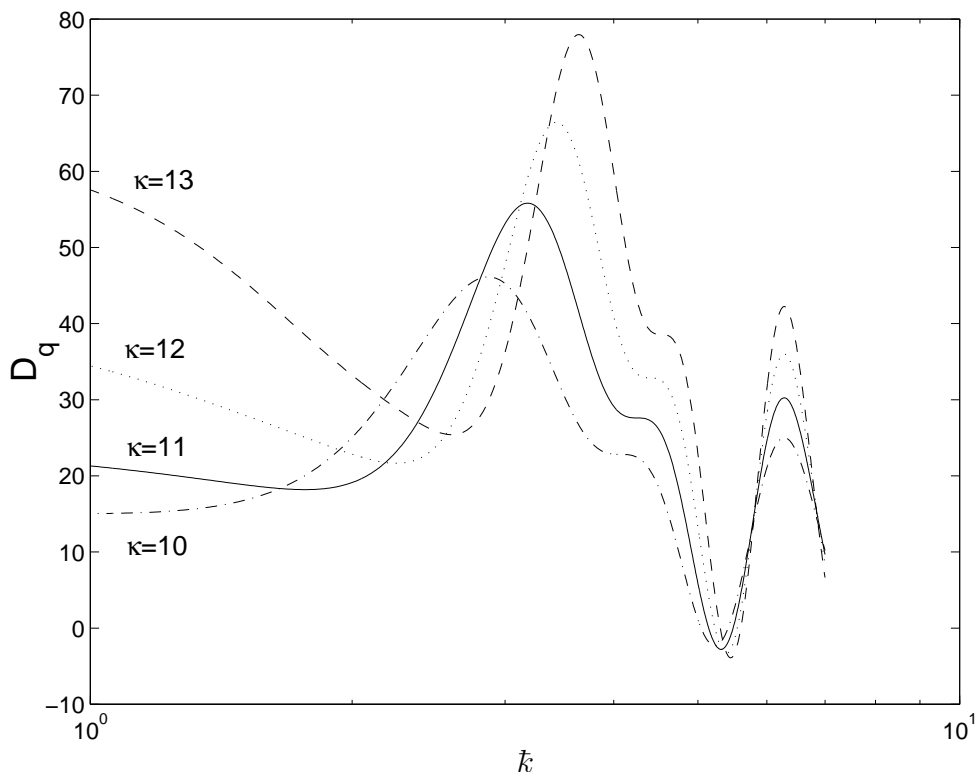


Figure 3.2: Initial quantum diffusion rates, as given by (3.35), showing enhanced diffusion peaks as a function of \bar{k} .

3.3.4 The Quantum Break Time

The initial quantum diffusion period ends with the onset of dynamical localisation, which results in the diffusion rate $D(n)$ tending rapidly to zero as $n \rightarrow \infty$. This can be clearly seen in figure 3.3, which shows the mean energy as a function of kick number for the quantum kicked rotor with an initial Gaussian distribution of momentum eigenstates.

Dynamical localisation manifests itself on a time scale N^* , called the quantum break time. N^* can be approximated by considering the overlap between Floquet states and momentum eigenstates, as is outlined by Cohen in reference [3]. In terms of the initial quantum diffusion rate, we find that

$$N^* \approx \frac{D_q}{\bar{k}^2}, \quad (3.36)$$

which arises from a relationship between the break time and the mean localisation length of the Floquet states, $\bar{\xi}$. This estimate gives a value of $N^* \approx 5.3$ for the system simulated in figure 3.3, which seems reasonable given that this is approximately where the diffusion rate moves away from the predicted initial quantum diffusion rate, D_q (see inset).

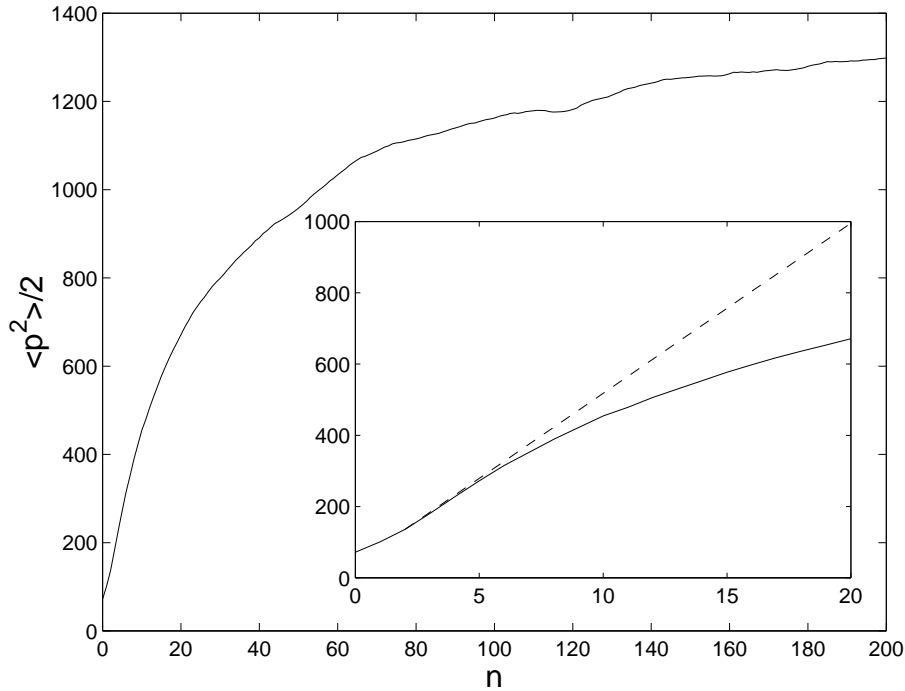


Figure 3.3: Simulation result for mean energy as a function of kick number for the quantum kicked rotor with $\alpha = 0.005$, $\kappa = 12$, $\bar{k} = 3$. The dotted line, drawn for comparison, shows diffusion from the third kick at a rate given by D_q from (3.35).

Chapter 4

The Atom Optics Kicked Rotor

4.1 Introduction

For some years, atomic physics has been an important testing ground for quantum chaos, and it is advances in atom optics that have seen the kicked rotor become a system of great interest in this field over the last ten years. The idea for an atom optics kicked rotor originated with a theoretical proposal by Graham *et al.* in 1992 [26], and was most prominently developed by Mark Raizen and his coworkers at the University of Texas at Austin in the mid 1990s [27, 28]. Similar experiments were set up at the University of Auckland in the late 1990s under the direction of Nelson Christensen [29, 30]. More recently other groups have become involved in this field, most notably the atom interferometry group from the University of Oxford [31, 32].

Essentially, these experiments involve a cloud of ultra-cold atoms (prepared using a magneto-optical trap) which interact with a standing wave of near resonant light formed by two counter-propagating plane polarised beams. This gives us a system with a Hamiltonian analogous to the standard kicked rotor system.

4.2 Theory

We consider an effective two level atom in a standing wave of near resonant light, formed by two counter propagating laser beams with wavenumber k_l . It is assumed that the beams are classical, that is, that mean photon numbers in the laser fields are large. The main process then involved in the interaction of light with the atoms is that of stimulated scattering [33], in which an atom absorbs a photon from one beam, and then coherently scatters the photon into either the same beam or the other beam. In the former case, no net momentum change results, but in the latter case (known as back scattering) a total change in momentum of $2\hbar k_l$ occurs. The other possible process, that of spontaneous emission (where an atom absorbs a photon from one beam, and then re-emits it in a random direction) is assumed to be negligible, although it will later be introduced in section 4.4 when we discuss decoherence in the atom optics

kicked rotor.

If the atoms have a natural transition frequency of ω_0 , then the detuning between the atomic resonance and the counter propagating beams is $\delta = \omega_0 - \omega_l$, where $\omega_l = k_l c$. The internal states of the atom will be denoted by $|g\rangle$ and $|e\rangle$ for the ground and excited states respectively, and thus we may write the atomic state raising and lowering operators as $|e\rangle\langle g|$ and $|g\rangle\langle e|$ respectively. Then, making use of the dipole and rotating wave approximations, the motion of a single atom along the standing wave axis is governed by the Hamiltonian [28, 34]

$$\hat{H} = \frac{\hat{p}^2}{2m} + \hbar\omega_0|e\rangle\langle e| + \hbar\Omega \cos(k_l\hat{x})(e^{-i\omega_l t}|e\rangle\langle g| + e^{i\omega_l t}|g\rangle\langle e|), \quad (4.1)$$

where \hat{x} and \hat{p} denote the position and momentum operators respectively for motion along the standing wave, m is the mass of the atoms, and $\Omega = \mu E_0/\hbar$ is the single beam resonant Rabi frequency with E_0 the field amplitude and μ the dipole moment coupling the two atomic states, $\mu = e|\langle e|\hat{\mathbf{r}}|g\rangle|$.

We can express this system in an interaction picture, choosing $\hat{H} = \hat{H}_0 + \hat{H}_I$ with $\hat{H}_0 = \hbar\omega_l|e\rangle\langle e|$. Under this formalism, we can write the Schrödinger equation for the state ket, $|\psi\rangle = \psi_g(x, t)|g\rangle + \psi_e(x, t)|e\rangle$, as two coupled differential equations,

$$i\hbar\frac{\partial\psi_g(x, t)}{\partial t} = -\frac{\hbar^2}{2m}\frac{\partial^2}{\partial x^2}\psi_g(x, t) + \hbar\Omega \cos(k_l x)\psi_e(x, t), \quad (4.2)$$

$$i\hbar\frac{\partial\psi_e(x, t)}{\partial t} = -\frac{\hbar^2}{2m}\frac{\partial^2}{\partial x^2}\psi_e(x, t) + \hbar\Omega \cos(k_l x)\psi_g(x, t) + \hbar\delta\psi_e(x, t). \quad (4.3)$$

In the case of large detuning, we can adiabatically eliminate the amplitude for the excited state [28, 35]. We see that $\psi_e(x, t) \approx -[\Omega/(2\delta)]\cos(k_l x)\psi_g(x, t)$, leaving us with the single differential equation

$$\begin{aligned} i\hbar\frac{\partial\psi_g(x, t)}{\partial t} &= -\frac{\hbar^2}{2m}\frac{\partial^2}{\partial x^2}\psi_g(x, t) - \frac{\hbar\Omega^2}{\delta}\cos^2(k_l x)\psi_g(x, t) \\ &= -\frac{\hbar^2}{2m}\frac{\partial^2}{\partial x^2}\psi_g(x, t) - \frac{\hbar\Omega^2}{2\delta}(1 + \cos(2k_l x))\psi_g(x, t). \end{aligned} \quad (4.4)$$

Thus in the regime of large detuning where we can eliminate the internal atomic dynamics, we have a system which is governed by the single particle Hamiltonian

$$\hat{H} = \frac{\hat{p}^2}{2m} - \frac{\hbar\Omega_{eff}}{2}\cos(2k_l\hat{x}), \quad (4.5)$$

where $\Omega_{eff} = \Omega^2/\delta$ is the effective potential strength.

In order to create a kicked rotor system, we then pulse the standing waves periodically, so that the system evolves freely when the standing wave is off, and evolves according to (4.5) when the standing wave is on. If we do this with a pulse profile $f(t)$ and a period T , the resulting Hamiltonian is given by

$$\hat{H} = \frac{\hat{p}^2}{2m} - \frac{\hbar\Omega_{eff}}{2}\cos(2k_l\hat{x})\sum_{n=0}^{\infty}f(t - nT). \quad (4.6)$$

This Hamiltonian may be transformed into dimensionless units by choosing $\hat{\phi} = 2k_l\hat{x}$, $\hat{\rho} = 2k_lT\hat{p}/m$, $t' = t/T$, and $\hat{H}' = (4k_l^2T^2/m)\hat{H}$, so that

$$\hat{H}' = \frac{\hat{\rho}^2}{2} - k \cos \hat{\phi} \sum_{n=0}^{\infty} f(t' - n), \quad (4.7)$$

which is equivalent to the dimensionless Hamiltonian for the quantum kicked rotor (3.9). The equivalent classical stochasticity parameter is given by $\kappa = k\alpha = 4\Omega_{eff}\omega_R T\tau_p$, where τ_p is the pulse length and $\omega_R = \hbar k_l^2/2m$, although as the pulses are necessarily of finite width, the kick strength will be somewhat momentum dependent, as was discussed in section 2.3.2. In these units, we have $[\hat{\phi}, \hat{\rho}] = i\bar{k}$, with $\bar{k} = 8\omega_R T$.

It is useful to note that the relationship between the momentum units in (4.6) and (4.7) may be expressed as

$$\frac{p}{2\hbar k_l} = \frac{\rho}{\bar{k}}. \quad (4.8)$$

This is especially important because momentum changes in the system are quantised in units of $2\hbar k_l$, so that for an atom with a well defined initial momentum ρ_0 , the momentum at a later time is restricted to a ladder of states, $\rho = \rho_0 + n\bar{k}$ for integer n . For $\rho_0 = 0$ these states will be exactly equivalent to the states of the quantum rotor, and for other values we may make small adjustments to our calculations with the quantum rotor states to account for the difference, as will be discussed in chapter 5.

4.3 Experiments at the University of Auckland

4.3.1 The Atom Trapping Laboratory

The Atom Trapping and Quantum Chaos group at the University of Auckland performs experiments on a kicked rotor system realised using Caesium atoms. This experiment was first assembled in 1996 (see reference [36]), and is shown in its current state in figure 4.1.

The central feature of the Atom Trapping Laboratory, the vacuum cell, is shown in figure 4.2. It is surrounded by Helmholtz coils which are used to cancel the Earth's magnetic field. The cell is constructed from glass, and has eight optically flat windows (made from Pyrex) to allow laser beams to pass through it. The pressure inside the cell is maintained at around 10^{-8} Torr using an ion pump, and the cell contains a low pressure vapour of ^{133}Cs , which is the only stable isotope of Caesium. These Caesium atoms are trapped and cooled using a magneto-optical trap (MOT), formed from six circularly polarised trapping beams, and magnetic fields induced by the anti-Helmholtz coils situated at the top and bottom of the glass cell. The techniques involved in this are well described by Metcalf and van der Straten [37], amongst many others, and it was for the development of these techniques that Claude Cohen-Tannoudji, Steven



Figure 4.1: The Atom Trapping Laboratory, Department of Physics, University of Auckland

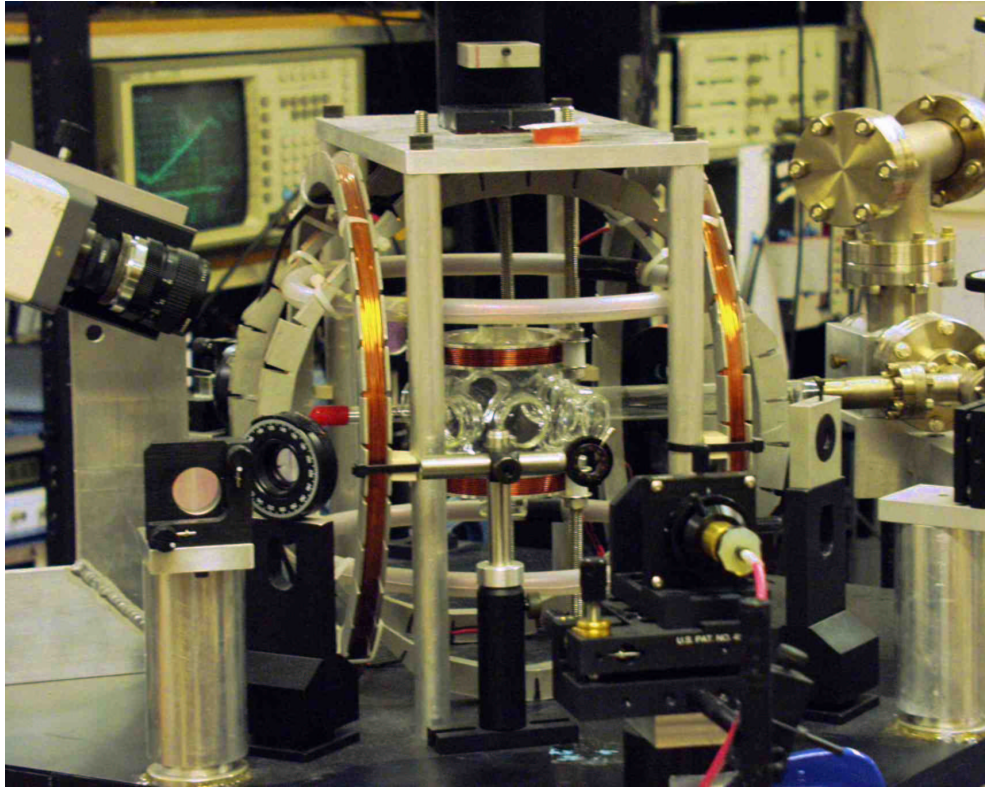


Figure 4.2: The main cell of the Atom Trapping Laboratory, as described in the text. See figure 4.1.

Chu, and William Phillips were awarded the Nobel Prize in Physics in 1997. Using the MOT, we can produce a cloud of cold Caesium atoms with a temperature of the order of $10\mu\text{K}$, situated at the centre of the cell. Typically we observe around 10^6 atoms in the cloud, which has a width of around $600\mu\text{m}$.

The Caesium atoms are observed using a CCD camera (on the left hand side in figure 4.2), which captures the infra-red light given off by the Caesium atoms when they fluoresce. Signals from the CCD camera are captured using computer software, which is used to analyse the properties of the cloud. The same computer software (written in LabView^{®1}) controls the experiment by turning the trapping beams and magnetic field on and off as required, and as the cloud is allowed to expand pulses a “kicking” beam on and off using acousto-optical modulators (AOMs). The kicking beam is used to create the standing wave across the cell which gives us the kicked rotor system. It is blue detuned from the $6S_{1/2} \rightarrow 6P_{3/2}$ transition in Caesium ($F = 4 \rightarrow F' = 5, 4, 3$), which corresponds to a wavelength near 852 nm, and which is also used as the trapping transition. The maximum power available in the kicking beam is 22 mW, and the beam is typically detuned from the transition frequency by around 300 - 1000 MHz.

¹LabView[®] is a registered trademark of National Instruments Corporation

The momentum distribution of the cloud is determined by allowing the cloud to freely expand for a specified time period after the kicking has been completed, and then switching on the trapping beams (but not the magnetic field) to slow the expansion and taking a picture of the cloud using the CCD camera. The momentum distribution of the atoms will then be related to the position distributions before and after the free expansion period via a convolution. In practice, the position distribution will closely resemble the momentum distribution, and it is often unnecessary to compute a full deconvolution.

4.3.2 Structure of Caesium

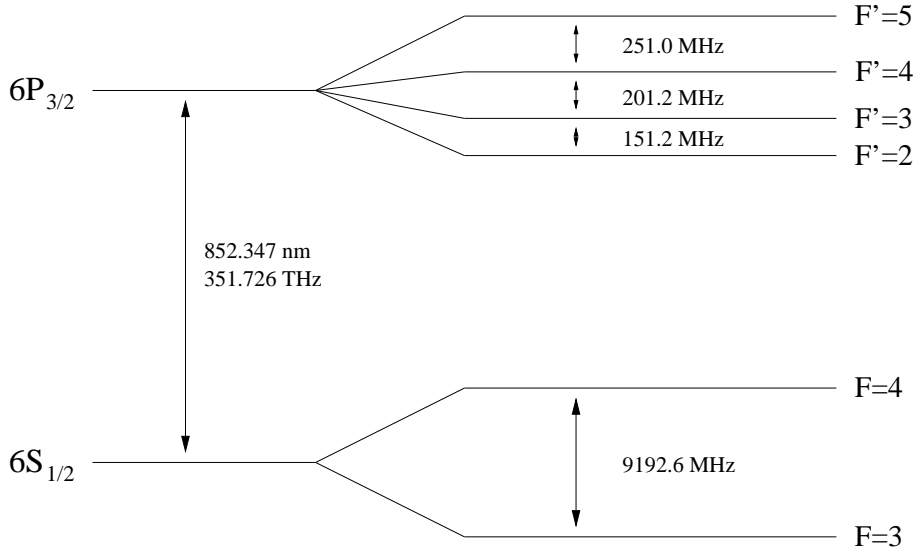


Figure 4.3: Hyperfine structure of the D_2 transition for Caesium.

The hyperfine structure of the $6S_{1/2} \rightarrow 6P_{3/2}$ transition for Caesium is shown in figure 4.3. The nontrivial structure of this transition complicates our basic two state model in two ways. Firstly, the single Rabi frequency used in (4.6) is not sufficient to describe our system because the interaction of an atom with the standing wave will lead to transitions from the $F = 4$ state to states with $F' = 3, 4$ and 5 , with each transition having its own Rabi frequency. We can account for this by taking a weighted average of the Rabi frequencies for the individual transitions, where the weightings depend on the relative probabilities of the different transitions. The effective potential strength is then given by

$$\Omega_{eff} = \Omega^2 \left(\frac{s_{45}}{\delta_{45}} + \frac{s_{44}}{\delta_{44}} + \frac{s_{43}}{\delta_{43}} \right), \quad (4.9)$$

where δ_{ij} is the corresponding detuning for the transition from $F = i$ to $F' = j$, and

s_{ij} are weighting factors. If we assume equal populations in all Zeeman sublevels, then $s_{45} = 11/27$, $s_{44} = 7/36$ and $s_{43} = 7/108$ [29].

Secondly, there is a small but significant probability that an atom in the $F' = 3$ or $F' = 4$ state might decay into the $F = 3$ hyperfine level of the ground state. When this occurs, the atom will begin to interact much more weakly with the kicking beam (because of the larger detuning) and will essentially be lost from our kicked rotor system. To counteract this effect, another beam of the same circular polarisation as the MOT beams, tuned to the $F = 3 \rightarrow F' = 4$ transition and known as the repump beam, is used to restore the atoms to the system. In fact, the repump beam is also an integral part of the trapping and cooling process, and is simply left on when the main trapping beams are switched off.

The values in figure 4.3 come from Daniel Steck's compilation of Caesium D Line Data [38]. Values involving the $6P_{3/2}$ state come from measurements made by Tanner and Wieman [39], whilst the separation of the $F = 3$ and $F = 4$ line is exact, $\Delta f = 9.192631770$ GHz, based on the use of these states in the current definition of the second.

4.3.3 Theory and Experiment

In addition to the nontrivial structure of the Caesium atom, there are a few obvious factors that can cause discrepancies between the theoretical model of the quantum kicked rotor and the atom optics realisation of that system.

Finite Width of the Cloud

The first discrepancy comes from the finite width of the cloud with respect to the kicking beam which produces the standing wave. The kicking beam has a Gaussian radial intensity profile, so that the intensity becomes lower away from the axis of the beam. The cloud of Caesium atoms is centred on the axis of the standing wave, but atoms which are further from the axis will be in regions of lower intensity, and so will experience a lower effective kick strength. In fact, the beam radius for the kicking beam has often been as low as only twice the half width of the cloud. Furthermore, as the cloud expands, atoms will move into regions of different intensity and so will not experience a constant kick strength. It is difficult to predict the effects of this phenomenon, and mostly we have modelled it by adding some noise to the kick strength in our simulations. In fact, amplitude noise of this sort is used deliberately in some of our investigations (see section 4.5). Unfortunately, the effects here are more systematic than those accounted for by the introduction of amplitude noise, and some discrepancy is likely to occur between theoretical predictions and experimental results because of this.

Another possible area of concern is that the atoms at the outside of the cloud experience the lowest kick strength, which could bias the momentum distribution which we calculate from the position distribution after the free expansion period (see section

4.3.1). However, the effects of this should be small due to the large expansion of the cloud during the free expansion period.

Pulse Shape

Experimentally, it is impossible to directly realise the δ -kicked rotor, as the kicking beam pulses must have some finite length in time. Thus, we attempt to approximate results for the δ -kicked rotor by realising the rectangular pulse-kicked rotor. We use as small an α value as is practical so that we eliminate effects due to the variation of effective kick strength with momentum value, which was discussed in relation to the classical kicked rotor in section 2.3.2 and which also holds for the quantum kicked rotor. All of our simulations take this finite pulse length into account, so that no discrepancies between simulation results and experimental results should result from it.

Of course, even the rectangular pulse-kicked rotor is an approximation, as the pulse must have a finite rise time and fall time, based primarily on the response time of the AOMs. The resulting effects are relatively small except in the case of very small pulse lengths. Generally, pulse durations of 200 - 600 ns are used, and the rise and fall times are around 50 ns at each end of the pulse. We note from the resonance analysis in section 2.3.2 that for the low momentum values to which we want to restrict the system (i.e., those with an effective kick strength $\approx \kappa = k\alpha$), the important frequency components in the pulse are the low frequency components. Because the finite rise and fall times only significantly alter the high frequency components (the pulse shape we get is very similar to a low-pass filtered version of a rectangular pulse), this should make little difference to our system.

Other Limiting Factors

In addition to the finite width of the cloud and the non-ideal shape of the pulse, the main difficulties in conducting these experiments relate to the accurate detection of the final position distribution. The biggest problems are generated by the dark current noise level on the CCD camera and also the need to accurately subtract background light levels from all of the pictures. Other difficulties include non-idealities in the trapping beams which are used to slow the expansion of the cloud while the position distribution is photographed, including spatially varying intensity due to interference fringes caused by reflections of the beams from the windows of the vacuum cell. All of these factors will contribute to uncertainties in the data, which can only be improved upon by the use of better equipment in future experiments.

4.4 Decoherence and Spontaneous Emission Noise

Any real macroscopic quantum system couples in some way to its environment, and this coupling results in a loss of coherence from the system. In the case of the atom optics kicked rotor, this decoherence, as it is termed, occurs in the form of spontaneous

emissions, in which atoms in the excited state emit photons spontaneously in a random direction. Spontaneous emissions result in a loss of phase coherence, as well as giving the atom a random momentum kick which can have any value in the range $[-\hbar k_l, \hbar k_l]$ when projected onto the standing wave axis. (Note that because of the continuous value of this momentum kick projected onto our one dimensional system, the offset of the ladder states available to the system, ρ_0 , is changed.) It is assumed throughout that the system remains essentially one-dimensional - i.e. that spontaneous emissions do not create any form of entanglement between motions of the atom in orthogonal directions.

4.4.1 Measurement and Decoherence in Quantum Mechanics

The investigation of decoherence has become very important in quantum chaos over the last 20 years as its role in explaining the interaction between the quantum world and the classical world has taken on more significance. One of the biggest difficulties in quantum mechanics since its inception in the 1920s has been the inability to reconcile the principle of superposition with our everyday experience of the classical world. Essentially, the linearity of Schrödinger's equation means that given any initial state $|\psi\rangle$ describing some element of the classical universe, the state will almost certainly evolve into a superposition of many alternatives which do not appear to co-exist in the universe we are used to experiencing. The most common example of this is the paradox of Schrödinger's cat, in which a cat is hypothetically shut inside a box with poisonous gas which is to be released when triggered by a radioactive source. After a short time such a cat should, according to quantum mechanics, be in a superposition of the macroscopic states of being alive and being dead - an idea that is in strong contrast with our perceptions of the classical world.

The first attempted explanation of how a single outcome emerges from a quantum mechanical superposition was proposed by Niels Bohr in 1928, and is known as the Copenhagen interpretation [40]. Bohr insisted that a classical apparatus must be used to make measurements on a quantum system, thus creating a dividing line between the quantum world and the classical world. Unfortunately, this approach is inadequate, as it is very unclear as to where such a line would be drawn, with many examples of supposedly macroscopic systems demonstrating clearly quantum properties [41]. Another prominent proposal, the many-worlds interpretation, was initiated by Everett [42] and Wheeler [43] in the 1950s. This interpretation suggests that the whole universe is quantum mechanical, with a wavefunction that splits whenever two quantum systems interact, so that it develops down particular branches, with all different possibilities accounted for in different branches. The problem with this is that there is still no explanation as to why the universe as we observe it develops down a particular branch, and thus why we observe a particular instance of the possible outcomes.

The key to the most modern interpretation, which is championed by Zurek [41, 44] amongst others, is that real macroscopic quantum systems are never isolated from their environments, and so should not be expected to follow Schrödinger's equation,

which applies only to closed systems. Instead, in real macroscopic quantum systems decoherence occurs through the coupling of the system to extraneous degrees of freedom of the environment, and leakage of coherence information into the environment imposes the necessary restriction on the observed outcomes of the system. Essentially, the notion of decoherence has eliminated the need for a conscious observer to make a measurement in order to collapse the wavefunction into a single state.

4.4.2 Spontaneous Emission rate for a Two-Level Atom

As was previously mentioned, the main form of decoherence in the atom optics kicked rotor system is via spontaneous emission processes, which amount to a coupling between the system and the vacuum electromagnetic field. The most convenient way to analyse spontaneous emission processes is to consider a two level atom at rest in a light field. We then need only consider the internal states of the atom, which for a pure state are most conveniently described using the density operator

$$\hat{w} = \sum_{i \in \{g,e\}} \sum_{j \in \{g,e\}} w_{ij} |i\rangle \langle j|, \quad (4.10)$$

for some complex numbers w_{ij} . This is often expressed in matrix form as

$$\begin{pmatrix} |e\rangle & |g\rangle \end{pmatrix} \begin{pmatrix} w_{ee} & w_{eg} \\ w_{ge} & w_{gg} \end{pmatrix} \begin{pmatrix} \langle e| \\ \langle g| \end{pmatrix}. \quad (4.11)$$

The evolution of the system due to coupling to the light field and spontaneous emissions may then be expressed in terms of the optical Bloch equations [34, 37, 38], which are given by

$$\dot{w}_{gg} = \frac{i\Omega}{2}(\tilde{w}_{ge} - \tilde{w}_{eg}) + \Gamma w_{ee}, \quad (4.12a)$$

$$\dot{\tilde{w}}_{ge} = -\left(\frac{\Gamma}{2} + i\delta\right)\tilde{w}_{ge} - \frac{i\Omega}{2}(w_{ee} - w_{gg}), \quad (4.12b)$$

$$\dot{w}_{ee} = -\dot{w}_{gg}, \quad (4.12c)$$

$$\dot{\tilde{w}}_{eg} = \dot{\tilde{w}}_{ge}^*, \quad (4.12d)$$

where $\tilde{w}_{ge} = w_{ge}e^{-i\delta t}$, $\tilde{w}_{eg} = \tilde{w}_{ge}^*$ and Γ is the decay rate of the excited state population,

$$\Gamma = \frac{\omega_0^3 \mu^2}{3\pi\epsilon_0 \hbar c^3}. \quad (4.13)$$

The steady state solutions of the optical Bloch equations may be found if we note that $w_{eg} = w_{ge}^*$ and $w_{ee} + w_{gg} = 1$. Then, for $t \rightarrow \infty$ we have

$$w_{gg} - w_{ee} = \frac{1}{1 + s} \quad (4.14a)$$

and

$$w_{eg} = \frac{i\Omega}{2(\Gamma/2 - i\delta)(1 + s)}, \quad (4.14b)$$

where s , the saturation parameter, is given by

$$s = \frac{2\Omega^2}{\Gamma^2 + 4\delta^2}.$$

The steady state population of the excited state is

$$w_{ee,ss} = \frac{s}{2(1 + s)} = \frac{\Omega^2}{\Gamma^2 + 2\Omega^2 + 4\delta^2}. \quad (4.15)$$

This is often expressed in terms of the intensity ratio (I/I_s),

$$\frac{I}{I_s} = \frac{2\Omega^2}{\Gamma^2}, \quad (4.16a)$$

where I_s , the saturation intensity, is given by

$$I_s = \frac{2\pi^2\hbar c\Gamma}{3\lambda^2}. \quad (4.16b)$$

It is important to note that often $2I_s$ is referred to as the saturation intensity, and that all of these expressions depend on our definition of the Rabi frequency, which often varies in the relevant literature by factors of 2 or $\sqrt{2}$.

In terms of (I/I_s), we may write (4.15) as

$$w_{ee,ss} = \left(\frac{1}{2}\right) \frac{(I/I_s)}{1 + (I/I_s) + 4(\delta/\Gamma)^2}. \quad (4.17)$$

We note that as the saturation parameter s becomes large (i.e., for strong intensities), $w_{ee,ss} \rightarrow 1/2$. Thus, for high s half of the population will be in each state, whereas for low s , $w_{ee,ss}$ is small, and most of the population is in the ground state.

The spontaneous emission rate in steady state, R_{sp} , is given by

$$R_{sp} = \Gamma w_{ee,ss} = \left(\frac{\Gamma}{2}\right) \frac{(I/I_s)}{1 + (I/I_s) + 4(\delta/\Gamma)^2} = \frac{\Gamma\Omega^2}{\Gamma^2 + 2\Omega^2 + 4\delta^2}. \quad (4.18)$$

Again, we see here that in the very high intensity limit, $R_{sp} \rightarrow \Gamma/2$. The most useful limit, however, is the one where the detuning, δ , is large compared with Ω and Γ . In this limit, (4.18) reduces to

$$R_{sp} \approx \frac{\Gamma\Omega^2}{4\delta^2} \propto \frac{\Omega^2}{\delta^2}. \quad (4.19)$$

4.4.3 Spontaneous Emission Noise in the Atom Optics Kicked Rotor

With some minor corrections for the multi-level nature of Caesium (see reference [38]), the theory of spontaneous emission rates for a two level atom applies well to our system. We characterise the amount of spontaneous emission by the probability of spontaneous emission per kick, η , which is given by

$$\eta = \tau_p R_{sp} = \frac{\tau_p \Gamma \Omega^2}{\Gamma^2 + 2\Omega^2 + 4\delta^2}. \quad (4.20)$$

It is assumed that $\tau_p R_{sp}$ is small, so that η constitutes a probability, rather than just the average number of spontaneous emissions per kick.

Spontaneous emission levels may be controlled either (i) by adjusting the intensity and detuning of the kicking beam, or (ii) by strongly detuning the kicking beam so as to make spontaneous emissions due to it small, and instead leaking some near-resonant light from trapping beams into the cell in order to induce spontaneous emissions. Because we are interested in the limit of large detuning, η scales as Ω^2/δ^2 , and so the spontaneous emission probability per kick due to the kicking beam may be adjusted independently of the potential well depth, which scales as Ω^2/δ (see section 4.2).

Experimentally, both methods have been used to generate spontaneous emissions, with the Auckland group primarily using the kicking beam and the Austin group primarily using methods involving leaked trapping beams.

The method used by the Auckland group generates position dependent spontaneous emission noise because the intensity of the standing wave varies as $\cos(2k_l x)$. We model this situation, again under the assumption of a large detuning ($\Omega_{eff}/\delta \ll 1$), using a master equation which fully describes the behaviour of an atom in the standing wave [45, 46]. This is given by

$$\begin{aligned} \dot{\hat{w}} &= -\frac{i}{\hbar} [\hat{H}, \hat{w}] - \frac{\eta}{\alpha} \sum_{n=1}^N f(t-n) [\cos^2(\hat{\phi}/2), \hat{w}]_+ \\ &+ 2\frac{\eta}{\alpha} \sum_{n=1}^N f(t-n) \int_{-1}^1 du N(u) e^{iu\hat{\phi}/2} \\ &\times \cos(\hat{\phi}/2) \hat{w} \cos(\hat{\phi}/2) e^{-iu\hat{\phi}/2}, \end{aligned} \quad (4.21)$$

where $N(u)$ is the projection onto the standing wave axis of the distribution of recoil momenta, and $[\cdot, \cdot]_+$ denotes an anti-commutator. The first term of this equation describes the motion of the atom in the standing wave potential, while the other terms account for momentum diffusion due to spontaneous emissions. Note that η in this equation is a **position averaged** probability of spontaneous emission per kick. That is, it is approximately half the value of η given in (4.20), which is the spontaneous emission probability per kick at the intensity antinodes of the standing wave. In the large detuning limit, $\delta^2 \gg \Omega^2$, η is exactly one half of the value given in (4.20).

The additional correction if we were not in this limit would arise from the Ω^2 term in the denominator, which would play a part in the position averaging of the whole expression once we substitute $\Omega^2(x) = \Omega^2 \cos^2(k_l x)$. We use the position averaged η to quantify the spontaneous emission rate in our system so that the decoherence arising from a particular value of η is comparable to that introduced by the same value of η in experiments not involving standing waves. Another consequence of this is that the last two terms in (4.21) as written are a factor of two larger than they would be if η was defined exactly as it is in equation (4.20).

The method used by the Austin group creates position independent spontaneous emission noise because the trapping beams that are leaked into the trap consist of two counter-propagating beams of opposite circular polarisation, and the intensity of the beams is independent of position. An additional difference in these experiments is that the beams are leaked into the cell during the whole kicking period, so that spontaneous emissions can occur during the free evolution period between kicks (unlike in the Auckland experiments, where no spontaneous emissions occur if the kicking beam is off). The master equation to describe this process is given by

$$\begin{aligned} \dot{\hat{w}} = & -\frac{i}{\hbar} [\hat{H}, \hat{w}] - \eta \hat{w} \\ & + \eta \int_{-1}^1 du N(u) e^{iu\hat{\phi}/2} \hat{w} e^{-iu\hat{\phi}/2}. \end{aligned} \quad (4.22)$$

Note that η in this equation can unambiguously be defined exactly as in equation (4.20), as there is no position dependence in the probability of spontaneous emission per kick.

Both master equations have been simulated using techniques described in chapter 5. The numerical results we get from each type of spontaneous emission noise for a particular value of η are very similar, as is shown in chapter 6. Because of this, we primarily model spontaneous emission noise from equation (4.21) throughout most of our work.

4.4.4 Decoherence and the Kicked Rotor

With the control over spontaneous emission decoherence that the atom optics kicked rotor experiments provide, the kicked rotor has become prominent in investigations of decoherence, and the role that it plays in the quantum-classical transition. There have been numerous studies of this sort, both theoretical (for example, see references [45, 46, 47, 48, 3]) and experimental [30, 49, 50, 51, 52], which have mainly focussed on how increased levels of decoherence “drive” the system towards classical behaviour. An example of such behaviour is the destruction of dynamical localisation, which occurs because dynamical localisation depends on quantum coherences which are lost through spontaneous emissions. Instead of settling into a localised state, the atom optics kicked rotor with spontaneous emission noise settles into a non-zero late time diffusion rate, a property which we study in detail in chapter 6

The focus of our investigation is a little different to many earlier studies. We look at how the dynamics change if we fix the level of decoherence, and then make the system either more or less macroscopic by varying the total action, and hence the effective Planck's constant, \hbar . We find interesting structures in diffusion rates as we do this, especially in the late time diffusion rates. This is similar to the approach taken by Bhattacharya *et al.* [1] in their numerical investigation of the quantum δ -kicked rotor where decoherence was introduced by way of a continuous position measurement. The structures that they observed in late time diffusion rates are similar to some of our results, which are presented in chapter 6, although our results are in the context of a specific experimental system.

4.5 Amplitude Noise

Another form of noise that can be used in the atom optics kicked rotor in order to diminish correlations and drive the system towards a more classical behaviour is amplitude noise. This is generated by varying the intensity of the kicking beam from one kick to the next, hence changing the depth of the potential well and creating noise on the kicking strength. We find that amplitude noise, like spontaneous emission decoherence, prevents the system from settling down into a localised state. As with spontaneous emission decoherence, the system instead settles into a (quasi-)steady state with a non-zero late time diffusion rate.

The scaled Hamiltonian for the kicked rotor with amplitude noise may be expressed as

$$\hat{H} = \frac{\hat{p}^2}{2} - \cos \phi \sum_{n=0}^{\infty} \frac{\kappa(n)}{\alpha} f(t - n), \quad (4.23)$$

where $\kappa(n)$ is randomly chosen from some pre-defined distribution. We generally use a uniform distribution on some interval $\kappa(n) \in [\kappa - \delta\kappa, \kappa + \delta\kappa]$. In this case, we refer to the amount of noise as a percentage given by:

$$\text{noise} = \frac{2\delta\kappa}{\kappa}. \quad (4.24)$$

For example, if $\kappa(n)$ is uniformly sampled on the interval $[5, 15]$, then we say that the system has parameters $\kappa = 10$ and noise = 100%. Uniform noise distributions are particularly convenient to generate experimentally as we do not need to restrict $\kappa(n)$ from becoming negative, as we would have to do with a Gaussian distribution.

There is always some natural amplitude noise present in the system through small fluctuations in the power and detuning, and because of the finite width of the cloud compared with the kicking beam (see section 4.3.3). Additional amplitude noise is generated in our experiments using a purpose built electronic pulsing box, which controls the AOMs and is capable of generating arbitrary waveforms which can be downloaded to the box from a desktop PC. Amplitude noise is included in most of our simulations, which are described in chapter 5.

4.6 The Classical Limit of the Atom Optics Kicked Rotor

It is both interesting and important to consider the parameters of the classical system that we obtain if we take the limit of the atom optics kicked rotor as $\hbar \rightarrow 0$. This system is not experimentally realisable using the atom optics setup, but is the system to which we are essentially comparing our quantum system when we fix κ and α and vary \hbar .

Because we fix κ and α , these parameters are the same in the $\hbar = 0$ limit. However, our initial momentum distribution and recoil momentum kicks from spontaneous emissions exhibit interesting behaviour. Because the initial momentum distribution has a fixed width, σ_p , in real momentum units (the width is controlled by the initial temperature of the cloud), the width of this distribution in dimensionless momentum units, σ_ρ , changes as \hbar is varied. In fact, because $\rho/\hbar = p/(2\hbar k_l)$, we have that $\sigma_\rho = \sigma_p \hbar / (2\hbar k_l)$, and we see that $\sigma_\rho \rightarrow 0$ as $\hbar \rightarrow 0$. Similarly, because the momentum recoil due to spontaneous emissions is given by $\Delta p \in [-\hbar k_l, \hbar k_l]$, we see that $\Delta \rho \in [-\hbar/2, \hbar/2]$. Thus, as $\hbar \rightarrow 0$, $|\Delta \rho| \rightarrow 0$.

Physically, this scaling occurs because $\Omega_{eff} \tau_p / 2 = \kappa / (4\omega_R T) = 2\kappa / \hbar$, so that to obtain the limit $\hbar \rightarrow 0$ for constant κ , we must make $\Omega_{eff} \rightarrow \infty$. The physical potential well depth thus becomes very large, and the diffusion rates and momenta as measured in real momentum units also become very large, making σ_ρ and Δp relatively insignificant.

The effects of narrowing the initial momentum distribution in classical and quantum systems are discussed in more detail in chapter 9, but in general the quantum results for initial quantum diffusion rates and late time diffusion rates are not changed significantly. Narrow initial momentum distributions can have an effect on the corresponding classical results, particularly for κ values near the anomalous diffusion peaks (the peaks near $\kappa \sim 7$, $\kappa \sim 14$ or $\kappa \sim 20$ in figure 2.16). Near such peaks, the diffusion rates can increase noticeably for very narrow momentum distributions. However, the largest effects occur when κ is small, and, even for $\kappa \approx 14$, the changes in the diffusion rates are not very significant. Thus, for most of the comparisons we want to make between classical and quantum diffusion rates, the width of the initial momentum distribution will not qualitatively alter the results.

The fact that the classical system obtained by making $\hbar \rightarrow 0$ has no momentum recoil due to spontaneous emission events is not significant, because the change in the momentum diffusion rates due to the momentum recoils from any ordinary level of spontaneous emission noise is small. This can be clearly seen from classical simulation results which are discussed in chapter 6.

An alternative way of treating the system, in which the physical potential well depth, $\hbar \Omega_{eff} / 2$, is kept constant as T is varied is discussed in chapter 8.

Chapter 5

Techniques for Simulation of the Kicked Rotor

5.1 Introduction

Many of the results presented in this thesis come from extensive simulations of diffusion rates in the atom optics kicked rotor. These simulations are based on the work of Marte *et al.* [53], who use the Monte-Carlo Wave Function (MCWF) method [54], which is described in section 5.3.1. The simulations take into account the effects of finite pulse lengths, as well as modelling spontaneous emission noise and amplitude noise. For comparison purposes, simulations of the classical kicked rotor have also been performed, both for δ -kicks and for rectangular-pulse kicks. Amplitude noise and momentum recoils due to spontaneous emissions have also been included in the classical simulations.

This chapter describes in detail the simulation methods used in the programs. Example source code for most of these methods may be found in appendix C.

5.2 Classical Simulations

5.2.1 General Method

Classical kicked rotor simulations were performed by choosing initial conditions for an ensemble of rotors, and then evolving each set of initial conditions using Hamilton's equations of motion. Generally we use about 4000 rotors in the ensemble, with the initial position, ϕ_0 , chosen from a uniform distribution on $[-\pi, \pi)$, and the initial momentum, ρ_0 , chosen from a Gaussian distribution centred on $\rho = 0$ with a width of σ_ρ .

For the δ -kicked rotor, evolving the initial states means evolving the position ϕ and momentum ρ based on the classical standard map (2.38). An example of this is the program to produce Poincaré sections for the δ -kicked rotor, which is included in

appendix C.

For the pulse-kicked rotor there are two parts to the evolution in each step. Firstly, we must calculate the motion during the kick by evolving ϕ and ρ through a pendulum potential for a time $\Delta\tau = \alpha$. Then we account for the free evolution of ϕ by computing $\Delta\phi = (1 - \alpha)\rho$.

There are two methods for computing the evolution in a pendulum potential. We can numerically integrate Hamilton's equations of motion, or we can use the analytical solutions for this motion in terms of Jacobi elliptic functions, which was quoted in section 2.2. Integrating the differential equations allows more flexibility for considering arbitrary pulse shapes, and can also be easily generalised to different potential shapes. However, for an ordinary rectangular pulse-kicked rotor the use of the analytical results is considerably more efficient. Source code is shown in appendix C for a program written in C (based on integration and random number generation routines from *Numerical Recipes in C* [55]) which integrates the differential equations, and also for a program written in MATLAB[®]¹ which computes the analytical solutions.

MATLAB[®] is distributed with the function file `ellipj.m` which computes the Jacobi elliptic functions $\text{sn}(x)$, $\text{cn}(x)$ and $\text{dn}(x)$. The $\text{sn}^{-1}(x)$ function is not provided, and so a program written in C by S. M. Tan using the MATLAB[®] MEX interface and based on code from *Numerical Recipes in C* [55] is called from within MATLAB[®] to calculate expressions involving this inverse elliptic function.

5.2.2 Addition of Amplitude and Spontaneous Emission Noise

In order for proper comparisons to be drawn between simulation results for the classical and quantum kicked rotors, we must be able to include in our classical simulations the effects of amplitude noise and spontaneous emissions. The implementation of amplitude noise is straight forward, as we simply need to randomly choose a separate $\kappa(n)$ for each kick from the appropriate distribution of possible κ values. We then repeat this process around 20 times, using a different set of $\kappa(n)$ values each time (a different “realisation” of the noise), and average over all 20 resulting distributions of ϕ and ρ values.

Classically, spontaneous emission noise is not as large an influence as it is in quantum systems, as by assumption there are already no significant quantum coherences in the classical system, and so decoherence cannot affect the evolution of the system. However, small increases in momentum diffusion rates arise because of momentum recoils during spontaneous emissions, and it is important to be able to evaluate the significance of this effect.

We do this by adding momentum recoils to the classical simulations. Essentially, for each set of initial conditions we choose a set of times at which spontaneous emission events will occur, and then at those times we introduce a random change in momentum of $\Delta\rho \in [-1/2, 1/2]$. The times are chosen by selecting a set of random numbers c_i

¹MATLAB[®] is a registered trademark of The Mathworks, Inc.

from a uniform distribution on $(0, 1]$, and saying that the i th spontaneous emission event occurs at a time τ_i after the $(i - 1)$ th event, where

$$e^{-\eta\tau_i} = c_i, \quad (5.1)$$

so that we have,

$$\tau_i = \frac{-\log_e(c_i)}{\eta}. \quad (5.2)$$

Note that the mean time before a spontaneous emission event is given by

$$\langle \tau_i \rangle = \frac{\langle -\log_e(c_i) \rangle}{\eta} = \frac{1}{\eta}, \quad (5.3)$$

as we expect.

Examples of code to implement spontaneous emission noise in a classical kicked rotor system may be found in appendix C.

5.3 Quantum Simulations

5.3.1 The Monte-Carlo Wavefunction Method

The Monte-Carlo Wavefunction Method (MCWF) for simulating the density matrices of dissipative systems in quantum optics and similar related methods were developed independently by several different groups during the 1990s. In all of these methods, system wavefunctions are evolved in time, and dissipation occurs in the form of quantum jumps (which might, for example, involve a spontaneous emission event). Mølmer, Castin, and Dalibard published a paper [54] in 1992 which formalised this method for use with a fixed timestep, while independently Dum, Zoller and Ritsch [56] formulated a similar method which calculated the times for quantum jumps based on a delay function. This method was further developed by Dum, Parkins, Zoller and Gardiner [57], and it is an adaption of this method (see section 5.3.2) that we use to perform our quantum simulations. Another similar method, originally applied to photoelectron counting systems, was devised by Carmichael [58], and is known as the method of quantum trajectories.

In this section, the MCWF method is described, closely following the presentation in reference [54]. This method explicitly involves small, fixed timesteps, but is easily generalised to longer timesteps for which we apply the principles of the method described in reference [57].

Our goal is to simulate a system described by the master equation

$$\dot{\hat{w}} = \frac{i}{\hbar}[\hat{w}, \hat{H}_s] + \mathcal{L}(\hat{w}), \quad (5.4)$$

where \hat{w} is the density operator for the reduced system, \hat{H}_s is the Hamiltonian for the isolated system, and \mathcal{L} is the Liouvillian superoperator describing the coupling of the system to the environment. $\mathcal{L}(\hat{w})$ is assumed to take the form

$$\mathcal{L}(\hat{w}) = -\frac{1}{2}(\hat{C}^\dagger \hat{C} \hat{w} + \hat{w} \hat{C} \hat{C}^\dagger) + \hat{C} \hat{w}^\dagger \hat{C}, \quad (5.5)$$

where \hat{C} is the system operator involved in the coupling of the system to the reservoir. In reference [54] the MCWF is shown to work with a slight generalisation of this form, but this is not required for our purposes.

Now we assume that at time t , the system is in a state given by $|\psi(t)\rangle$. The evolution to the state at time $t + \delta t$ occurs in two steps.

Firstly, we calculate $|\psi_1(t + \delta t)\rangle$, which is defined as the state we get when we evolve the state $|\psi(t)\rangle$ through a time interval δt with the non-Hermitian Hamiltonian

$$\hat{H} = \hat{H}_s - \frac{i\hbar}{2} \hat{C}^\dagger \hat{C}. \quad (5.6)$$

For small δt , this gives

$$|\psi_1(t + \delta t)\rangle = \left(1 - \frac{i\hat{H}\delta t}{\hbar}\right) |\psi(t)\rangle. \quad (5.7)$$

Note that because \hat{H} is not Hermitian, $|\psi_1(t + \delta t)\rangle$ will not be normalised. In fact,

$$\langle \psi_1(t + \delta t) | \psi_1(t + \delta t) \rangle = \langle \psi(t) | \left(1 + \frac{i\hat{H}^\dagger \delta t}{\hbar}\right) \left(1 - \frac{i\hat{H}\delta t}{\hbar}\right) | \psi(t) \rangle \quad (5.8a)$$

$$= 1 - \delta f, \quad (5.8b)$$

where

$$\delta f \approx \delta t \frac{i}{\hbar} \langle \psi(t) | (\hat{H} - \hat{H}^\dagger) | \psi(t) \rangle \quad (5.9a)$$

$$= \delta t \langle \psi(t) | \hat{C}^\dagger \hat{C} | \psi(t) \rangle. \quad (5.9b)$$

We see that $\delta f \geq 0$, and we adjust δt so that δf is small.

The second part of the evolution of the state from $|\psi(t)\rangle$ to $|\psi(t + \delta t)\rangle$ tests for the occurrence of a quantum jump (such as a spontaneous emission event). To decide whether such a jump happens we choose a random number, ϵ , from a uniform distribution on the interval $[0, 1]$. If $\delta f < \epsilon$ then we say that no quantum jump occurs, and we simply renormalise the state at time $t + \delta t$, i.e.,

$$|\psi(t + \delta t)\rangle = \frac{|\psi_1(t + \delta t)\rangle}{\sqrt{1 - \delta f}}. \quad (5.10a)$$

If $\delta f > \epsilon$, we say that a quantum jump does occur, and we set

$$|\psi(t + \delta t)\rangle = \frac{\hat{C}|\psi(t)\rangle}{\sqrt{\delta f/\delta t}}, \quad (5.10b)$$

where the normalising factor of $\sqrt{\delta f/\delta t}$ comes from equation (5.9b), as we have $|\hat{C}|\psi(t)\rangle|^2 = \langle\psi(t)|\hat{C}^\dagger\hat{C}|\psi(t)\rangle = \delta f/\delta t$ to first order in δt .

So now, we have a probability distribution for the state at time $t + \delta t$ given the state at time t . If we average over the two possible outcomes for the density operator, \hat{w} , and then apply equations (5.6) and (5.7), we obtain

$$\overline{\hat{w}(t + \delta t)} = (1 - \delta f) \frac{|\psi_1(t + \delta t)\rangle \langle\psi_1(t + \delta t)|}{\sqrt{1 - \delta f}} + \delta f \frac{\hat{C}|\psi(t)\rangle \langle\psi(t)|\hat{C}^\dagger}{\sqrt{\delta f/\delta t} \sqrt{\delta f/\delta t}} \quad (5.11)$$

$$= \hat{w}(t) + \delta t \frac{i}{\hbar} [\hat{w}(t), \hat{H}_s] + \delta t \mathcal{L}(\hat{w}(t)). \quad (5.12)$$

If we average this equation over the possible states at time t , then for sufficiently small δt we have

$$\frac{d\overline{\hat{w}}}{dt} = \frac{i}{\hbar} [\overline{\hat{w}}, \hat{H}_s] + \mathcal{L}_{diss}(\overline{\hat{w}}), \quad (5.13)$$

which is equivalent to the master equation, (5.4). We can thus simulate this class of system using our two evolution steps, either by using very small time steps δt , or, in appropriate situations, by generalising this method to allow the use of macroscopic time steps. This second method is essentially the MCWF method formulated by Dum, Zoller and Ritsch, as described in references [56] and [57]. It involves replacing the operator $(1 - \hat{H}\delta t/\hbar)$ in equation (5.7) with the ordinary time evolution operator, $\exp[-i\hat{H}\Delta t/\hbar]$, and choosing a random threshold c from a uniform distribution on the interval $[0, 1]$. We then say that when the norm of the wavefunction falls below the threshold, a quantum jump occurs, and at that point in time, t_c , we apply the ‘‘collapse’’ operator \hat{C} to the state $|\psi(t_c)\rangle$. This is the way we implement the MCWF method in the simulation of the atom optics kicked rotor, as is described in the next section, 5.3.2.

The above description is applied to a density matrix describing an initial pure state, but can be easily generalised to a mixed state if we choose a set of initial wave functions $|\psi_i(0)\rangle$ according to the probability distribution of the initial mixed state. We can then evaluate the expectation value for any operator at a time t , $\langle\hat{A}(t)\rangle = \text{Tr}[\hat{A}\hat{w}(t)]$, by evaluating $\langle\psi_i(t)|\hat{A}|\psi_i(t)\rangle$ and averaging these values over all i . For a sufficiently large set of initial wavefunctions, the linearity of expectation values means that this will be a good approximation to $\langle\hat{A}(t)\rangle$.

5.3.2 The Atom Optics Kicked Rotor with Spontaneous Emission Noise

Our simulations of the atom optics kicked rotor are very similar to those performed by Doherty *et al.* [46], which, as described in the introduction to this chapter, are specifically based on an application of the MCWF method by Marte *et al.* [53]. We choose initial plane wave states with momenta chosen from a Gaussian distribution (representing the initial thermal distribution of the atoms), and evolve them in time using evolution operators based on the free Hamiltonian

$$\hat{H}_{free} = \frac{\hat{p}^2}{2} \quad (5.14)$$

when the kicking beam is off, and based on the non-Hermitian Hamiltonian

$$\hat{H}_{kick} = \frac{\hat{p}^2}{2} + \frac{\kappa}{\alpha} \cos(\hat{\phi}) - i\bar{k} \frac{\eta}{2\alpha} (1 + \cos(\hat{\phi})) \quad (5.15)$$

when the kicking beam is switched on. Note that the $\cos(\hat{\phi})$ dependence in the last term reflects the position dependence of the intensity along the standing wave, as the probability of spontaneous emission per kick is intensity dependent, and that this term originates from the master equation (4.21) [see the definition of \hat{C} , (5.16), and the Hamiltonian definition (5.6)]. Also note that η is the position averaged spontaneous emission probability per kick, as appeared in equation (4.21).

When the norm of the wavefunction drops below some randomly chosen threshold a spontaneous emission event is deemed to have occurred (this is equivalent to a finite time generalisation of step 2 as discussed in section 5.3.1), and the “collapse” operator

$$\hat{C} = \cos\left(\frac{\hat{\phi}}{2}\right) e^{-in\hat{\phi}} \quad (5.16)$$

is applied. Here $n \in [-\bar{k}/2, \bar{k}/2]$ is the projection of the momentum recoil onto the standing wave axis, and is randomly chosen from a uniform distribution. The wavefunction is then normalised, and evolution continues. Once the evolution of a single wavefunction has been completed, another plane wave state is chosen, and the process is repeated. We average the expectation value for any given operator across all of the wavefunctions (typically we use around 1000 initial plane wave states) to obtain the actual simulation expectation value for that operator for the initial mixed state (our Gaussian distribution of momentum eigenstates).

Discretising the Momentum Basis

For this to be performed numerically, an appropriately discretised momentum basis must be set up. We make use of the invariance of the Hamiltonian under translations of $\Delta\phi = 2\pi$ by storing only one period of the wavefunction in position space. This is

a technique borrowed from solid state physics, and significantly decreases the computational time involved in the simulations. This choice leads naturally via a Discrete Fourier Transform (DFT) relationship to a basis spacing of $\Delta\rho = \hbar k$ in momentum space, which works well because all momentum changes while the standing wave is on are quantised in steps of $\hbar k$. We are then also free to choose the extent of our basis in momentum space, which will set the basis spacing in position space, although there are no strict requirements as to how closely spaced that basis needs to be. In order to account for the fact that states of the atom optics kicked rotor may have any continuous value of momenta, and only the changes in momentum are quantised, we store another quantity called a quasi-momentum, q . This is a momentum value in the range $[-\hbar k/2, \hbar k/2]$, and when a plane wave state is first chosen q is set to the difference between the momentum of the state and the momentum of the nearest basis state. This quasi-momentum is added to the momenta of the basis states when any of the Hamiltonians are computed, and is only changed by spontaneous emission events. In fact, when we apply the collapse operator to the wavefunction, we must treat separately the changing of the quasimomentum and the translation of the wavefunction (in momentum space) by a particular number of basis states (which is effected by the translation operator $\exp(-in\hat{\phi})$).

Boundary Conditions

Because we have some finite number, N , of basis states, these states must be restricted to some finite range, $\rho \in \{m_{min}\hbar k, \dots, m_{max}\hbar k\}$. Unfortunately, there are no boundary conditions which will accurately represent normal dynamics for the states $|m_{min}\rangle$ or $|m_{max}\rangle$. It is imperative, then, that we choose N so that the amplitudes of these boundary states are always negligibly small. Then these states, along with all states outside the range of the basis, are unimportant in determining the system dynamics and the expectation values for important operators. This essentially gives us a self-consistency requirement for the simulations: we know that N is sufficiently large provided that the amplitudes of the boundary states are very small. Typically we find that $N = 2^{10} = 1024$ is an appropriate choice to cover most of our range of values for $\hbar k$ and κ . The choice of a power of 2 allows us to use the Fast Fourier Transform (FFT) algorithm to implement the DFT transforming between position space and momentum space. Having made this choice of N , we proceed using periodic boundary conditions as these are implicit in the DFT relationship.

System Evolution and Non-commuting Operators

The DFT is used throughout the simulations to transfer between position and momentum space. This is done so that parts of the evolution involving $\hat{\phi}$ and $\hat{\rho}$ in the Hamiltonian may be performed in the position basis and momentum basis respectively. This causes a small problem when we consider evolution during the kick, as \hat{H}_{kick} contains both $\hat{\phi}$ and $\hat{\rho}$. To get around this problem, we break the evolution during the kick into several steps, and compute the evolution due to each part of the Hamiltonian

separately for each step. Provided the number of steps is sufficiently large (or equivalently that each step is sufficiently short), this introduces negligibly small errors into the simulations, and the choice of this number can be tested by observing the stability of the simulation results as the number of steps is changed. Because α is small, and so the kick is already very short, only a few steps are necessary (for our work ~ 5 steps was sufficient).

The Spontaneous Emission Collapse Operator

For a kicked rotor system without spontaneous emissions, the momentum basis spacing of \hbar , which corresponds to the storing of one period in position space, works well. However, we strike problems when we try to act on a wavefunction with the spontaneous emission operator, $\cos(\hat{\phi}/2) \exp(-in\hat{\phi})$, because of its dependence on $\cos(\hat{\phi}/2)$. Physically, the exponentials into which the cosine function may be decomposed are translation operators in momentum space, which in a continuous space would translate the wavefunction by $\hbar/2$. However, this cannot be done in a discrete basis and instead we end up with an unwanted effect in the DFT which is known in the field of signal processing as spectral leakage [9].

Essentially, if we have any discretely sampled complex exponential,

$$x[s] = A \exp(i2\pi s\tau), \quad (5.17)$$

where $s \in \{0, 1, \dots, N-1\}$ and τ is the sampling interval, and we define the DFT by

$$X[r] = \frac{1}{N} \sum_{s=0}^{N-1} x[s] \exp(-\frac{i2\pi rs}{N}), \quad (5.18)$$

then

$$X[r] = \frac{A}{N} \sum_{s=0}^{N-1} \exp[-\frac{i2\pi s}{N}(N\tau - r)]. \quad (5.19)$$

If τ is an integer, then $X[r] = A$ if $r - N\tau$ is a multiple of N and $X[r] = 0$ otherwise. However, if τ is not an integer, then we have

$$X[r] = \frac{A}{N} \exp(-i\pi(N-1)(r - N\tau)/N) \frac{\sin[\pi(r - N\tau)]}{\sin[\pi(r - N\tau)/N]}. \quad (5.20)$$

We can see from figure 5.1 that all elements of our DFT will be non-zero, due to the sidelobes of the circular sinc function shown in that figure. In signal processing, this relates to the smearing out of a single frequency component into surrounding frequencies, which is the origin of the term ‘‘spectral leakage’’.

This has a large effect on our momentum distribution, because through what is essentially a numerical error, there are significant increases in the amplitudes of basis states with large momenta which should normally have amplitude ≈ 0 . Such a situation

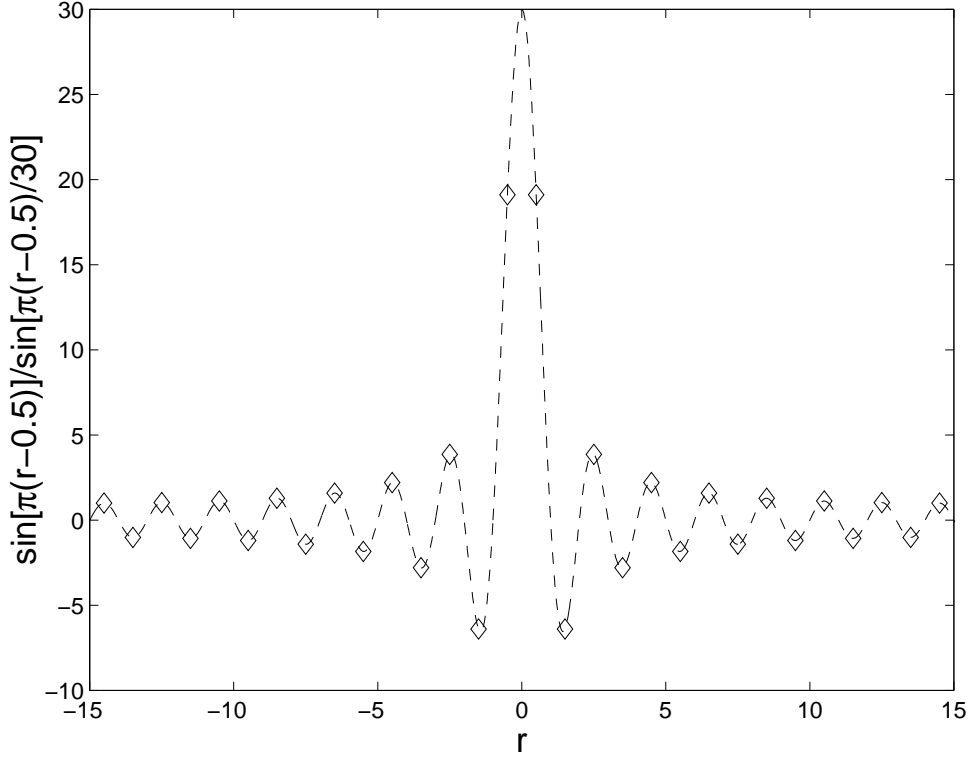


Figure 5.1: Plot of $\sin[\pi(r - 0.5)]/\sin[\pi(r - 0.5)/30]$ against r , showing the smearing of a single component of a DFT into adjacent components. The diamonds mark the values of the function for integer r .

is shown in figure 5.2, where the tails of the momentum distribution decrease slowly to around 10^{-10} . This is significant, especially when we compute $\langle \hat{\rho}^2 \rangle$ for the momentum distribution, as the states which are affected most significantly are those corresponding to large values of ρ . The only way to overcome this problem is to decrease the basis spacing in momentum space to $\bar{k}/2$ and hence store two periods in position space. This allows us to act on the position space wavefunction with a collapse operator that will now correspond to a translation along integer numbers of basis states in momentum space. We also increase our basis size to $N = 2^{11} = 2048$ so that the extent of the basis does not change. This leaves us with momentum distributions similar to that shown in figure 5.3, where there is an obvious cut off at the edge of the momentum distribution, and the tails are at a level around 10^{-31} .

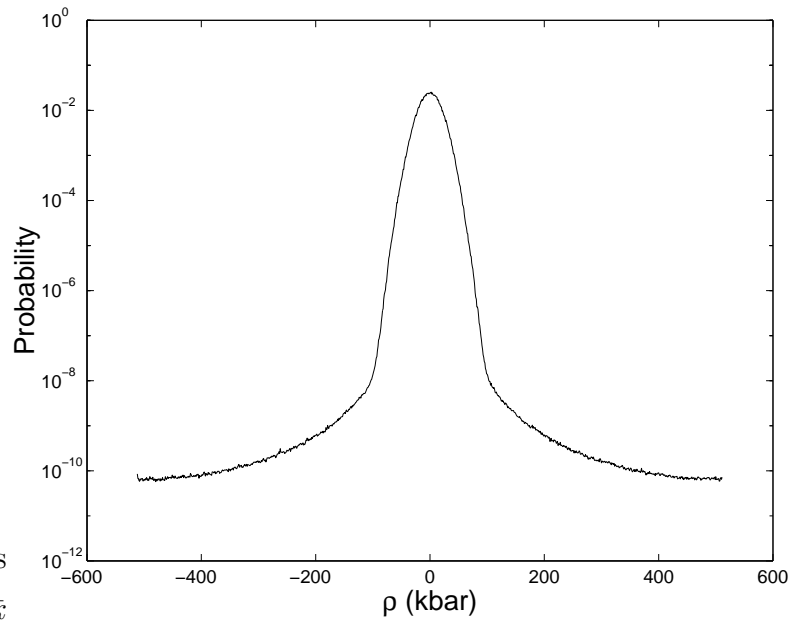


Figure 5.2: Simulation momentum distribution after 200 kicks for $\kappa = 10$, $\eta = 0.1$, $\alpha = 0.005$, $k = 4.0$, with a basis spacing of k , showing the effects of spectral leakage in the DFT.

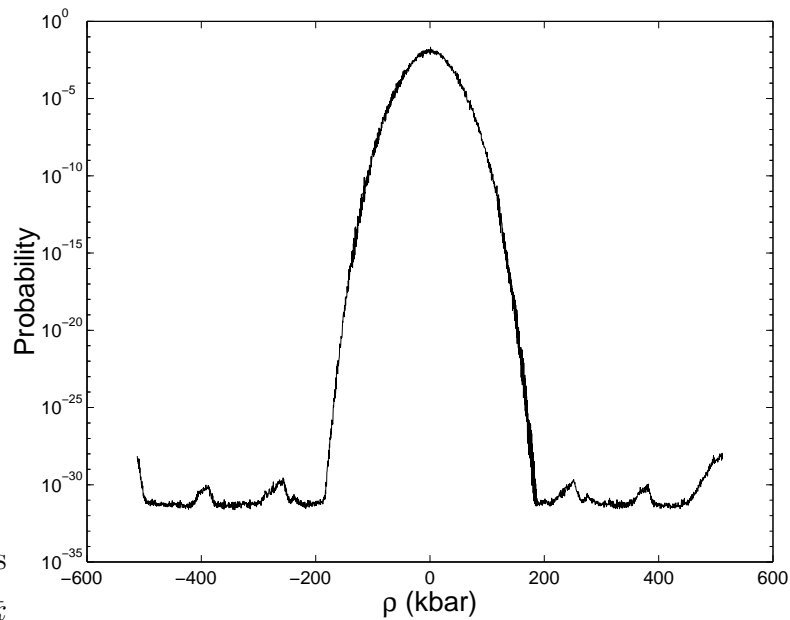


Figure 5.3: Simulation momentum distribution after 200 kicks for $\kappa = 10$, $\eta = 0.1$, $\alpha = 0.005$, $k = 4.0$, with a basis spacing of $k/2$, showing the expected momentum distribution without spectral leakage in the DFT.

Example code written in MATLAB[®] for the MCWF simulation of the atom optics kicked rotor with decoherence from spontaneous emission noise is given in Appendix C.

5.3.3 Amplitude Noise

Amplitude noise is introduced into the quantum simulations in a very similar manner to the way in which it is implemented in the classical simulations. $\kappa(n)$ is chosen randomly for each kick, and then evolution proceeds as normal with the appropriate value of κ used for each kick. In each simulation we generally choose 20 different sets of $\kappa(n)$ values, and evolve 50 basis states for each of these “realisations” of the noise. This gives us the standard total of 1000 trajectories. Example code for quantum simulations with amplitude noise is shown in appendix C.

5.3.4 Estimation of Errors

The stochastic nature of these simulations means that there will be uncertainties in the final calculated simulation values. In order to estimate these errors for expectation values calculated from the quantum simulations, the trajectories are divided into 10 groups of 100 initial random plane wave states. Expectation values are then calculated for all 10 groups and averaged, allowing the error in the final result to be estimated as the standard error ($\sigma/\sqrt{10}$, where σ is the estimate of the population standard deviation from the sample of 10 values) in the calculated values. Representative error bars are shown in various figures throughout this thesis where simulation results are displayed. Grouping of sets of initial conditions is used in a similar way to calculate the analogous statistical errors for the classical simulations.

Chapter 6

Diffusion in the QKR with Decoherence

6.1 Introduction

The investigation of momentum diffusion rates in the atom optics kicked rotor has featured significantly in many studies of the role that decoherence plays in the quantum - classical transition. However, before our work, none of these studies had looked at how diffusion rates change as \hbar is varied, i.e., as the dynamics are made either more or less macroscopic by varying the characteristic action of the system. Other studies had instead fixed the action and varied the level of decoherence. We choose to fix the decoherence, or the level of coupling to the environment, while we vary \hbar .

One of the major motivating factors for our investigation was a study of the quantum δ -kicked rotor with a continuous position measurement performed by Bhattacharya *et al.* [1]. This study was motivated by earlier work by the same group [59], which dealt with the role of a continuous position measurement in the emergence of classical chaos from a quantum mechanical system. Essentially, the continuous measurement provides the environmental coupling required for decoherence (see section 4.4).

The master equation for the density operator, \hat{w} , describing this system is of the form

$$\dot{\hat{w}} = -\frac{i}{\hbar}[\hat{H}, \hat{w}] - \xi[\hat{\phi}, [\hat{\phi}, \hat{w}]], \quad (6.1)$$

where \hat{H} is the Hamiltonian for the δ -kicked rotor, (3.12), and ξ is a parameter characterising the measurement strength, i.e., the rate at which information is extracted from the system. Bhattacharya *et al.* investigated numerically the behaviour of the late time momentum diffusion rates in this system as a function of \hbar for various different measurement strengths. They found very interesting structures, in which diffusion was enhanced for particular “resonant” values of \hbar , both in a general enhanced diffusion peak near $\hbar = 3$ for $\kappa = 10$, and as part of a peak near the quantum anti-resonance (often referred to simply as a quantum resonance) at $\hbar = 2\pi$.

Our goal was to investigate similar structures and structures in related regimes (for example, diffusion rates outside of the late time regime) for a specific experimental system - one which has real finite pulse widths and natural decoherence, and which is realisable in a laboratory. The atom optics kicked rotor with spontaneous emission noise provides an easily controllable system fitting exactly these criteria.

We performed numerical investigations of the quasilinear diffusion regime, the initial quantum diffusion period, and the late time diffusion rates for various values of κ and η , across large ranges of $\hbar k$ values. We have also investigated analytically the relationship between the early and late time diffusion rates. Our main results have been published in Physical Review E (see reference [2]), and these are presented in this chapter, along with many other interesting features of the system.

6.2 Early Time Diffusion Rates

From our numerical simulations we can determine values for $\langle \rho^2 \rangle$ after each kick, and then we can calculate the diffusion rate for each kick from equation (3.30). The diffusion rates for the first five kicks ($n=0,1,2,3,4$) are shown as a function of $\hbar k$ in figure 6.1 for $\kappa = 10$ and in figure 6.2 for $\kappa = 12$.

In both of these figures, quasilinear behaviour can be clearly seen for the first two kicks. Aside from some noise in the results for the first kick at large $\hbar k$ values, we see that the diffusion rates are constant with respect to $\hbar k$, and we have $D_{quasilinear} = 25$ for $\kappa = 10$ and $D_{quasilinear} = 36$ for $\kappa = 12$. The behaviour we observe in the second kick is dependent on the width of the initial momentum distribution, as will be discussed in chapter 9, but here we use $\sigma_\rho = 4$, which corresponds to a thermal distribution of around $10\mu\text{K}$. This value is sufficiently large to generate quasilinear diffusion in the second kick for all values of $\hbar k$ that we simulate here.

It can be clearly seen from figure 6.1 and figure 6.2 that once we reach the third kick ($n=2$), the behaviour of the system moves abruptly away from the quasilinear regime. For all of the next three kicks we obtain resonance structures very similar to those predicted in Shepelyansky's formula, (3.35) as shown in figure 3.2. We observe an enhanced diffusion peak for each kick and for both κ values near $\hbar k = 3$, as well as a peak near the quantum resonance at $\hbar k = 2\pi$. These features are compared with those predicted by Shepelyansky in section 6.3.2.

6.3 The Initial Quantum Diffusion Period

It is difficult to decide how to estimate the initial quantum diffusion rate, D_q , from the data as presented in figures 6.1 and 6.2. It would be nice if we could plot the mean energy, $\langle \rho^2/2 \rangle$, as a function of kick number, n , and then fit a straight line through the energies in the initial quantum diffusion period. The slope of the line would then be our estimate for D_q . Unfortunately, there are difficulties in doing this, particularly in deciding where dynamical localisation begins to set in, and hence through which points

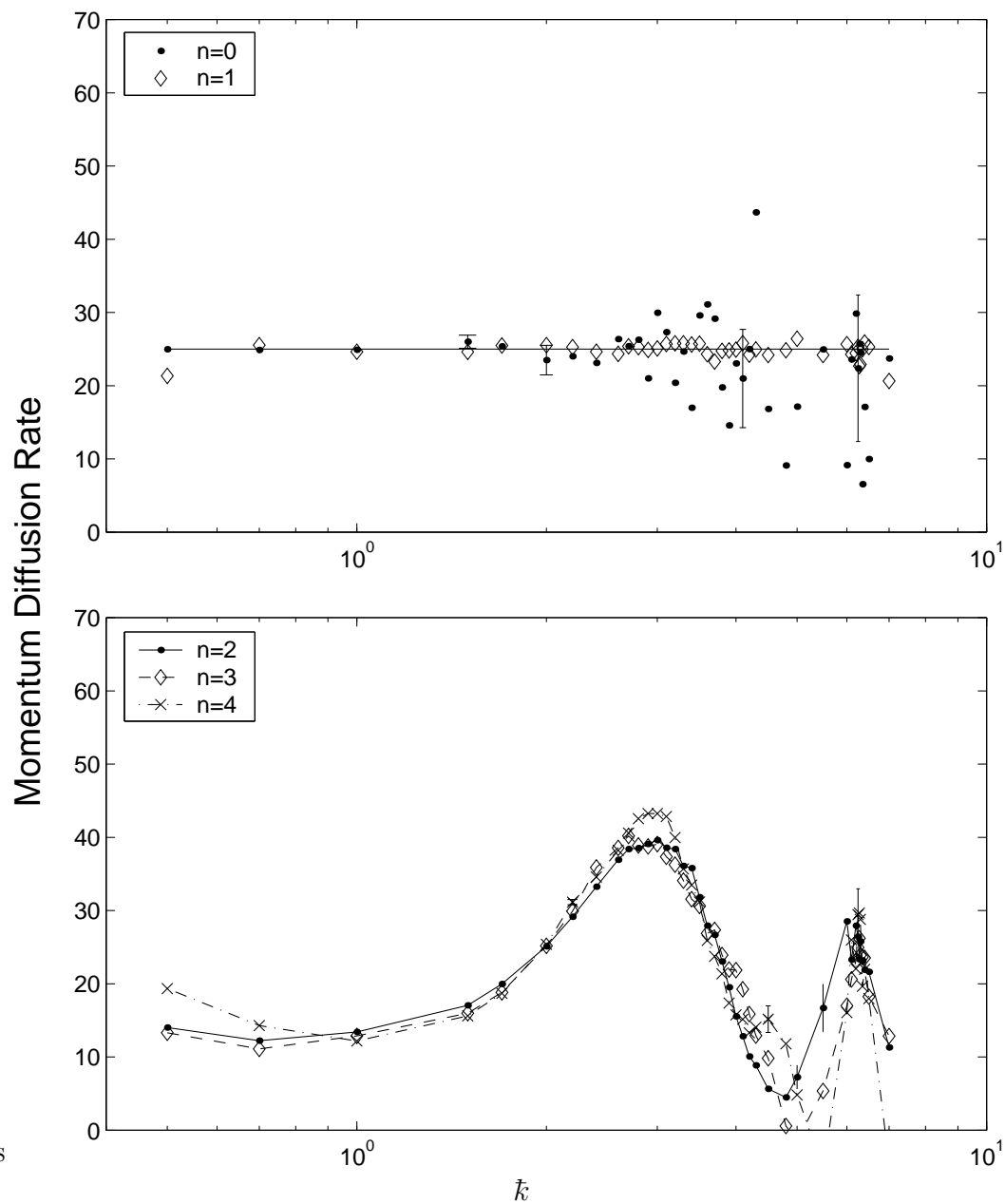


Figure 6.1: Diffusion Rates, $D(n)$, for the quantum kicked rotor with $\alpha = 0.005$, $\kappa = 10$, $\eta = 10\%$ and $\sigma_\rho = 4$, plotted as a function of \bar{k} for $n = 0, 1, 2, 3, 4$. The horizontal line on the top graph marks $D = \kappa^2/4 = 25$.

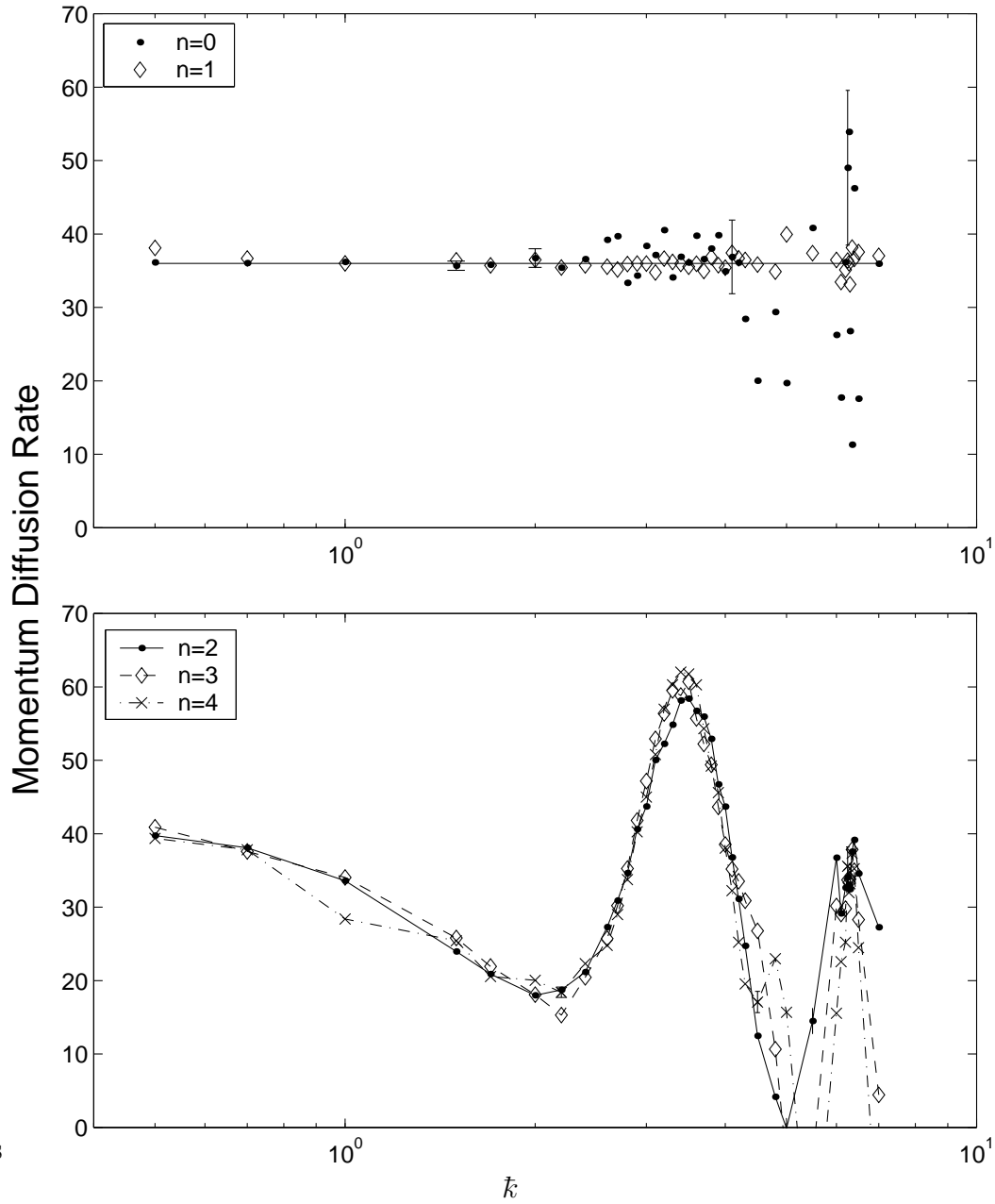


Figure 6.2: Diffusion Rates, $D(n)$, for the quantum kicked rotor with $\alpha = 0.005$, $\kappa = 12$, $\eta = 1\%$ and $\sigma_\rho = 4$, plotted as a function of \bar{k} for $n = 0, 1, 2, 3, 4$. The horizontal line on the top graph marks $D = \kappa^2/4 = 36$.

we need to fit the line. Instead of using a qualitative process, we decided to choose an objective measure, in particular to average the diffusion rates $D(2-5)$ to get our estimate for D_q .

6.3.1 The Effects of Varying κ

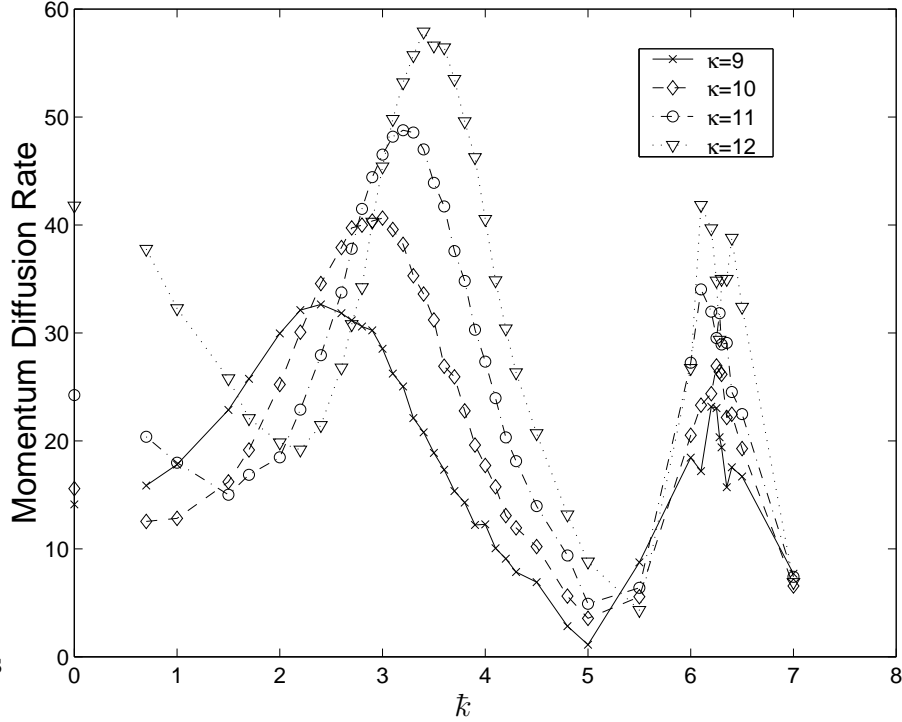


Figure 6.3: Simulation results for initial quantum diffusion rates, D_q , of the quantum kicked rotor with $\alpha = 0.005$ and $\eta = 10\%$. These results are obtained by averaging the diffusion rates $D(2-5)$. Corresponding classical values are marked as points for $\bar{k} = 0$.

The remarkable structure of resonances in the initial quantum diffusion rates as a function of \bar{k} is easily seen from figure 6.3. For various values of κ (in this figure $\kappa = 9, 10, 11, 12$) we observe the enhanced diffusion peak, which increases in magnitude and shifts to the right as we increase κ . All values of κ exhibit the quantum resonance peak at $\bar{k} = 2\pi$, and this peak does not shift as we vary κ . The classical diffusion rates, D_{class} , as given by equation (2.64) and confirmed by classical simulations, are marked on the vertical axis at $\bar{k} = 0$. It can be seen clearly that the initial quantum diffusion rates in the enhanced diffusion peak are higher than the late time rates (i.e., the rate in the 3rd kick, $D(2)$, and later) in the corresponding classical system. This is because the enhanced diffusion peak is a uniquely quantum phenomenon which arises from resonances in the quantum correlations which determine the diffusion rates.

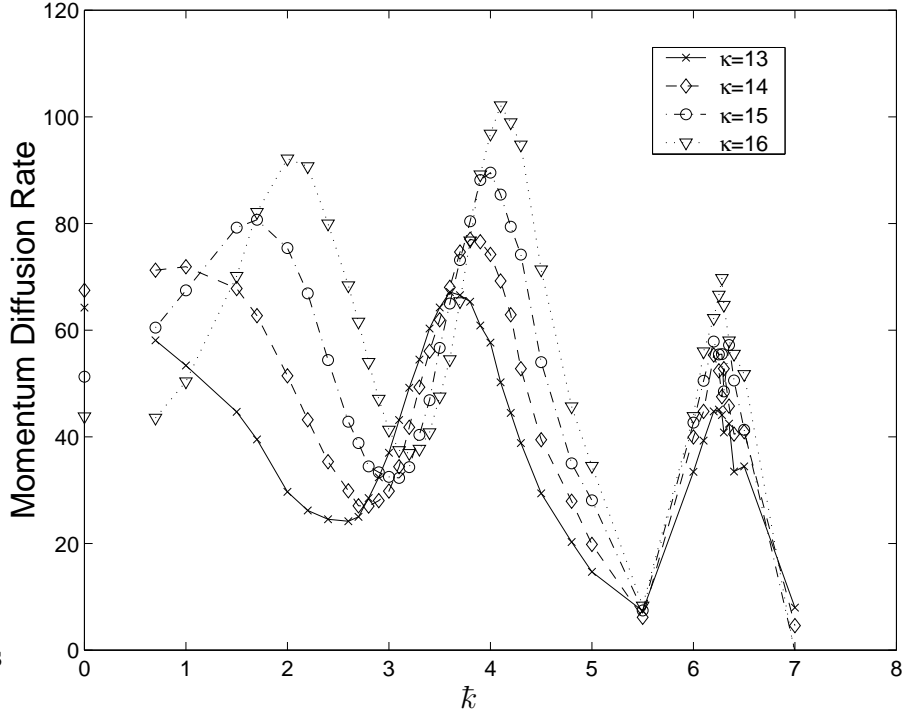


Figure 6.4: Simulation results for initial quantum diffusion rates, D_q , of the quantum kicked rotor with $\alpha = 0.005$ and $\eta = 10\%$. These results are obtained by averaging the diffusion rates $D(2 - 5)$. Corresponding classical values are marked as points for $\bar{k} = 0$.

Figure 6.4 shows very similar structure, again with similar comparisons to the classical system, for $\kappa = 13, 14, 15$, and 16 . We see that the enhanced diffusion peak continues to shift to the right and increase in magnitude as we increase κ . This is interesting, because we see from figure 2.16 and from the classical values marked on the vertical axis of figure 6.4 that the classical diffusion rates have reached the top of an anomalous diffusion peak, and are decreasing as κ is increased. In contrast, the position and magnitude of the enhanced diffusion peak appear to exhibit monotonic behaviour as κ is varied, with no strange effects similar to the anomalous diffusion phenomenon of the classical diffusion rates. We notice that as κ is increased a second enhanced diffusion peak forms at lower \bar{k} values. This not surprising given that Shepelyansky's formula for the initial diffusion rates involves Bessel functions with an argument $2\kappa \sin(\bar{k}/2)/\bar{k}$, and that the Bessel functions exhibit oscillations (see figure A.1). As κ is increased, we would expect the Bessel functions to undergo more oscillations in the same range of \bar{k} values, and hence it is not surprising that we observe more peaks in the resulting diffusion rates.

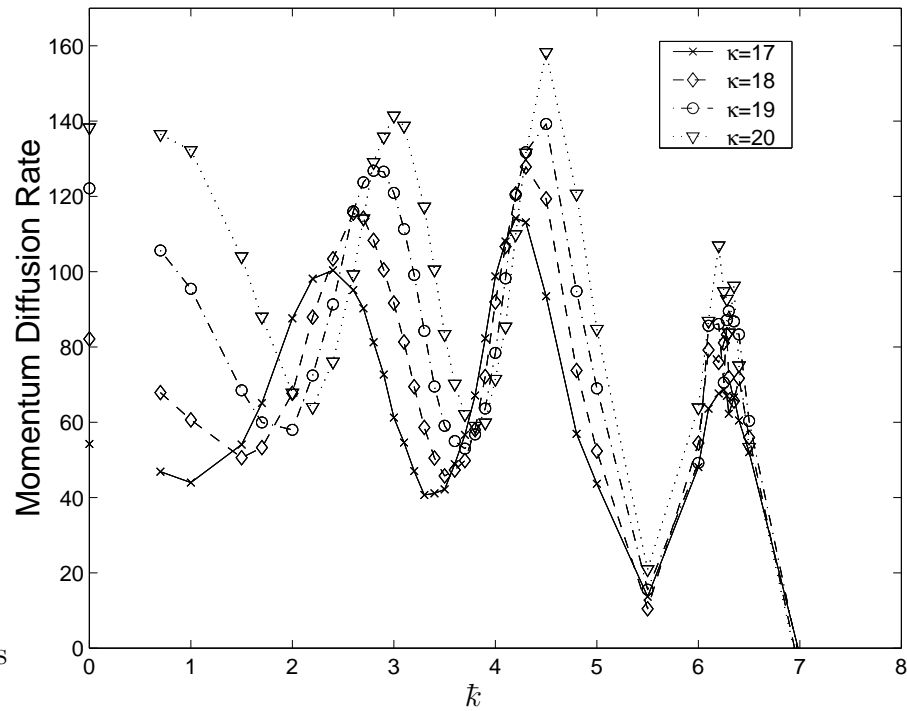


Figure 6.5: Simulation results for initial quantum diffusion rates, D_q , of the quantum kicked rotor with $\alpha = 0.005$ and $\eta = 10\%$. These results are obtained by averaging the diffusion rates $D(2 - 5)$. Corresponding classical values are marked as points for $\bar{k} = 0$.

The same patterns continue for even higher values of κ , as is shown in figure 6.5 for $\kappa = 17, 18, 19$, and 20 . The extra enhanced diffusion peak becomes more pronounced, and both the new peak and the original peak continue to shift to the right and increase in magnitude as κ is increased. Diffusion rates in both enhanced diffusion peaks rise above the corresponding classical values (which again are marked on the vertical axis), and for $\kappa = 20$, we can see the beginnings of a third enhanced diffusion peak at low values of \bar{k} .

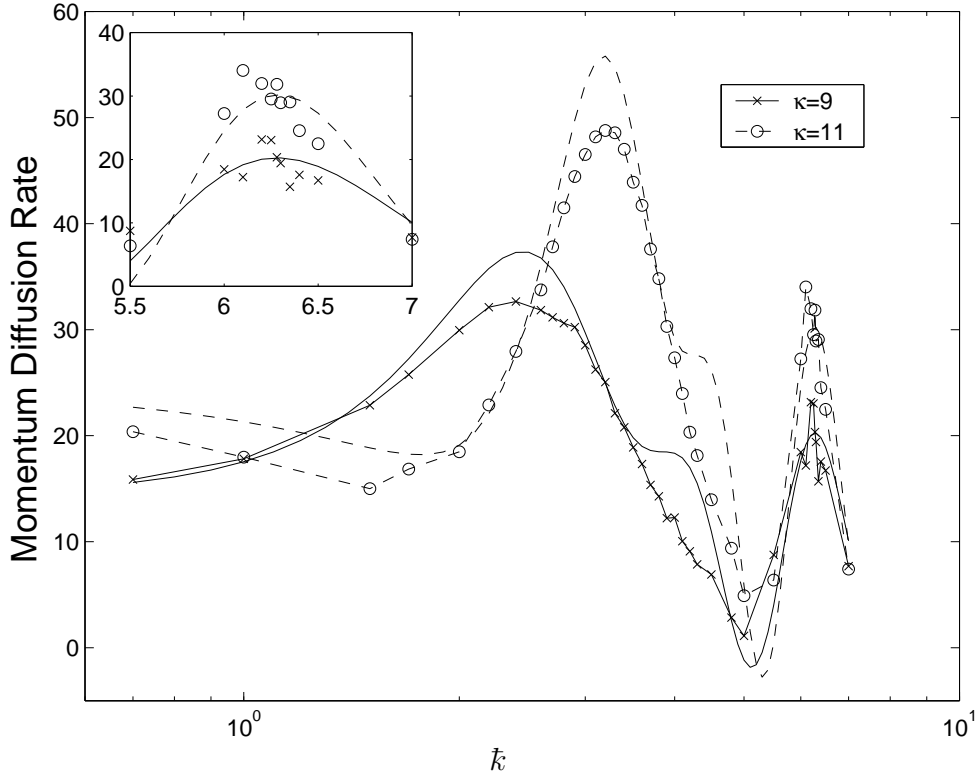


Figure 6.6: Comparison between simulation results and Shepelyansky's formula for initial quantum diffusion rates, D_q , in the quantum kicked rotor with $\alpha = 0.005$ and $\eta = 10\%$. Simulation results are obtained by averaging the diffusion rates $D(2-5)$, and are shown as points with joining lines. Shepelyansky's result's are shown as lines without points. The inset focusses on the region around the quantum resonance peak.

6.3.2 Comparison with Shepelyansky's Formula

Before our investigation of initial quantum diffusion rates, no full numerical test of Shepelyansky's result had ever, to our knowledge, been performed. The agreement between our results and Shepelyansky's result is strikingly good, especially considering that the condition $\kappa \gg \tilde{k}$, which is required both by approximations in Shepelyansky's formula and by the need for the break time to be long so that averaging over $D(2-5)$ gives us a sensible measure of diffusion rates in the initial quantum diffusion period, does not hold for our large \tilde{k} values. (See section 6.3.5 for an even more dramatic example of this unexpected level of agreement.) Representative samples of our simulation results are plotted along with Shepelyansky's analytical result in figures 6.6 and 6.7. The consistency is very good around the quantum resonance peak, and the position of the enhanced diffusion peak is well predicted.

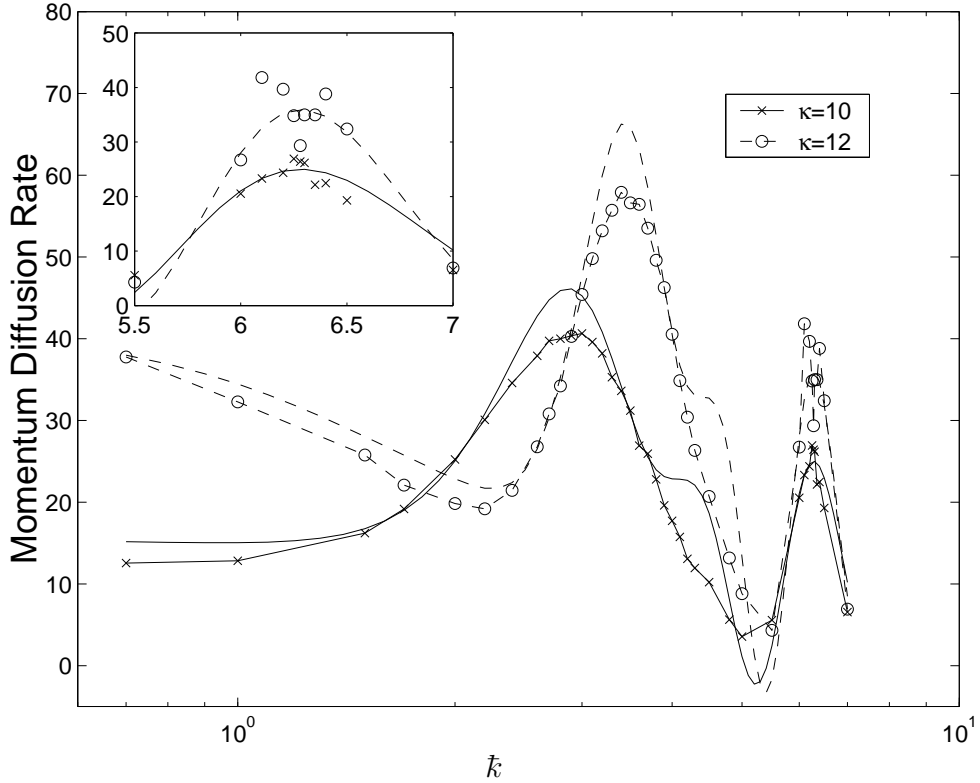


Figure 6.7: Comparison between simulation results and Shepelyansky’s formula for initial quantum diffusion rates, D_q , in the quantum kicked rotor with $\alpha = 0.005$ and $\eta = 10\%$. Simulation results are obtained by averaging the diffusion rates $D(2 - 5)$, and are shown as points with joining lines. Shepelyansky’s results are shown as lines without points. The inset focusses on the quantum resonance peak.

The discrepancy in the height of the enhanced diffusion peak arises mainly because of our choice to average over the diffusion rates $D(2 - 5)$. Often the system will have already begun to settle towards its late time diffusion period by the 5th and 6th kicks, and the diffusion rates near the top of the enhanced diffusion peak will have decreased significantly. In general we find that the diffusion rate curve for the kick which has the highest diffusion rate in the enhanced diffusion peak for a particular system is very close to Shepelyansky’s result near the top of the enhanced diffusion peak. However, the kick on which this occurs varies from system to system, and it becomes difficult to choose an objective measure of the initial quantum diffusion rate while taking this fact into account. We thus adopt our choice of averaging over 4 pre-defined kicks, and sacrifice some agreement near the centre of the enhanced diffusion peak.

There is an extra “shoulder” on the high k side of the enhanced diffusion peak in Shepelyansky’s result, which does not appear for most kicks in our simulations. The disagreement occurs because of a combination of the truncation of the Bessel function expansion in Shepelyansky’s formula and our choice to average over kicks for $n = 2, 3, 4$

and 5. From the derivation of Shepelyansky's result summarised in appendix B, we know that the correlations included are all of those on time scales of $\Delta\tau = 3$ or less, and some of those on the time scale $\Delta\tau = 4$. The shoulder, as we can see from figures 6.1 and 6.2, does actually occur for the fifth kick, i.e., $n = 4$, once all of these correlations have become important, but is washed out when we average the diffusion rate from all four kicks. Comparing Shepelyansky's result with simulations of the diffusion rate in just the fifth kick does not give perfect quantitative agreement because Shepelyansky's result does not include all of the correlations involved up to this point. Furthermore, the result in the fifth kick alone cannot be said to be completely representative of the initial quantum diffusion period. In effect, we sacrifice a small amount of disagreement with Shepelyansky's result in order to obtain a more meaningful measure of the initial quantum diffusion rate.

In addition, around this region the approximation $\kappa \gg \hbar$ is beginning to break down, so it is surprising that we even get as much agreement as we already observe between our results and Shepelyansky's formula. Not only does the calculation of the fifth correlation for Shepelyansky's formula ignore terms for small κ/\hbar , but in such a regime we also observe a short break time, N^* , meaning that the diffusion rate decreases rapidly from kick to kick, and averaging over $D(2) - D(5)$ becomes a less sensible estimate of the initial quantum diffusion rate because of the large range of values being averaged.

6.3.3 Varying Levels of Spontaneous Emission Noise

It is a very interesting point that the initial quantum diffusion rates appear completely unchanged for physically realistic amounts of spontaneous emission noise. This is clearly illustrated in figures 6.8 and 6.9, where initial quantum diffusion rates (respectively for $\kappa = 9$ and $\kappa = 11$) are plotted for various values of η . The explanation for this lies in the fact that the main effect of spontaneous emission noise is to create decoherence in the system. This is unimportant in the initial quantum diffusion regime because the individual decoherence events occur on a relatively long time scale (\sim once every 10 kicks for $\eta = 10\%$), and so they disrupt the quantum correlations on that same relatively long time scale, whereas initial quantum diffusion rates are produced by correlations over only 3-5 kicks. The other possible action of spontaneous emission noise is to create momentum recoils, but for physically realistic spontaneous emission rates these are not significant in determining diffusion rates at all. This can be clearly seen from the classical simulations described in the next section.

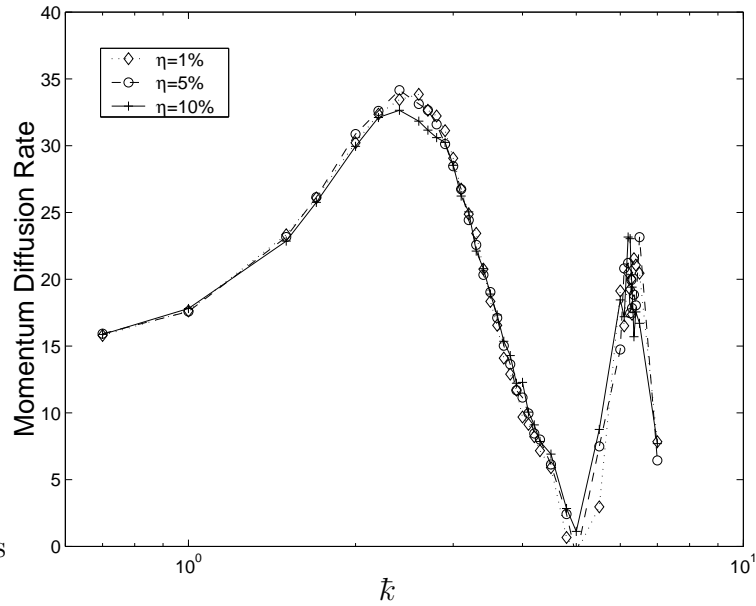


Figure 6.8: Simulation results for initial quantum diffusion rates, D_q , of the quantum kicked rotor with $\alpha = 0.005$ and $\kappa = 9$, showing the lack of variation as we change η . These results are obtained by averaging over the diffusion rates $D(2 - 5)$.

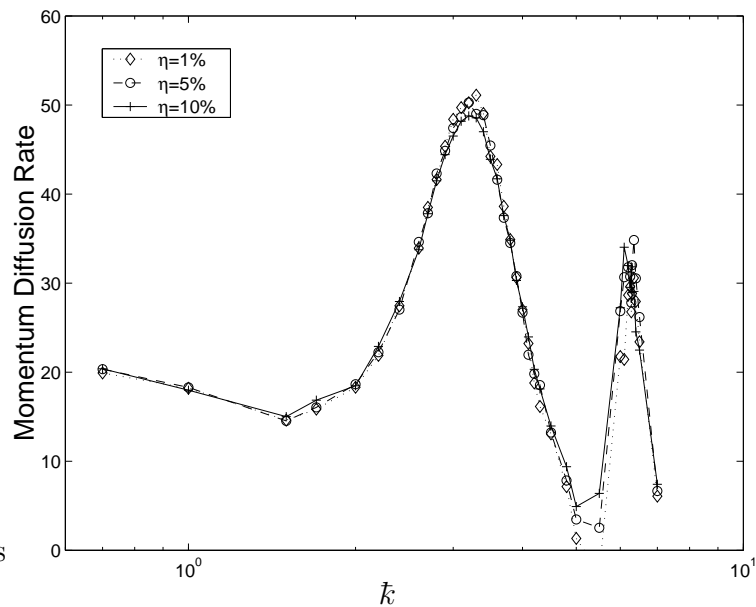


Figure 6.9: Simulation results for initial quantum diffusion rates, D_q , of the quantum kicked rotor with $\alpha = 0.005$ and $\kappa = 11$, showing the lack of variation as we change η . These results are obtained by averaging over the diffusion rates $D(2 - 5)$.

6.3.4 Momentum Diffusion from Spontaneous Emission Recoils - Classical Results

In order to evaluate the effects on momentum diffusion rates of momentum recoils due to spontaneous emission events, we performed classical simulations in which at randomly selected times a trajectory receives a momentum kick in the range $(-1/2, 1/2)$. The simulation methods used for this are described in section 5.2.2 and example source code is given in appendix C.

We started with an initial momentum distribution of width $\sigma_\rho = 4$, and calculated the late time classical momentum diffusion rate, D_{class} . We looked at both implementations of noise (the Auckland experiment style, with the spontaneous emissions during the kick only, and the Austin experiment style, with the spontaneous emissions throughout the whole cycle) and obtained very similar results for both types of noise. Our results are summarised in table 6.1 for spontaneous emissions occurring only during the kick, and are highly representative of all other similar investigations that we performed. The diffusion rates for all values of η are the same within statistical error, with only the odd statistical outlier (for example the diffusion rate for $\kappa = 9$, $\eta = 10\%$). This indicates that recoils due to spontaneous emission events do not make a significant difference to the diffusion rate. This explains the lack of η dependence in the initial quantum diffusion rates, as described in section 6.3.3, and means that any significant effects of spontaneous emission in the diffusion rates in other regimes must come from its decoherence properties. This is confirmed by the lack of a trend in the average ratio of simulation results to analytical predictions for diffusion rates as we vary η . Note that the discrepancy between numerical and analytical results in the diffusion rates for $\kappa = 13$ arises from the differences between rates in the pulse-kicked rotor and the δ -kicked rotor (see figures 2.15 and 2.16). We obtain the results in this table by averaging the diffusion rates in kicks $n = 3-50$.

κ	$\eta = 0\%$	$\eta = 10\%$	$\eta = 20\%$	$\eta = 30\%$	Theoretical
9	15.7 ± 0.8	15.1 ± 0.9	16.0 ± 0.9	15.7 ± 0.9	15.6
10	13.3 ± 0.8	16.1 ± 0.7	14.2 ± 0.9	15.8 ± 0.8	14.1
11	23.8 ± 1.3	24.2 ± 1.1	22.8 ± 1.0	24.9 ± 1.4	24.2
12	42.5 ± 2.0	39.4 ± 2.0	40.1 ± 1.9	44.2 ± 1.7	41.8
13	70.7 ± 2.7	68.8 ± 2.3	69.3 ± 2.7	72.5 ± 2.2	64.2
$\langle D_{sim}/D_{class} \rangle$	1.01 ± 0.02	1.02 ± 0.02	1.00 ± 0.02	1.07 ± 0.02	1.0

Table 6.1: Simulation results for momentum diffusion rates in the classical kicked rotor with $\alpha = 0.005$, including spontaneous emission recoils for varying η . The last row shows the average ratio of the simulated diffusion rates in the columns above to the predicted classical diffusion rate, D_{class} , without spontaneous emissions.

6.3.5 Results for high values of \tilde{k}

In figure 6.10 we show simulation results for initial diffusion rates in the quantum kicked rotor at high values of \tilde{k} . These results are representative of other such simulations, and show an interesting structure in which peaks appear at all of the quantum resonances (at integer multiples of 2π), without significant structure in between these peaks (the only other main structure consists of the enhanced diffusion resonances for $\tilde{k} < 2\pi$). The most surprising fact about the structure we observe here is the very good agreement with Shepelyansky's result, which is derived under the assumption that $\kappa \gg \tilde{k}$. Here we have $\kappa = 12$, but for $\tilde{k} \sim 20$ the agreement is still very good within statistical errors.

It appears that the approximations made by Shepelyansky which required this assumption do not have a large impact on the final formula. The truncation of the Bessel function expansion appears to give us extra structure which we do not see in our simulations (such as the shoulder on the right hand side of the enhanced diffusion peak), however the agreement of the formula is very good even for high \tilde{k} values, as shown. It becomes almost prohibitive to investigate much higher \tilde{k} values, as we need to average over many more trajectories to overcome statistical errors in the simulations.

6.4 Simulation Results in the Late Time Diffusion Regime

Probably the most important part of our study is the investigation of the late time diffusion regime which results when decoherence disrupts the onset of dynamical localisation. These results for the atom optics kicked rotor are the equivalent of the study performed by Bhattacharya *et al.* [1] for the quantum kicked rotor with a continuous position measurement, and also are the most accessible area of our research in terms of current atom optics experiments. In order to measure the corresponding diffusion rates we investigate the variation in $\langle \rho^2 \rangle$ as a function of kick number, and determine when the system has settled into its steady late time diffusion regime (usually after 30 - 50 kicks). We then calculate the diffusion rate as the average of the diffusion rates for all kicks from when the system has initially settled up until the 200th kick.

6.4.1 Results for Varying κ

The results that we obtain for the late time diffusion rates exhibit very similar structures to the initial quantum diffusion rate, as can be seen in figures 6.11, 6.12, and 6.13. We again observe diffusion resonances in the form of an enhanced diffusion peak and a quantum resonance peak, although the quantum resonance peak is now a much sharper resonance than we observed for the initial diffusion rates. The quantum resonance peak naturally remains at $\tilde{k} = 2\pi$ as we vary κ , but as we saw for the initial quantum diffusion rates, the enhanced diffusion peak shifts to the right and increases in magnitude as we increase κ . We also note that for higher values of κ , extra enhanced

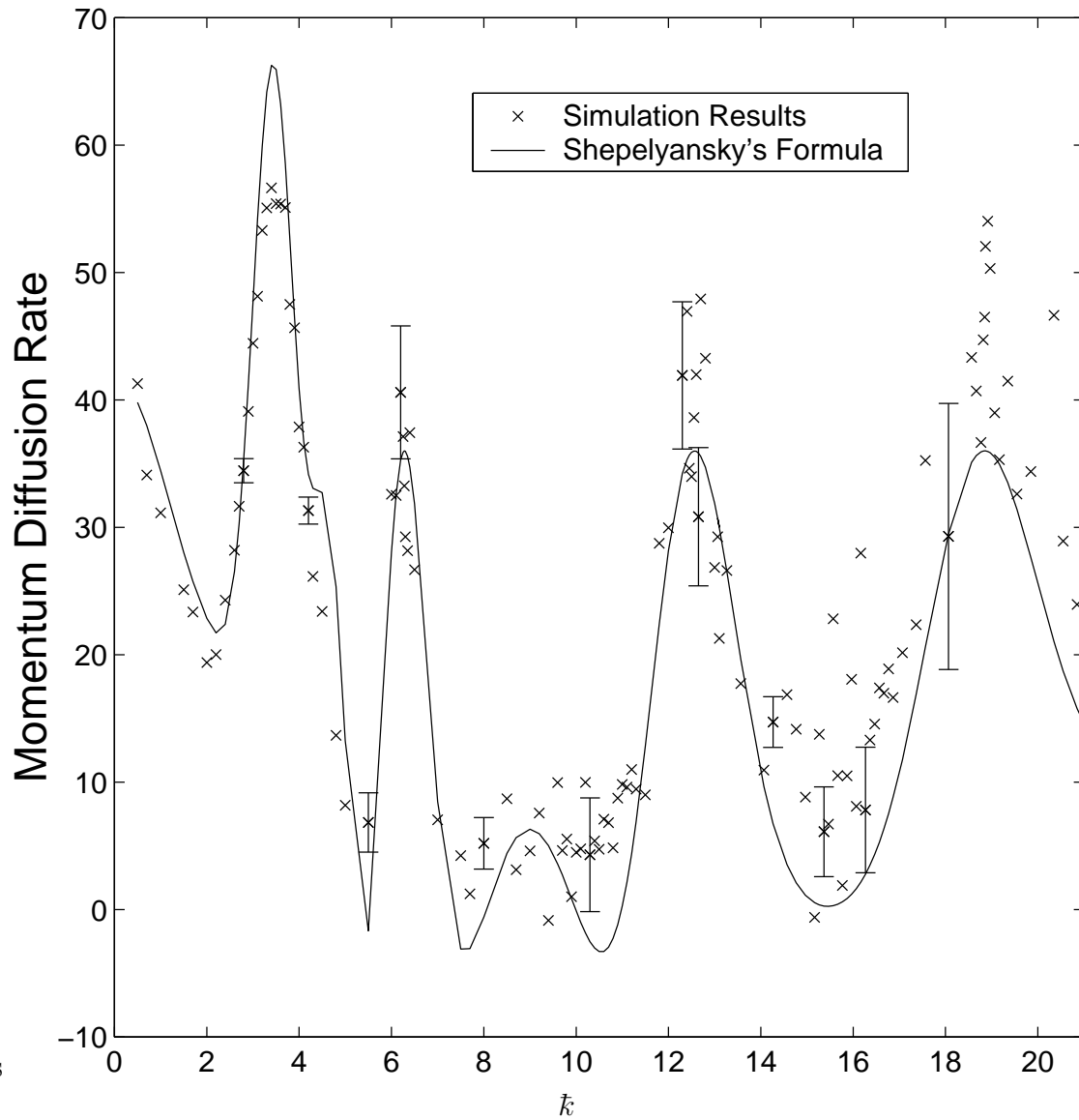


Figure 6.10: Simulation results for initial quantum diffusion rates of the QKR with $\alpha = 0.005$, $\kappa = 12$ and $\eta = 10\%$, showing the behaviour for high values of k and a comparison of this with Shepelyansky's formula.

diffusion peaks begin to appear at lower values of \bar{k} , again as we saw for the initial quantum diffusion rates.

The most striking feature of these diffusion structures, though, is the fact that again, for appropriate values of κ and η , we observe quantum diffusion rates which are higher than the corresponding classical diffusion rates. In fact, with $\eta = 10\%$ we observe this effect for $\kappa = 9, 10, 11, 15, 16$ and 17 , and for the last three values it occurs twice in separate enhanced diffusion peaks. This is particularly dramatic because the chaotic nature of the classical system makes it highly unexpected that the late time rates in the corresponding quantum system could ever be higher than the classical rates. Quantum effects in systems with chaotic classical analogues almost always involve the quantum system having a momentum diffusion rate lower than the classical system to which it corresponds, because the diffusion of trajectories is limited by coherence phenomena such as dynamical localisation. We will see in section 6.5.1 that this phenomenon appears to result from the same short time quantum correlations which produce initial quantum diffusion rates that are faster than corresponding classical rates (see figure 6.3), in conjunction with decoherence which essentially “locks in” the effects of those short time quantum correlations. These resonance structures, including the quantum resonance peak, have exactly the same form as those investigated by Bhattacharya *et al.* [1]. Having these results in the specific context of an atom optics kicked rotor with practically realistic system parameters now makes this work concerning diffusion resonances across the classical-quantum transition experimentally relevant.

6.4.2 Varying levels of Decoherence

Figures 6.14 and 6.15 show the dependence on η of the late time quantum diffusion rates for systems with $\kappa = 9$ and $\kappa = 11$ respectively. We see that these diffusion rates are strongly dependent upon the level of decoherence, and hence varying this level can determine whether or not the rates near the centre of diffusion resonances become higher than the corresponding classical values.

6.4.3 Results for high values of \bar{k}

The structure of the late time diffusion rates at higher values of \bar{k} , shown in figure 6.16, follows a similar pattern to that of the initial quantum diffusion rates (see figure 6.10). As expected, we observe relatively sharp quantum resonance peaks at integer multiples of 2π , and little structure between the peaks. This is a particularly interesting point, in that it makes the extra diffusion resonance structure in the range $0 < \bar{k} < 2\pi$ rather unique. The most interesting structure therefore only occurs when we make the system sufficiently macroscopic that $\bar{k} \sim 1$, i.e., that the classical action is of the order of \hbar . If we decrease the action further, we observe the uniquely quantum phenomenon of quantum resonance peaks, but no significant additional diffusion resonances. Thus, in a sense the enhanced diffusion peak structure is a characteristic of the quantum - classical transition region for fixed η and varying action.

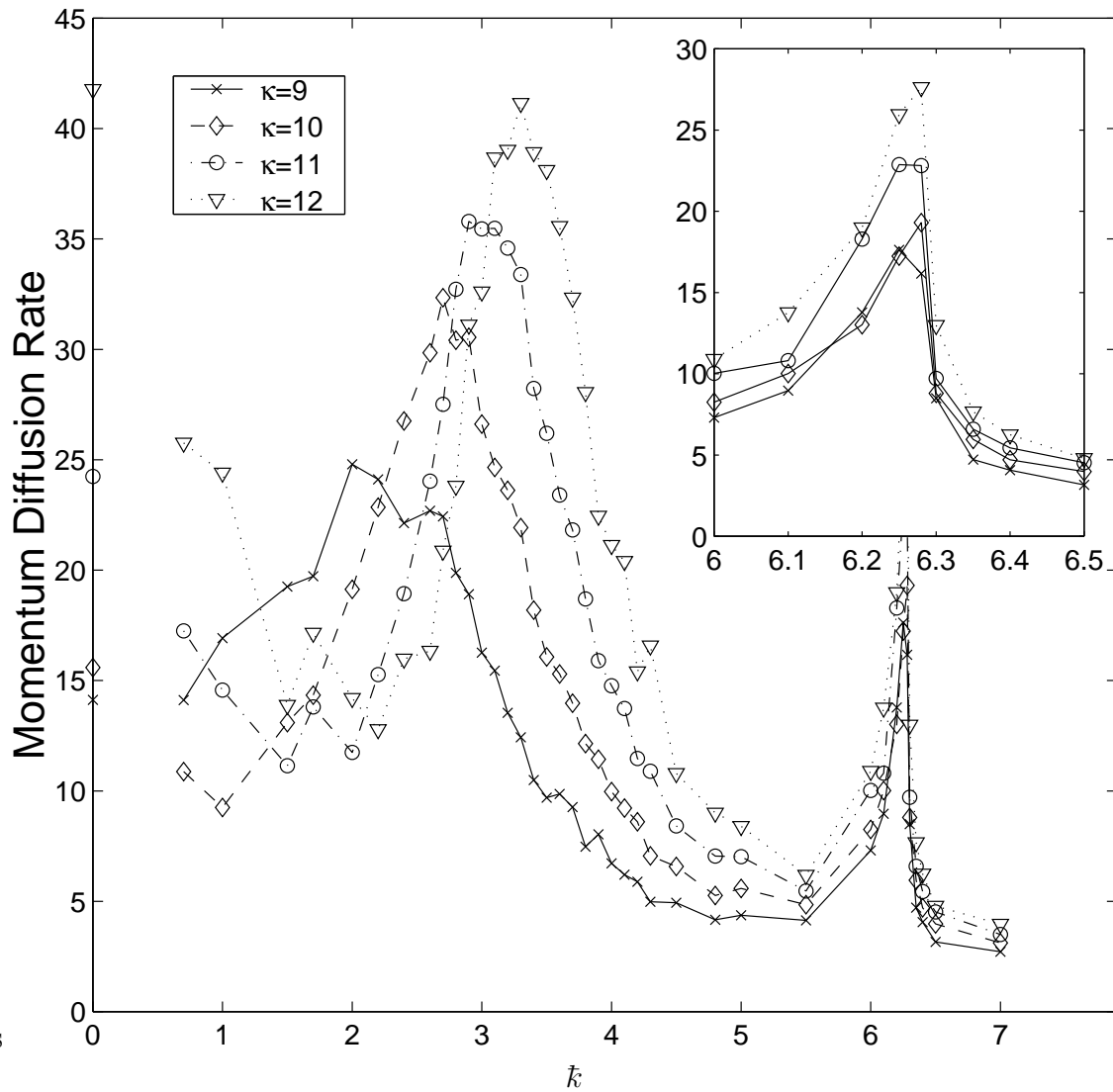


Figure 6.11: Simulation results for late time quantum diffusion rates for the QKR with $\alpha = 0.005$ and $\eta = 10\%$. Corresponding classical values are marked for $\bar{k} = 0$. The inset shows more clearly the behaviour near the quantum resonance peak at $\bar{k} = 2\pi$.

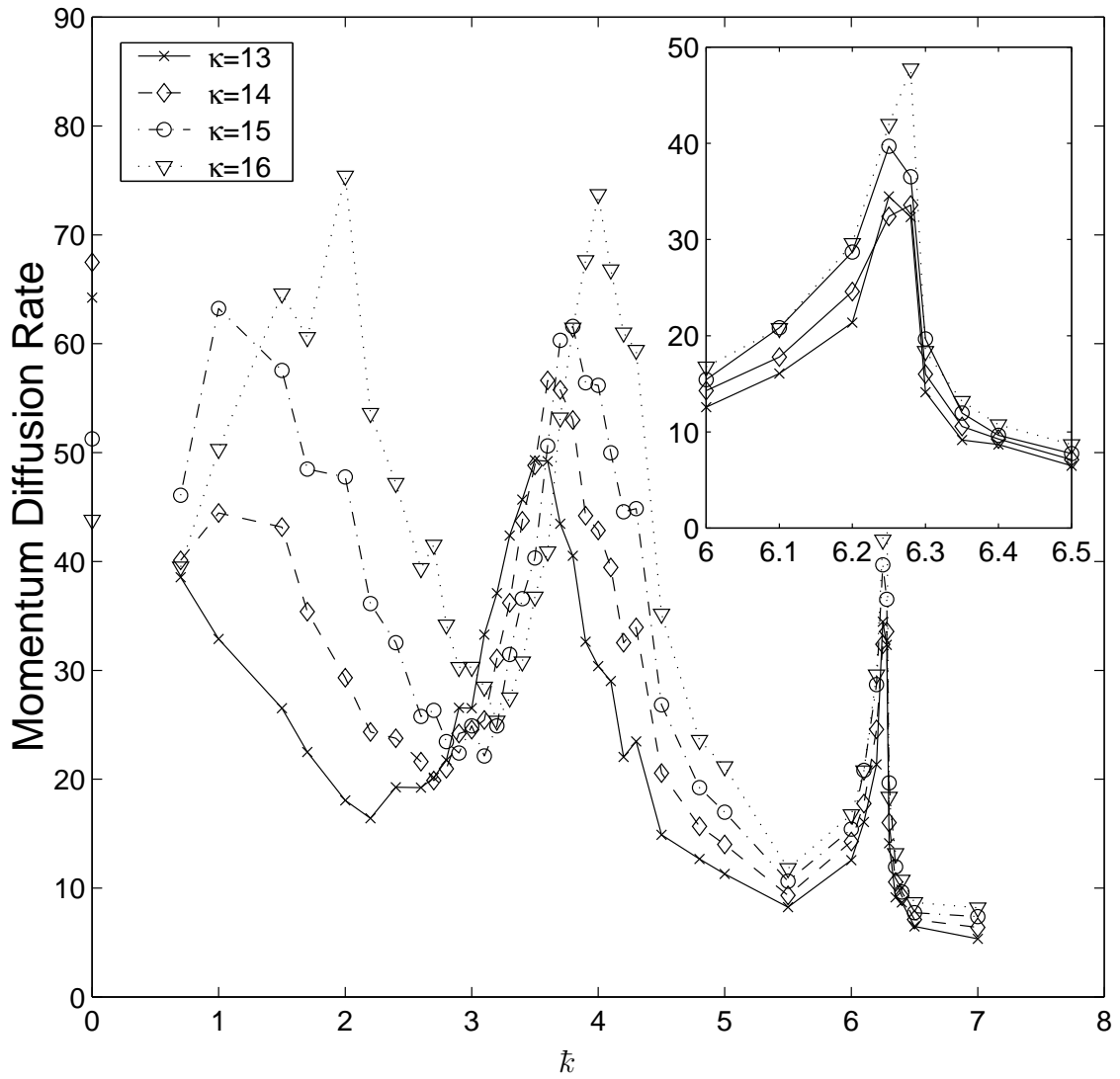


Figure 6.12: Simulation results for late time quantum diffusion rates for the QKR with $\alpha = 0.005$ and $\eta = 10\%$. Corresponding classical values are marked for $\bar{k} = 0$. The inset shows more clearly the behaviour near the quantum resonance peak at $\bar{k} = 2\pi$.

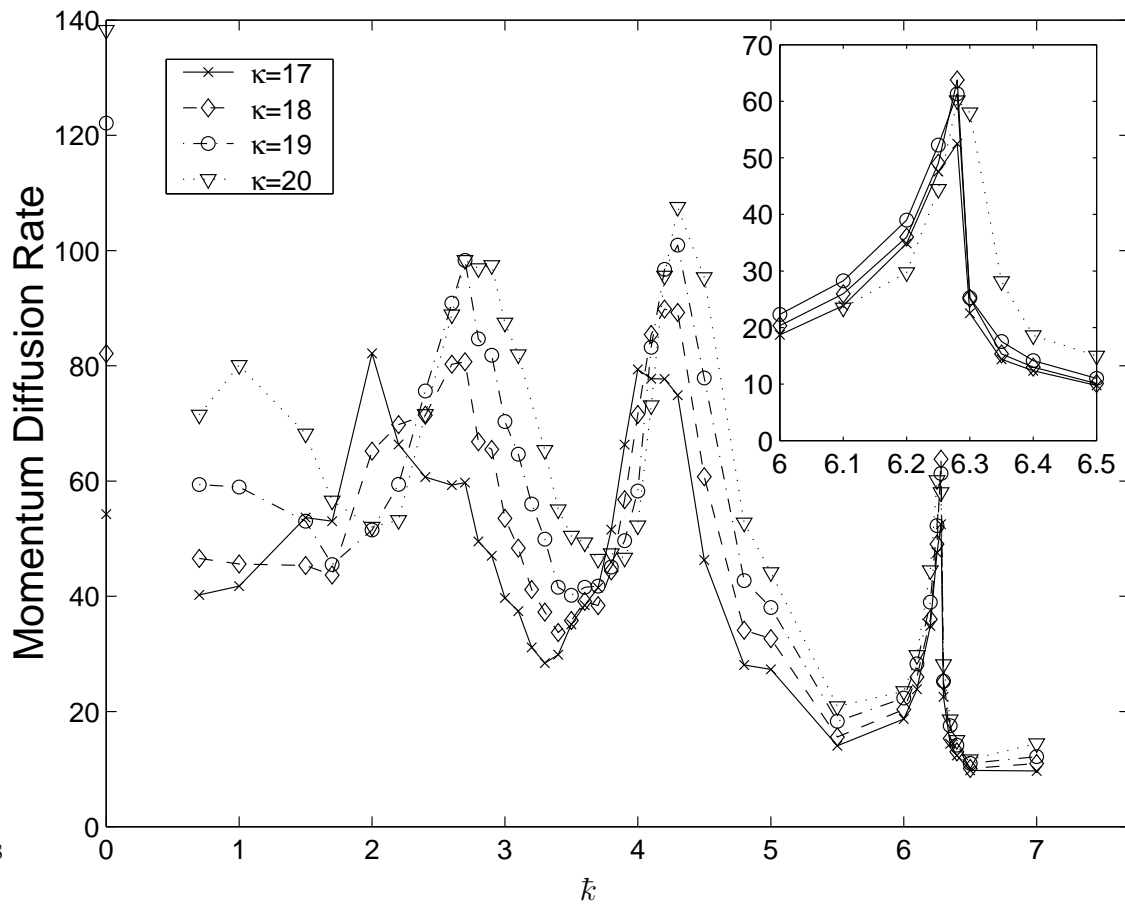


Figure 6.13: Simulation results for late time quantum diffusion rates for the QKR with $\alpha = 0.005$ and $\eta = 10\%$. Corresponding classical values are marked for $\bar{k} = 0$. The inset shows more clearly the behaviour near the quantum resonance peak at $\bar{k} = 2\pi$.

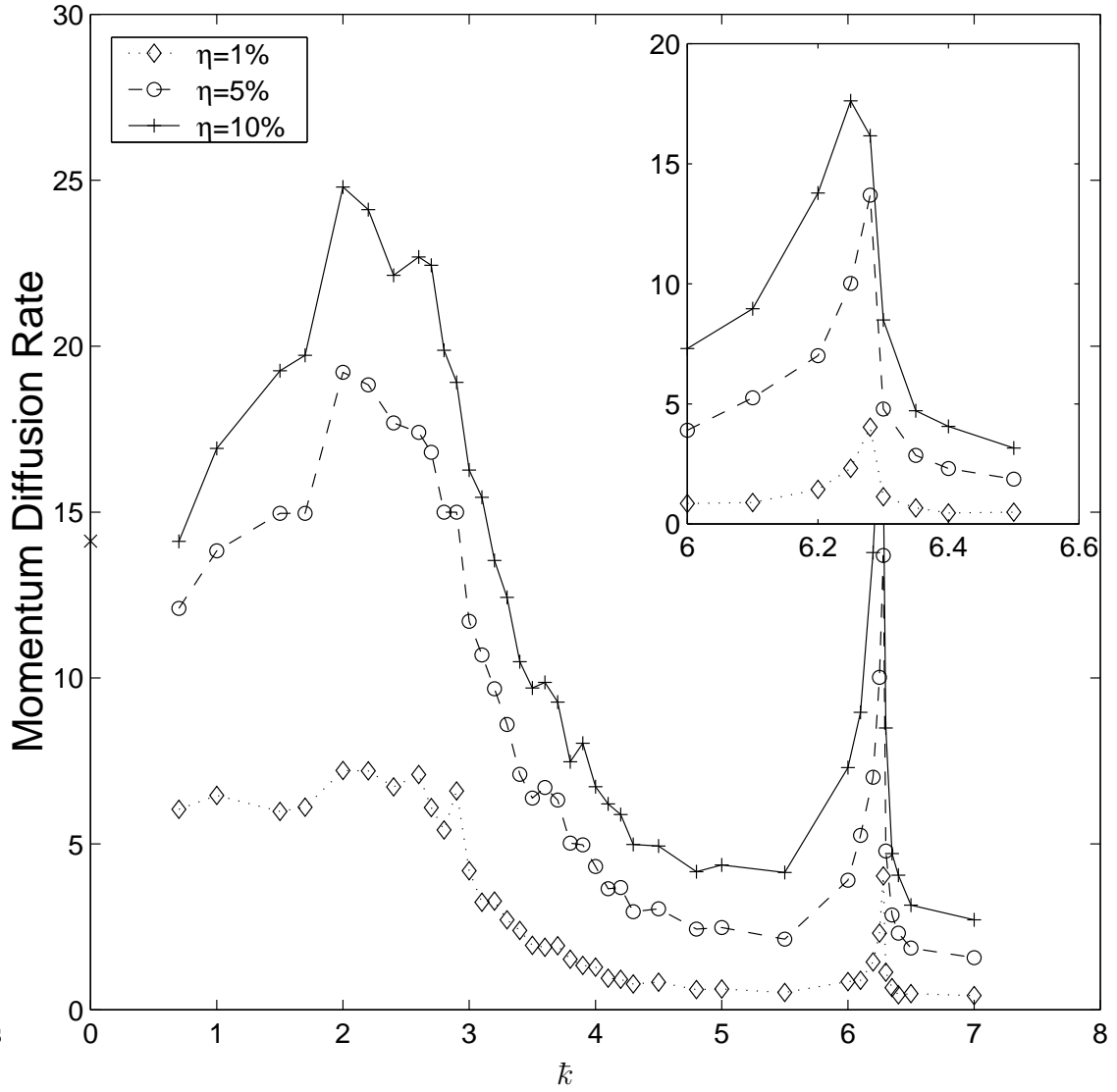


Figure 6.14: Simulation results of late time quantum diffusion rates for the QKR with $\alpha = 0.005$ and $\kappa = 9$, showing the variation with η . The corresponding classical value is marked for $\bar{k} = 0$, and the inset shows the behaviour near the quantum resonance peak at $\bar{k} = 2\pi$.

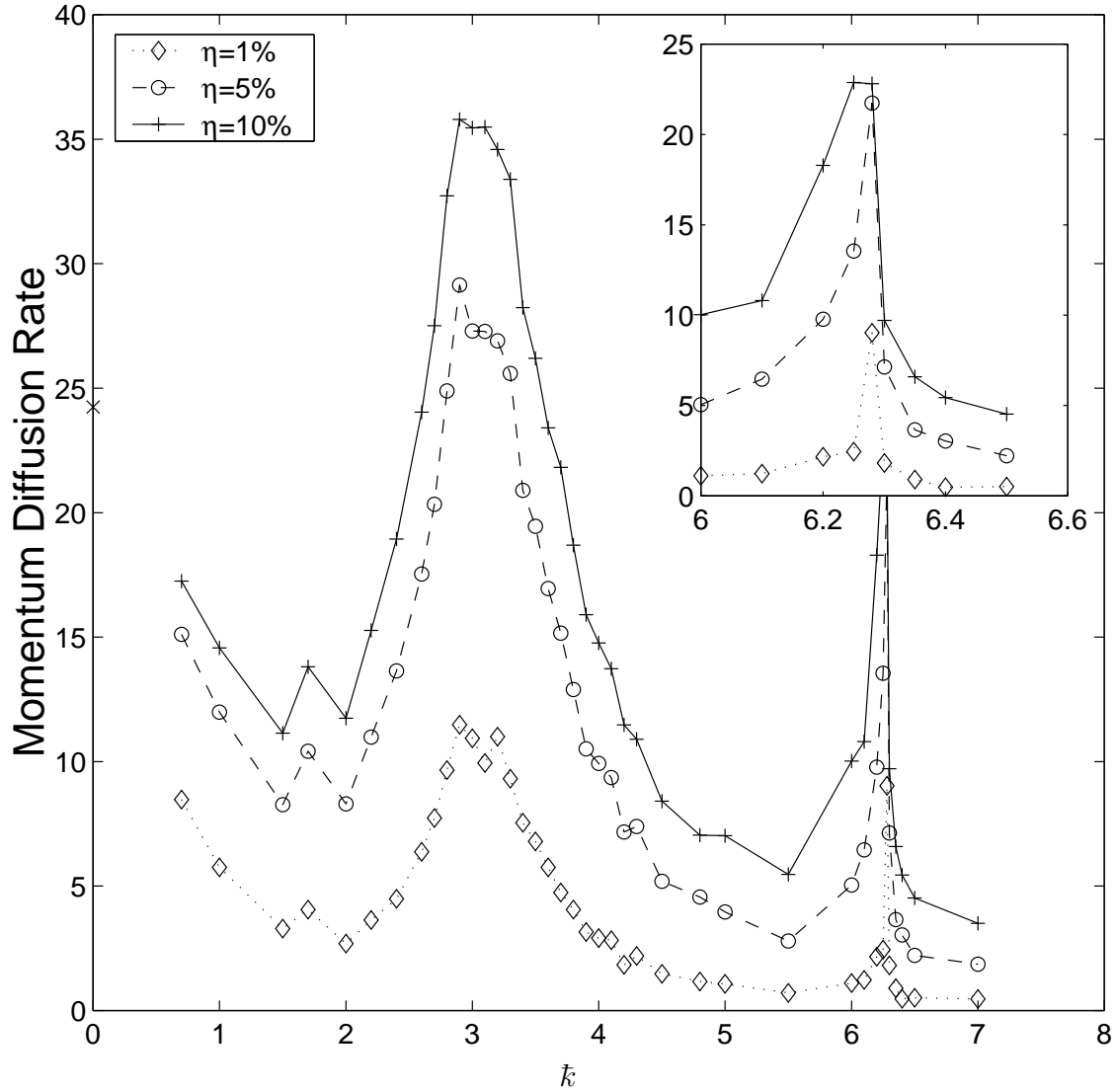


Figure 6.15: Simulation results of late time quantum diffusion rates for the QKR with $\alpha = 0.005$ and $\kappa = 11$, showing the variation with η . The corresponding classical value is marked for $\bar{k} = 0$ and the inset shows the behaviour near the quantum resonance peak at $\bar{k} = 2\pi$.

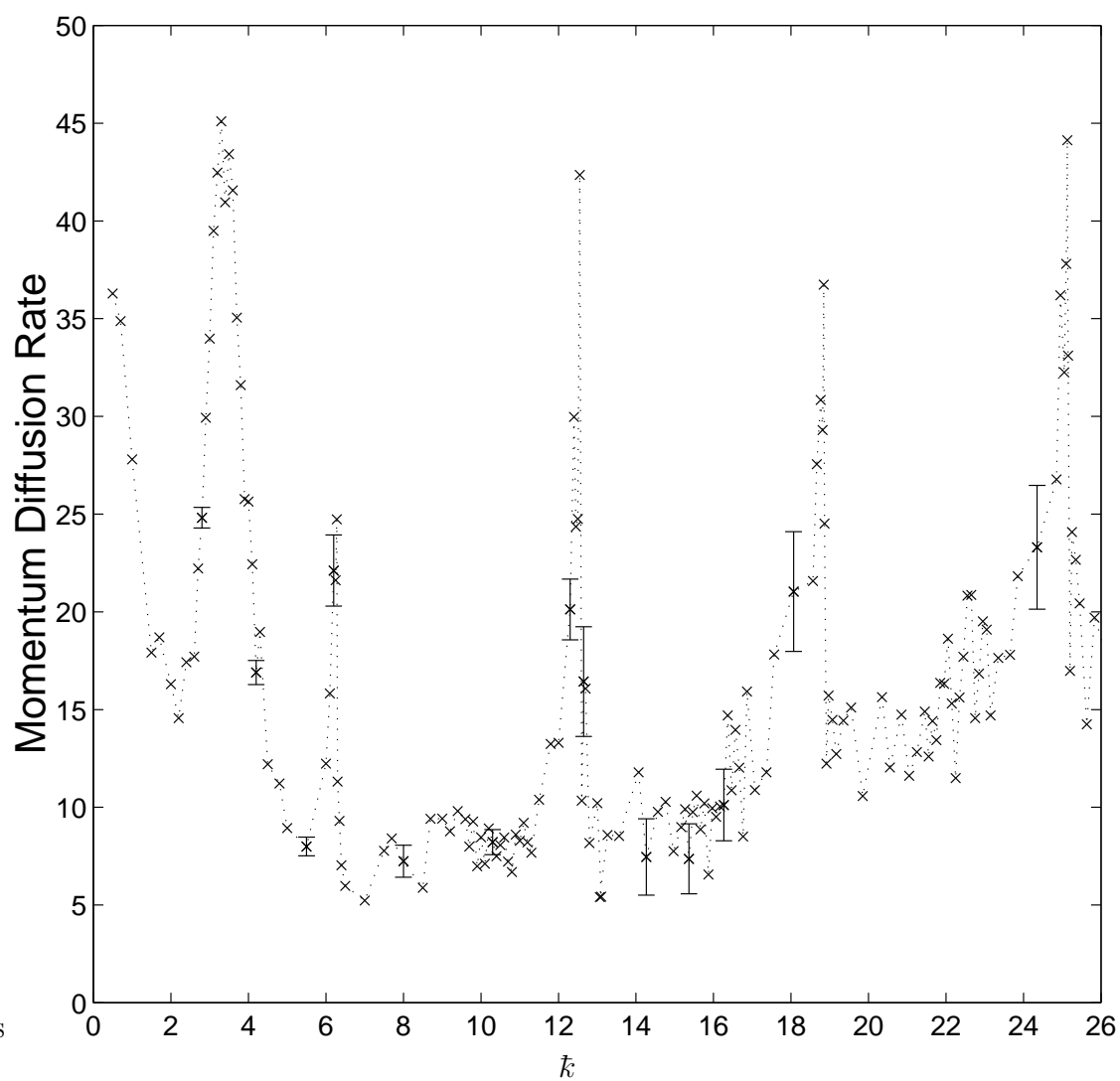


Figure 6.16: Simulation results of late time quantum diffusion rates for the QKR with $\alpha = 0.005$, $\kappa = 12$ and $\eta = 10\%$, showing the behaviour at large values of \bar{k} .

6.5 Analytical Results for Late Time Diffusion Rates

6.5.1 Relationship with Early Time Diffusion Rates

It is possible to derive an analytical result for the late time diffusion rates in terms of early time diffusion rates based on work originally presented by Cohen [3]. Cohen's result was derived for a δ -kicked rotor with a noise term in the quantum standard map, and is based on a perturbation treatment of the transition between "quasienergy eigenstates".

We define a function $P(t)$ which gives the probability that a transition between quasienergy eigenstates has occurred after a time t . We also define $\dot{P}(t) = P(t+1) - P(t)$, which is the discrete time derivative of $P(t)$, i.e., the probability that the decay occurs in the step leading to time $(t+1)$, having not occurred at any stage up to time t . From (3.31) and the quantum analogue of (2.60) the late time diffusion rate (for a system with no noise) is given by

$$\tilde{D}_{0,\infty} = \kappa^2 \sum_{\tau=-\infty}^{\infty} C_s(\tau), \quad (6.2)$$

where $C_s(i-j) = \langle \sin(\hat{\phi}_i) \sin(\hat{\phi}_j) \rangle = \langle \sin(\hat{\phi}_{i-j}) \sin(\hat{\phi}_0) \rangle$. Leading order perturbation theory then yields the result that if we add noise to the system, the late time diffusion rates are given by this formula, but with the correlation functions weighted by the probability that a decay has not yet occurred [3]. That is,

$$\tilde{D}_{\infty} = \kappa^2 \sum_{\tau=-\infty}^{\infty} C(\tau), \quad (6.3)$$

where

$$C(t) = [1 - P(t)]C_s(t). \quad (6.4)$$

Thus,

$$\tilde{D}_{\infty} = \kappa^2 \sum_{\tau=-\infty}^{\infty} P(\tau)(-C_s(\tau)) + \kappa^2 \sum_{\tau=-\infty}^{\infty} C(\tau) \quad (6.5)$$

$$= 2\kappa^2 \sum_{\tau=1}^{\infty} P(\tau)(-C_s(\tau)) \quad (6.6)$$

$$= \sum_{\tau=0}^{\infty} \dot{P}(\tau)\tilde{D}_0(\tau), \quad (6.7)$$

where $\tilde{D}_0(t)$ are the diffusion rates as a function of t in the quantum kicked rotor with no noise. Here we have made use of the fact that $\tilde{D}_{0,\infty} = 0$ (due to dynamical

localisation), and that $P(0) = 0$, and the last step comes from a discrete analogue of integration by parts.

Now, we can attempt to apply this result to the phenomenon of decoherence due to spontaneous emissions in the atom optics kicked rotor if take $P(t)$ to be the probability that a spontaneous emission has occurred after a time t . This would seem to be reasonable even without rigorous perturbation theory if we assume that the occurrence of a spontaneous emission event destroys the quantum coherences entirely, so that the correlation functions involving position operators before and after the event evaluate to zero. Then, in calculating the diffusion rate, we should weight the correlation function over a particular time interval by the probability that a spontaneous emission event does not happen in that time interval. This gives us $C(t) = [1 - P(t)]C_s(t)$ as above, which again leads to the result (6.7). Now, if the probability of spontaneous emission per kick is η then we have

$$P(t) = 1 - (1 - \eta)^t, \quad (6.8)$$

so that

$$\dot{P}(t) = \eta(1 - \eta)^t. \quad (6.9)$$

Then, the late time diffusion rate for the atom optics kicked rotor can be expressed as

$$D_\infty = \sum_{\tau=0}^{\infty} \eta(1 - \eta)^\tau D_0(\tau), \quad (6.10)$$

where the tildes on the diffusion rate symbols have been dropped for convenience because of the near equivalence of our two definitions of the diffusion rate. This tells us that the late time diffusion rates are given by a weighted average over the diffusion rates as the kicked rotor evolves, with the weighting for $D_0(n)$ being the probability that the first spontaneous emission event occurs on kick number $n + 1$, i.e., $\eta(1 - \eta)^n$. In a sense, the early time diffusion rates are “locked in” by the loss of phase coherence. This explains where the phenomenon of “superdiffusion”, or diffusion at faster rates than those which occur in the corresponding classical system, arises from. We saw in the simulation results for the initial quantum diffusion rates that these could be faster than the rates for the corresponding classical system, and when we add decoherence these faster rates essentially become locked in. It is thus a combination of quantum correlations and decoherence which drives diffusion in the quantum system at a rate faster than that in the classical system.

Figures 6.17 and 6.18 show a comparison between the two sides of (6.10), where D_∞ is computed from simulations for the kicked rotor with decoherence, and the values for $D_0(t)$ are also taken from simulations of the kicked rotor, but without decoherence. There is a small discrepancy near the quantum resonance peak at $\bar{k} = 2\pi$ where the simulation results for the late time diffusion rates do not exhibit a symmetric peak, but elsewhere the agreement is very good, particularly near the enhanced diffusion peak. This level of agreement means that the model we put forward which led to (6.10) is a good model for predicting the values of the late time diffusion rates.

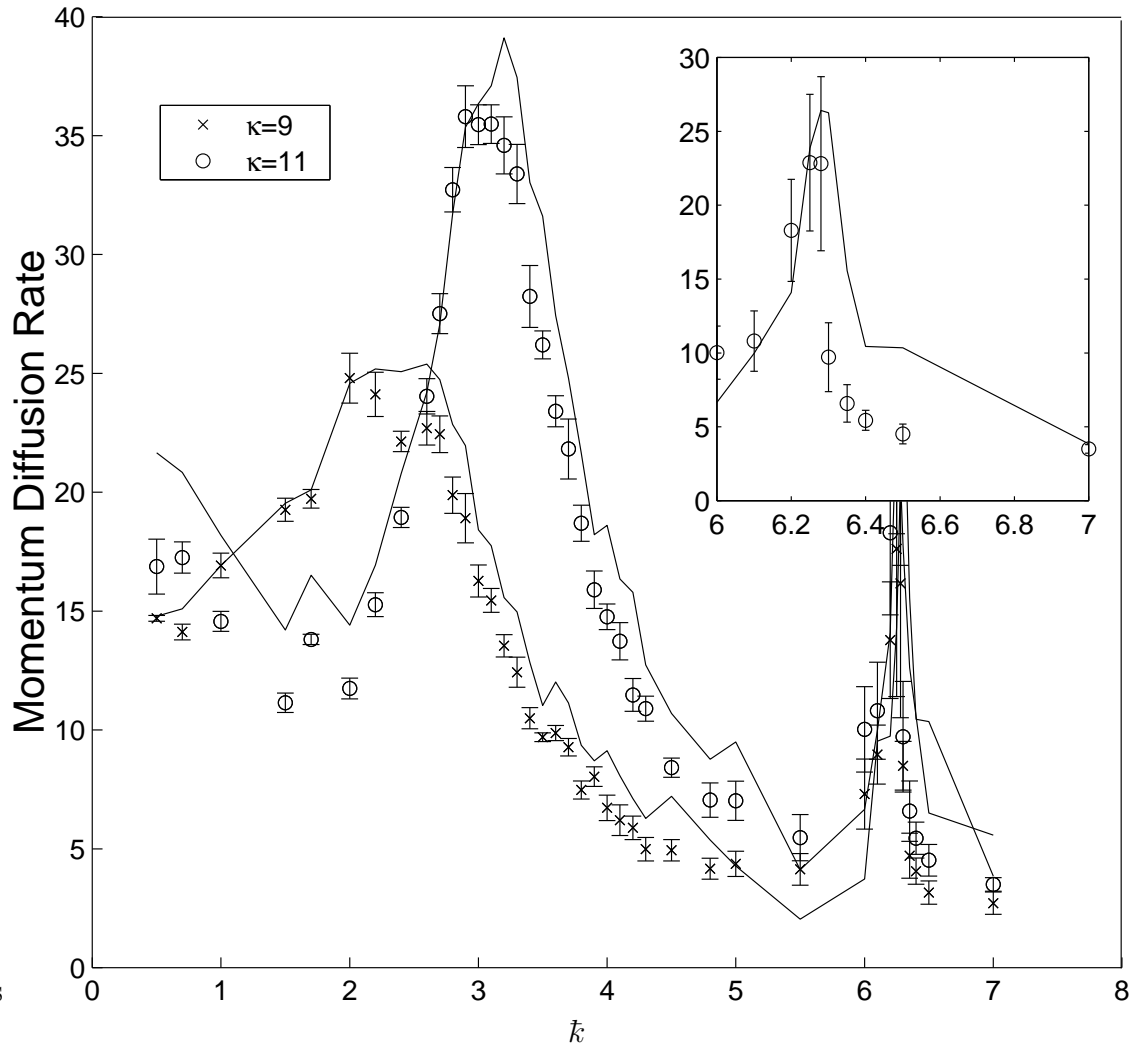


Figure 6.17: Comparison of simulation results for late time quantum diffusion rates (points) and results from the right hand side of (6.10) (lines) for the QKR with $\alpha = 0.005$ and $\eta = 10\%$. Note that the lines have statistical errors associated with them of a similar magnitude to those associated with the points. The inset shows the peak near the quantum resonance at $\bar{k} = 2\pi$ for $\kappa = 11$.

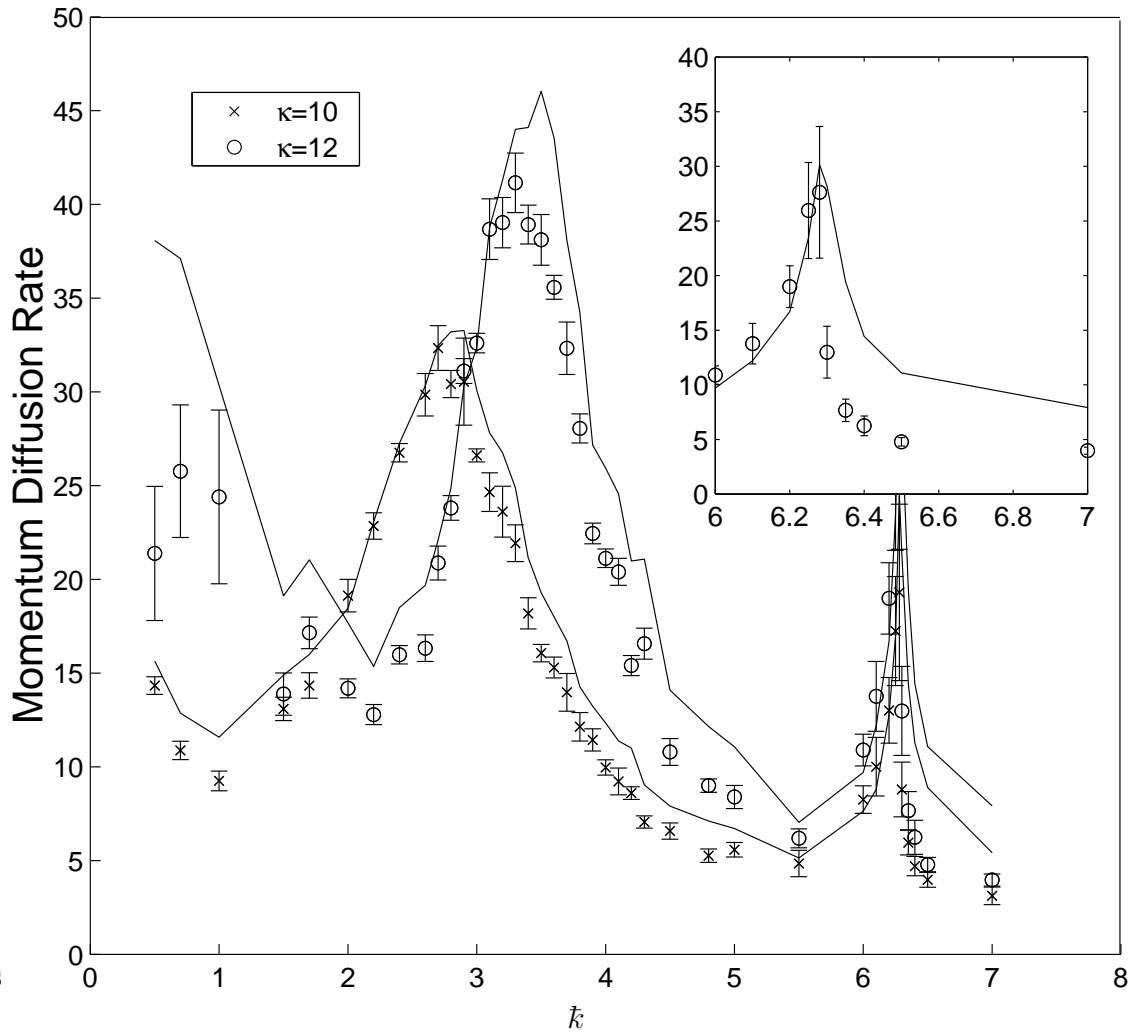


Figure 6.18: Comparison of simulation results for late time quantum diffusion rates (points) and results from the right hand side of (6.10) (lines) for the QKR with $\alpha = 0.005$ and $\eta = 10\%$. Note that the lines have statistical errors associated with them of a similar magnitude to those associated with the points. The inset shows the peak near the quantum resonance at $\bar{k} = 2\pi$ for $\kappa = 12$.

6.5.2 A Fully Analytical Result

By making assumptions about the form of $D_0(\tau)$ it is possible to derive a fully analytical result from (6.10). The most commonly quoted equation of this form is that used by Ammann *et al.* [30], where they assume an exponentially decaying $D_0(\tau)$ as dynamical localisation sets in, i.e., $D_0(\tau) = D_0 \exp(-\tau/N^*)$. This yields the relationship

$$D_\infty = \frac{\eta N^* D_0}{1 + \eta N^*}. \quad (6.11)$$

Normally, D_0 is taken to be D_q , as given by Shepelyansky's result and N^* is approximated by D_q/\bar{k}^2 . However, in most published work involving this formula, D_0 and N^* are used as fitted parameters. The reason why this is necessary is apparent from figure 6.19, which shows a comparison between simulation results for the late time diffusion rates and the prediction of this formula for $D_0 = D_q$ and $N^* = D_q/\bar{k}^2$. There is a large inaccuracy in the predicted diffusion rates near the enhanced diffusion peak, and this becomes more pronounced near $\bar{k} = 5$, where the predicted diffusion rates become very close to zero.

In order to produce a fully analytical expression to predict the late time diffusion rates, we need to use a better approximation for $D_0(\tau)$. Firstly, we need to include the effects of the quasilinear diffusion period in our form, so we choose

$$D(0) = D(1) = \frac{\kappa^2}{4}.$$

Then, we need to include the result from Cohen's work [3] which indicates that where the exponential decay of the diffusion rate is an appropriate approximation, the corresponding time constant should be $2N^*$, rather than just N^* , as it is normally defined. Then, for $\tau \geq 2$, $D(\tau) = D_q \exp[-(\tau - 2)/(2N^*)]$, and from (6.10) we have

$$\begin{aligned} D_\infty &= \frac{\kappa^2}{4} [\eta + \eta(1 - \eta)] + \sum_{\tau=2}^{\infty} \eta(1 - \eta)^\tau D_q e^{-(\tau-2)/(2N^*)} \\ &= \frac{\kappa^2}{4} [\eta(2 - \eta)] + \frac{\eta(1 - \eta)^2 D_q}{1 - (1 - \eta)e^{-1/(2N^*)}} \\ &\approx \frac{\kappa^2}{4} [\eta(2 - \eta)] + \frac{N^* D_q \eta(1 - \eta)^2}{1/2 + \eta N^*}, \end{aligned} \quad (6.12)$$

where the last step assumes the case of large N^* . As can be seen in figures 6.20, 6.21 and 6.22 this expression gives much better agreement with the simulation results than (6.11). The correction of the exponential decay constant has improved the agreement near the enhanced diffusion peak, and the inclusion of the quasilinear behaviour has improved the predictions near $\bar{k} = 5$. The agreement is also much better for low values of \bar{k} .

The largest discrepancy which still remains is that near the quantum resonance peak, where the fully analytical expression (6.12) gives a much broader and lower

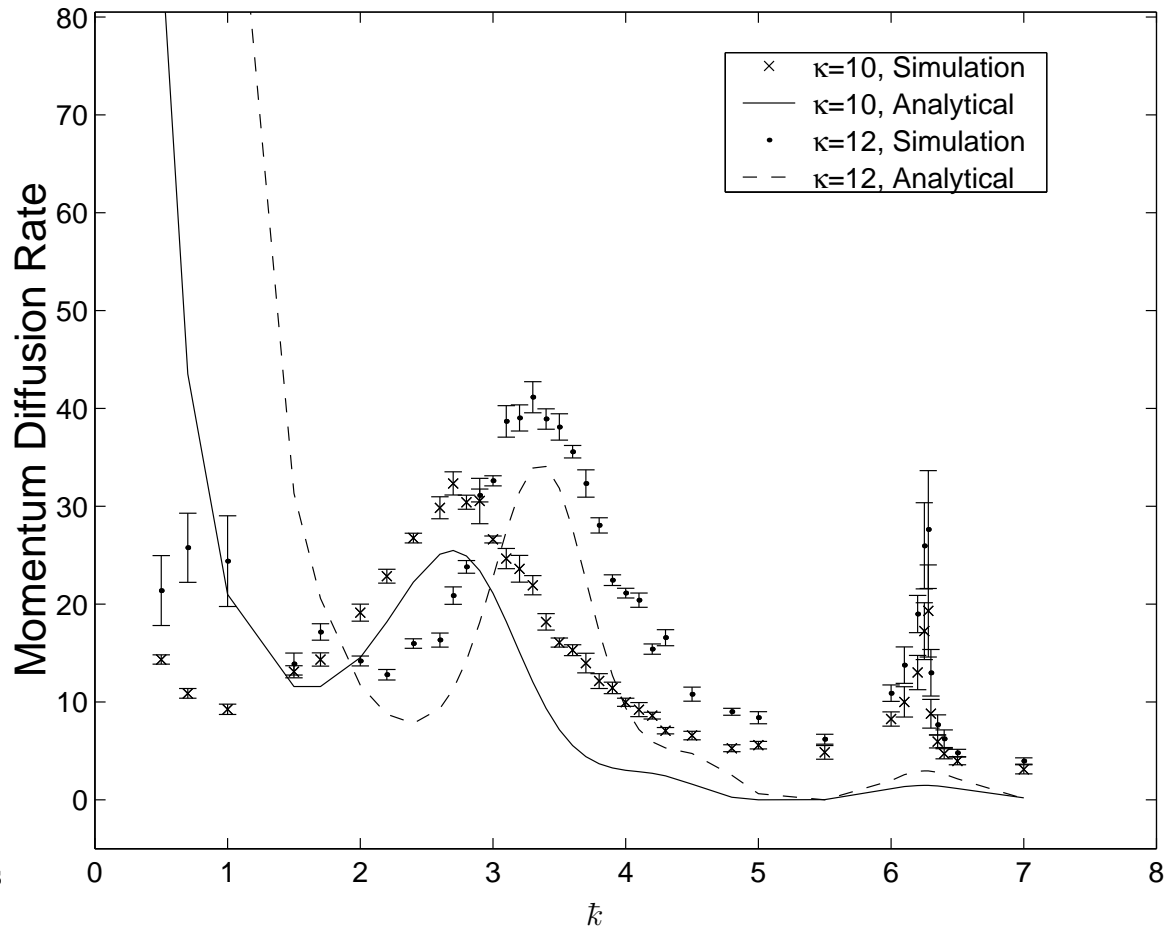


Figure 6.19: Comparison of simulation results for late time quantum diffusion rates with the analytical expression of Ammann *et al.* [30], (6.11), for the QKR with $\alpha = 0.005$ and $\eta = 10\%$

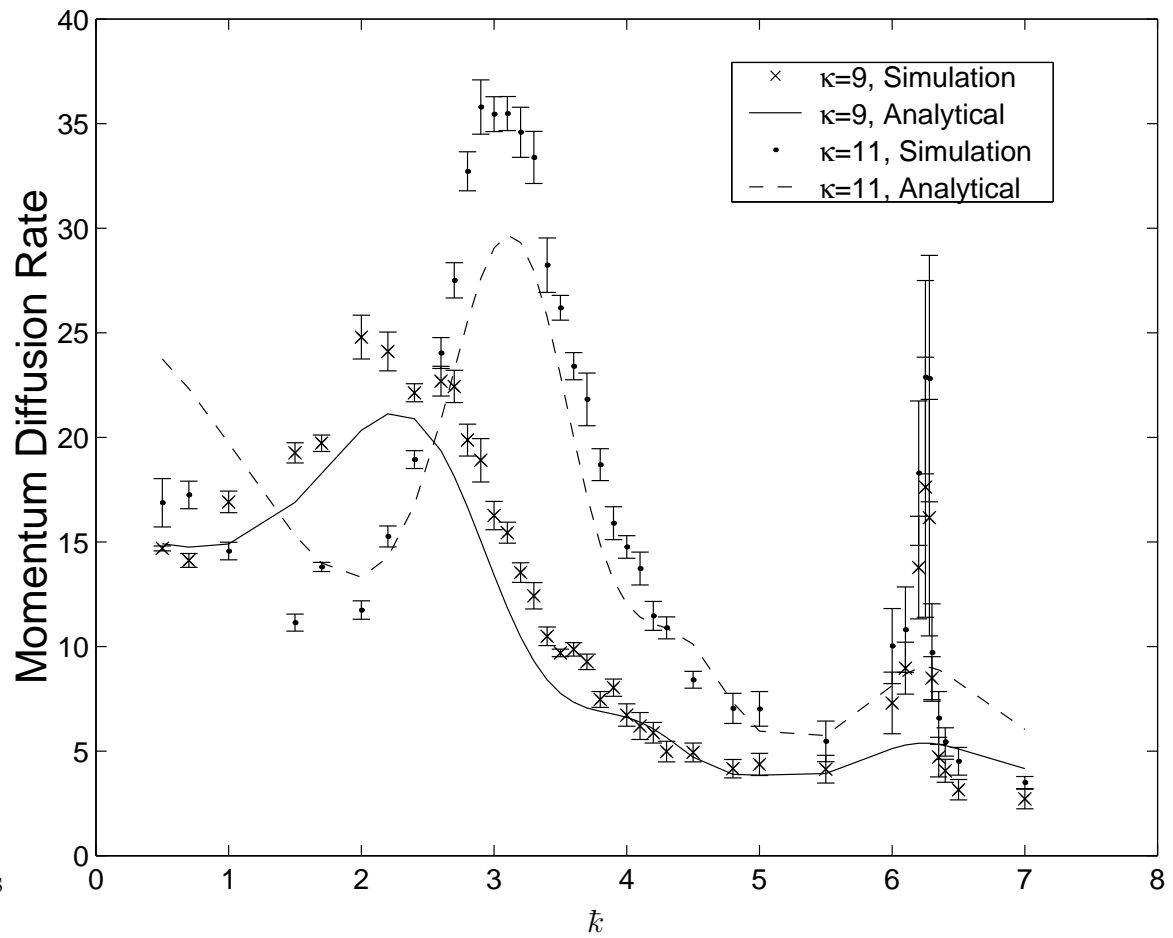


Figure 6.20: Comparison of simulation results for late time quantum diffusion rates with the analytical expression from (6.12), for the QKR with $\alpha = 0.005$, $\eta = 10\%$, and $\kappa = 9, 11$.

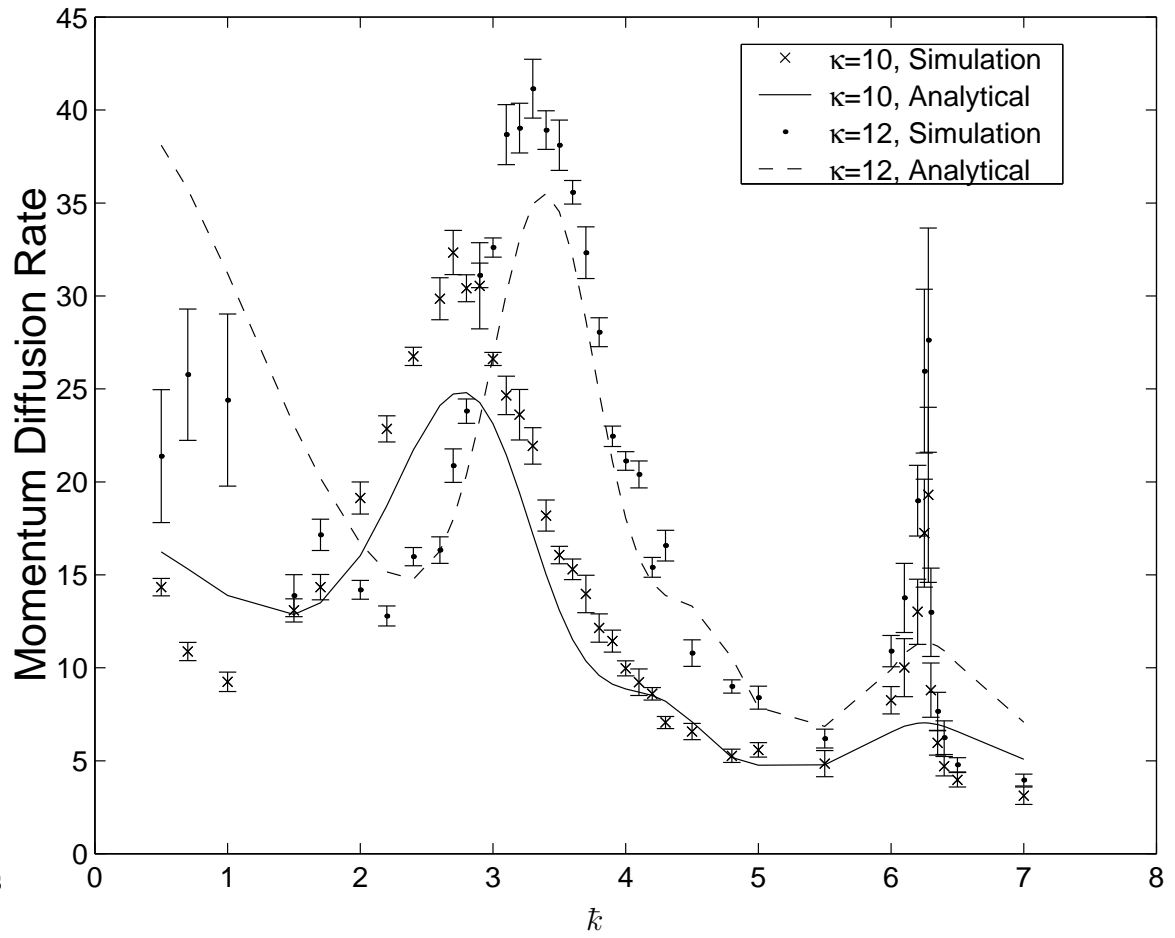


Figure 6.21: Comparison of simulation results for late time quantum diffusion rates with the analytical expression from (6.12), for the QKR with $\alpha = 0.005$, $\eta = 10\%$, and $\kappa = 10, 12$.

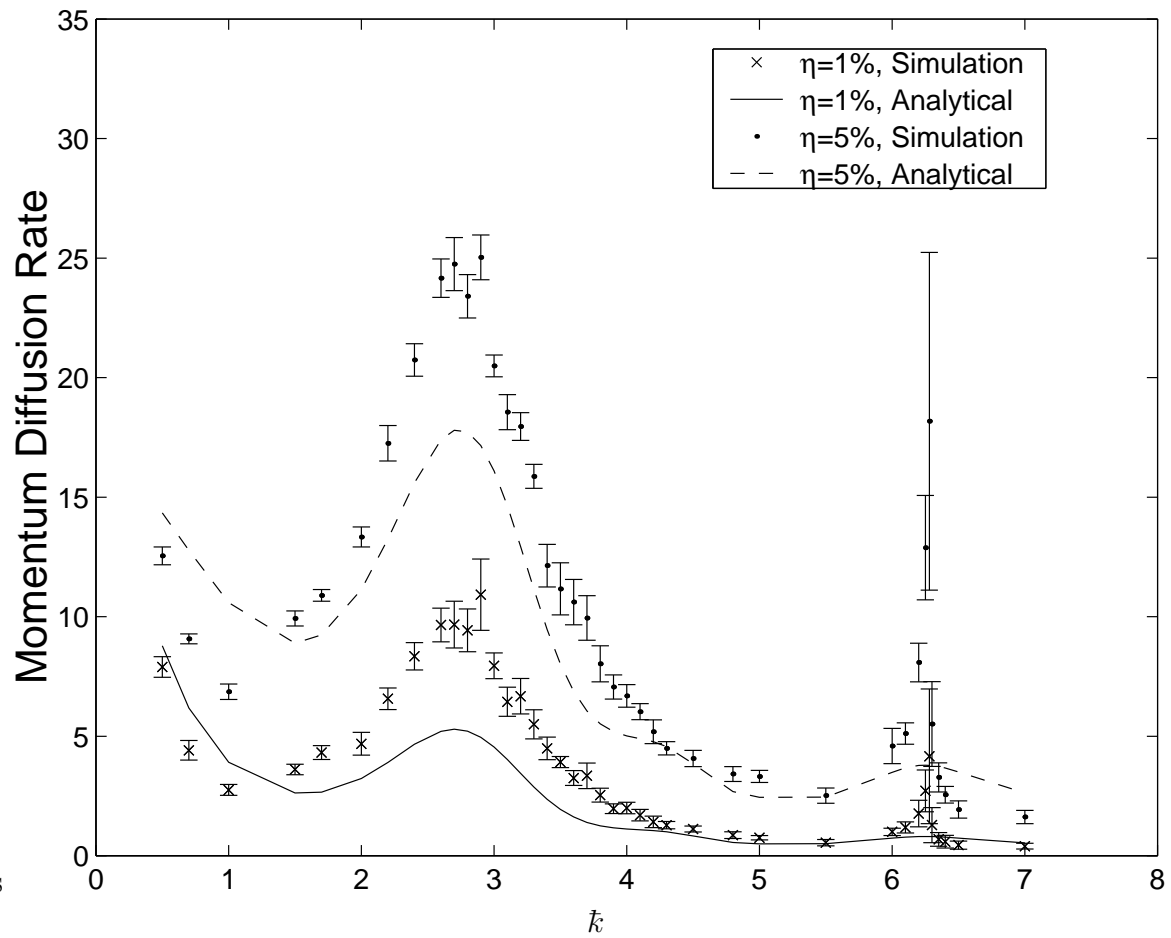


Figure 6.22: Comparison of simulation results for late time quantum diffusion rates with the analytical expression from (6.12), for the QKR with $\alpha = 0.005$ and $\kappa = 10$, showing variation with changing η .

magnitude peak than is given either by the numerical evaluation of (6.10) or by the full simulation results. The reason for this is clear from the graphs in figures 6.23 and 6.24, which show simulation results for $D_0(\tau)$ for various values of \bar{k} . For lower values of \bar{k} the approximation of an exponential decay into a localised state after the initial quasilinear diffusion period appears to be a good one, whereas around the quantum resonance, oscillations in the diffusion rates as a function of kick number start to occur, and so the assumptions which lead to (6.12) break down. These oscillations have a period which becomes longer closer to the quantum resonance itself, and this period appears to become approximately infinite at the resonance itself (the nearest value corresponding to a graph in figure 6.24 is $\bar{k} = 6.28$). The amplitudes of the oscillations decay, but if the system is left for around 150 kicks the oscillations begin to undergo revivals, with the same period as they exhibited originally. This is a very interesting and uniquely quantum mechanical phenomenon, although it would require a great deal of accuracy in measurements of the cloud widths to reproduce these results in traditional atom optics kicked rotor experiments.

6.6 Austin Method for generating Spontaneous Emissions

As described in section 4.4.3, two different methods are used for generating spontaneous emissions in the atom optics kicked rotor. All of our simulations so far have modelled the method used by the Auckland experimental group, which involves spontaneous emissions being generated by the kicking beam during the kick. In this section we present the results of some simulations of the late time diffusion rates where spontaneous emissions are generated throughout the cycle by a beam with no position dependence in its intensity. This is the type of implementation used by the group in Austin.

Figure 6.25 shows the late time diffusion rates for $\kappa = 10$ and $\kappa = 12$. Comparison of this graph with figure 6.11 shows that both the structure and quantitative diffusion rates generated by the two different methods are very similar. The main difference between the two is that spontaneous emission noise implemented using the Austin method produces a quantum resonance peak which is symmetric about the centre, whereas spontaneous emission noise implemented using the Auckland method produces a quantum resonance peak which is skewed to the left. This is particularly noticeable in figure 6.26, which shows the comparison between the diffusion rates predicted by the series in (6.10) and the simulation values for late time diffusion rates produced using the Austin method for generating spontaneous emission noise. The symmetric quantum resonance peak is in agreement with the series expansion, unlike the results shown for Auckland style generation of spontaneous emissions, which were shown in figures 6.17 and 6.18.

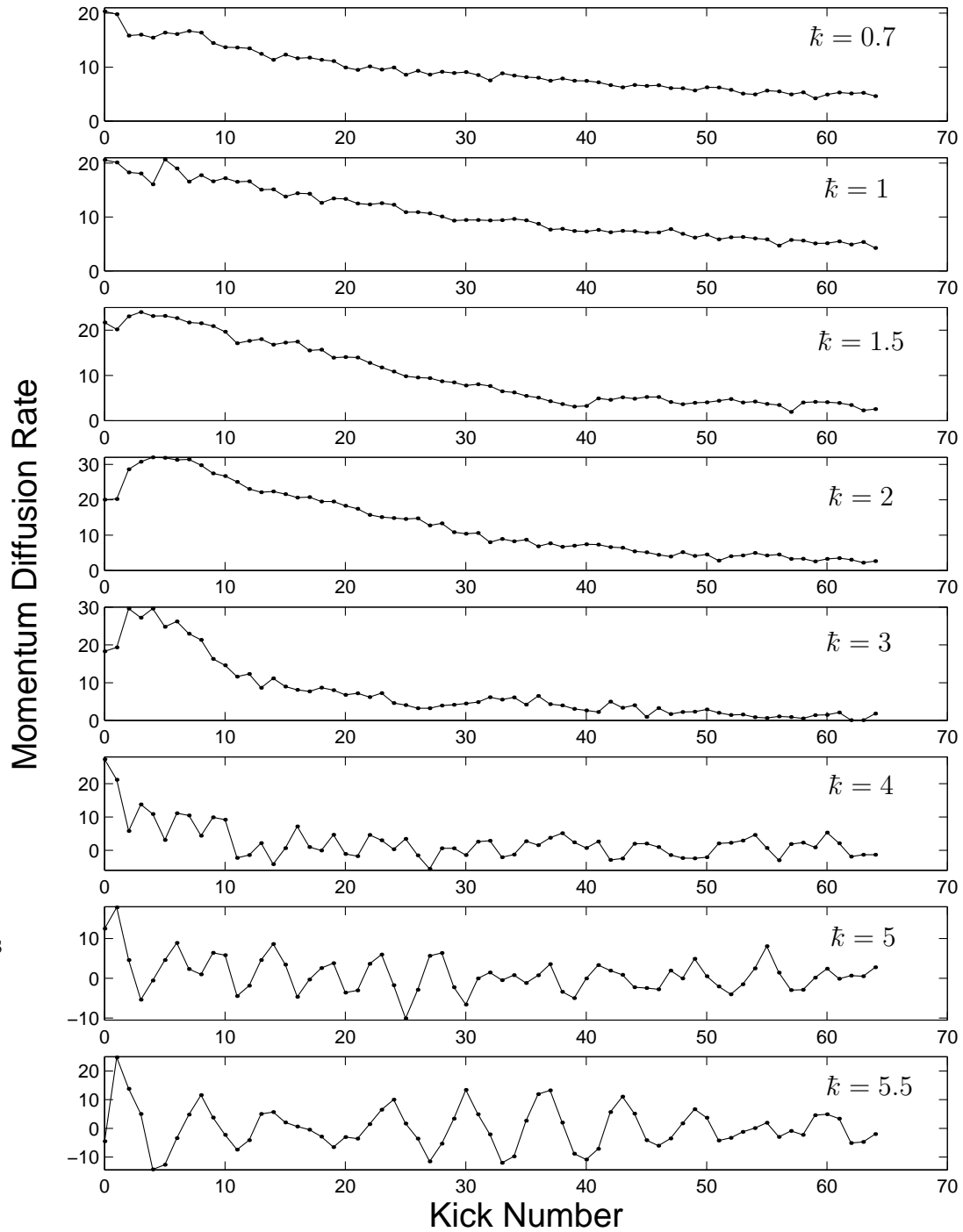


Figure 6.23: Diffusion rates, $D_0(n)$, for the quantum kicked rotor without noise, shown as a function of kick number and demonstrating the variation in behaviour with changing \bar{k} for $\bar{k} \leq 5.5$.

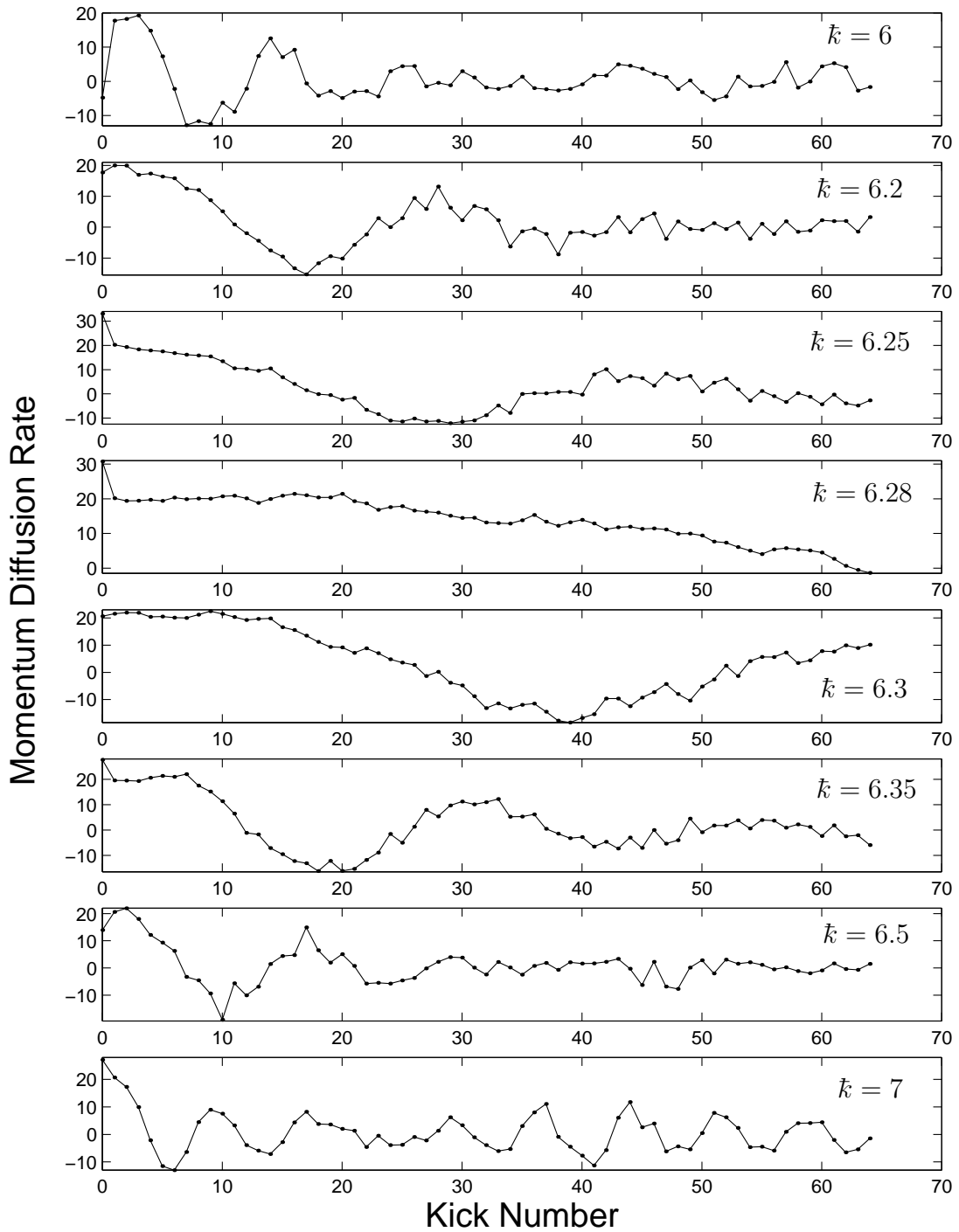


Figure 6.24: Diffusion rates, $D_0(n)$, for the quantum kicked rotor without noise, shown as a function of kick number and demonstrating the variation in behaviour with changing \bar{k} for values around the quantum resonance at $\bar{k} = 2\pi$.

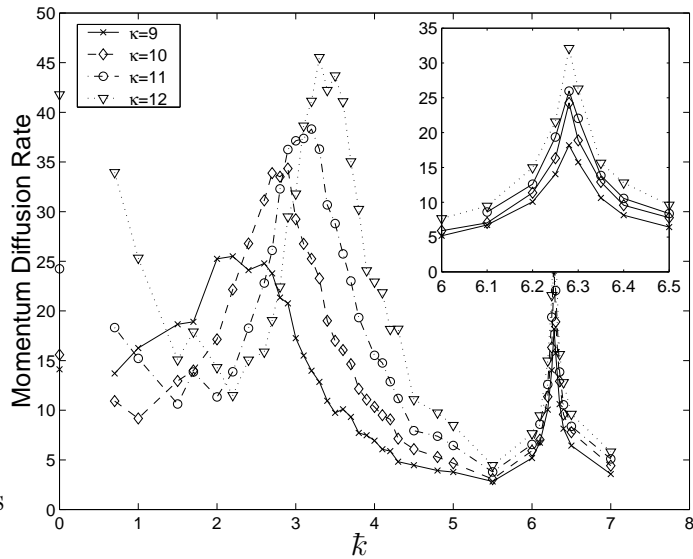


Figure 6.25: Simulation results for late time quantum diffusion rates for the QKR with $\alpha = 0.005$ and $\eta = 10\%$. Spontaneous emission noise is implemented in the Austin style. The inset shows the behaviour near the quantum resonance at $\tilde{k} = 2\pi$.

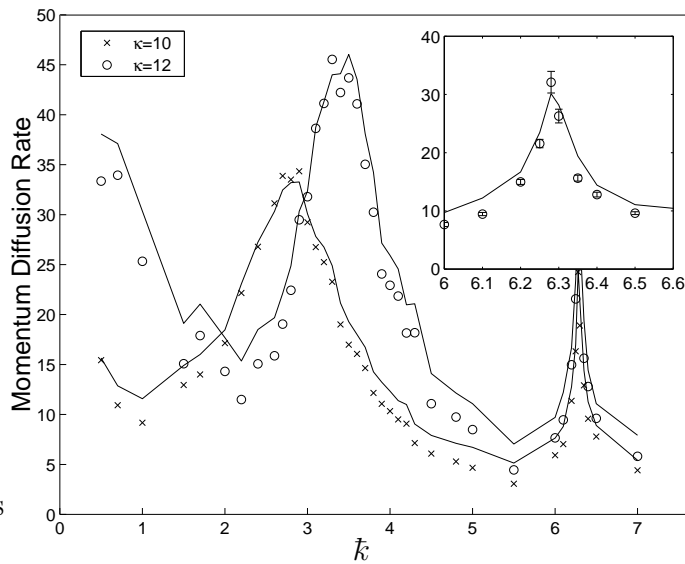


Figure 6.26: Comparison of simulation results for late time quantum diffusion rates with Austin-style spontaneous emission noise (points) and results from the right hand side of (6.10) (lines) for the QKR with $\alpha = 0.005$ and $\eta = 10\%$. Note that the lines have statistical errors associated with them of a similar magnitude to those associated with the points. The inset shows the peak near the quantum resonance at $\tilde{k} = 2\pi$ for $\kappa = 12$.

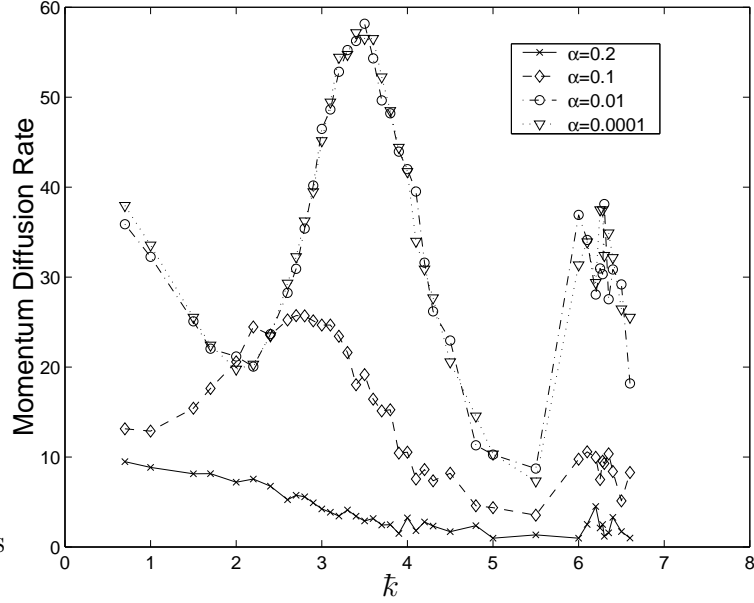


Figure 6.27: Simulation results of initial quantum diffusion rates for the QKR with $\kappa = 12$ and $\eta = 10\%$, showing the effects of varying α .

6.7 The Effects of Varying α

We know from section 2.3.2 that as we make α larger, the effective kick strength decreases for higher momentum values. This is clearly reflected in figures 6.27 and 6.28, which demonstrate the problems encountered when using α values which are too high to adequately approximate the δ -kicked rotor.

Figure 6.27 shows the enhanced diffusion peak in the initial diffusion rates shifting to the left and decreasing in magnitude as α is made larger, as we would expect as the effective kick strength decreases. We notice, however, that the initial quantum diffusion rates for $\alpha = 0.01$ and $\alpha = 0.0001$ are almost identical. This indicates that at those diffusion rates the system wavefunction does not spread during the first 6 kicks to regions of momentum values in which there is a significant decrease in the effective kick strength.

Figure 6.28 shows that for $\alpha = 0.1$ and $\alpha = 0.2$, momentum diffusion ceases almost entirely as the presence of the KAM boundary present for relatively low values of momentum acts as a barrier to the diffusion. We also observe that as the wavefunction spreads, the effective kick strength experienced by the system with $\alpha = 0.01$ is obviously decreasing, resulting in smaller late time diffusion rates for that system than we observe when $\alpha = 0.0001$ (and the corresponding shift of the enhanced diffusion peak). Comparison of the result for $\alpha = 0.0001$ with figure 6.11 suggests that both $\alpha = 0.005$ and $\alpha = 0.0001$ are good approximations to the δ -kicked rotor for these diffusion rates for the first 200 kicks.

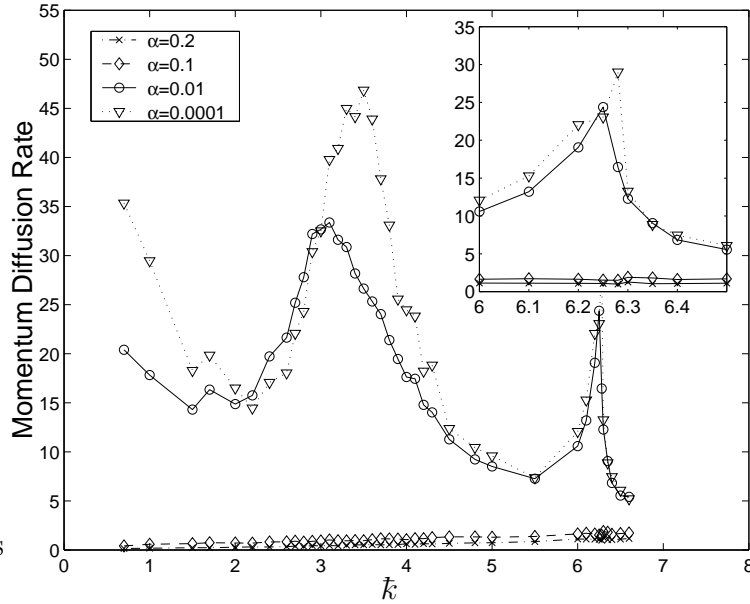


Figure 6.28: Simulation results of late time quantum diffusion rates for the QKR with $\kappa = 12$ and $\eta = 10\%$, showing the effects of varying α .

6.8 Varying Widths of the Initial Momentum Distribution

As well as κ , η , and α , diffusion rates in the atom optics kicked rotor are, in general, dependent on the width of the initial momentum distribution. This momentum distribution is determined by the initial temperature of the cloud of atoms at $t = 0$, and if σ_p is the real width of the momentum distribution corresponding to a particular temperature in units of $(2\hbar k_l)$, then the width in the units of ρ is given by $\sigma_\rho = \bar{k}\sigma_p$. Thus, the effective width becomes smaller as \bar{k} becomes smaller. Unless otherwise stated, all simulations in this thesis use a width of $\sigma_p = 4$, which corresponds to a temperature of $10\mu\text{K}$. Various simulations have shown that both initial and late time quantum diffusion rates are unchanged if this width is made larger (specifically we have simulated up to temperatures of $80\mu\text{K}$, or $\sigma_p = 8$), although the actual widths of the cloud after each kick are obviously increased.

If much narrower initial momentum distributions are used, there are no significant changes to the late time quantum diffusion rates, but the quasilinear behaviour which is normally expected in the second kick ($n=1$) is replaced under certain circumstances by a rate which exhibits dramatic resonance structures as \bar{k} is varied. These structures are quite different to those which are normally observed in the initial and late time quantum diffusion rates, and are dealt with in more detail in chapter 9.

Chapter 7

Diffusion in the QKR with Amplitude Noise

7.1 Introduction

As was described in section 4.5, another form of noise which may be added to the atom optics kicked rotor is amplitude noise, in which the depth of the potential well is randomly varied from one kick to the next. Like spontaneous emission noise, amplitude noise has the effect of destroying long time correlations, and hence preventing the onset of dynamical localisation. By destroying those correlations, amplitude noise can remove the quantum character of the system, “driving” it back towards classical behaviour as correlations become important only on progressively shorter timescales, in much the same way as is observed with decoherence from spontaneous emissions. This onset of classical-like behaviour was studied in detail experimentally for fixed values of $\hbar k$ by Steck *et al.* [51].

Amplitude noise, however, is fundamentally different to spontaneous emission noise. Rather than being a dissipative process causing irreversible decoherence events, amplitude noise is a unitary process, and is in principle reversible. It also preserves the structure (and specifically the offset) of the momentum ladder, whereas spontaneous emissions break the symmetry of this ladder and essentially cause immediate loss of coherence. Amplitude noise has the effect of disrupting the correlations over a period of time, rather than doing so in single events. It is also more straight forward to use large amounts of amplitude noise than to induce large amounts of spontaneous emission noise because we are restricted to relatively low levels of spontaneous emissions for which the excited state population is not large (otherwise the assumptions we used in deriving the kicked rotor Hamiltonian begin to break down). Thus, using amplitude noise allows us to drive the system towards the classical diffusion rates (for a fixed value of $\hbar k$) more easily, even though correlations in the system are destroyed more effectively by individual spontaneous emission events.

It is interesting to see the effects that amplitude noise has on the structure of the diffusion rates as we vary $\hbar k$ for a fixed noise distribution. Specifically, we want to study

the structures in the initial quantum diffusion rates and also in the late time diffusion rates in the regime produced when amplitude noise prevents the onset of dynamical localisation. We also want to compare these late time diffusion structures with those produced by spontaneous emission, and to investigate what structures are produced when the two forms of noise are combined.

7.2 Amplitude Noise in the CKR

It is important to consider the effect that amplitude noise has on the diffusion rates in the classical kicked rotor, in order to compare this with the behaviour we observe in the quantum kicked rotor. If we choose $\kappa(n) = \kappa + \Delta\kappa(n)$, where $\Delta\kappa(n)$ comes from some probability distribution $P(\Delta\kappa)$, then from references [51, 15] we know that (2.64) may be modified to account for amplitude noise and its effects on classical correlations. It turns out that the Bessel Functions $J_i(\kappa)$ become weighted averages over the possible $\kappa(n)$ values, so that we get

$$\frac{\kappa^2 + \text{Var}(\Delta\kappa)}{4} + \frac{\kappa^2}{2}[-\tilde{J}_2(\kappa) - \tilde{J}_1^2(\kappa) + \tilde{J}_2^2(\kappa) + \tilde{J}_3^2(\kappa)], \quad (7.1a)$$

where $\text{Var}(\Delta\kappa)$ denotes the variance of the distribution $P(\Delta\kappa)$ and

$$\tilde{J}_i(\kappa) = \int_{-\infty}^{\infty} P(\Delta\kappa) J_i(\kappa + \Delta\kappa) d(\Delta\kappa). \quad (7.1b)$$

Note that because each factor of κ and $J_i(\kappa)$ enters this expansion from the generalisation of the correlation functions as an independent variable (see the derivation of this expression in appendix B), each is averaged independently (as opposed to the square of each factor being averaged over the distribution of κ values). The functions $\tilde{J}_i(\kappa)$ are essentially the convolution of the corresponding Bessel functions with the noise distribution. Thus, as the noise distribution is broadened, the Bessel functions will be smoothed out, essentially destroying the effects of the correlations which originally produced the terms involving Bessel functions. This formula is plotted in figure 7.1 as a function of κ for a uniform noise distribution on the interval $[-\delta\kappa, \delta\kappa]$,

$$P(\Delta\kappa) = \begin{cases} 1/(2\delta\kappa) & |\Delta\kappa| \leq \delta\kappa \\ 0 & |\Delta\kappa| > \delta\kappa \end{cases}, \quad (7.2)$$

with various values of $\delta\kappa$. We see immediately that large amounts of noise have the effect of destroying the anomalous diffusion behaviour, returning the system to an almost quasilinear diffusion rate. This is symptomatic of the washing out of the correlation functions by the noise, because it is the correlations over more than one kick that give rise to anomalous diffusion. Initially, the overall increase in diffusion rates is small (i.e., we return to rates very close to $\kappa^2/4$), but as the noise is increased further the diffusion rates increase because of the contribution from the term in (7.1) containing the variance of the noise distribution. Note that we quantify the noise level using the parameter $\text{noise} = 2(\delta\kappa)/\kappa$, which we almost always express as a percentage.

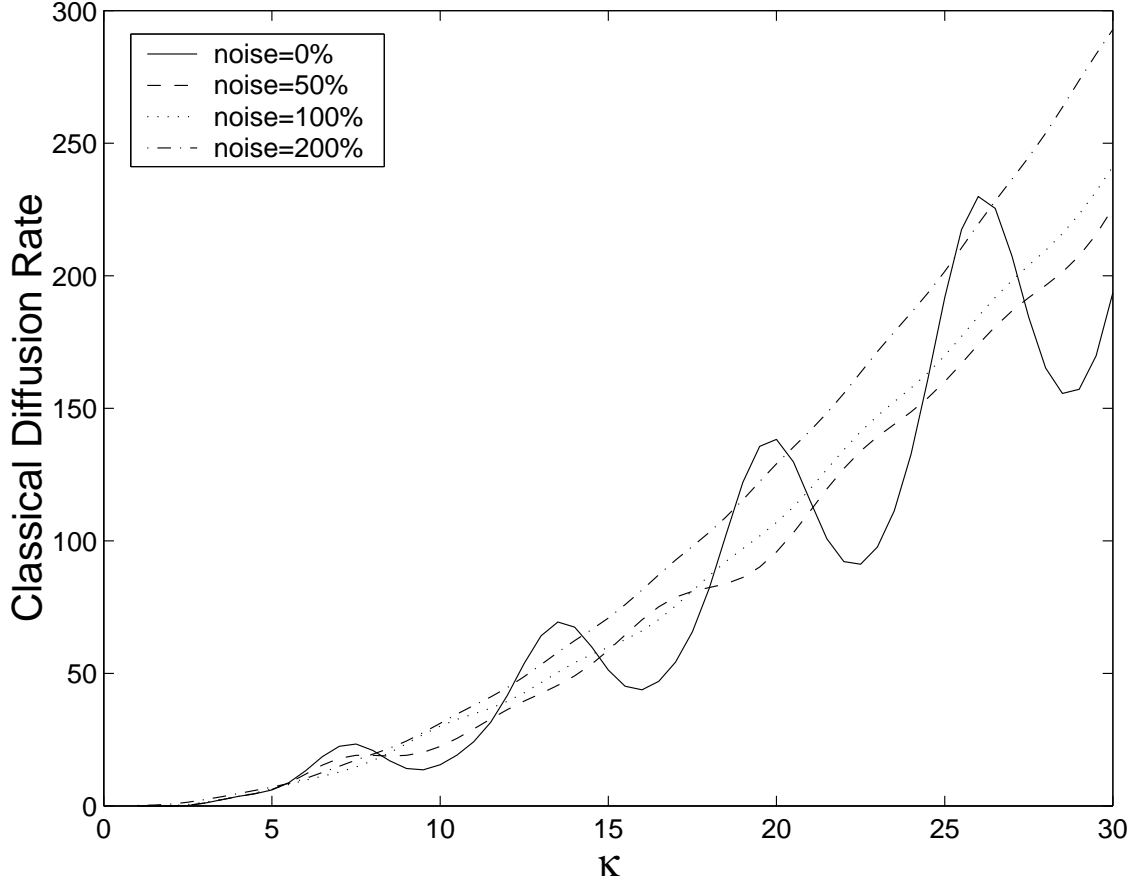


Figure 7.1: Classical diffusion rates for the CKR with amplitude noise, from (7.1), plotted as a function of κ for different levels of noise.

noise(%)	$\kappa = 10$	$\kappa = 11$	$\kappa = 12$	$\kappa = 10$	$\kappa = 11$	$\kappa = 12$
0	16.2 ± 0.1	23.4 ± 0.1	40.2 ± 0.1	15.6	24.2	41.8
10	15.5 ± 0.1	23.4 ± 0.2	39.8 ± 0.4	15.8	24.4	41.4
25	17.0 ± 0.1	25.2 ± 0.4	38.7 ± 0.6	17.3	25.4	39.8
50	22.0 ± 0.4	28.5 ± 0.7	35.6 ± 0.6	22.4	29.1	36.4
100	30.3 ± 0.6	35.7 ± 0.9	40.2 ± 0.7	30.1	34.7	39.5
200	30.9 ± 1.0	36.1 ± 1.1	44.4 ± 1.5	31.2	37.9	44.7

Table 7.1: Table showing classical diffusion rates for varying κ and varying levels of noise, both from (left) numerical simulations of the classical kicked rotor with $\alpha = 0.005$ and (right) from the analytical result (7.1).

We have verified the result given in (7.1) using classical simulations with amplitude noise. The results we obtain generally exhibit good agreement with the analytical result, particularly considering the small discrepancies which already exist between the δ -kicked rotor and the pulse kicked rotor. Some sample results are displayed in table 7.1.

7.3 Initial Quantum Diffusion Rates

Unlike spontaneous emission noise, amplitude noise has significant effects on the structures exhibited by the initial diffusion rates. This is because reasonable amounts of amplitude noise will disrupt correlations on very short timescales, as was shown in the previous section for the case of the classical kicked rotor. By comparison, spontaneous emissions at realisable levels generally disrupt correlations on longer time scales, and so have little effect on early time diffusion.

7.3.1 The Generalised Shepelyansky Formula

As in the case of the classical kicked rotor, we can account for the effects of amplitude noise in our treatment of the correlation functions. In the case of the initial quantum diffusion rate, this results in a generalised version of Shepelyansky's formula, (3.35), given by [51]

$$D_q(\kappa, \bar{k}) = \frac{\kappa^2 + \text{Var}(\Delta\kappa)}{4} + \frac{\kappa^2}{2} (-Q_2(K_q) - Q_1^2(K_q) + Q_2^2(K_q) + Q_3^2(K_q)), \quad (7.3a)$$

$$(7.3b)$$

where

$$Q_i(K_q) = \int_{-\infty}^{\infty} P(\Delta\kappa) J_i[K_q + \delta K_q(\Delta\kappa)] d(\Delta\kappa), \quad (7.3c)$$

and

$$\delta K_q(\Delta\kappa) = \Delta\kappa \frac{\sin(\bar{k}/2)}{\bar{k}/2}. \quad (7.3d)$$

For the case of a uniform noise distribution on the interval $[-\delta\kappa, \delta\kappa]$ this reduces to

$$D_q(\kappa, \bar{k}) = \frac{\kappa^2 + (\delta\kappa)^2/3}{4} + \frac{\kappa^2}{2} (-Q_2(K_q) - Q_1^2(K_q) + Q_2^2(K_q) + Q_3^2(K_q)), \quad (7.4a)$$

$$(7.4b)$$

where

$$Q_i(K_q) = \frac{1}{2\delta\kappa} \frac{\bar{k}/2}{\sin(\bar{k}/2)} \int_{x_{min}}^{x_{max}} J_i(x) dx, \quad (7.4c)$$

with $x_{max} = 2(\kappa + \delta\kappa) \sin(\bar{k}/2)/\bar{k}$ and $x_{min} = 2(\kappa - \delta\kappa) \sin(\bar{k}/2)/\bar{k}$.

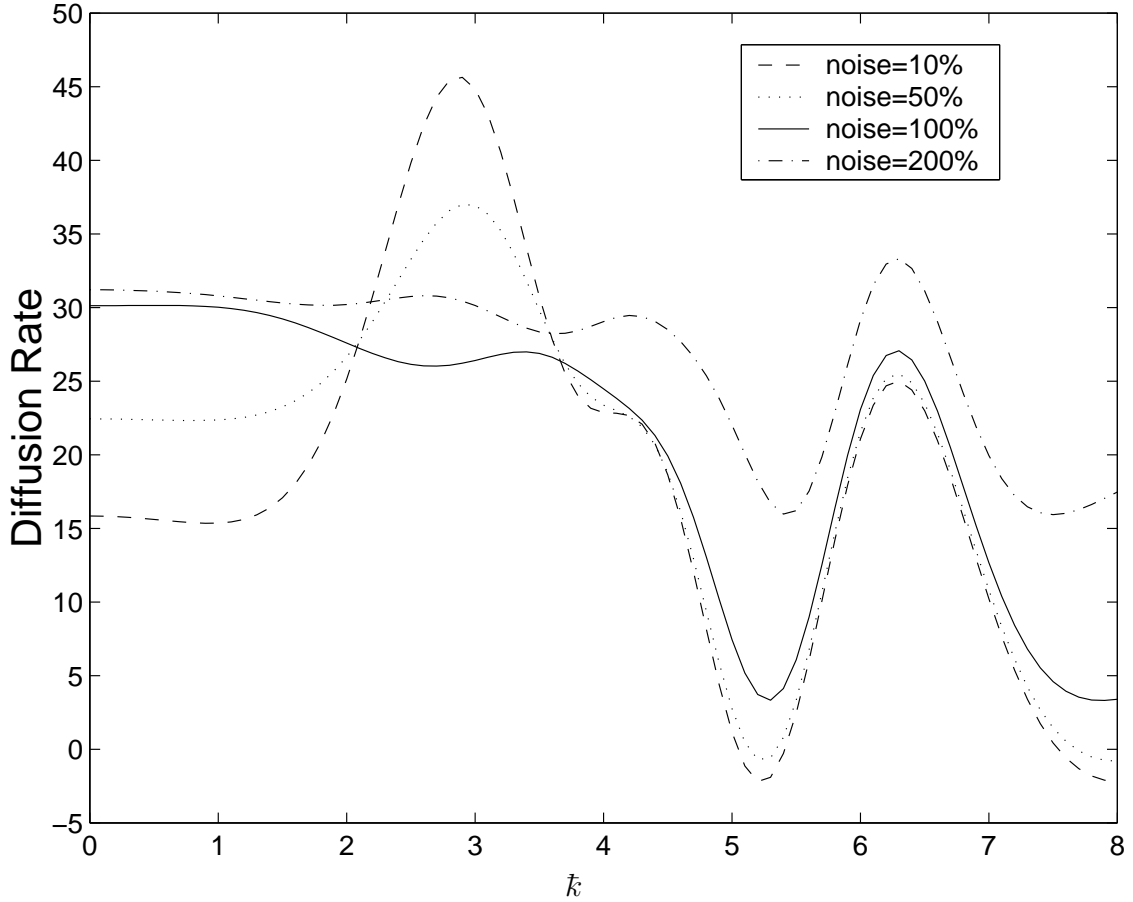


Figure 7.2: Initial quantum diffusion rates as predicted by the modified Shepelyansky formula with the inclusion of amplitude noise, (7.3), for the quantum δ -kicked rotor with $\kappa = 10$.

The diffusion rates predicted by this formula are shown in figures 7.2 and 7.3 with varying levels of noise, and for $\kappa = 10$ and $\kappa = 13$ respectively. We see that the peak structure is unchanged for small amounts of noise, and the system exhibits the same enhanced diffusion peak and quantum resonance peak observed in the system without amplitude noise. However, for larger values of the noise, the quantum correlations that produce the enhanced diffusion peak begin to be destroyed, and for noise=200% we see that the rate is predicted to be very close to the classical rate (with amplitude noise included) up to $\bar{k} \sim 5$. This is a good example of the system being driven back to classical behaviour by destruction of quantum correlations over short time intervals. For $\bar{k} > 5$ we see a return to the quantum resonance peak structure, which only starts to be smoothed over for noise=200%. This indicates for less macroscopic systems (in terms of their total action), we require a higher level of noise to drive the system back to classical behaviour.

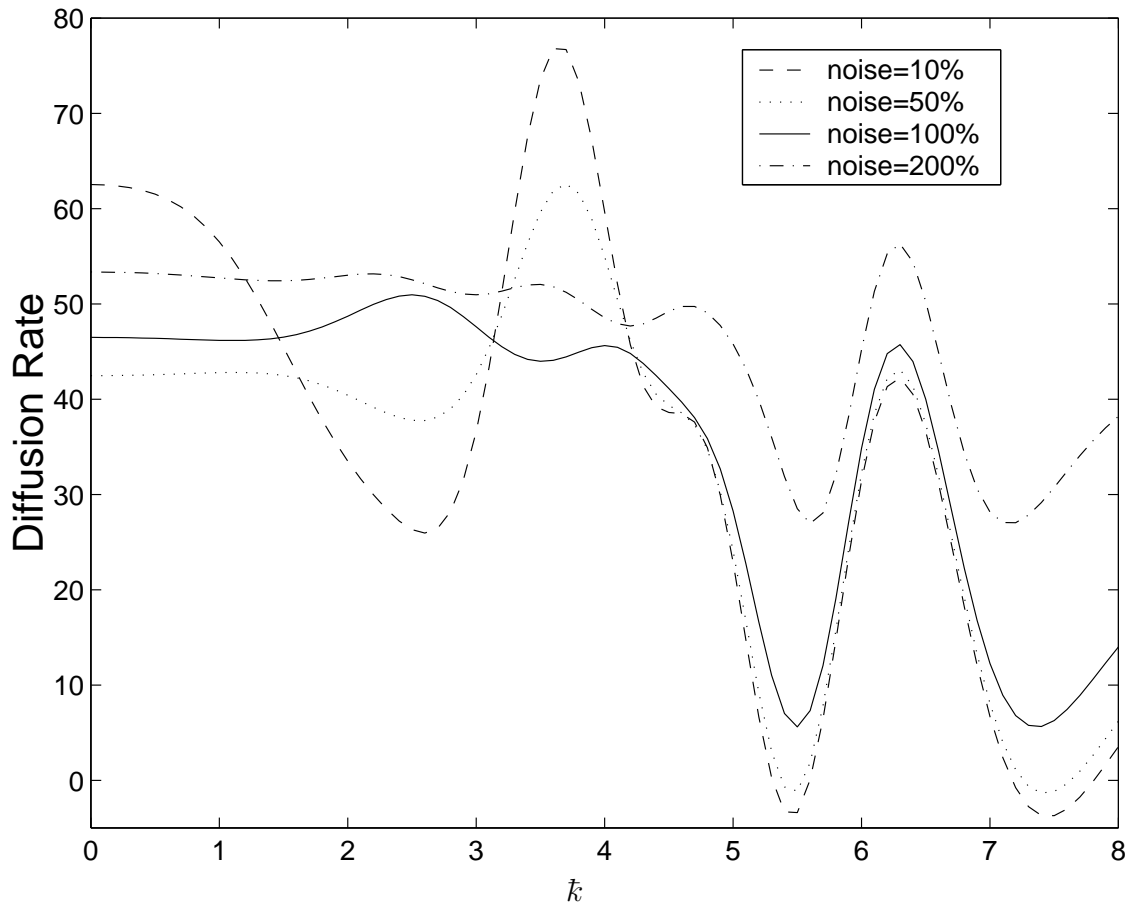


Figure 7.3: Initial quantum diffusion rates as predicted by the modified Shepelyansky formula with the inclusion of amplitude noise, (7.3), for the quantum δ -kicked rotor with $\kappa = 13$.

7.3.2 Simulation Results

Figures 7.4 and 7.5 show comparisons of the simulated initial quantum diffusion rates with the values predicted in (7.3) for varying values of noise and κ respectively. As in chapter 6, we obtain the simulation results by averaging over the diffusion rates $D(2 - 5)$. As with the results without amplitude noise (shown in section 6.3.2) the agreement is generally very good. There is some discrepancy again related to the non-existent shoulder on the right hand side of our main enhanced diffusion peak, but the trends of magnitude variation and peak shifting as noise and κ are varied are well predicted by the analytical result. Most discrepancies arise from a combination of the approximations in the derivation of the generalised Shepelyansky formula (7.3) equivalent to those made in deriving the original Shepelyansky formula, (3.35), and our choice to average over $D(2 - 5)$, as is described in section 6.3.2.

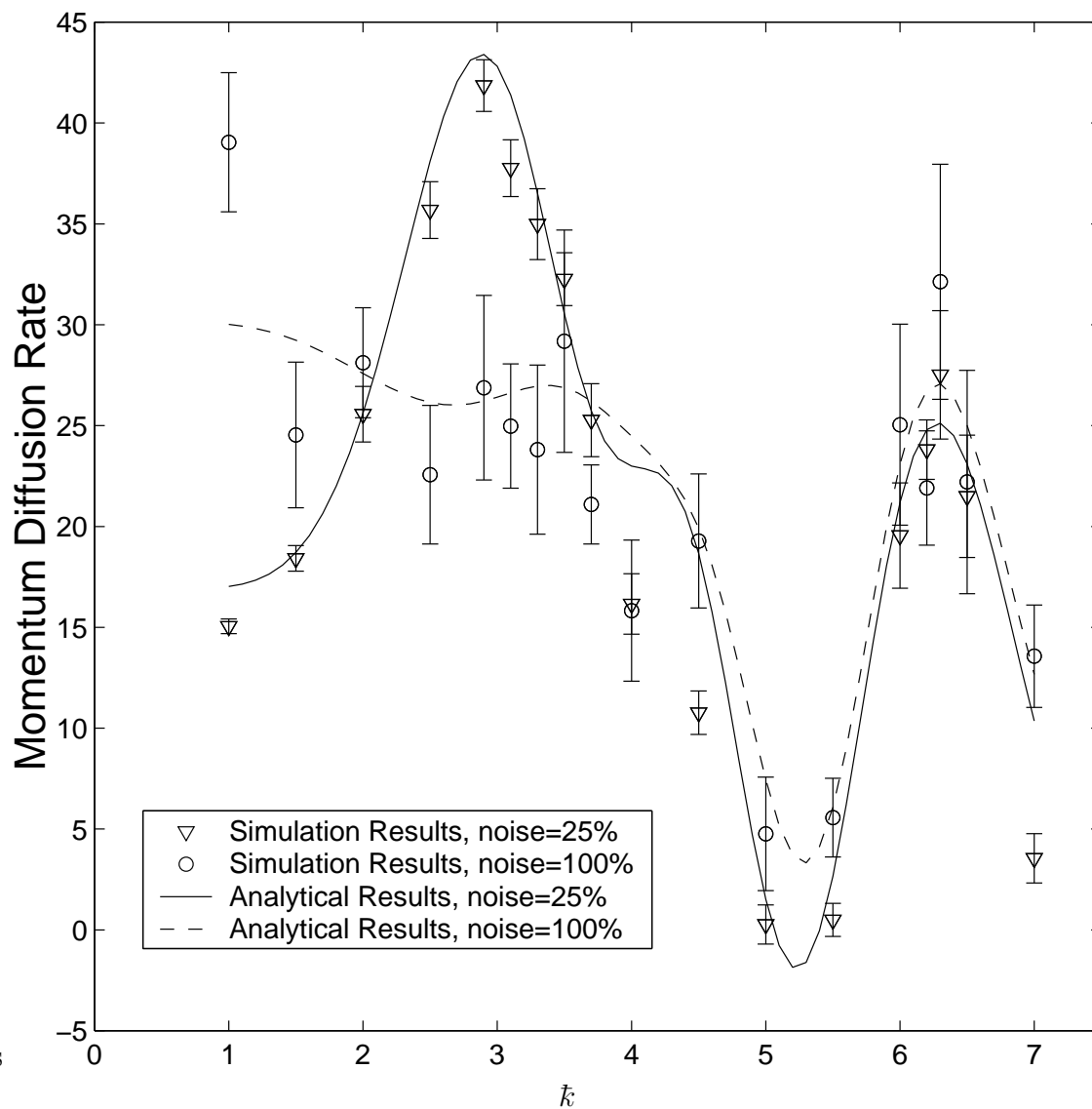


Figure 7.4: Comparison of initial quantum diffusion rates computed from simulation results with those predicted by the modified Shepelyansky formula with the inclusion of amplitude noise, (7.3), for the quantum δ -kicked rotor with $\kappa = 10$.

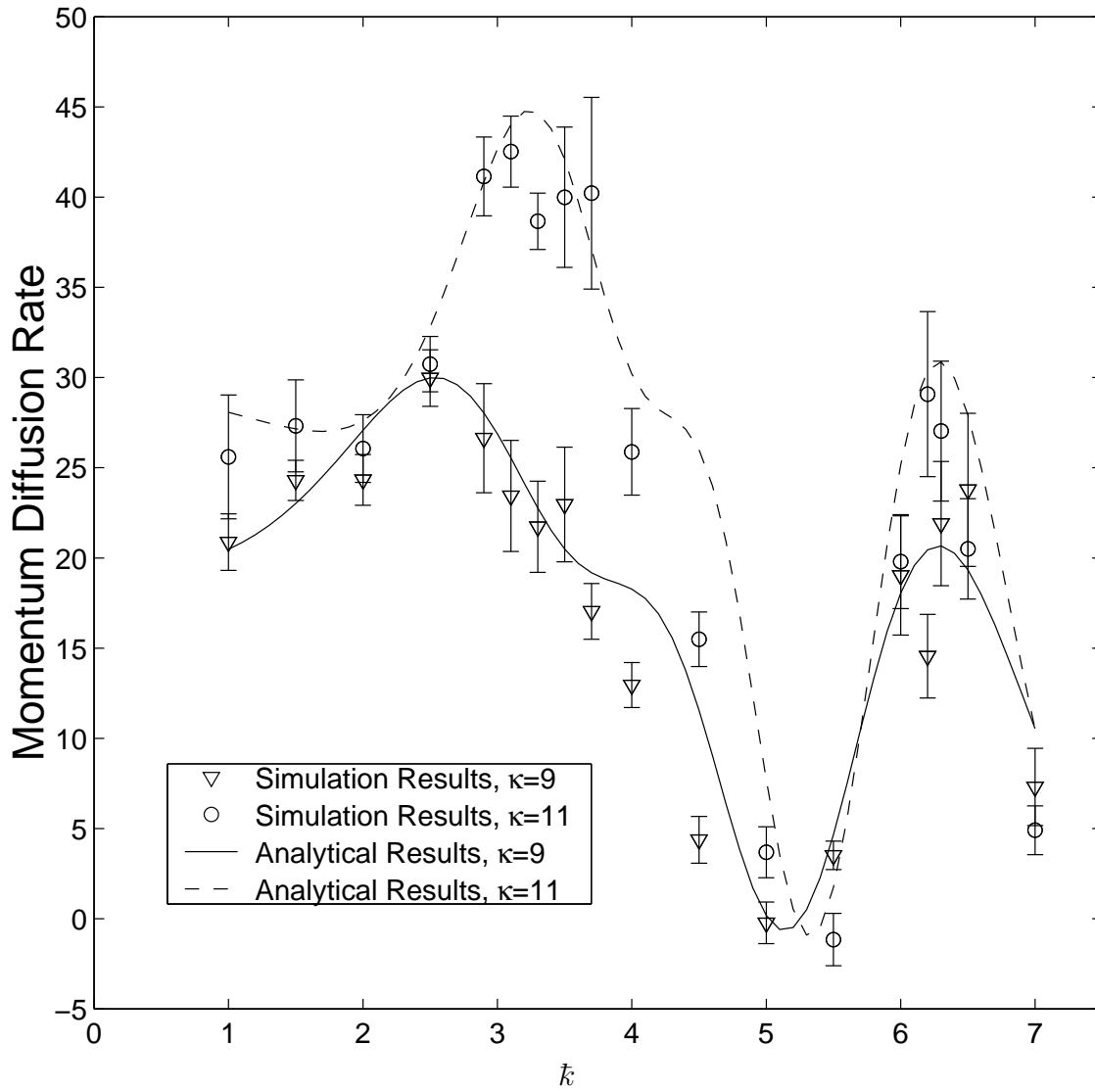


Figure 7.5: Comparison of initial quantum diffusion rates computed from simulation results with those predicted by the modified Shepelyansky formula with the inclusion of amplitude noise, (7.3), for the quantum δ -kicked rotor with noise=50%.

7.4 Late Time Diffusion Rates

7.4.1 Simulation Results

As described in section 7.1, the destruction of long time correlations by amplitude noise prevents the system from settling down into a localised state. This is well illustrated in figure 7.6, where we show simulation results for the late time diffusion rates in a system with varying levels of amplitude noise (this is computed in the same way as the late time rates for the system with spontaneous emission noise, i.e., we calculate the average diffusion rate after the system has settled into its quasi steady-state regime). We see that for low values of noise (around noise=10%), the diffusion rates are correspondingly low. As we increase the level of noise, the results return, especially for lower values of \tilde{k} , towards the quasilinear behaviour we observed for the initial quantum diffusion rates with noise=200%. For $\tilde{k} < 5$ and for noise < 100% we observe the same enhanced diffusion peak structure that we observed in the initial quantum diffusion rates. This enhanced diffusion peak appears to be washed out for noise=100%, as occurred in the initial quantum diffusion rates for noise=200%. There is preliminary experimental evidence of some of these features for the structures in unscaled units [60], which is displayed in chapter 8. However, we notice that the effects of amplitude noise on the correlations is such that the quantum resonance peak, which is present in the initial quantum diffusion rates for both types of noise and in the late time diffusion rates for spontaneous emission noise is washed out in the late time diffusion rates generated by amplitude noise. This is a particularly striking feature, and appears to be related to the relative strength with which amplitude noise diminishes correlations on different time scales.

Figure 7.7 shows the familiar shifting and scaling of the enhanced diffusion peak as we vary κ . This also confirms the lack of a quantum resonance peak at $\tilde{k} = 2\pi$ for all of the simulated κ values with 50% amplitude noise.

7.4.2 Towards an Analytical Theory

It would be very useful to have a general analytical theory of the diffusion produced in the late time regime by the introduction of amplitude noise. However, it is unclear how such a theory could be simply formulated. In the case of small levels of amplitude noise we can make some progress, though, because we expect that Cohen's perturbation theory result [3], which was discussed briefly in section 6.5.1, should be applicable.

Cohen's result comes from the addition of noise to the quantum standard map in such a way that the one step propagation operator becomes

$$\hat{U} = e^{(i/\tilde{k})\tilde{f}(t)\hat{X}} \exp[-i\hat{p}^2/(2\tilde{k})] \exp[-i\kappa \cos(\hat{\phi})/\tilde{k}], \quad (7.5)$$

for some operator \hat{X} , and a random variable $\tilde{f}(t)$ with $\langle \tilde{f}(t) \rangle = 0$ and $\langle \tilde{f}(t')\tilde{f}(t) \rangle = \nu(t-t')$. To represent amplitude noise we select $\hat{X} = \kappa \cos(\hat{x})$ and we also make the approximation that $\nu(t'-t) = a\delta(t'-t)$ where $a = \langle \tilde{f}^2(t) \rangle$.

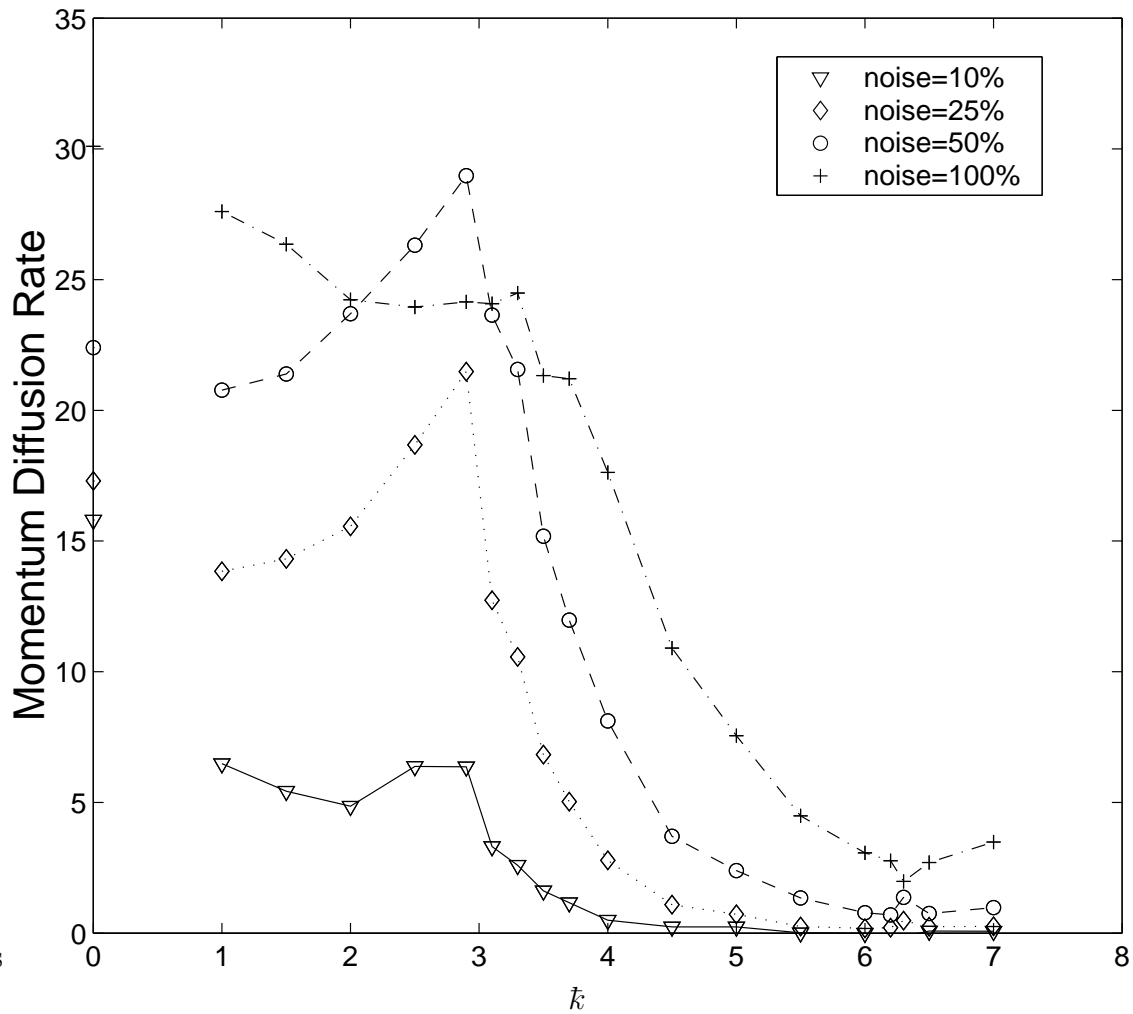


Figure 7.6: Late time diffusion rates from simulation results for the quantum kicked rotor with $\kappa = 10$, $\alpha = 0.005$, and varying levels of amplitude noise.

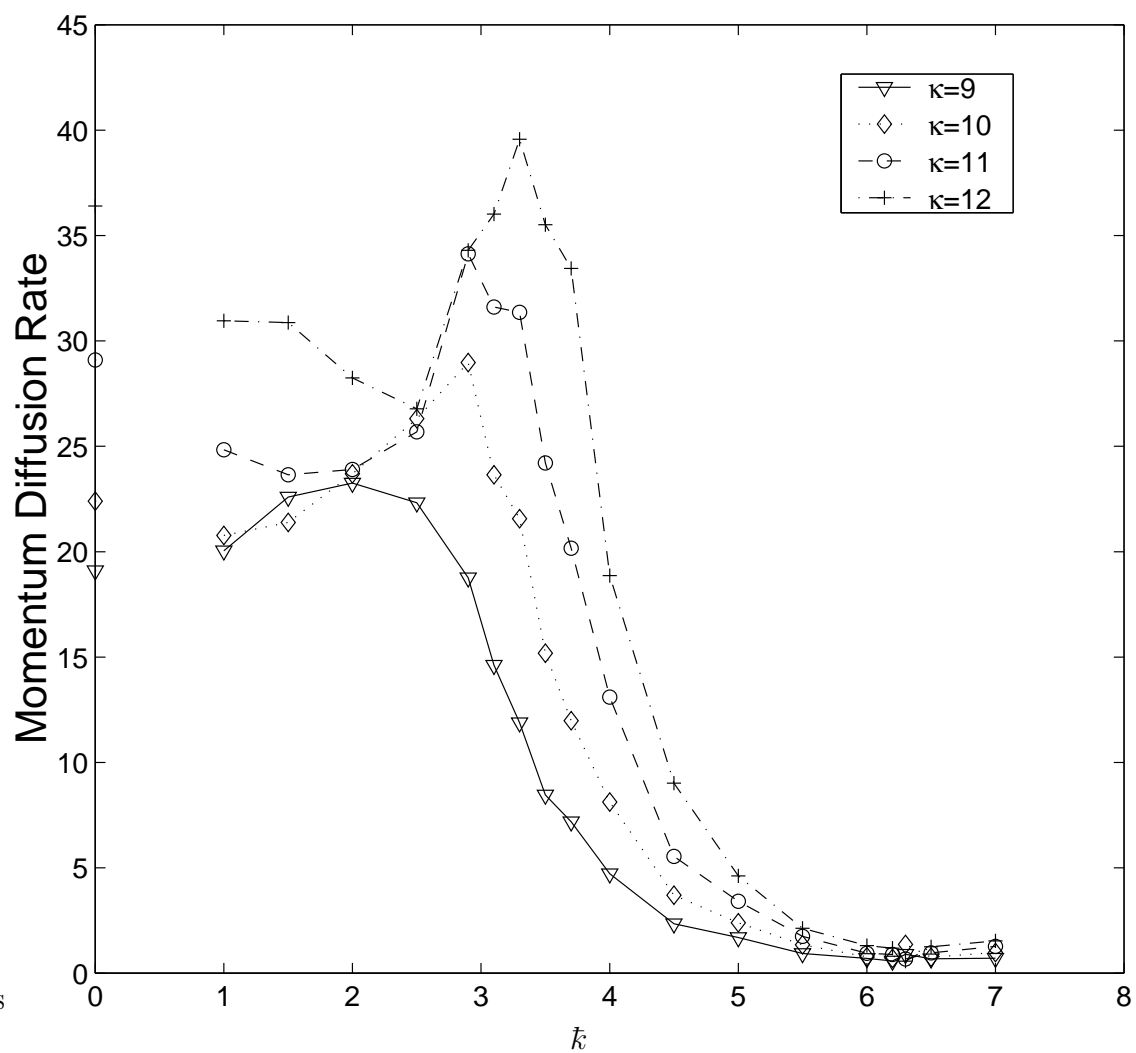


Figure 7.7: Late time diffusion rates from simulation results for the quantum kicked rotor with amplitude noise=50%, $\alpha = 0.005$, and varying values of κ .

Cohen then derives the result, as described in section 6.5.1, that $D = \sum_{\tau=0}^{\infty} \dot{P}(\tau) \tilde{D}_0(\tau)$, having shown that the discrete derivative, $\dot{P}(t)$, of the probability that a transition between quasienergy eigenstates has occurred after a time t is given by

$$\dot{P}(t) = \frac{1}{\hbar^2} \sum_{\tau=-t}^t C_X(\tau) \Phi(\tau; t). \quad (7.6)$$

In this formula,

$$C_X(t) = \langle \hat{X}(t) \hat{X}(0) \rangle - \langle \hat{X}(t) \rangle \langle \hat{X}(0) \rangle \quad (7.7)$$

$$= \langle \hat{X}(t) \hat{X}(0) \rangle - \langle \hat{X} \rangle^2 \quad (7.8)$$

$$= \kappa^2 \langle \cos(\hat{x}(t)) \cos(\hat{x}(0)) \rangle - \kappa^2 \langle \cos(\hat{x}) \rangle^2, \quad (7.9)$$

and $\Phi(\tau; t) = \Phi(t'', t')$ where $\tau = t'' - t'$, $t = \max(t', t'')$ and

$$\Phi(t, t') = \sum_{\tau=0}^{t'-1} \sum_{\tau'=0}^{t''-1} \nu(\tau - \tau') \quad (7.10)$$

$$= a \sum_{\tau=0}^{t'-1} \sum_{\tau'=0}^{t''-1} \delta(\tau - \tau') \quad (7.11)$$

$$= a \min(t', t''), \quad (7.12)$$

so that

$$\Phi(\tau; t) = a(t - |\tau|). \quad (7.13)$$

Thus,

$$\dot{P}(t) = \frac{a}{\hbar^2} \sum_{\tau=-t}^t C_X(\tau) (t - |\tau|) \quad (7.14)$$

and

$$\tilde{D}_{\infty} = \frac{2a}{\hbar} \sum_{t=1}^{\infty} \tilde{D}_0(t) \sum_{\tau=1}^t C_X(t) (t - \tau). \quad (7.15)$$

Unfortunately, it is not as easy to compare the results from this formula with simulation results for amplitude noise as it was for the formula for late time diffusion rates generated by spontaneous emission noise that was given in section 6.5.1. This is primarily because the cosine correlation functions must be determined numerically, which involves taking a numerical derivative of diffusion rates found from iterations of the quantum standard map. Numerical instabilities are introduced in this procedure, particularly when the diffusion rates become small as the system settles into a localised state. This causes difficult problems when we try to choose at which point we

will truncate the series. In addition, it is very difficult to quantify for what level of amplitude noise the perturbation theory results are appropriate. As yet, no quantitative match has been found between (7.15) and simulation results for the late time diffusion rate with amplitude noise. Some preliminary numerical investigation has suggested, however, that near the quantum resonance, where $D(t)$ exhibits decaying oscillations, the multiplication of this term with oscillating values of $\dot{P}(t)$ with a different phase may cause the diffusion rates calculated from the series to be zero. This is a possible explanation as to why the diffusion rates are zero near the quantum resonance peak in this late time regime when amplitude noise is applied.

7.5 Mixtures of Two Types of Noise

In laboratory situations we will always have both amplitude noise and spontaneous emission noise present to some degree, whether or not they are deliberately introduced. Thus, it is important to consider what structures are produced when the two forms of noise are combined. This is made particularly interesting by the distinct features exhibited in the late time rates for the two types of noise. For amplitude noise we observe no peak at the quantum resonances, while for spontaneous emission noise (on physically realisable levels, i.e., without creating sufficient excited state population that we lose the kicked rotor Hamiltonian altogether) such a peak does exist, and we observe a well defined enhanced diffusion peak (for $k < 5$) which we cannot wash out by adding allowed amounts of noise to the system.

These differences come from the different effects each type of noise has on correlations depending on the time scale involved. Spontaneous emission noise has little effect on short time correlations, but destroys long term correlations almost entirely because of the loss of quantum coherence when the first spontaneous emission event occurs. Amplitude noise, meanwhile, affects correlations on all time scales, and for sufficiently strong levels of noise can almost entirely destroy even short time correlations. It is thus not surprising that the interaction between the two forms of noise can produce combinations of interesting structures, particularly in the late time diffusion rates. For initial quantum diffusion rates we simply find that the same structures and quantitative values occur in the diffusion rates as we obtain with whatever level of amplitude noise we have chosen. The level of spontaneous emission noise does not affect these rates, again because they depend only on correlations over a small number of kicks (again note that we restrict ourselves to $\eta \leq 20\%$ to maintain the approximations required for the derivation of the kicked rotor Hamiltonian).

Figure 7.8 shows the behaviour in the late time diffusion rates as a function of k for a fixed level of amplitude noise (noise=50%) and varying levels of spontaneous emission noise. We see that the structure in the enhanced diffusion peak remains very similar (if anything there is a slight increase in the magnitude of the peak), but that the quantum resonance peak, which was non-existent for $\eta = 0\%$, appears for small amounts of spontaneous emission noise and increases in magnitude as η is

increased. This comes from the ability of spontaneous emission noise to destroy long time correlations entirely whilst leaving shorter time correlations (which have already been modified by the inclusion of amplitude noise) intact. This results here in the early time rates with amplitude noise being “locked in” much in the same way as the early time rates in the noiseless system were seen to be “locked in” by spontaneous emissions (see section 6.5.1). The enhanced diffusion peak does not change significantly because it is very similar in the initial and late time diffusion regimes with amplitude noise anyway, but the quantum resonance peak, which is present in the initial quantum diffusion rates but not the late time diffusion rates for amplitude noise, begins to appear as the only significant correlations become those occurring on shorter time scales. This type of behaviour has been observed experimentally in the context of an investigation of the quantum resonance peak in unscaled units by d’Arcy *et al.* [32], and can also be seen in the results presented in chapter 8.

Figure 7.9 shows the late time diffusion rates as a function of \bar{k} for $\eta = 10\%$ and varying levels of amplitude noise. Here, the correlations are already strongly diminished on longer term time scales, and so naturally we observe a significant quantum resonance peak for all of our values of the noise parameter. We do observe, however, the effects of amplitude noise on the short time correlations. This means that the structure of the enhanced diffusion peak near $\bar{k} = 3$ changes as the level of amplitude noise is increased, and as we reach values of noise near 200% the peak is entirely washed out (the rate tends, as with the initial quantum diffusion rate towards the same value as the classical rate), as we have previously observed in both the initial quantum diffusion rates and the late time diffusion rates with amplitude noise. Again, there is experimental evidence for this phenomenon occurring in unscaled units [60], which is displayed in chapter 8.

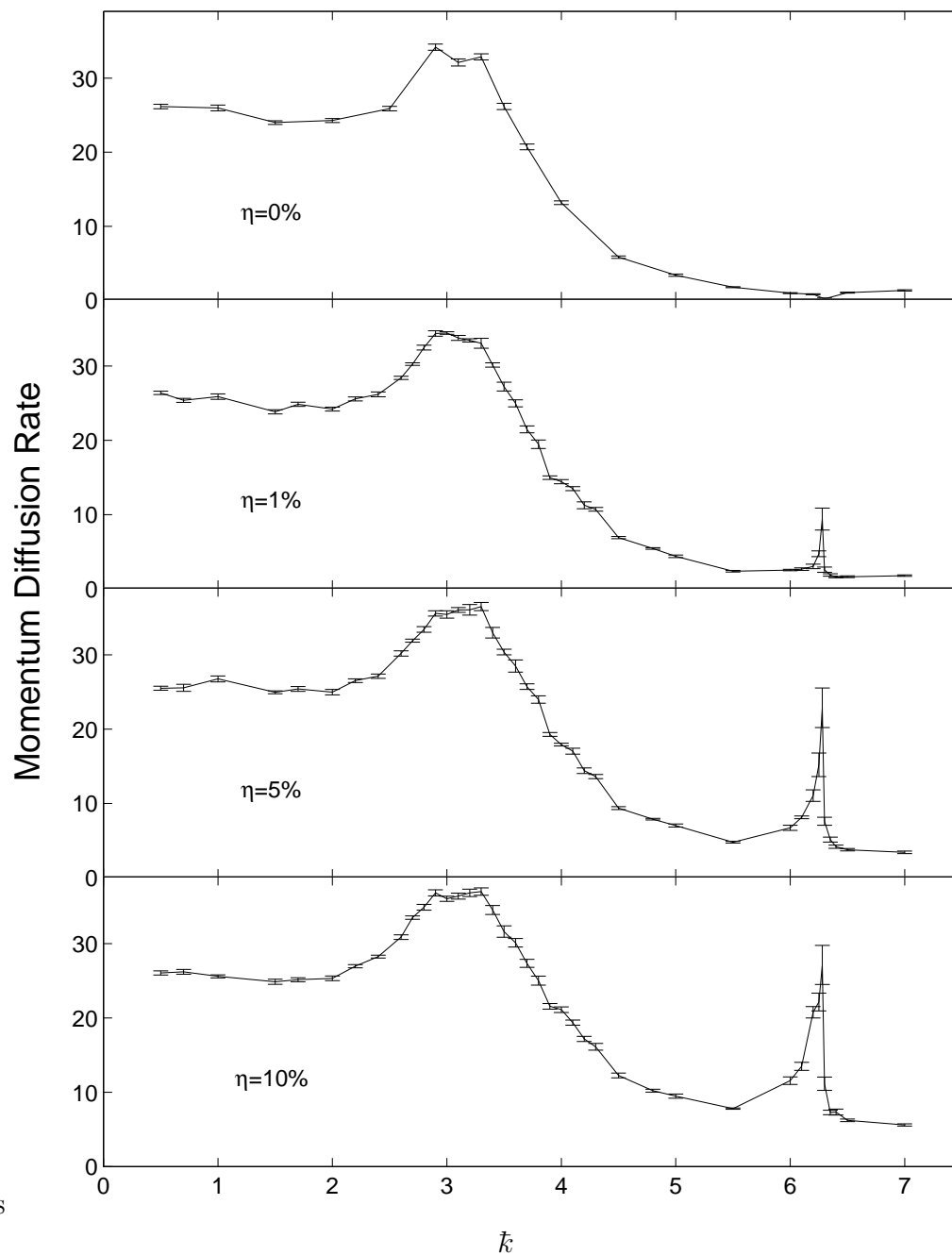


Figure 7.8: Simulation results of late time diffusion rates with a combination of spontaneous emission noise and amplitude noise, for the quantum kicked rotor with $\alpha = 0.005$, $\kappa = 11$, and amplitude noise=50%, with varying values of η .

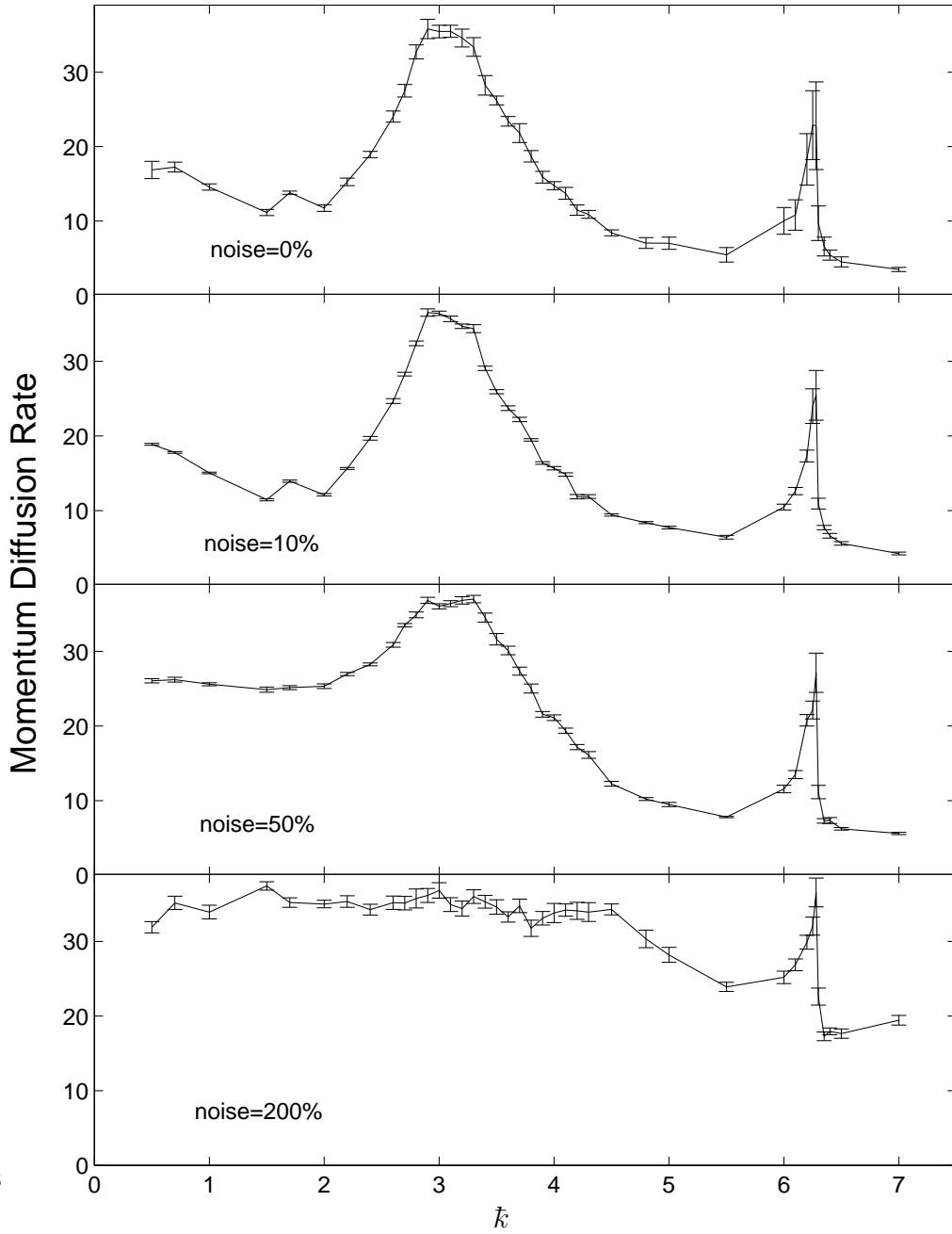


Figure 7.9: Simulation results of late time diffusion rates with a combination of spontaneous emission noise and amplitude noise, for the quantum kicked rotor with $\alpha = 0.005$, $\kappa = 11$, and $\eta=10\%$, with varying levels of amplitude noise.

Chapter 8

Diffusion Structures in Physical Units

8.1 Introduction

It has been common in previous experimental studies of the atom optics kicked rotor to express results obtained for a particular value of \bar{k} in physical momentum units, i.e., in terms of multiples of twice the photon recoil momentum, $p/(2\hbar k_l)$, instead of in the scaled units of the variable ρ (see section 4.2). This distinction is unimportant when we do not want to compare between results for different values of \bar{k} , because the conversion factor between ρ and p depends only on \bar{k} ($\rho/\bar{k} = p/(2\hbar k_l)$). However, in our study so far it has been important to maintain consistency by choosing the units of ρ as our momentum units. This is because ρ is the momentum variable appearing in our Hamiltonian and the conversion factor between ρ and p scales with \bar{k} , thus introducing an unwanted factor into our units when we compare results for systems with different values of \bar{k} .

Another quite interesting approach to choosing units to describe the kicked rotor has been taken recently in various experimental studies [31, 32, 60, 61]. This approach arises out of the fact that in order to hold κ and η constant as we vary \bar{k} , we must change both the power and the detuning of the kicking laser as we move from one point to the next. The reason for this is that in the original scaling, we set $\kappa = 4\Omega_{eff}\omega_R T\tau_p = \Omega_{eff}\tau_p\bar{k}/2$, so that Ω_{eff} must be changed to hold κ constant whenever \bar{k} is varied. Similarly, as we vary T to alter \bar{k} , τ_p must also be adjusted to hold α constant. This is complicated experimentally, and while our scaled units provide a convenient parameter (\bar{k}) to quantify the quantum-classical transition as a system is made more macroscopic (we have made use of this at length throughout the rest of this thesis), they make for difficult experiments and are not entirely compatible with an atom optics view of the quantum resonance peak [32]. Working from an atom optics based viewpoint, a group from the University of Oxford used a set of units and an approach to the kicked rotor system based on the original unscaled Hamiltonian, (4.6), in which the physical potential well depth and the actual pulse duration were

held constant rather than κ and α [31, 32]. The units they used have been applied more recently by the experimental group at Auckland, who have studied the effects of adding amplitude noise to the system and of changing the physical potential well depth [60, 61].

This chapter begins with a discussion of the quantities involved in each set of units, and then looks at all of the diffusion resonances observed using the physical system of units and how they relate to the diffusion resonances observed in the system with scaled units. We present a version of Shepelyansky’s formula for the scaled units, as well as a combination of simulation results and recent experimental results for systems with spontaneous emission noise and amplitude noise.

8.2 Physical Units vs. Scaled Units

In the system of unscaled or “physical” units, all units and quantities are based on the Hamiltonian from equation (4.6),

$$\hat{H} = \frac{\hat{p}^2}{2m} - \frac{\hbar\Omega_{eff}}{2} \cos(2k_l\hat{x}) \sum_{n=0}^{\infty} f(t - nT).$$

The kick strength in this system for a rectangular pulse-kicked rotor is denoted ϕ_d , and is given by $\phi_d = \Omega_{eff}\tau_p/2$ where τ_p is the pulse duration, which is held constant instead of α . Momentum is measured in units of the physical momentum p rather than ρ and is usually expressed in multiples of either one or two photon recoils. Our primary interest is in the structure of diffusion resonances as T , the cycle period, is varied. This roughly corresponds to the same resonance structure observed as \bar{k} is varied in the scaled units, and this correspondence is described in more detail in section 8.3.

Table 8.1 gives a comparison between important quantities in scaled and physical units, and states the various conversion factors between parameters of the two systems.

Quantity	Scaled Units	Physical Units	Relationship
Kick Strength	κ	ϕ_d	$\kappa = 8\phi_d\omega_R T = \phi_d\bar{k}$
Pulse Duration	α	τ_p	$\alpha = \tau_p/T = 8\omega_R\tau_p/\bar{k}$
Momentum	ρ	p	$\rho = \bar{k}p/(2\hbar k_l)$
Time	τ	t	$\tau = t/T$
Energy	$\rho^2/2$	$[p/(2\hbar k_l)]^2/2$	$\rho^2/2 = \bar{k}^2[p/(2\hbar k_l)]^2/2$
Varied Parameter	\bar{k}	T	$\bar{k} = 8\omega_R T$

Table 8.1: Comparison of and conversions between quantities in scaled units and physical units. Note that ω_R and k_l are transition frequency dependent. The Auckland group use the Caesium D2 line, so that $\bar{k} = 2\pi \implies T = 60.4\mu\text{s}$, whereas the Oxford group use the Caesium D1 line, so that $\bar{k} = 2\pi \implies T = 66.7\mu\text{s}$.

8.3 Initial Diffusion Rates

We expect that the diffusion resonance structures in both the initial quantum diffusion rates and the late time diffusion rates (qualitatively, but not quantitatively in the second case) will be well approximated by Shepelyansky's formula, as we observed for the equivalent structures in scaled units. To do this, we divide the diffusion rate by \bar{k}^2 to convert to the physical energy units, and then we substitute into (3.35) the equivalent expressions for κ and \bar{k} in physical units. The resulting expression is

$$D_q = \frac{\phi_d^2}{2} \left(\frac{1}{2} - J_2(K_p) - J_1^2(K_p) + J_2^2(K_p) + J_3^2(K_p) \right), \quad (8.1a)$$

with

$$K_p = 2\phi_d \sin(4\omega_R T). \quad (8.1b)$$

This formula is plotted as a function of T for various values of ϕ_d in figures 8.1 and 8.2. The most immediately noticeable feature is that the diffusion rates are periodic in T with period $\pi/(4\omega_R)$. This arises because the only occurrence of T is inside the sine function as part of the Bessel function argument K_p , in contrast with \bar{k} in the scaled expression, which appears in the form $\sin(\bar{k}/2)/\bar{k}$. Similarly, we observe a reflection symmetry within the periodic structure at odd multiples of $\pi/(8\omega_R T)$.

At multiples of $T = 60.4\mu\text{s}$ we observe quantum resonance peaks, which result from the same phenomenon as the quantum resonance peaks in scaled units (for the Caesium D2 transition, $\bar{k} = 2\pi \leftrightarrow T = 60.4\mu\text{s}$). In between the resonance peaks we observe more diffusion resonances, which are analogous to the enhanced diffusion peaks we observed in scaled units. As ϕ_d is increased, the Bessel functions oscillate more frequently during one period of the function $\sin(4\omega_R T)$, and so we observe the formation of extra resonance peaks. These form just after the value at $T = 30.2\mu\text{s}$ changes from being a local minimum to a local maximum or vice versa (i.e., when $\phi_d = n\pi/2$ for integer n). When the value changes from a local minimum to a local maximum (which occurs for $\phi_d = (n + 1/2)\pi$ with integer n), the new peak is the newly formed local maximum at $T = 30.2\mu\text{s}$ itself. When the value changes from a local maximum to a local minimum (which happens when $\phi_d = n\pi$ for integer n), the original peak splits into two, and the resulting peaks shift away from $T = 30.2\mu\text{s}$ (maintaining reflection symmetry) as ϕ_d is increased.

The formation of extra peaks here is a little analogous to the formation of extra enhanced diffusion resonances for $\bar{k} < 2\pi$ in the scaled units. In the physical units, however, the structure is not complicated by the factor of $1/\bar{k}$ in the argument of the Bessel functions.

One other interesting point to note is that the diffusion rates here increase as ϕ_d^2 . This is the same dependence as the mean diffusion rates exhibit as a function of κ in the scaled units, and represents a significant increase in diffusion rates, often for relatively small changes in the intensity of the kicking beam.

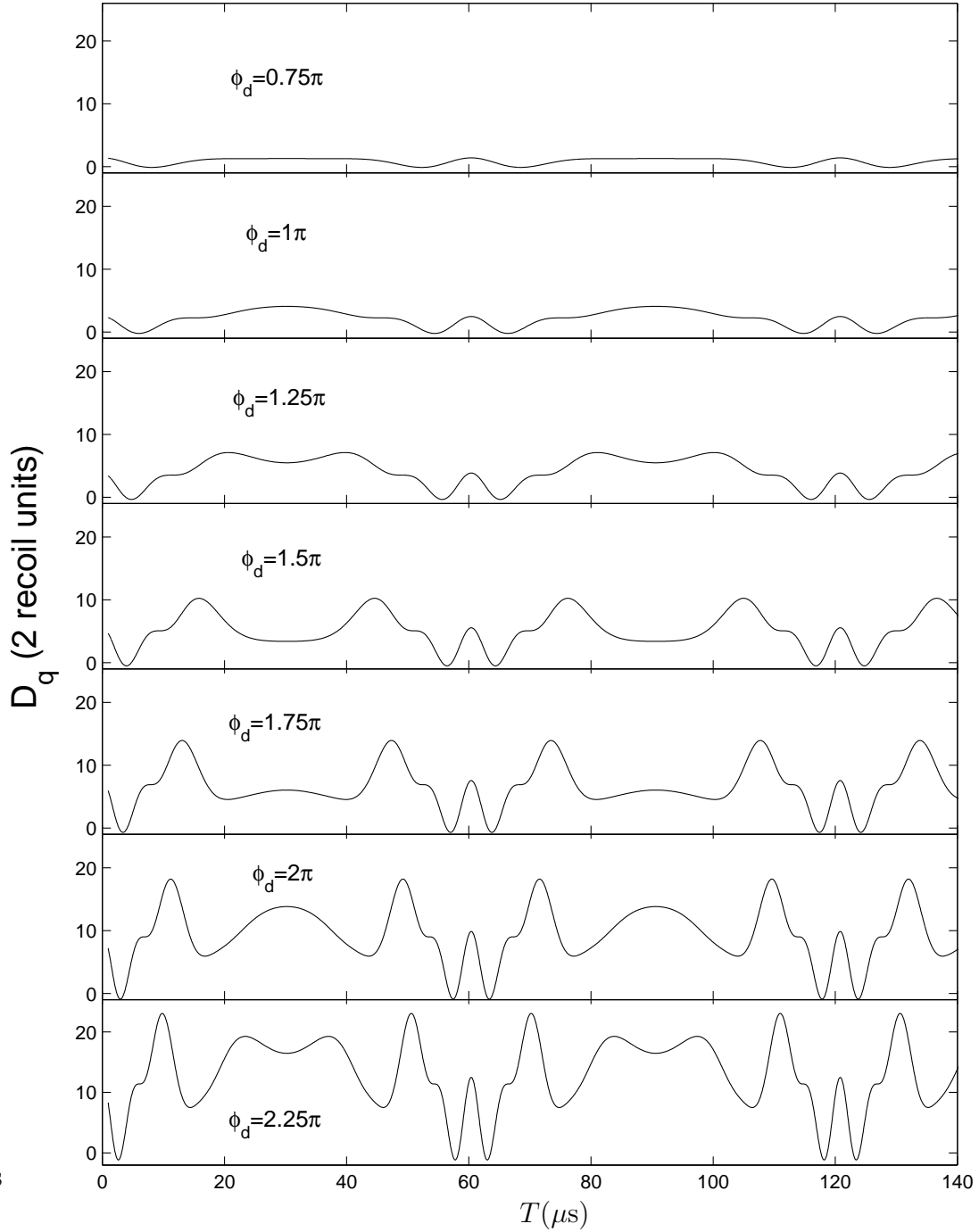


Figure 8.1: Initial quantum diffusion rates as a function of pulse separation, T , as predicted for physical units by Shepelyansky's formula (8.1) for the δ -kicked rotor. We use ω_R from the Caesium D2 transition, so that the first quantum resonance occurs at $T = 60.4\mu\text{s}$, and $\phi_d \in [0.75\pi, 2.25\pi]$

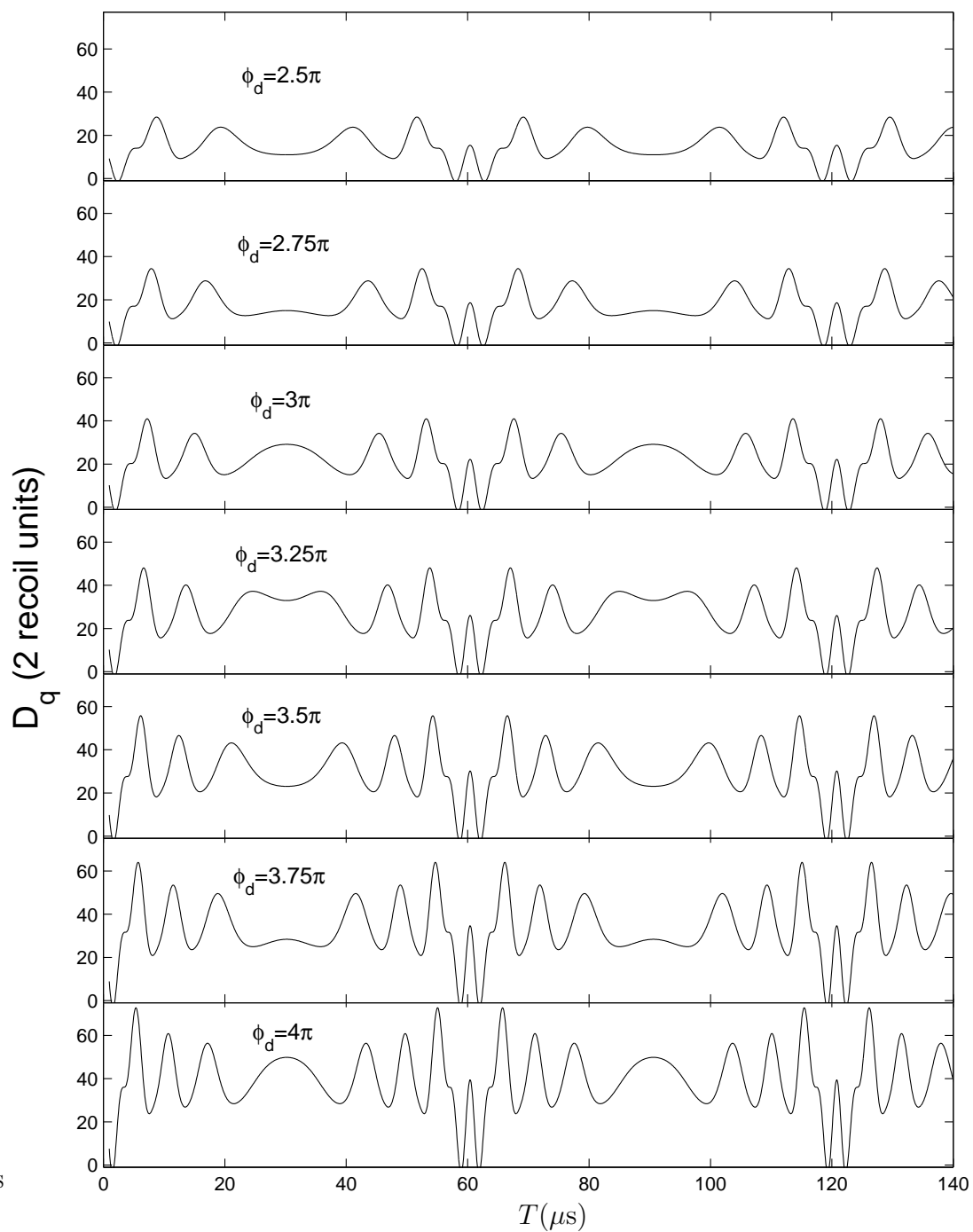


Figure 8.2: Initial quantum diffusion rates as a function of pulse separation, T , as predicted for physical units by Shepelyansky's formula (8.1) for the δ -kicked rotor. We use ω_R from the Caesium D2 transition, so that the first quantum resonance occurs at $T = 60.4\mu\text{s}$, and $\phi_d \in [2.5\pi, 4\pi]$

8.4 Classical Comparison

In the system of scaled units it is straight forward to relate our quantum system to a corresponding classical system by taking the limit as $\hbar \rightarrow 0$. In the physical units we have no such obvious comparison, and the only suitable way is to examine the system parameters for each configuration of the quantum system (i.e., at each point on each graph), and decide what the rate will be in a classical system with the same parameters. That is, we reduce the quantum system to its corresponding classical system at each point on our diffusion curves and make the comparison pointwise.

The simplest way to perform this calculation is to compute the scaled parameters for each point, calculate the diffusion rates in the scaled units, and then convert the diffusion rate back into the physical units. Doing this yields the classical equivalent of (8.1), i.e.,

$$D_{class} = \frac{\phi_d^2}{2} \left(\frac{1}{2} - J_2(8\phi_d\omega_R T) - J_1^2(8\phi_d\omega_R T) + J_2^2(8\phi_d\omega_R T) + J_3^2(8\phi_d\omega_R T) \right), \quad (8.2)$$

for the diffusion rate in units of 2 recoil energies. The values from this formula are plotted in figure 8.3 for various values of ϕ_d , and are overlaid on top of the initial quantum diffusion rates for the same parameter values. The classical rates exhibit oscillations as a function of T with maxima and minima which change with varying ϕ_d , and settle gradually for $T > 10$ towards a value of $\phi_d^2/4$. It is interesting to note that the highest resonance peaks for the initial quantum diffusion rates are higher than the corresponding classical rates, as we observed for these diffusion rates throughout chapter 6.

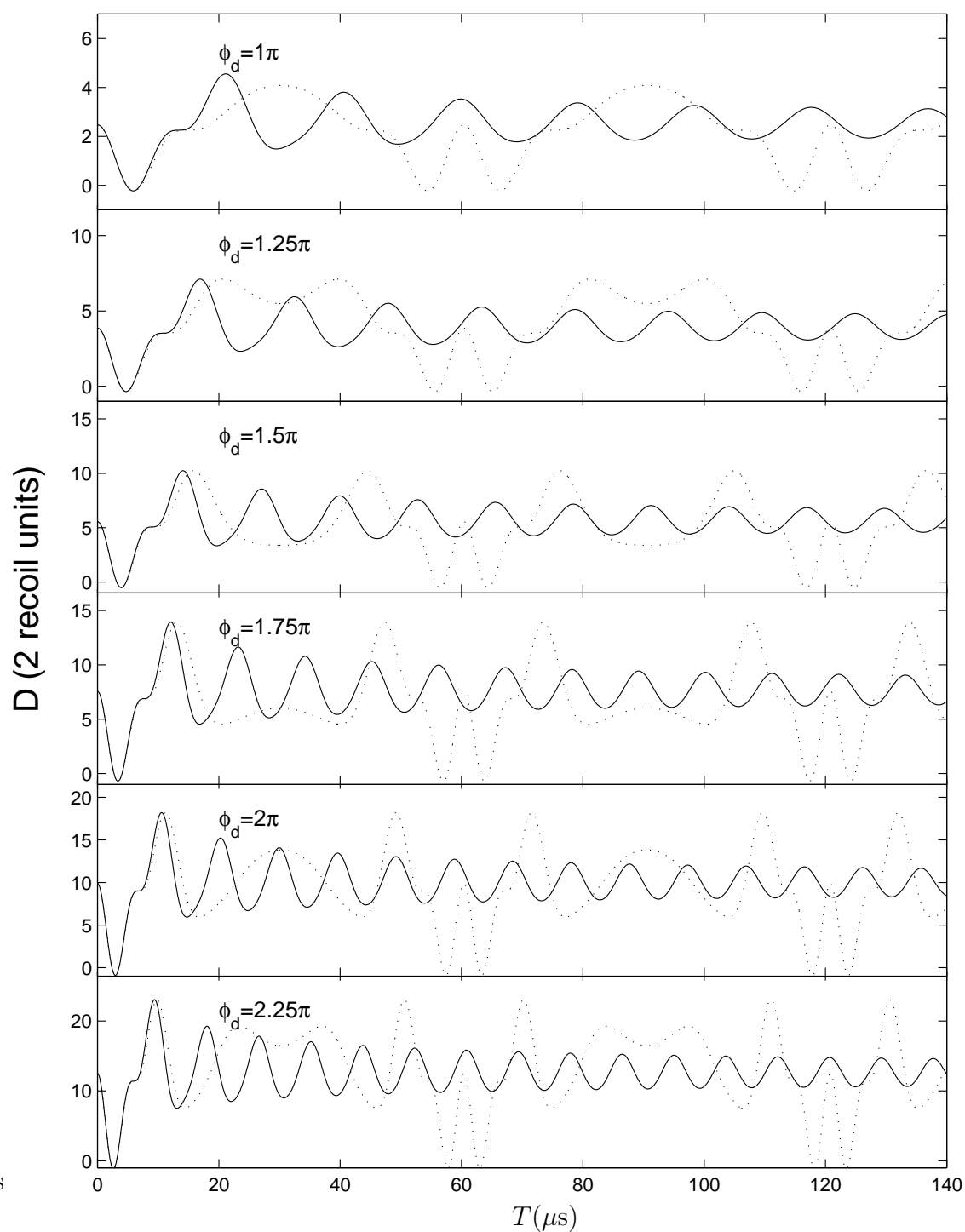


Figure 8.3: Diffusion rates for the δ -kicked rotor in physical momentum units, showing variation with T for the initial quantum diffusion rate (dotted line) and the classical diffusion rate (solid line), as predicted by (8.1) and (8.2) respectively.

8.5 Late Time Diffusion Structures with Decoherence

Experimentally it is the mean energy of the cloud after a pre-specified number of kicks that is measured directly, as opposed to the diffusion rate. By measuring the mean energy after different numbers of kicks the diffusion rate may be estimated, but it is also possible to get significant information from measuring the mean energy after a particular number of kicks, and plotting that as a function of T . The mean energy after N kicks gives us a sum over the diffusion rates for all kicks leading up to the one where the measurement is made. The structure represented is then an average over the structure in the initial quantum diffusion rate and the late time diffusion rate. If N is sufficiently large this will be a good approximation to the structure of the late time rate.

Figures 8.4 - 8.7 show the mean energy in physical momentum units as a function of T after 30 kicks for a quantum kicked rotor with decoherence and no deliberately added amplitude noise. Figures 8.4 and 8.6 show experimental results from the Oxford and Auckland groups respectively, whilst figures 8.5 and 8.7 show corresponding simulation values.

The Oxford results in figure 8.4 show the variation in the mean energy as a function of T with varying levels of spontaneous emission noise. The same periodic structure is exhibited here that was predicted in section 8.3, and we note that because the Oxford group uses the Caesium D1 transition for their experiments, the period in T is $66.7\mu s$ rather than $60.4\mu s$. We see that the mean energy after 30 kicks increases as we increase η , reflecting the corresponding increase that we expect to observe in the late time diffusion rate. The simulation results (which are from our numerical work) presented in figure 8.5 show remarkable agreement with the experimental results from the Oxford group. This is particularly striking given the level of uncertainty that is quoted in the experimental ϕ_d value by the Oxford group. In fact, they claim that any value in the range $(-\pi/2, 3\pi/2)$ would not be entirely incongruous with their experimental parameters [32]. This uncertainty arises mainly because of the large width of the cloud relative to the width of the beam for these experiments, which results in a large variation of the beam intensity and hence the kick strength across the cloud (as was described in section 4.3.3).

The simulation results include a small amount of amplitude noise to account for fluctuations in the kicking beam intensity and detuning. This amplitude noise appears to be producing an effect similar to that discussed in section 7.5, in which the quantum resonance peak is more prominent for higher levels of spontaneous emission noise. This effect is not so apparent in the simulation results, which suggests that we have underestimated the level of amplitude noise which should be included, possibly because of the amplitude noise associated with the variation of the kick strength across the cloud. Note that even in the case of high values of amplitude noise, and even if we could reduce spontaneous emissions to a completely negligible level, we would still expect to see a quantum resonance peak in these mean energy graphs. This is because

we observe a resonance peak in the initial quantum diffusion regime with amplitude noise, which contributes to the final mean energy.

The Auckland results in figure 8.6 show the variation in the structure observed in the mean energy after 30 kicks as ϕ_d is varied for a fixed level of spontaneous emission noise. We observe very similar variation in structure as was predicted from Shepelyansky's formula in section 8.3 (and we note that the quantum resonance peak returns to $t = 60.4\mu s$, due to the use of the Caesium D2 transition). This, along with the corresponding numerical results shown in figure 8.7, indicates that the same structures which are observed in the initial quantum diffusion rates are also observed in the late time diffusion rates. The simulation results agree reasonably well with the experimental results, especially considering the uncertainties in the value for ϕ_d , which is again large, particularly because of the variation in light intensity across the cloud. The poorest agreement is near the centres of the diffusion resonances themselves, which is not surprising given the sensitive dependence of the position of these resonances on the values of ϕ_d . This appears to result in peaks in the experimental results which are not as prominent as those predicted by the simulations.

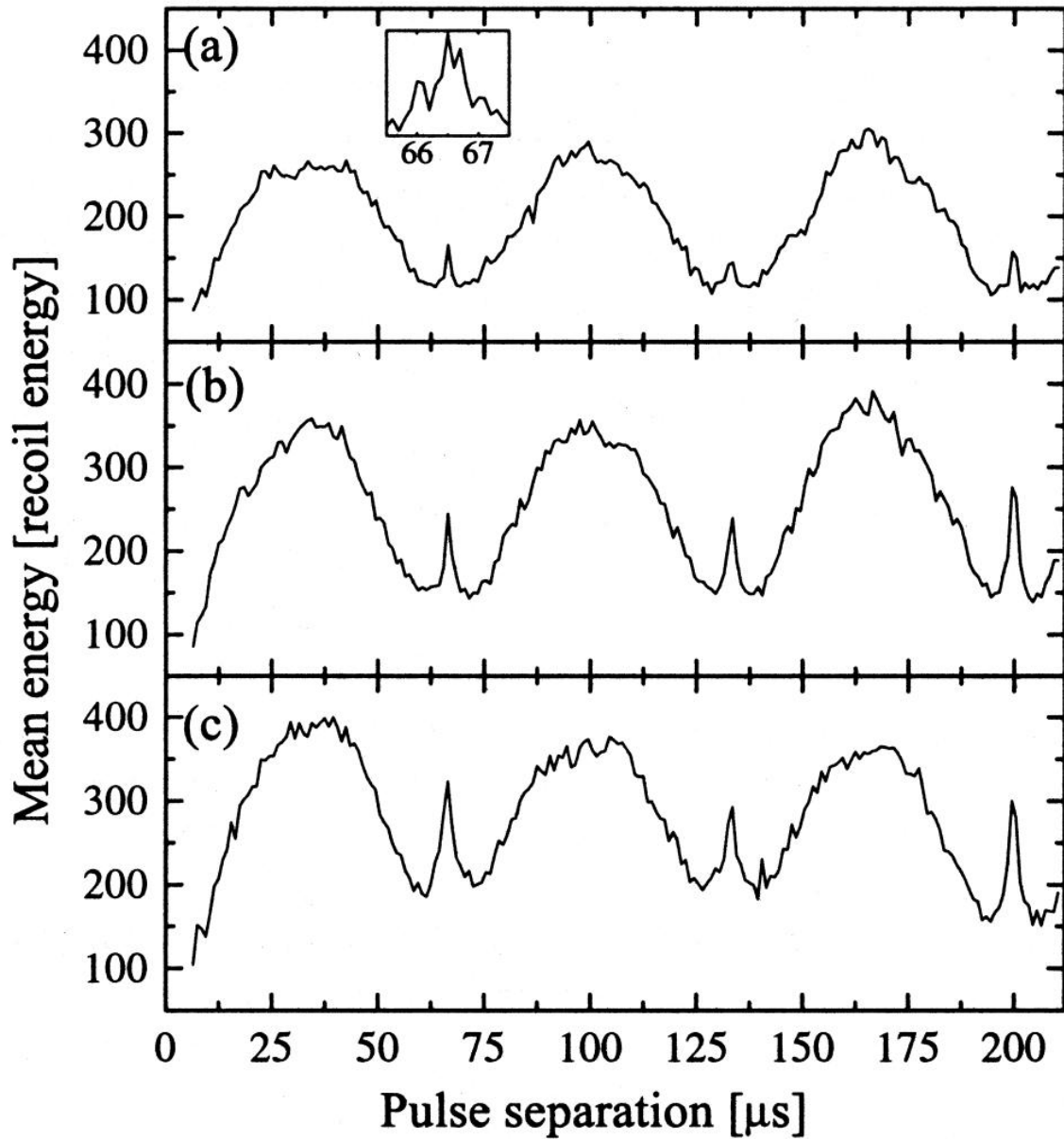


Figure 8.4: Experimental results from the group at the University of Oxford, showing mean energy of the cloud in physical units after 30 kicks for the quantum kicked rotor with $\phi_d \sim \pi$ and $\tau_p = 0.5 \mu\text{s}$. Each graph shows a different level of spontaneous emission noise, with (a) $\eta = 0\%$, (b) $\eta = 10\%$ and (c) $\eta = 20\%$, and the inset in (a) shows a higher resolution scan of values near the quantum resonance at $T = 66.7 \mu\text{s}$. This graph is reproduced with the authors' permission from M. B. d'Arcy, R. M. Godun, M. K. Oberthaler, D. Cassettari, and G. S. Summy, *Quantum Enhancement of Momentum Diffusion in the Delta-Kicked Rotor*, Phys. Rev. Lett. **87**, 074102 (2001) (reference [31]).

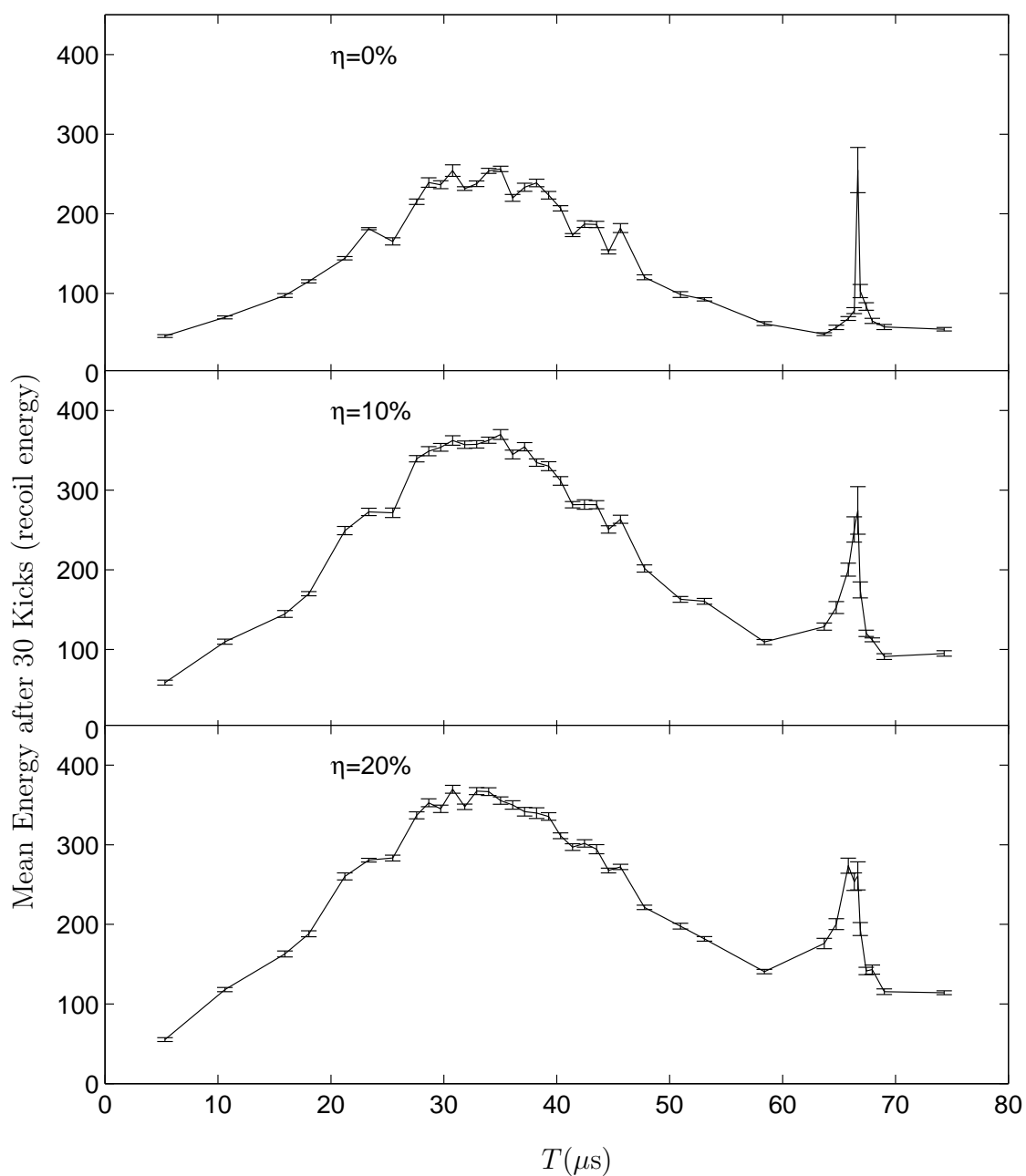


Figure 8.5: Simulation results for the mean energy of the cloud in physical units after 30 kicks for the quantum kicked rotor with $\phi_d = \pi$ and $\tau_p = 0.5\mu\text{s}$. Amplitude noise at the 10% level is included to model fluctuations in the power and detuning of the kicking beam.

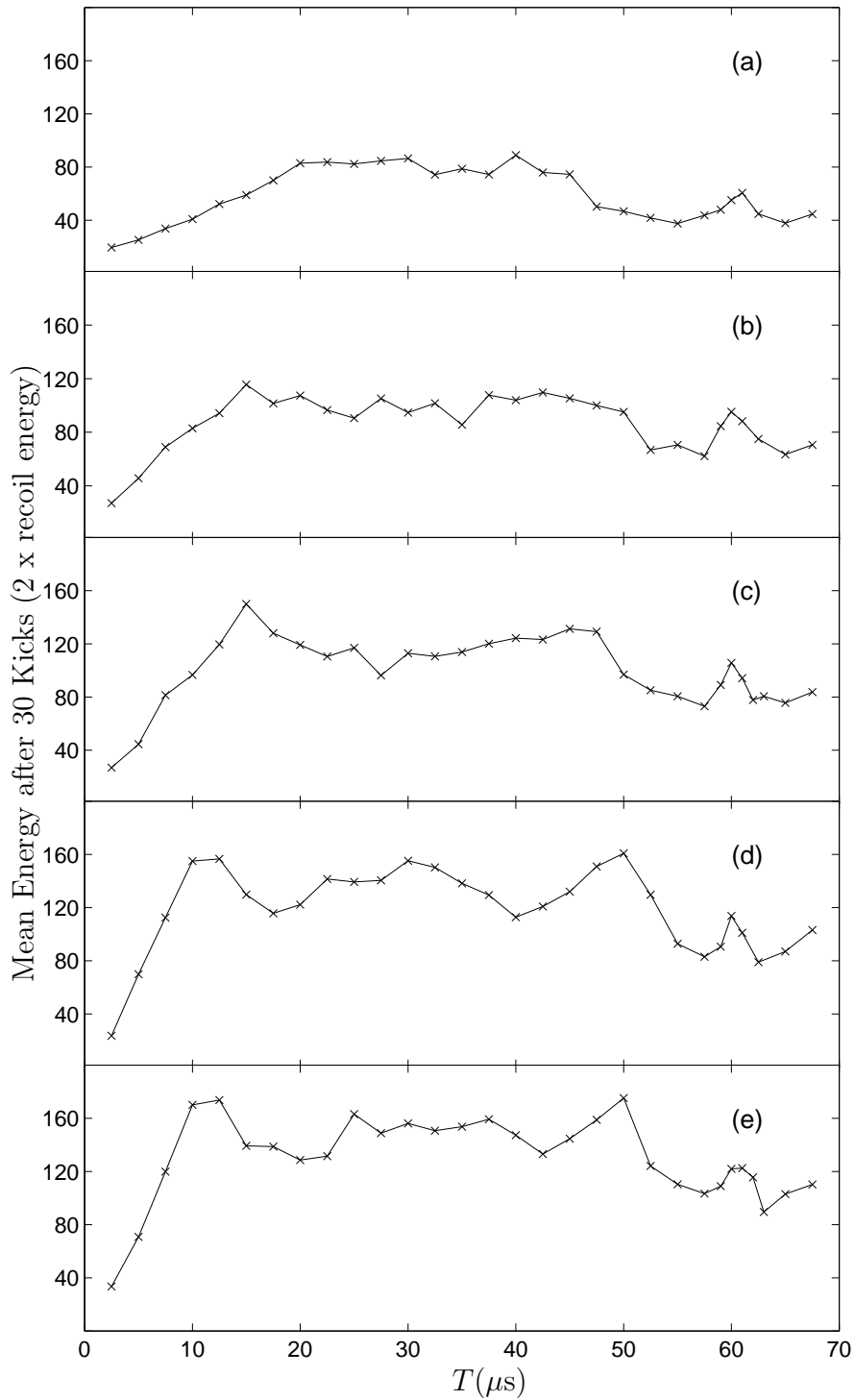


Figure 8.6: Experimental results for the mean energy of the cloud in physical units after 30 kicks for the quantum kicked rotor with $\eta = 1.2\%$ and $\tau_p = 0.52\mu\text{s}$, showing variation with changing ϕ_d . This graph was supplied by Mary Williams and is based on recent experimental data taken at the University of Auckland [61].

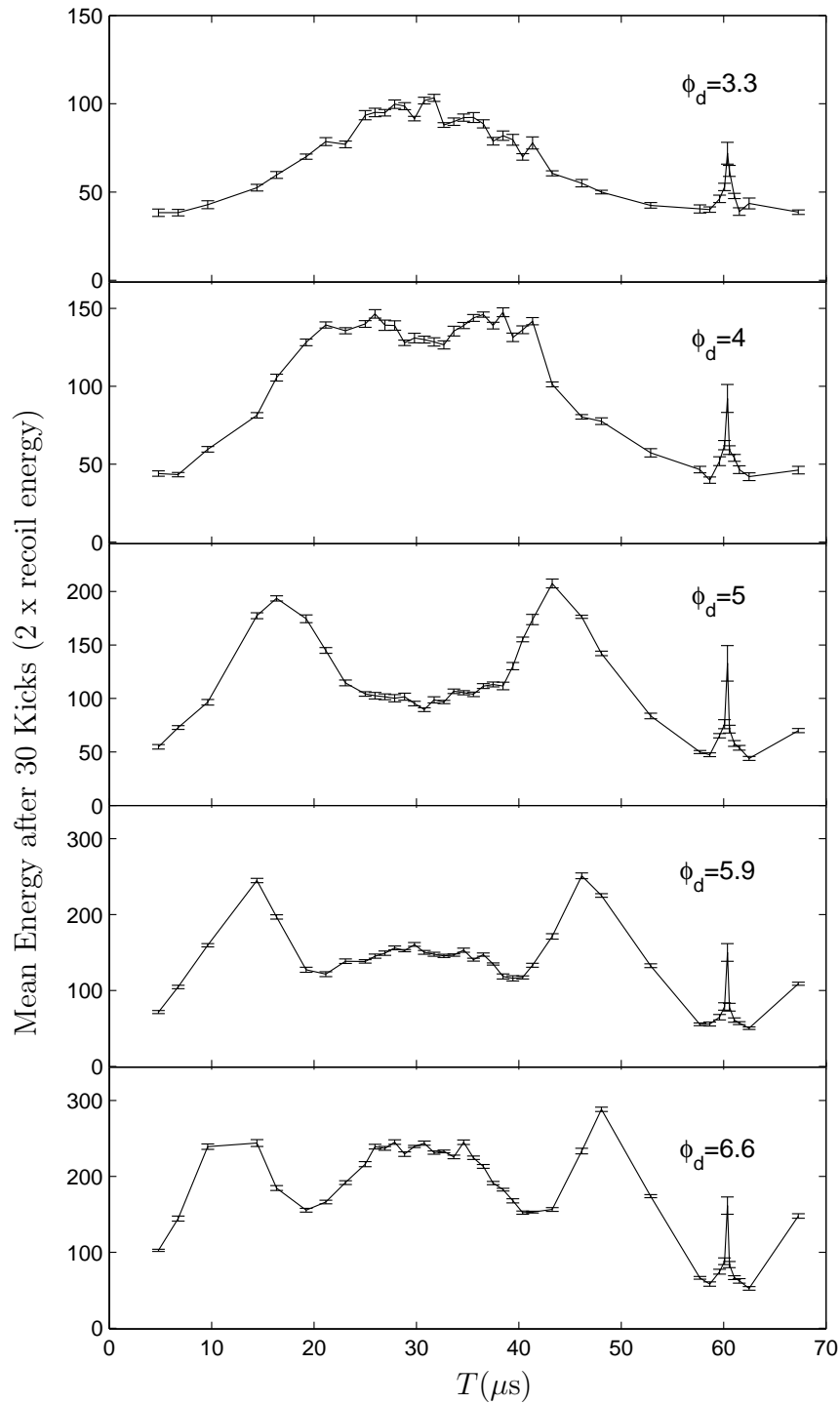


Figure 8.7: Simulation results for the mean energy of the cloud in physical units after 30 kicks for the quantum kicked rotor with $\eta = 1.2\%$ and $\tau_p = 0.52\mu s$. Amplitude noise at the 10% level is included to model fluctuations in the power and detuning of the kicking beam.

8.6 Late Time Diffusion Structures with Amplitude Noise

Figure 8.8 shows preliminary experimental results from the Auckland group which are similar to the results in figures 8.4 - 8.7, but are performed with the deliberate addition of amplitude noise. The graph shown below displays results after 20 kicks, and shows the change in structure from 10% amplitude noise to 200% amplitude noise. As we saw in chapter 7, most of the enhanced diffusion structure other than the quantum resonance peak is washed out by the addition of 200% amplitude noise, and the overall diffusion rate is increased. These are only preliminary results, but suggest that the simulation results shown in chapter 7 are reproducible experimentally, in physical units as well as in scaled units.

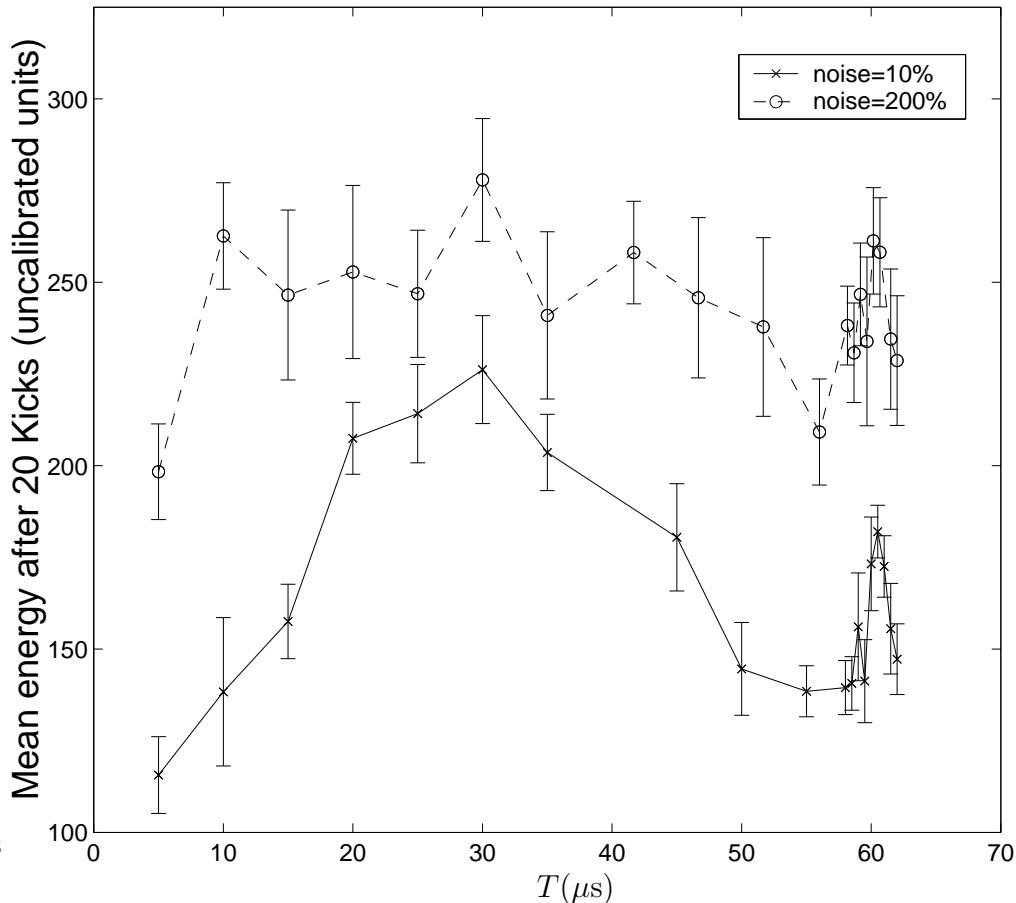


Figure 8.8: Experimental results for the mean energy of the cloud in physical units after 20 kicks for the quantum kicked rotor with $\eta = 1\%$ and $\tau_p = 0.2\mu s$, showing variation with changing levels of amplitude noise. These results were supplied by Mark Sadgrove, and are taken from recent experiments at the University of Auckland [60].

Chapter 9

Narrow Initial Momentum Distributions

9.1 Introduction

All of the results presented in chapters 6-8 were calculated for systems with an initial momentum distribution width of $\sigma_p/(2\hbar k_l) = 4$, i.e., $\sigma_p/\hbar k = 4$. This represents a typical thermal distribution found in atom optics kicked rotor experiments, with an initial cloud temperature of around $10\mu\text{K}$. Recent experiments by two groups investigating chaos-assisted dynamical tunnelling in the kicked rotor, though, have shown that it is possible to begin with much narrower momentum distributions. This may be achieved through the use of a Bose-Einstein condensate [62] or by selecting a narrow momentum slice out of a cloud from a normal magneto-optical trap using Raman transitions [63]. The latter method has been used to produce momentum distribution slices with a half width at half maximum of $\Delta p/(2\hbar k_l) = 0.03$, which corresponds to a Gaussian width of the same order of magnitude. (For a strictly Gaussian distribution, $\Delta p = 1.18\sigma_p$.)

As was mentioned in section 2.4.2 and again in section 3.3.2, the diffusion rate in the second kick for both the classical and quantum kicked rotor (when defined as the change in mean kinetic energy during one kick) is heavily dependent on the characteristics of the initial momentum distribution. We have extensively investigated this phenomenon for Gaussian distributions of different widths, centred on a range of momentum values, p_0 , and the results of this study are presented in this chapter. In addition we look briefly at how the initial quantum diffusion period is affected by changes in the width of the initial momentum distribution, and we also investigate the results of taking an initial distribution consisting of quantum superpositions of plane wave states.

9.2 Early Time Classical Diffusion Results

In section 2.4.2 it was discussed that the diffusion rate for the second kick, $D(1)$, in the classical kicked rotor was not strictly $\kappa^2/4$, i.e., the quasilinear value, for a uniform

initial position distribution, as was found with the diffusion rate for the first kick. Instead, the more complicated expression arising from the correlations was given by (2.63a),

$$\begin{aligned}
D(1) &= \frac{\langle \rho_2^2 \rangle}{2} - \frac{\langle \rho_1^2 \rangle}{2} \\
&= \frac{\kappa^2}{2} \langle \sin^2(\phi_1) \rangle + \kappa \langle \rho_1 \sin(\phi_1) \rangle \\
&= \frac{\kappa^2}{2} \langle \sin^2(\rho_1 + \phi_0) \rangle + \kappa \langle \rho_1 \sin(\phi_0 + \rho_1) \rangle \\
&= \frac{\kappa^2}{2} \langle \sin^2[\phi_0 + \rho_0 + \kappa \sin(\phi_0)] \rangle \\
&\quad + \kappa \langle \rho_0 \sin[\phi_0 + \rho_0 + \kappa \sin(\phi_0)] \rangle \\
&\quad + \kappa^2 \langle \sin(\phi_0) \sin[\phi_0 + \rho_0 + \kappa \sin(\phi_0)] \rangle. \tag{9.1}
\end{aligned}$$

In order to evaluate this expression we calculate the expectation value for each term above for a Gaussian momentum distribution centred on ρ_0 with width σ_ρ . We make use of the expansions given in (A.11), particularly the results

$$\cos[z \sin(\theta)] = J_0(z) + 2 \sum_{k=1}^{\infty} J_{2k}(z) \cos(2k\theta),$$

and

$$\sin[z \sin(\theta)] = 2 \sum_{k=0}^{\infty} J_{2k+1}(z) \sin[(2k+1)\theta],$$

and we also utilise the expressions

$$\int_{-\infty}^{\infty} \cos(\rho_0) G_0(\sigma_\rho) d\rho_0 = e^{-\sigma_\rho^2/2}, \tag{9.2a}$$

$$\int_{-\infty}^{\infty} \rho_0 \sin(\rho_0) G_0(\sigma_\rho) d\rho_0 = \sigma_\rho^2 e^{-\sigma_\rho^2/2}, \tag{9.2b}$$

$$\int_{-\infty}^{\infty} \cos(2\rho_0) G_0(\sigma_\rho) d\rho_0 = e^{-2\sigma_\rho^2}, \tag{9.2c}$$

where $G_0(\sigma_\rho)$ is a Gaussian distribution function centred on $\rho = 0$ with standard deviation σ_ρ .

The resulting formula for the classical diffusion rate in the second kick is given by

$$\begin{aligned}
D(1) &= \frac{\kappa^2}{4} (1 - J_2(2\kappa) e^{-2\sigma_\rho^2}) - \kappa J_1(\kappa) \sigma_\rho^2 e^{-\sigma_\rho^2/2} \\
&\quad + \frac{\kappa^2}{2} (J_0(\kappa) - J_2(\kappa)) e^{-\sigma_\rho^2/2}. \tag{9.3}
\end{aligned}$$

For large σ_ρ , $D(1) \rightarrow \kappa^2/4$, thus giving us the quasilinear result for broad momentum distributions that was discussed in section 2.4.2. However, for narrow momentum

distributions, we observe an important dependence of the diffusion rate on σ_ρ . In fact, as $\sigma_\rho \rightarrow 0$, $D(1) \rightarrow (\kappa^2/4)(1 - J_2(2\kappa)) + (\kappa^2/2)(J_0(\kappa) - J_2(\kappa))$. Note that this prediction, based on the definition in (2.55), which involves only the change in mean kinetic energy during a kick, is different to the diffusion rate which is usually obtained using (2.56), which gives a definition of the diffusion rates which is easier to express in terms of correlation functions. This is because the computation of these correlation functions involves the assumption of a broad initial momentum distribution, giving $C_s(1) = 0$ (see appendix B), and hence a quasilinear value for the diffusion rate in the second kick. If the correlations were computed without this assumption, we would expect to observe good agreement with our results, as the two definitions are equivalent for $\sigma_\rho = 0$ and $\rho_0 = 0$. It should be noted under any circumstances that the result which is important for us is that from the first definition, because it relates to the actual mean energy measurements which are made for the atom optics kicked rotor.

The behaviour described by (9.3) is plotted in figure 9.1. We essentially see a monotonic change in $D(1)$ as σ_ρ is increased, and the diffusion rate closely approaches the quasilinear value for $\sigma_\rho > 3$. This type of behaviour is important for comparison with the quantum system in the limit as $\hbar \rightarrow 0$, even when the initial momentum distribution is relatively broad. This is because the physical momentum distribution remains constant for the atom optics kicked rotor, but because $\sigma_\rho = \hbar \sigma_p / (2\hbar k_l)$, σ_ρ is small for low values of \hbar . In fact, in section 9.3 we observe behaviour in the quantum system very similar to that shown in figure 9.1 for systems with a typical thermal momentum distribution as \hbar , and hence σ_ρ , becomes small.

9.3 Early Time Quantum Diffusion Results

9.3.1 An Alternative Standard Map

There are several different versions of the standard map, which differ in the times during each cycle at which the momentum and position are computed and the time of the first kick. The version we have used so far, [(2.38) and (3.15)], involves writing ρ_n and ϕ_n as the position and momentum immediately before the kick at $\tau = n$, and writing the Hamiltonian for the kicked rotor such that the first kick occurs at $\tau = 0$. Different versions of the standard map are useful for different analytical purposes. In this section, we consider a map which relates to a system with the first kick occurring at $\tau = 1$, so that the position variable evolves through one cycle before the first kick. This mapping is given by

$$\hat{\phi}_{n+1} = \hat{\phi}_n + \hat{\rho}_n, \quad (9.4a)$$

$$\hat{\rho}_{n+1} = \hat{\rho}_n + \kappa \sin(\hat{\phi}_{n+1}). \quad (9.4b)$$

It is important to note that given an initial distribution of plane wave states (and hence uniform probability distributions in position space with arbitrary initial phases), the expectation values of ρ_n from this standard map will be identical to the expectation

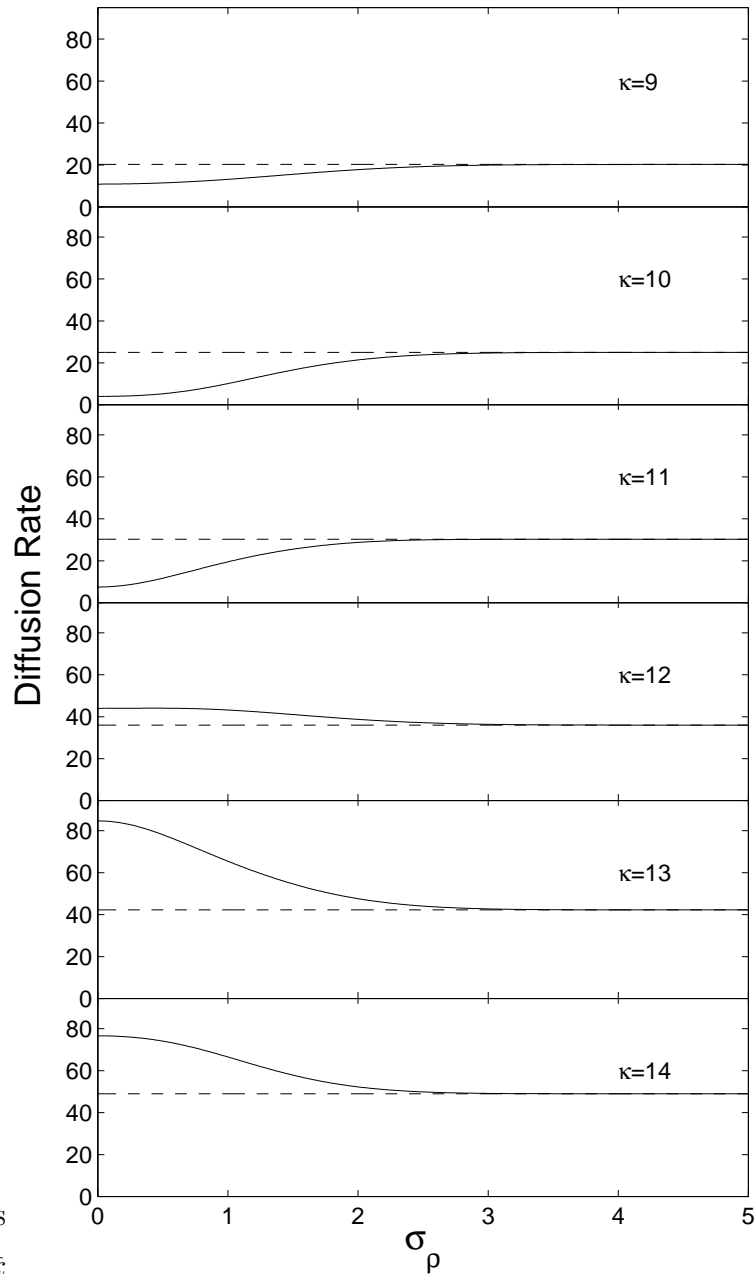


Figure 9.1: Diffusion rates in the second kick ($n=1$) for the classical δ -kicked rotor for varying widths of the initial momentum distribution, as given by equation (9.3). The solid lines show the value for $D(1)$, while the dashed lines show quasilinear values.

values of ρ_n evaluated using (3.15). Thus, we are free to use this version of the standard map to analytically evaluate the diffusion rates for the atom optics kicked rotor exactly as it was previously defined..

9.3.2 Analytical Results for the Second Kick

A similar result to that obtained for the classical kicked rotor in section 9.2 may be obtained for the quantum kicked rotor using the version of the standard map given in section 9.3.1. The equivalent of (3.34) for our alternative version of the standard map (9.4) is given by

$$\begin{aligned} D(1) &= \langle \hat{\rho}_1^2 \rangle / 2 - \langle \hat{\rho}_0^2 \rangle / 2 \\ &= \frac{\kappa^2}{2} \langle \sin^2(\hat{\phi}_2) \rangle + \frac{\kappa}{2} \langle \hat{\rho}_1 \sin(\hat{\phi}_2) + \sin(\hat{\phi}_2) \hat{\rho}_1 \rangle \\ &= \frac{\kappa^2}{2} \langle \sin^2(\hat{\rho}_1 + \hat{\phi}_1) \rangle + \frac{\kappa}{2} \langle \hat{\rho}_1 \sin(\hat{\phi}_1 + \hat{\rho}_1) + \sin(\hat{\phi}_1 + \hat{\rho}_1) \hat{\rho}_1 \rangle. \end{aligned}$$

Now, this expression may be evaluated in a manner analogous to the classical expression, except that the process is complicated significantly by our need to respect commutation relations and to treat dynamical observables as operators acting on a state ket. The resulting calculation was originally performed by Scott Parkins [64]. Essentially, it involves calculating the expectation values for a specific initial momentum eigenstate, $|\rho_0\rangle$, and then taking an incoherent average of the resulting expression over a Gaussian distribution.

We begin by noting a special case of the Baker-Hausdorff relation, in particular,

$$e^{\hat{A}+\hat{B}} = e^{\hat{B}} e^{\hat{A}} e^{[\hat{A},\hat{B}]/2} \quad (9.5)$$

for \hat{A} and \hat{B} such that $[\hat{A}, [\hat{A}, \hat{B}]] = [\hat{B}, [\hat{B}, \hat{A}]] = 0$. Using this we can write

$$e^{i(\hat{\phi}_1+\hat{\rho}_1)} = e^{i\hat{\phi}_1} e^{i\hat{\rho}_1} e^{-ik/2}. \quad (9.6)$$

Then,

$$\begin{aligned} \sin(\hat{\phi}_1 + \hat{\rho}_1) &= \frac{1}{2i} (e^{i(\hat{\phi}_1+\hat{\rho}_1)} - e^{-i(\hat{\phi}_1+\hat{\rho}_1)}) \\ &= \frac{1}{2i} (e^{i\hat{\phi}_1} e^{i\hat{\rho}_1} e^{-ik/2} - e^{-i\hat{\phi}_1} e^{-i\hat{\rho}_1} e^{-ik/2}) \\ &= e^{-ik/2} [\sin(\hat{\phi}_1) \cos(\hat{\rho}_1) + \cos(\hat{\phi}_1) \sin(\hat{\rho}_1)]. \end{aligned} \quad (9.7)$$

Using this and the related expression for $\cos(\hat{\phi}_1 + \hat{\rho}_1)$, we can then rewrite (3.34) as

$$\begin{aligned}
\langle \hat{\rho}_2^2 \rangle - \langle \hat{\rho}_1^2 \rangle &= \frac{\kappa^2}{2} - \frac{\kappa^2}{2} \langle \cos[2(\hat{\phi}_1 + \hat{\rho}_1)] \rangle \\
&\quad + \kappa e^{-i\kappa/2} \langle [\hat{\rho}_1, \sin(\hat{\phi}_1) \cos(\hat{\rho}_1) + \cos(\hat{\phi}_1) \sin(\hat{\rho}_1)]_+ \rangle \\
&= \frac{\kappa^2}{2} - \frac{\kappa^2}{2} e^{-2i\kappa} \langle \cos(2\hat{\phi}_1) \cos(2\hat{\rho}_1) - \sin(2\hat{\phi}_1) \sin(2\hat{\rho}_1) \rangle \\
&\quad + \kappa e^{-i\kappa/2} \langle [\hat{\rho}_1, \sin(\hat{\phi}_0 + \hat{\rho}_0) \cos(\hat{\rho}_1) + \cos(\hat{\phi}_0 + \hat{\rho}_0) \sin(\hat{\rho}_1)]_+ \rangle \\
&= \frac{\kappa^2}{2} - \frac{\kappa^2}{2} e^{-2i\kappa} \langle \cos[2(\hat{\phi}_0 + \hat{\rho}_0)] \cos(2\hat{\rho}_1) - \sin[2(\hat{\phi}_0 + \hat{\rho}_0)] \sin(2\hat{\rho}_1) \rangle \\
&\quad + \kappa e^{-i\kappa/2} \langle [\hat{\rho}_0, \sin(\hat{\phi}_0 + \hat{\rho}_0) \cos(\hat{\rho}_1) + \cos(\hat{\phi}_0 + \hat{\rho}_0) \sin(\hat{\rho}_1)]_+ \rangle \\
&\quad + \kappa^2 e^{-i\kappa/2} \langle \sin^2(\hat{\phi}_0 + \hat{\rho}_0) \cos(\hat{\rho}_1) + \sin(\hat{\phi}_0 + \hat{\rho}_0) \cos(\hat{\phi}_0 + \hat{\rho}_0) \sin(\hat{\rho}_1) \\
&\quad + [\sin(\hat{\phi}_0 + \hat{\rho}_0) \cos(\hat{\rho}_1) + \cos(\hat{\phi}_0 + \hat{\rho}_0) \sin(\hat{\rho}_1)] \sin(\hat{\phi}_0 + \hat{\rho}_0) \rangle. \quad (9.8)
\end{aligned}$$

We then express the trigonometric operator expressions involving $\hat{\rho}_1$ in terms of $\hat{\phi}_0$ and $\hat{\rho}_0$. We write

$$\exp(i\hat{\rho}_1) = \exp[i\hat{\rho}_0 + i\kappa \sin(\hat{\phi}_0 + \hat{\rho}_0)] \quad (9.9)$$

$$= \exp\left[i\hat{\rho}_0 + \frac{\kappa}{2} \left\{ e^{i(\hat{\phi}_0 + \hat{\rho}_0)} - e^{-i(\hat{\phi}_0 + \hat{\rho}_0)} \right\}\right], \quad (9.10)$$

and then we apply another special case of the Baker-Hausdorff relation, which states that

$$\exp(\hat{A} + \hat{B}) = \exp[\hat{B}(e^c - 1)/c] \exp(\hat{A}), \quad (9.11)$$

for \hat{A} and \hat{B} such that $[\hat{A}, \hat{B}] = c\hat{B}$ where c is a constant. If we choose

$$\hat{a} = i\hat{\rho}_0 + \frac{\kappa}{2} e^{i(\hat{\phi}_0 + \hat{\rho}_0)}, \quad (9.12a)$$

and

$$\hat{b} = -\frac{\kappa}{2} e^{-i(\hat{\phi}_0 + \hat{\rho}_0)} \quad (9.12b)$$

then

$$[\hat{a}, \hat{b}] = -i\kappa\hat{b}, \quad (9.12c)$$

and from (9.11) we obtain the expression

$$\exp(i\hat{\rho}_1) = \exp\left[\frac{(e^{-i\kappa} - 1)\kappa}{i\kappa} e^{-i(\hat{\phi}_0 + \hat{\rho}_0)}\right] \exp\left[i\hat{\rho}_0 + \frac{\kappa}{2} e^{i(\hat{\phi}_0 + \hat{\rho}_0)}\right]. \quad (9.13)$$

Applying (9.11) to the second exponential factor of this equation and combining the terms, we get

$$\begin{aligned}
\exp(i\hat{\rho}_1) &= \exp\left[\frac{(e^{-i\bar{k}} - 1)\kappa}{i\bar{k}}\frac{\kappa}{2}e^{-i(\hat{\phi}_0 + \hat{\rho}_0)}\right] \exp\left[\frac{(e^{i\bar{k}} - 1)\kappa}{i\bar{k}}\frac{\kappa}{2}e^{i(\hat{\phi}_0 + \hat{\rho}_0)}\right] e^{i\hat{\rho}_0} \\
&= \exp\left[\frac{2e^{i\bar{k}/2}}{\bar{k}}\sin(\bar{k}/2)\frac{\kappa}{2}e^{i(\hat{\phi}_0 + \hat{\rho}_0)} - \frac{2e^{-i\bar{k}/2}}{\bar{k}}\sin(\bar{k}/2)\frac{\kappa}{2}e^{-i(\hat{\phi}_0 + \hat{\rho}_0)}\right] e^{i\hat{\rho}_0} \\
&= \exp\left[iK_q \sin\left(\hat{\phi}_0 + \hat{\rho}_0 + \frac{\bar{k}}{2}\right)\right] e^{i\hat{\rho}_0}, \tag{9.14}
\end{aligned}$$

where $K_q = 2\kappa \sin(\bar{k}/2)/\bar{k}$.

We now apply the expressions given in (A.11), specifically

$$\cos[z \sin(\theta)] = J_0(z) + 2 \sum_{k=1}^{\infty} J_{2k}(z) \cos(2k\theta)$$

and

$$\sin[z \sin(\theta)] = 2 \sum_{k=0}^{\infty} J_{2k+1}(z) \sin[(2k+1)\theta],$$

to give us

$$\begin{aligned}
\exp(i\hat{\rho}_1) &= \left\{ \cos[K_q \sin(\hat{\phi}_0 + \hat{\rho}_0 + \bar{k}/2)] + i \sin[K_q \sin(\hat{\phi}_0 + \hat{\rho}_0 + \bar{k}/2)] \right\} e^{i\hat{\rho}_0} \\
&= J_0(K_q) e^{i\hat{\rho}_0} + 2 \sum_{k=1}^{\infty} J_{2k}(K_q) \cos[2k(\hat{\phi}_0 + \hat{\rho}_0 + \bar{k}/2)] e^{i\hat{\rho}_0} \\
&\quad + 2i \sum_{k=0}^{\infty} J_{2k+1}(K_q) \sin[(2k+1)(\hat{\phi}_0 + \hat{\rho}_0 + \bar{k}/2)] e^{i\hat{\rho}_0} \\
&= J_0(K_q) e^{i\hat{\rho}_0} + 2 \sum_{k=1}^{\infty} J_{2k}(K_q) \{ \cos[2k(\hat{\phi}_0 + \hat{\rho}_0)] \cos(k\bar{k}) \\
&\quad - \sin[2k(\hat{\phi}_0 + \hat{\rho}_0)] \sin(k\bar{k}) \} e^{i\hat{\rho}_0} \\
&\quad + 2i \sum_{k=0}^{\infty} J_{2k+1}(K_q) \{ \sin[(2k+1)(\hat{\phi}_0 + \hat{\rho}_0)] \cos[(2k+1)\bar{k}/2] \\
&\quad + \cos[(2k+1)(\hat{\phi}_0 + \hat{\rho}_0)] \sin[(2k+1)\bar{k}/2] \} e^{i\hat{\rho}_0}, \tag{9.15}
\end{aligned}$$

where we have used the fact that $\cos[2k(\hat{\phi}_0 + \hat{\rho}_0 + \bar{k}/2)] e^{i\hat{\rho}_0} = e^{i\hat{\rho}_0} \cos[2k(\hat{\phi}_0 + \hat{\rho}_0 - \bar{k}/2)]$.

Using a similar procedure, we can obtain the result

$$\begin{aligned}
\exp(-i\hat{\rho}_1) &= J_0(K_q)e^{-i\hat{\rho}_0} + 2 \sum_{k=1}^{\infty} J_{2k}(K_q) \{ \cos[2k(\hat{\phi}_0 + \hat{\rho}_0)] \cos(k\hat{k}) \\
&\quad + \sin[2k(\hat{\phi}_0 + \hat{\rho}_0)] \sin(k\hat{k}) \} e^{-i\hat{\rho}_0} \\
&\quad - 2i \sum_{k=0}^{\infty} J_{2k+1}(K_q) \{ \sin[(2k+1)(\hat{\phi}_0 + \hat{\rho}_0)] \cos[(2k+1)\hat{k}/2] \\
&\quad - \cos[(2k+1)(\hat{\phi}_0 + \hat{\rho}_0)] \sin[(2k+1)\hat{k}/2] \} e^{-i\hat{\rho}_0}. \quad (9.16)
\end{aligned}$$

We are then able to express the operators $\cos(\hat{\rho}_1)$, $\sin(\hat{\rho}_1)$, $\cos(2\hat{\rho}_1)$ and $\sin(2\hat{\rho}_1)$ which occur in (9.8) in terms of these expansions. For example,

$$\begin{aligned}
\cos(\hat{\rho}_1) &= J_0(K_q) \cos(\hat{\rho}_0) + 2 \sum_{k=1}^{\infty} J_{2k}(K_q) \cos(k\hat{k}) \cos[2k(\hat{\phi}_0 + \hat{\rho}_0)] \cos(\hat{\rho}_0) \\
&\quad - 2i \sum_{k=1}^{\infty} J_{2k}(K_q) \sin(k\hat{k}) \sin[2k(\hat{\phi}_0 + \hat{\rho}_0)] \sin(\hat{\rho}_0) \\
&\quad + 2i \sum_{k=0}^{\infty} J_{2k+1}(K_q) \sin[(2k+1)\hat{k}/2] \cos[(2k+1)(\hat{\phi}_0 + \hat{\rho}_0)] \cos(\hat{\rho}_0) \\
&\quad - 2 \sum_{k=0}^{\infty} J_{2k+1}(K_q) \cos[(2k+1)\hat{k}/2] \sin[(2k+1)(\hat{\phi}_0 + \hat{\rho}_0)] \sin(\hat{\rho}_0), \quad (9.17)
\end{aligned}$$

(9.18)

and

$$\begin{aligned}
\cos(2\hat{\rho}_1) &= J_0(K_{2q}) \cos(2\hat{\rho}_0) + 2 \sum_{k=1}^{\infty} J_{2k}(K_{2q}) \cos(2k\hat{k}) \cos[2k(\hat{\phi}_0 + \hat{\rho}_0)] \cos(2\hat{\rho}_0) \\
&\quad - 2i \sum_{k=1}^{\infty} J_{2k}(K_{2q}) \sin(2k\hat{k}) \sin[2k(\hat{\phi}_0 + \hat{\rho}_0)] \sin(2\hat{\rho}_0) \\
&\quad - 2 \sum_{k=0}^{\infty} J_{2k+1}(K_{2q}) \cos[(2k+1)\hat{k}] \sin[(2k+1)(\hat{\phi}_0 + \hat{\rho}_0)] \sin(2\hat{\rho}_0) \\
&\quad + 2i \sum_{k=0}^{\infty} J_{2k+1}(K_{2q}) \sin[(2k+1)\hat{k}] \cos[(2k+1)(\hat{\phi}_0 + \hat{\rho}_0)] \cos(2\hat{\rho}_0), \quad (9.19)
\end{aligned}$$

where $K_{2q} = 2\kappa \sin(\hat{k})/\hat{k}$.

We then expand the terms in $\sin[2(\hat{\phi}_0 + \hat{\rho}_0)]$ and $\cos[2(\hat{\phi}_0 + \hat{\rho}_0)]$, and consider the action of the operators $\sin(2k\hat{\phi}_0)$ and $\cos(2k\hat{\phi}_0)$ on a state ket $|\rho_0\rangle$. Noting, for example, that

$$\cos[2k(\hat{\phi}_0 + \hat{\rho}_0)]|\rho_0\rangle = \frac{1}{2} e^{-i\hat{k}(2k)^2/2} [e^{2ik\rho_0} |\rho_0 + 2k\hat{k}\rangle + e^{-2ik\rho_0} |\rho_0 - 2k\hat{k}\rangle], \quad (9.20)$$

we get expressions for the action of the operators $\cos(\hat{\rho}_1)$, $\sin(\hat{\rho}_1)$, $\cos(2\hat{\rho}_1)$ and $\sin(2\hat{\rho}_1)$ on a state ket $|\rho_0\rangle$. For example,

$$\begin{aligned}
& \cos(\hat{\rho}_1)|\rho_0\rangle \\
= & J_0(K_q) \cos(\rho_0)|\rho_0\rangle \\
& + \sum_{k=1}^{\infty} J_{2k}(K_q) e^{-\frac{1}{2}i\bar{k}(2k)^2} \{ \cos(k\bar{k}) \cos(\rho_0) [e^{2ik\rho_0} |\rho_0 + 2k\bar{k}\rangle + e^{-2ik\rho_0} |\rho_0 - 2k\bar{k}\rangle] \\
& \quad - \sin(k\bar{k}) \sin(\rho_0) [e^{2ik\rho_0} |\rho_0 + 2k\bar{k}\rangle - e^{-2ik\rho_0} |\rho_0 - 2k\bar{k}\rangle] \} \\
& + i \sum_{k=0}^{\infty} J_{2k+1}(K_q) e^{-\frac{1}{2}i\bar{k}(2k+1)^2} \\
& \quad \{ \sin[(2k+1)\bar{k}/2] \cos(\rho_0) [e^{i(2k+1)\rho_0} |\rho_0 + (2k+1)\bar{k}\rangle + e^{-i(2k+1)\rho_0} |\rho_0 - (2k+1)\bar{k}\rangle] \\
& \quad + \cos[(2k+1)\bar{k}/2] \sin(\rho_0) [e^{i(2k+1)\rho_0} |\rho_0 + (2k+1)\bar{k}\rangle - e^{-i(2k+1)\rho_0} |\rho_0 - (2k+1)\bar{k}\rangle] \}, \tag{9.21}
\end{aligned}$$

and

$$\begin{aligned}
& \cos(2\hat{\rho}_1)|\rho_0\rangle \\
= & J_0(K_q) \cos(\rho_0)|\rho_0\rangle \\
& + \sum_{k=1}^{\infty} J_{2k}(K_{2q}) e^{-\frac{1}{2}i\bar{k}(2k)^2} \{ \cos(k\bar{k}) \cos(2\rho_0) [e^{2ik\rho_0} |\rho_0 + 2k\bar{k}\rangle + e^{-2ik\rho_0} |\rho_0 - 2k\bar{k}\rangle] \\
& \quad - \sin(k\bar{k}) \sin(2\rho_0) [e^{2ik\rho_0} |\rho_0 + 2k\bar{k}\rangle - e^{-2ik\rho_0} |\rho_0 - 2k\bar{k}\rangle] \} \\
& + i \sum_{k=0}^{\infty} J_{2k+1}(K_{2q}) e^{-\frac{1}{2}i\bar{k}(2k+1)^2} \\
& \quad \{ \sin[(2k+1)\bar{k}/2] \cos(2\rho_0) [e^{i(2k+1)\rho_0} |\rho_0 + (2k+1)\bar{k}\rangle + e^{-i(2k+1)\rho_0} |\rho_0 - (2k+1)\bar{k}\rangle] \\
& \quad + \cos[(2k+1)\bar{k}/2] \sin(2\rho_0) [e^{i(2k+1)\rho_0} |\rho_0 + (2k+1)\bar{k}\rangle - e^{-i(2k+1)\rho_0} |\rho_0 - (2k+1)\bar{k}\rangle] \}. \tag{9.22}
\end{aligned}$$

We are now in a position to evaluate the expectation values in (9.8). We consider each term in this expression separately, evaluating the series expansion for the operator involving $\hat{\rho}_1$, and then retaining only the terms which have a non-zero inner product with $\langle\rho_0|$. For example,

$$\cos[2(\hat{\phi}_0 + \hat{\rho}_0)] \cos(2\hat{\rho}_1) = e^{-2i\bar{k}} [\cos(2\hat{\phi}_0) \cos(2\hat{\rho}_0) - \sin(2\hat{\phi}_0) \sin(2\hat{\rho}_0)] \cos(2\hat{\rho}_1), \tag{9.23}$$

and when we operate on the series resulting from $\cos(2\hat{\rho}_1)$ with the operators $\cos(2\hat{\phi}_0)$ and $\sin(2\hat{\phi}_0)$, the only surviving terms are those of the form

$$\cos(2\hat{\phi}_0)|\rho_0 \pm 2\bar{k}\rangle \rightarrow \frac{1}{2}|\rho_0\rangle \tag{9.24a}$$

and

$$\sin(2\hat{\phi}_0)|\rho_0 \pm 2\bar{k}\rangle \rightarrow \mp \frac{1}{2i}|\rho_0\rangle. \tag{9.24b}$$

Thus we see that

$$\begin{aligned} & \langle \rho_0 | \cos(2\hat{\phi}_0) \cos(2\hat{\rho}_0) \cos(2\hat{\rho}_1) | \rho_0 \rangle \\ = & \langle \rho_0 | \frac{1}{2} J_2(K_{2q}) \cos(2\hat{k}) \cos(2\rho_0) e^{-2i\hat{k}} [e^{2i\rho_0} \cos(2\rho_0 + 4\hat{k}) + e^{-2i\rho_0} \cos(2\rho_0 - 4\hat{k})] | \rho_0 \rangle \\ & - \langle \rho_0 | \frac{1}{2} J_2(K_{2q}) \sin(2\hat{k}) \sin(2\rho_0) e^{-2i\hat{k}} [e^{2i\rho_0} \cos(2\rho_0 + 4\hat{k}) - e^{-2i\rho_0} \cos(2\rho_0 - 4\hat{k})] | \rho_0 \rangle \end{aligned}$$

and

$$\begin{aligned} & \langle \rho_0 | \sin(2\hat{\phi}_0) \sin(2\hat{\rho}_0) \cos(2\hat{\rho}_1) | \rho_0 \rangle \\ = & \langle \rho_0 | \frac{1}{2i} J_2(K_{2q}) \cos(2\hat{k}) \cos(2\rho_0) e^{-2i\hat{k}} [-e^{2i\rho_0} \sin(2\rho_0 + 4\hat{k}) + e^{-2i\rho_0} \sin(2\rho_0 - 4\hat{k})] | \rho_0 \rangle \\ & \langle \rho_0 | \frac{1}{2i} J_2(K_{2q}) \sin(2\hat{k}) \sin(2\rho_0) e^{-2i\hat{k}} [e^{2i\rho_0} \sin(2\rho_0 + 4\hat{k}) + e^{-2i\rho_0} \sin(2\rho_0 - 4\hat{k})] | \rho_0 \rangle, \end{aligned}$$

and combining these terms and simplifying gives

$$\langle \rho_0 | \cos[2(\hat{\phi}_0 + \hat{\rho}_0)] \cos(2\hat{\rho}_1) | \rho_0 \rangle = \langle \rho_0 | J_2(K_{2q}) \cos(2\hat{k}) \cos(2\rho_0) | \rho_0 \rangle. \quad (9.25)$$

Proceeding in this manner through the rest of the terms, we eventually arrive at the expression

$$\begin{aligned} \langle \rho_0 | \hat{\rho}_2^2 | \rho_0 \rangle - \langle \rho_0 | \hat{\rho}_1^2 | \rho_0 \rangle &= \frac{1}{2} \kappa^2 [1 - J_2(K_{2q}) \cos(2\rho_0)] - 2\kappa J_1(K_q) \rho_0 \sin(\rho_0) \\ &+ \kappa^2 [J_0(K_1) - J_2(K_1)] \cos(\rho_0) \cos(\hat{k}/2). \end{aligned} \quad (9.26)$$

If we now average this over an incoherent Gaussian distribution for ρ_0 values which is centred on $\rho_0 = 0$ and has width σ_ρ , making use of the relations in (9.2), we get

$$\begin{aligned} 2D(1) &= \frac{1}{2} \kappa^2 (1 - J_2(K_{2q}) e^{-2\sigma_\rho^2}) - 2\kappa J_1(K_q) \sigma_\rho^2 e^{-\sigma_\rho^2/2} \\ &+ \kappa^2 (J_0(K_q) - J_2(K_q)) \cos(\hat{k}/2) e^{-\sigma_\rho^2/2}, \end{aligned} \quad (9.27)$$

where $K_q = 2\kappa \sin(\hat{k}/2)/\hat{k}$ and $K_{2q} = 2\kappa \sin(\hat{k})/\hat{k}$.

This is our final expression for the diffusion rate in the second kick, and we notice immediately that it reduces to the quasilinear value as the initial momentum distribution becomes broader, but it predicts complicated and interesting structure as a function of \hat{k} for sufficiently small σ_ρ . As in the classical case, this result is in contrast with the normally quoted result for the diffusion rate definition (3.31). Again, this is because the calculation of the correlations (outlined in appendix B) involves the assumption of a broad initial momentum distribution, and thus results in quasilinear diffusion in the second kick. Once more we note that for narrow momentum distributions centred on $\rho_0 = 0$ we expect good agreement between diffusion rates from the two definitions, and that it is the definition in terms of the change in mean energy during each kick that interests us most, as this is how the momentum diffusion rate is measured for the atom optics kicked rotor.

Figure 9.2 shows equation (9.27) plotted as a function of \bar{k} for four values of κ and six values of $\sigma_n = \sigma_p/(2\hbar k_l)$. Note that $\sigma_\rho = \sigma_n \bar{k}$. We see, as we expect, that for large values of σ_n , the diffusion rate is quasilinear except at low values of \bar{k} , where it tends to the diffusion rate for a single initial eigenstate, $|\rho_0 = 0\rangle$ as $\bar{k} \rightarrow 0$. For lower values of σ_n , we see a complicated resonance structure as a function of \bar{k} . This structure is a uniquely quantum effect, because it relies on the \bar{k} dependence of the correlations. In addition, this is particularly surprising quantum structure because the normally accepted values for the correlation function generated by (3.31) predict a simple quasilinear behaviour in the second kick. Moreover, this structure should be experimentally realisable as narrow momentum distributions with $\sigma_n \approx 0.1$ can be produced using Raman transitions, as demonstrated in reference [63]. Also, the structure should be measurable with equipment of reasonable resolution as the diffusion rates involved are very large compared with the initial mean energy of the cloud, and often are even large compared with the quasilinear rate (which will still be the diffusion rate for the first kick). The possibility of experimental realisability is emphasised by the simulation results presented in figure 9.3 which show the diffusion rates in the second kick with finite pulse length and spontaneous emissions taken into account. These results exhibit excellent quantitative agreement with the analytical results from (9.27).

It is interesting to note how the resonance structure in the diffusion rate during the second kick changes if the initial momentum distribution is not centred on $\rho_0 = 0$. The modified version of (9.27) is found by averaging (9.26) over our translated Gaussian distribution. We use the results

$$\int_{-\infty}^{\infty} \cos(\rho_0) G(\rho_i, \sigma_\rho) d\rho_0 = e^{-\sigma_\rho^2/2} \cos(\rho_i), \quad (9.28a)$$

$$\int_{-\infty}^{\infty} \rho_0 \sin(\rho_0) G(\rho_i, \sigma_\rho) d\rho_0 = \sigma_\rho^2 e^{-\sigma_\rho^2/2} \cos(\rho_i) + \rho_i e^{-\sigma_\rho^2/2} \sin(\rho_i), \quad (9.28b)$$

$$\int_{-\infty}^{\infty} \cos(2\rho_0) G(\rho_i, \sigma_\rho) d\rho_0 = e^{-2\sigma_\rho^2} \cos(2\rho_i), \quad (9.28c)$$

where $G(\rho_i, \sigma_\rho)$ is a Gaussian distribution function centred on $\rho = \rho_i$ with standard deviation σ_ρ , and obtain the final expression

$$\begin{aligned} 2D(1) = & \frac{1}{2} \kappa^2 [1 - J_2(K_{2q}) e^{-2\sigma_\rho^2} \cos(\rho_i)] \\ & - 2\kappa J_1(K_q) [\sigma_\rho^2 e^{-\sigma_\rho^2/2} \cos(\rho_i) + \rho_i e^{-\sigma_\rho^2/2} \sin(\rho_i)] \\ & + \kappa^2 (J_0(K_q) - J_2(K_q)) \cos(\bar{k}/2) e^{-\sigma_\rho^2/2} \cos(\rho_i), \end{aligned} \quad (9.29)$$

where, as previously defined, $K_q = 2\kappa \sin(\bar{k}/2)/\bar{k}$ and $K_{2q} = 2\kappa \sin(\bar{k})/\bar{k}$.

This equation is plotted in figure 9.4 for various values of $\rho_0 = \rho_i/\bar{k} = p_0/(2\hbar k_l)$, and $\sigma_n = 0.01$. As with the diffusion rates for $\rho_0 = 0$, these rates exhibit interesting structure, which will be washed out for large σ_n . This washing out can be seen from

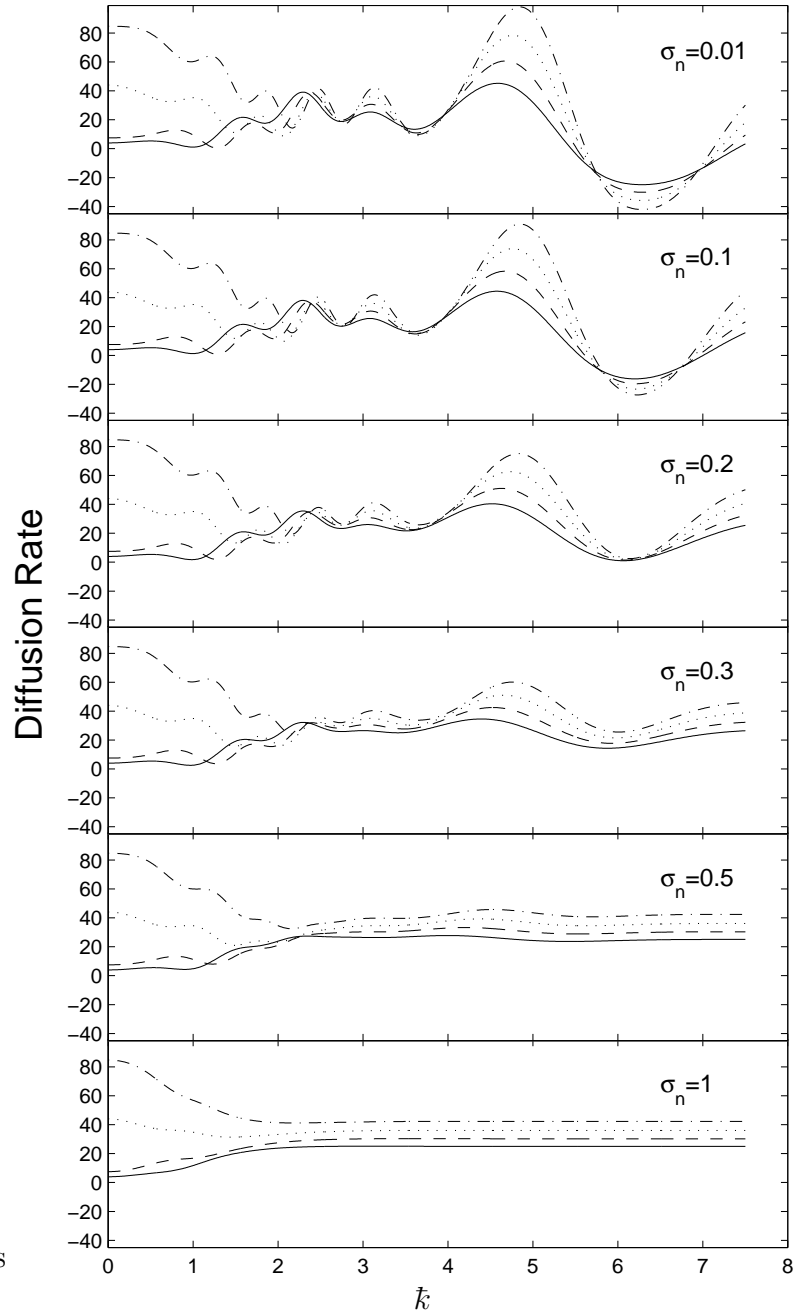


Figure 9.2: Diffusion rates in the second kick, $D(1)$, for the quantum δ -kicked rotor as a function of \bar{k} plotted for various values of $\sigma_n = \sigma_p/(2\hbar k_l)$, as predicted by (9.27). Kick strengths are $\kappa = 10$ (solid lines), 11 (dashed line), 12 (dotted line) and 13 (dash-dot line).

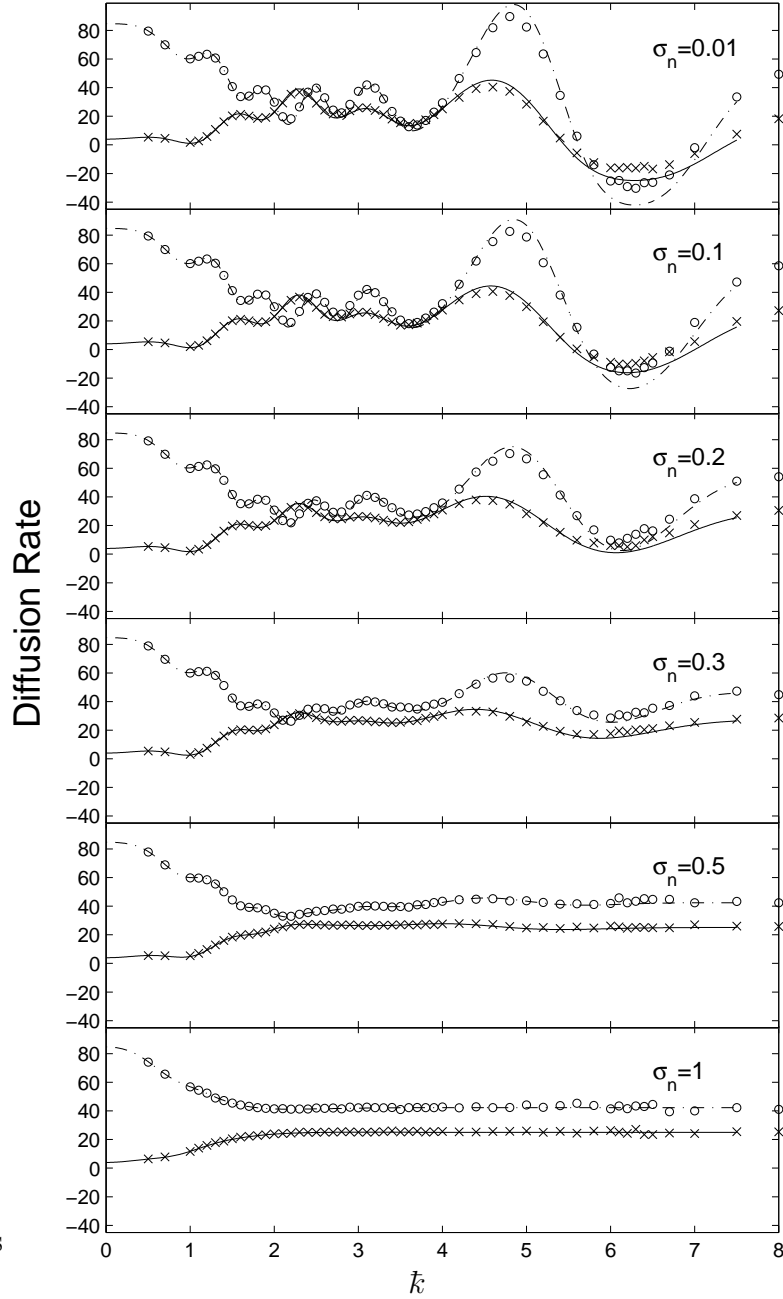


Figure 9.3: Comparison of simulated diffusion rates in the second kick, $D(1)$, for the quantum kicked rotor ($\alpha = 0.005$, $\eta = 10\%$) with analytical values predicted from (9.27). Kick strengths are $\kappa = 10$ (solid lines and crosses) and 13 (dash-dot line and circles).

the dependence of (9.29) on the width of the initial momentum distribution. The most interesting feature here is that the positions and number of the diffusion rate peaks are both strongly dependent on the value of ρ_0 . This is partly because different values of ρ_i give different weighting to different terms in the diffusion rate expression, but largely it results from the \hbar dependence of ρ_i that occurs due to the scaling of our momentum units.

Simulation results show excellent agreement with the analytical results, on a similar level to that shown in figure 9.3. Because it is possible to create initial momentum distributions with non-zero mean momentum with respect to the standing wave axis (see, for example, reference [63]), these results should be experimentally realisable.

9.3.3 Higher Kick Numbers

Figures 9.5, 9.6 and 9.7 show simulation results for the diffusion rates in the 3rd, 4th and 5th kicks respectively. The settling of the system into the initial quantum diffusion period is illustrated, with the behaviour contrasted for different values of σ_n . Essentially, the broader the initial momentum distribution, the more rapidly the system settles into the familiar pattern of diffusion with the structure as a function of \hbar for $0 < \hbar < 8$ encompassing an enhanced diffusion peak and a quantum resonance peak. This reflects the relative times at which the momentum distribution for the system becomes sufficiently broad that the σ_n dependent terms in the short time correlations become washed out. By the fifth kick ($n = 4$), all distributions with $\sigma_n \geq 0.1$ have essentially settled into the standard initial quantum diffusion regime, as described by Shepelyansky's formula, (3.35).

9.4 Quantum Superpositions in Initial States

It is of interest to consider what results we get for diffusion rates in the kicked rotor if we begin with something other than a Gaussian momentum distribution. One such example is if we take a distribution consisting of a coherent quantum superposition of two states, $\frac{1}{\sqrt{2}}(|p_0\rangle + |p_0 + 2\hbar k_l\rangle)$, mixed over an incoherent Gaussian distribution of p_0 values. This may possibly be generated experimentally either by way of Raman transitions or by the splitting of a Bose condensate, although there are possible problems with both of these techniques, mainly in relation to phase factors which are introduced between the superimposed states due to Doppler shifts. Thus it is presently unclear as to whether this distribution is experimentally realisable, but the results associated with it are interesting, and are possible indicators of what we might expect from more general superpositions between initial states, which may be experimentally realisable.

The derivation of (9.27) may be repeated for this superposition of states by including the cross terms from the expectation values in (9.8) between $|\rho_0\rangle$ and $|\rho_0 + \hbar k\rangle$. To do this, we proceed to the series expansions for the operators $\cos(\hat{\rho}_1)$, $\sin(\hat{\rho}_1)$, $\cos(2\hat{\rho}_1)$ and $\sin(2\hat{\rho}_1)$ acting on $|\rho_0\rangle$, and then when we evaluate the expressions in (9.8), we

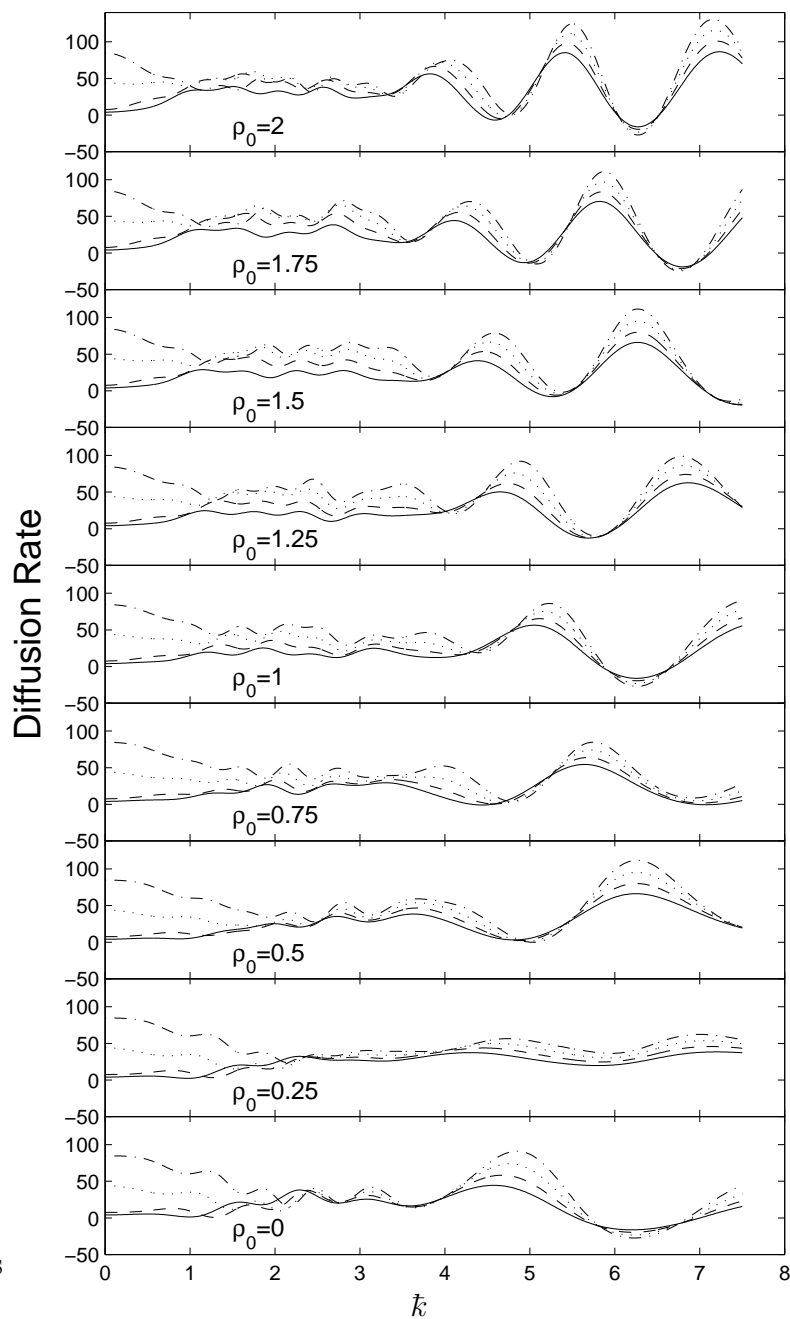


Figure 9.4: Diffusion rates in the second kick, $D(1)$, for the quantum δ -kicked rotor with $\sigma_n = 0.01$, plotted as a function of \bar{k} for various values of $\rho_0 = p_0/(2\hbar k_l)$, as predicted by (9.29). Kick strengths are $\kappa = 10$ (solid lines), 11 (dashed line), 12 (dotted line) and 13 (dash-dot line).

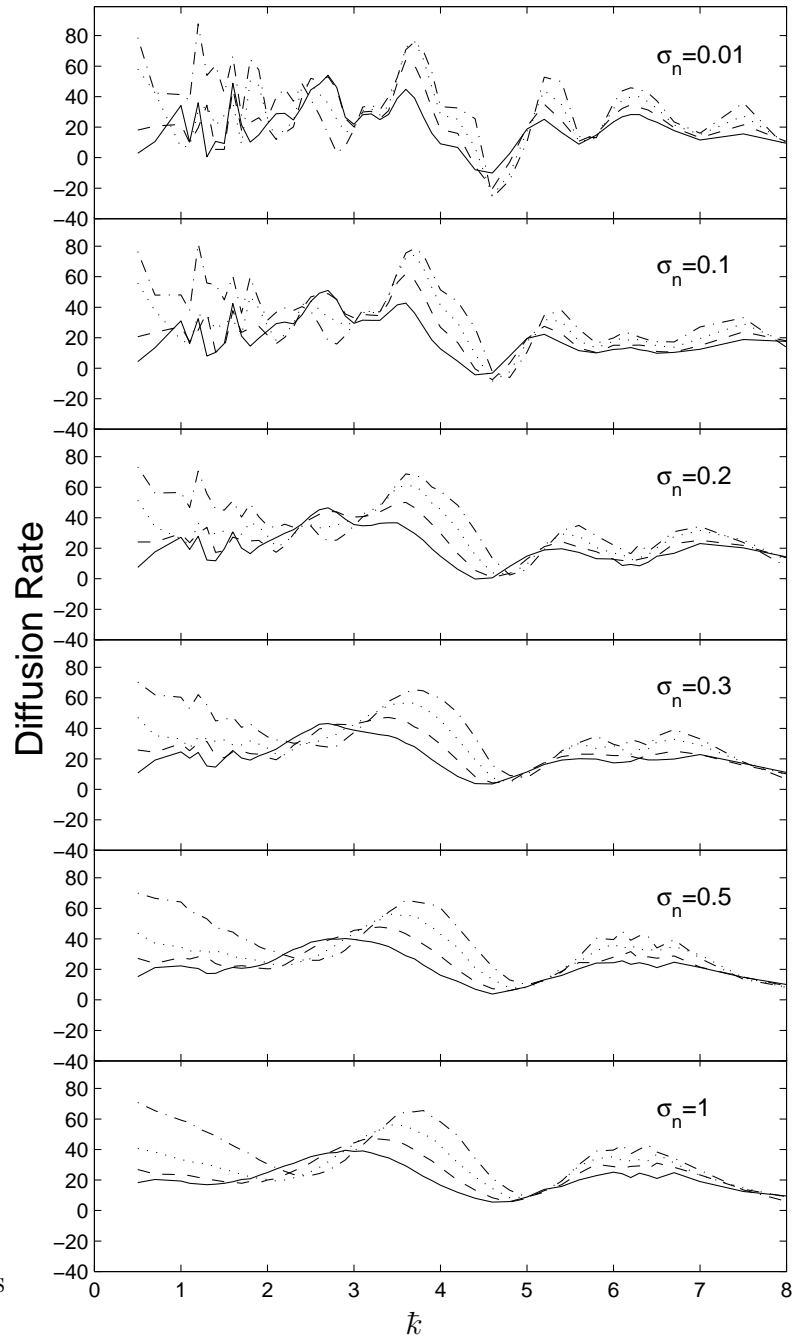


Figure 9.5: Simulated diffusion rates in the third kick, $D(2)$, for the quantum kicked rotor with $\alpha = 0.005$, and $\eta = 10\%$ plotted as a function of \bar{k} for various values of σ_n . Kick strengths are $\kappa = 10$ (solid lines), 11 (dashed line), 12 (dotted line) and 13 (dash-dot line).

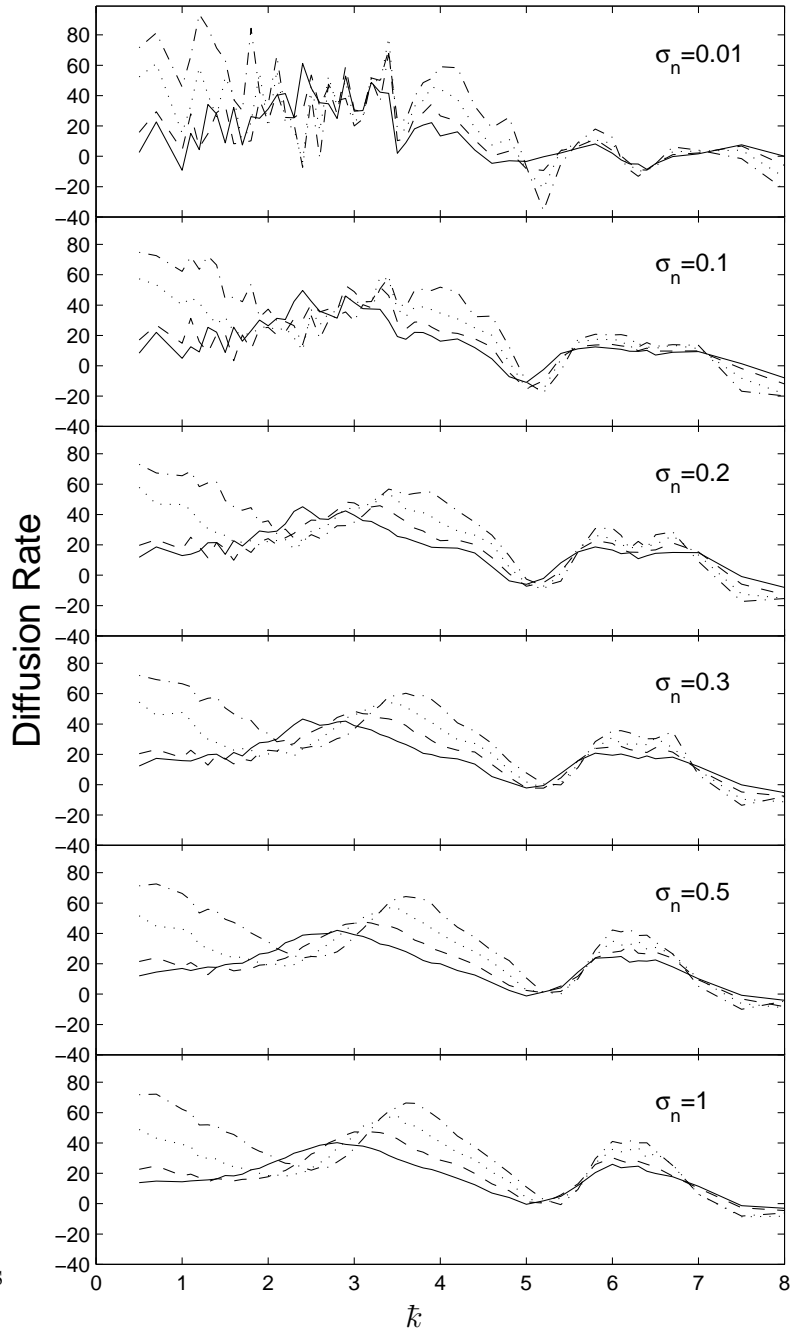


Figure 9.6: Simulated diffusion rates in the fourth kick, $D(3)$, for the quantum kicked rotor with $\alpha = 0.005$, and $\eta = 10\%$ plotted as a function of k for various values of σ_n . Kick strengths are $\kappa = 10$ (solid lines), 11 (dashed line), 12 (dotted line) and 13 (dash-dot line).

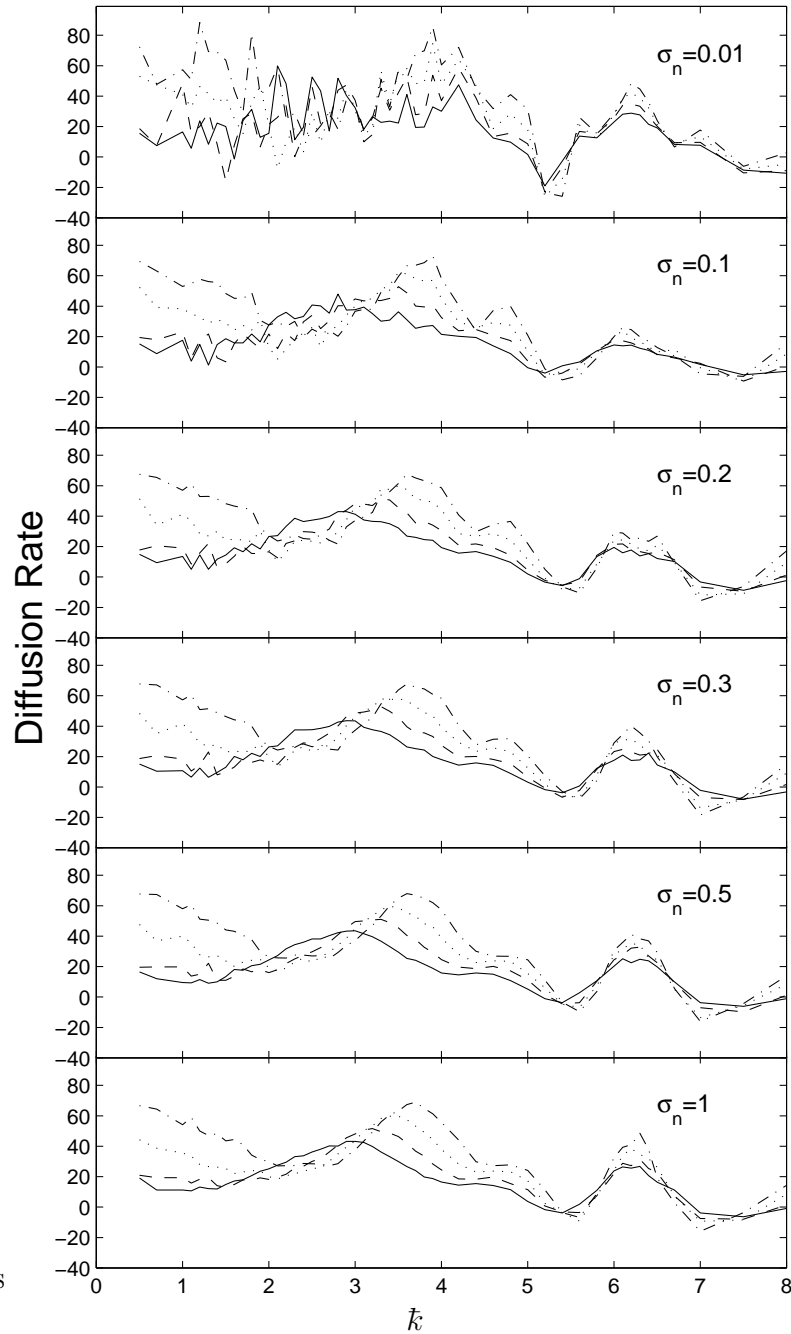


Figure 9.7: Simulated diffusion rates in the fifth kick, $D(4)$, for the quantum kicked rotor with $\alpha = 0.005$, and $\eta = 10\%$ plotted as a function of \bar{k} for various values of σ_n . Kick strengths are $\kappa = 10$ (solid lines), 11 (dashed line), 12 (dotted line) and 13 (dash-dot line).

retain only the terms which contain $|\rho_0 + \hbar k\rangle$.

We note that $\langle \rho_0 + \hbar k | \dots | \rho_0 \rangle = (\langle \rho_0 | \dots | \rho_0 + \hbar k \rangle)^\dagger$ for the terms in (9.8), and hence we evaluate

$$\frac{1}{2}(\langle p_0 | + \langle p_0 + 2\hbar k_l |) \dots (|p_0\rangle + |p_0 + 2\hbar k_l\rangle)$$

to give us an expression analogous to (9.26) for our coherent superposition. If we then average over an incoherent Gaussian distribution of ρ_0 values that is centred on $\rho_0 = 0$ with width σ_ρ , we obtain the final expression for the diffusion rate in the second kick, which is given by

$$\begin{aligned} 2D(1) = & \frac{\kappa^2}{2}[1 - J_2(K_{2q})e^{-2\sigma_\rho^2}(1 + \cos(2\hbar k))] \\ & - 2\kappa J_1(K_q)[\sigma_\rho^2 e^{-\sigma_\rho^2/2}(1 + \cos(\hbar k)) + \hbar k \sin(\hbar k)e^{-\sigma_\rho^2/2}] \\ & + \kappa^2(J_0(K_q) - J_2(K_q)) \cos(\hbar k/2)e^{-\sigma_\rho^2/2}(1 + \cos(\hbar k)) \\ & + \frac{\kappa^2}{4}[J_3(K_{2q})e^{-\sigma_\rho^2/2} \cos(\hbar k/2) + J_1(K_{2q})e^{-9\sigma_\rho^2/2} \cos(3\hbar k/2)] \\ & + \kappa[J_0(K_q)\sigma_\rho^2 e^{-2\sigma_\rho^2} \cos(\hbar k)] \\ & - \frac{\kappa^2}{2}[J_1(K_q) \cos(\hbar k/2)(1 - \cos(\hbar k))e^{-2\sigma_\rho^2}] \\ & + \frac{\kappa^2}{2}\{J_3(K_q) \cos(\hbar k/2) + J_1(K_q)e^{-2\sigma_\rho^2}[\cos(\hbar k/2) + \cos(3\hbar k/2)]\} \quad (9.30) \end{aligned}$$

where $K_q = 2\kappa \sin(\hbar k/2)/\hbar k$ and $K_{2q} = 2\kappa \sin(\hbar k)/\hbar k$. This result is shown in figure 9.8 along with simulated diffusion rates which again exhibit excellent agreement with our analytical values. We see that for small σ_n , the structure is very similar to that for an incoherent superposition of states - that is to say, we get the same result as we do from averaging (9.29) over $p_0 = 0$ and $p_0 = 2\hbar k_l$. However, as σ_n is increased, and Gaussian distributions centred on $\rho_0 = 0$ and $\rho_0 = 2\hbar k_l$ begin to overlap, the diffusion rates deviate substantially from the incoherent case (where the results, as they did for a single Gaussian distribution, will tend to quasilinear rates), and we observe significant structure, even for large values of σ_n . If we take the limit of large σ_ρ in (9.30), we see that

$$D(1) \approx (\kappa^2/4)\{1 + \cos(\hbar k/2)[J_3(K_q) - J_1(K_q)]\}. \quad (9.31)$$

This shows excellent agreement with simulation results for $\sigma_n = 4$, as is illustrated in figure 9.9, indicating that by taking a coherent superposition of initial momentum eigenstates, it may be possible to observe distinctly quantum structure in the second kick even with a large initial momentum spread. There may be problems in reproducing these results experimentally, both in producing the initial superposition, and in doing so with a large enough thermal distribution to observe the main predictions made here. However, further theoretical investigations should be made into the superpositions of a variety of states with different relative phase factors as it may be possible to set up some particular combination of such states using Raman transitions.

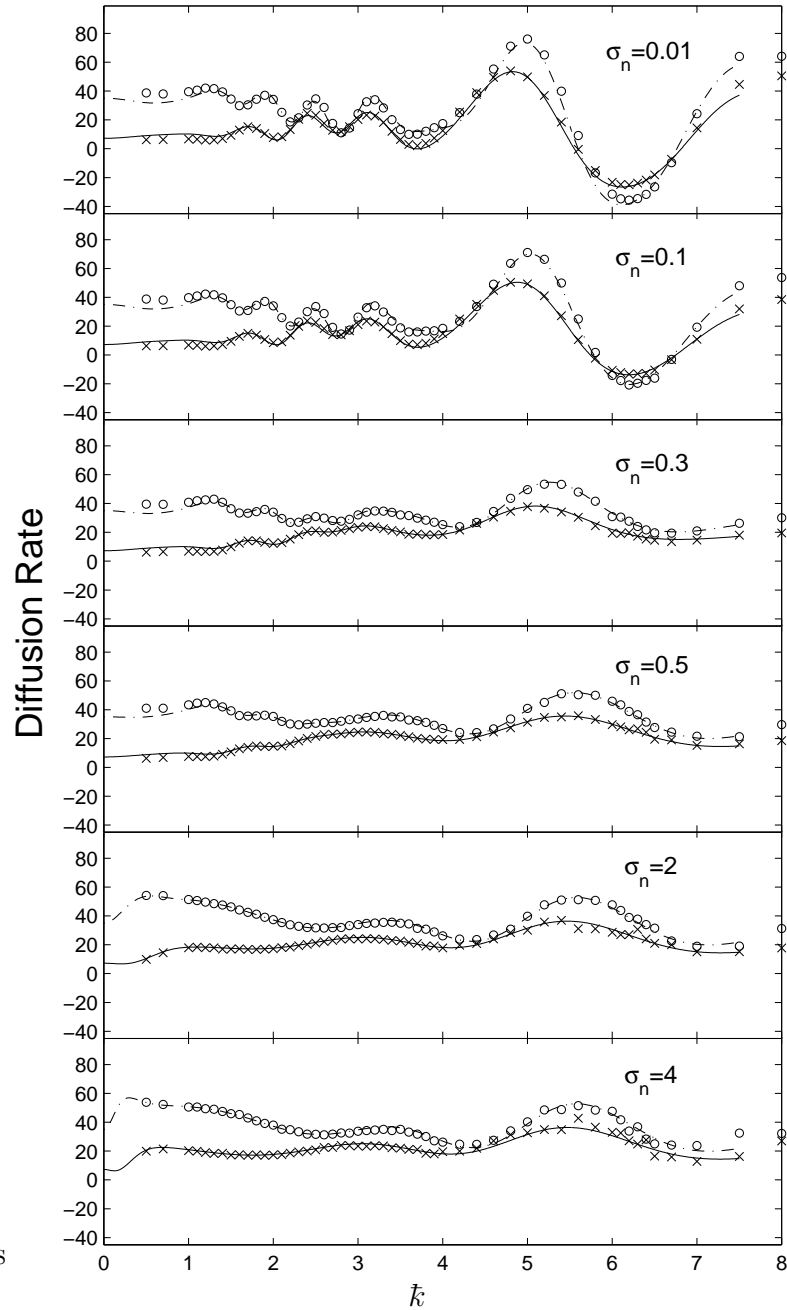


Figure 9.8: Simulated diffusion rates (points) and analytical predictions (lines) for the second kick in the quantum kicked rotor with $\alpha = 0.005$ and $\eta = 10\%$. The initial momentum distribution used is a coherent superposition of states separated by $2\hbar k_l$, which are sampled from a Gaussian distribution centred on $\rho_0 = 0$ with various values of σ_n . Kick strengths are $\kappa = 10$ (solid lines, crosses) and $\kappa = 12$ (dash-dot line, circles).

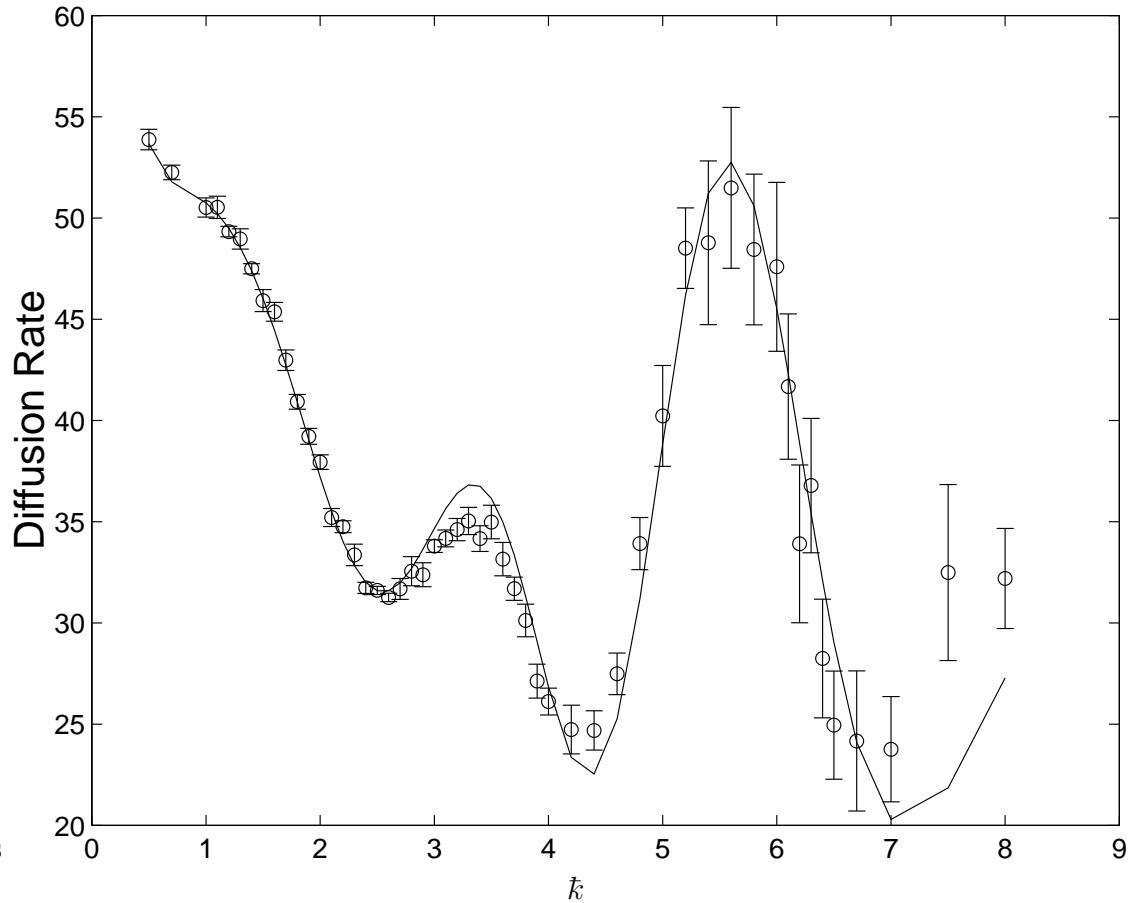


Figure 9.9: Comparison of analytical prediction (line) from (9.31) with simulated diffusion rates (points) in the second kick for the quantum kicked rotor with $\alpha = 0.005$, $\kappa = 12$ and $\eta = 10\%$, and with an initial coherent superposition of states separated by $2\hbar k_l$, and initially sampled from a Gaussian distribution centred on $\rho_0 = 0$ with $\sigma_n = 4$.

Chapter 10

Conclusion and Future Directions

10.1 Conclusions

Prior to the investigations contained in this thesis, the understanding of diffusion resonances in action space for a kicked rotor was limited to the work performed by Bhattacharya *et al.* involving decoherence through a continuous position measurement and the resulting diffusion rates in the late time regime [1]. This was true despite the fact that Shepelyansky's calculation of quantum correlations, made in the 1980s [25, 16], reveals such a resonance structure in the initial quantum diffusion regime which until our study had not, to our knowledge, been properly investigated. In our work we have confirmed by numerical simulation the existence of such structure in the specific experimental setting of the atom optics kicked rotor, and we have observed similar and related structures under various diffusion regimes. We have also investigated the effect of amplitude noise and decoherence on these structures, and we have used these structures as a device to probe the more fundamental effects of the different types of noise.

10.1.1 Spontaneous Emission Decoherence

Through numerical simulations of the atom optics kicked rotor, we have observed diffusion resonances as a function of \bar{k} in the initial quantum diffusion regime. These resonances, which are in very good agreement with Shepelyansky's results, consist of an enhanced diffusion peak in the range $0 < \bar{k} < 2\pi$ and quantum resonance peaks at 2π and higher integer multiples of 2π . The enhanced diffusion peak shifts to the right and increases in magnitude as κ , the kick strength, is increased, and for sufficiently large values of κ we observe the appearance of additional diffusion resonances which also shift and scale in a similar fashion to the original peak. From classical simulations we observed no change in the diffusion rates for large amounts of spontaneous emission noise, indicating that the only significant effects that this type of noise can have on the diffusion rates of the system come from its decoherence properties, and not directly from the momentum recoils themselves. The timescale of the decoherence effects is

limited by the fact that we must keep levels of spontaneous emissions low enough that the population of atoms in the excited state is reasonably small (otherwise our Hamiltonian deviates from that of the kicked rotor). Thus it is not surprising that the structures in the initial quantum diffusion rates (for kick numbers, $n \ll 10$, and probability of spontaneous emission per kick $\eta \sim 10\%$) are unaffected by the addition of spontaneous emission noise on physically realisable levels.

The inclusion of decoherence through spontaneous emissions disrupts the settling of the system into a dynamically localised state, and instead we observe a final, late time diffusion regime. The diffusion rate in this regime exhibits a similar resonance structure to that found for the initial quantum diffusion period. In fact, based on the successful predictions of our semi-analytical model it appears that when spontaneous emission events occur at a particular time, correlations between positions before and after that time are completely washed out. This results in a “locking in” of the early time diffusion rates because the only correlations which remain important are those on the same timescale as, or on shorter timescales than, that on which the spontaneous emission events occur. The early time diffusion rates, naturally, are based only on short timescale correlations.

Perhaps the most important result in this part is that for sufficiently large values of η and appropriate values of κ , the late time diffusion rates in the quantum system can be higher than those in the corresponding classical system. This is because early time quantum diffusion rates, which can be higher than the corresponding late time classical diffusion rates, become locked in by the addition of spontaneous emission noise. This is strange, because we are more accustomed to uniquely quantum effects in the kicked rotor system slowing the diffusion rate (as dynamical localisation does), whereas here decoherence combines with quantum correlations to accelerate the diffusion to a rate greater than that observed in the corresponding classical system. It is particularly interesting that this phenomenon occurs only in the enhanced diffusion peaks found in the range $0 < \hbar k < 2\pi$, that is, when the classical action is of the order of \hbar . This combination of quantum correlations and decoherence to produce resonances exhibiting “super-diffusion” is thus a characteristic of the mesoscopic region which constitutes the boundary between quantum and classical behaviour.

Our results make those of Bhattacharya *et al.* [1] experimentally relevant. They also give us insight into the behaviour of the quantum kicked rotor in the mesoscopic regime, and provide experimentally measurable results for diffusion resonances in the kicked rotor system. In addition they provide a model for the destruction of quantum correlations in the kicked rotor by decoherence in the form of spontaneous emission events, which is verified by the comparison of predicted and simulated late time diffusion rates.

10.1.2 Amplitude Noise

The first thing that we notice from our numerical simulations with amplitude noise included is that, unlike spontaneous emission noise, amplitude noise has the ability to

affect correlations on very short timescales, and sufficiently large amounts of amplitude noise can disrupt the initial quantum diffusion rates. Generally, for large amounts of noise, the system is returned to near-classical behaviour, with the diffusion rates becoming close to the quasilinear value aside from some additional diffusion produced by the noise (this increase is also observed in the classical system). Again we observe an enhanced diffusion peak and a quantum resonance peak with similar properties to those found with spontaneous emission decoherence, but the enhanced diffusion peak is washed out for sufficiently large amounts of noise (around 100%-200%). The quantum resonance peak remains intact even for 200% spontaneous emission noise, indicating that it is more difficult to disrupt correlations in less macroscopic systems. All of these results agree well with a generalised version of Shepelyansky's formula.

The effects of amplitude noise on a longer time scale are particularly interesting, because while the enhanced diffusion peak appears for the late time rates and exhibits similar properties to those observed in the initial quantum diffusion rates (both as a function of κ and noise level), no quantum resonance peak occurs in this regime. This must be a product of the manner in which amplitude noise disrupts correlations. It obviously does not simply make longer timescale correlations completely unimportant as we observed with spontaneous emission noise, but instead changes the values of the individual correlations whilst leaving their importance in terms of the settling of the system into a late time diffusion regime intact. Around the quantum resonance peak, the inclusion of long time correlations results in the system settling to a diffusion rate of zero. Note that as with observations of dynamical localisation, we often have to extend well beyond 30 or 40 kicks worth of correlations to notice the full effect of the disappearance of the quantum resonance peak.

10.1.3 Combination of Spontaneous Emissions and Amplitude Noise

The difference in the mechanisms of correlation disruption is seen even more clearly when we combine amplitude noise with spontaneous emission noise. The early time diffusion rates in this regime are the same as those that occur for amplitude noise, as we would expect given that amplitude noise disrupts the values of the correlations on all timescales, whereas spontaneous emission decoherence "waters down" correlations over longer time scales. The late time results, meanwhile, show features from both types of noise, most notably a quantum resonance peak which increases in magnitude as we increase η for a fixed level of amplitude noise. This indicates that amplitude noise is disrupting the values of the correlations, whilst spontaneous emission noise is fixing the timescales on which correlations will become less significant altogether, as the early time correlations with amplitude noise give diffusion rates which exhibit a quantum resonance peak. In a sense, spontaneous emissions in this context appear to "lock in" the early time diffusion rates as already modified by the amplitude noise.

10.1.4 Unscaled Units

Our work on the diffusion resonances in unscaled, or “physical” units presents an alternative viewpoint for looking at diffusion resonances in both early and late time regimes, and with the addition of spontaneous emission noise and amplitude noise. Systems expressed in this way are more convenient to measure experimentally, and are very useful for comparing experimental and theoretical predictions, even though comparisons with the corresponding classical systems become more complex (it is important to note that the diffusion resonance peaks in the periodic structure exhibited in physical units do still offer the possibility for the observation of “super-diffusion”). Our simulations have exhibited good qualitative and often impressive quantitative agreement with recent experimental results, as was demonstrated in chapter 8.

10.1.5 Narrow Initial Momentum Distributions

The most commonly used definition of the momentum diffusion rate in theoretical investigations of the quantum kicked rotor is modified slightly from the rate of increase in mean energy in order to produce a more convenient expression to work with in terms of the two time $\sin(\phi)$ correlation function. When these correlations are evaluated (see for example appendix B), it is assumed that there is a uniform distribution of both initial positions and initial momenta. Because of this, we obtain from this definition a diffusion rate of $\kappa^2/4$ for the second kick, that is, the quasilinear value. It is thus often accepted that this rate is characteristic of the momentum diffusion in the second kick. However, our investigation of narrow initial momentum distributions has shown distinctly quantum structure in this diffusion rate as a function of \bar{k} . Simulation results have shown good agreement with an expression derived by Scott Parkins [64], and these results are likely to be experimentally realisable. Interesting structure is also exhibited for broader initial momentum distributions when we take a coherent quantum superposition of states in the initial distribution with states translated by $2\hbar k_l$. We have derived an analytical expression which again shows excellent agreement with simulation results for this structure, although there may be problems with the experimental realisability of these initial superpositions.

10.2 Future Directions

There are various future directions and extensions which are possible for this research. It would firstly be very good to see experimental realisations of the results predicted in the initial quantum diffusion regime, and in the late time diffusion regime generated by the addition of spontaneous emission noise. In the case of the late time diffusion rates, there have already been various promising measurements made, especially in the context of physical momentum units, and it will be interesting to see these extended to varying levels of spontaneous emission noise with the possibility of an experimental observation of super-diffusion. It will also be interesting to see experimental realisations of the initial and late time diffusion rates with amplitude noise, as well as the diffusion structure in the rates for the second kick with narrow initial momentum distributions.

There were notable differences in the structures observed in our simulations with the two different styles of spontaneous emission noise used in the Auckland experiments and the Austin experiments, particularly in the symmetry or the lack thereof about the quantum resonance peak. It would be interesting to investigate this more closely, especially in terms of whether the asymmetry is caused by the position dependence of the Auckland-style noise or by the occurrence of spontaneous emissions only during the kick rather than during the entire cycle.

The structure in the second kick has not been investigated in the context of amplitude noise, and given the disruption of initial quantum diffusion rates (i.e., the diffusion rates in the third kick and for a few kicks afterwards) by amplitude noise, such a study has the potential to generate interesting effects as well as useful information about how amplitude noise affects correlations on very short time scales. It would also be useful to have a better understanding of how amplitude noise alters correlations on longer time scales, and it would be particularly useful to have a general analytical theory for this process.

Further work needs to be done on investigating coherent superpositions of initial states in experimentally realisable combinations. It is possible that states may be realised which provide interesting structure in the second kick, and if so then such structure will probably also exist for other kicks in the early time diffusion regime.

Two larger future directions could be the introduction of period noise and the generalisation of all of these results to a two-dimensional kicked rotor system. The introduction of period noise, i.e., variation in the time separation of the kicks, should drive the system towards classical behaviour, and should disrupt the quantum coherences which produce dynamical localisation. It would be interesting to see whether this type of noise produces similar structures in the diffusion rates to those observed with amplitude noise and spontaneous emission noise. The two-dimensional kicked rotor, meanwhile, has also not been well investigated in terms of the relationship between decoherence and diffusion through KAM tori in phase space, and so would be an interesting system to realise experimentally in the future. It would thus be useful and experimentally interesting to have an understanding of diffusion resonances in the two dimensional system.

It is also possible that these types of resonance structures could exist in the mesoscopic regime for other quantum systems. It would be interesting to see if such a pattern in quantum behaviour exists, with a view to bringing about a better understanding of the behaviour of quantum systems in general as they undergo transitions to classical behaviour.

Appendix A

Bessel Functions

A.1 The Bessel Differential Equation

Bessel functions, which arise in various contexts throughout this work are defined as solutions $C_\nu(z)$ of the Bessel differential equation,

$$z^2 \frac{d^2 C}{dz^2} + z \frac{dC}{dz} + (z^2 - \nu^2)C = 0, \quad (\text{A.1})$$

where z is a complex variable, and ν is a complex parameter.

Various functions $C_\nu(z)$ exist, and they are categorized and given symbols in the following way:

$J_\nu(z)$	Ordinary Bessel Functions of the First Kind
$Y_\nu(z)$	Ordinary Bessel Functions of the Second Kind
$H_\nu^{(1)}(z), H_\nu^{(2)}(z)$	Hankel Functions.

Complete Solutions to the Bessel Differential Equation may be formed from

$$\begin{aligned} c_1 J_\nu(z) + c_2 J_{-\nu}(z) & \quad \text{if } \nu \text{ is not an integer} \\ c_1 J_\nu(z) + c_2 Y_\nu(z) & \quad \text{for any complex } \nu \\ c_1 H_\nu^{(1)}(z) + c_2 H_\nu^{(2)}(z) & \quad \text{for any complex } \nu. \end{aligned}$$

The properties of all of these functions are well documented in Abramowitz and Stegun[65], and are also summarised well in the *CRC Standard Mathematical Tables and Formulae*[66]. A brief synopsis of some of the most important properties is given here to facilitate an understanding of the results presented in this thesis which involve the ordinary Bessel functions of the first kind, $J_\nu(z)$. Graphs of $J_\nu(z)$ and $Y_\nu(z)$ are shown in figures A.1 and A.2 for $\nu = 0, 1, 2$ and $z \in [0, 15]$.

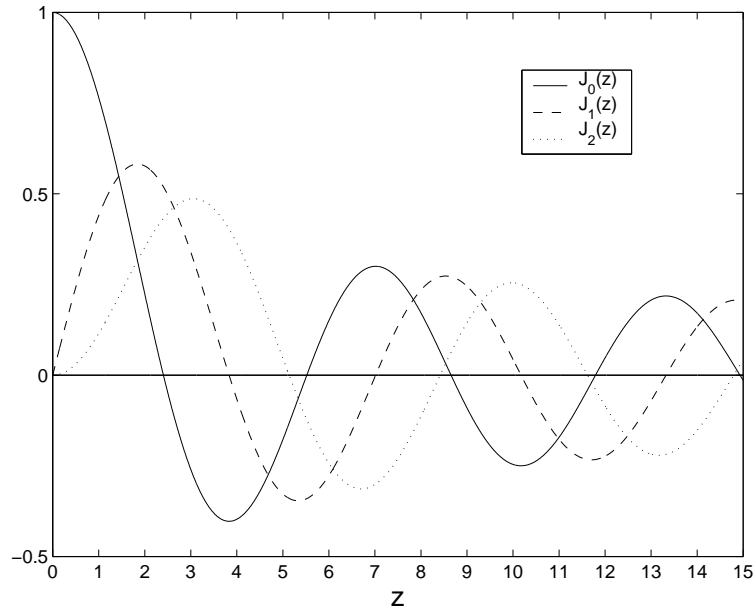


Figure A.1: Ordinary Bessel functions of the first kind, $J_\nu(z)$ for $\nu = 0, 1, 2$

A.2 Relationships between solutions

Bessel functions of the second kind, $Y_\nu(z)$ may be expressed in terms of Bessel functions of the first kind, $J_\nu(z)$ as

$$Y_\nu(z) = \frac{\cos(\nu\pi)J_\nu(z) - J_{-\nu}(z)}{\sin(\nu\pi)}, \quad (\text{A.2})$$

where if $\nu = n$ for integer n , we must take the limit of the right hand side of this expression as $\nu \rightarrow n$.

The Hankel Functions, $H_\nu^{(i)}(z)$ for $i = 1, 2$, are formed from combinations of the ordinary Bessel functions as

$$H_\nu^{(1)}(z) = J_\nu(z) + iY_\nu(z) \quad (\text{A.3a})$$

$$H_\nu^{(2)}(z) = J_\nu(z) - iY_\nu(z). \quad (\text{A.3b})$$

Note also that for ordinary Bessel functions of integer order n ,

$$J_{-n}(z) = (-1)^n J_n(z). \quad (\text{A.4})$$

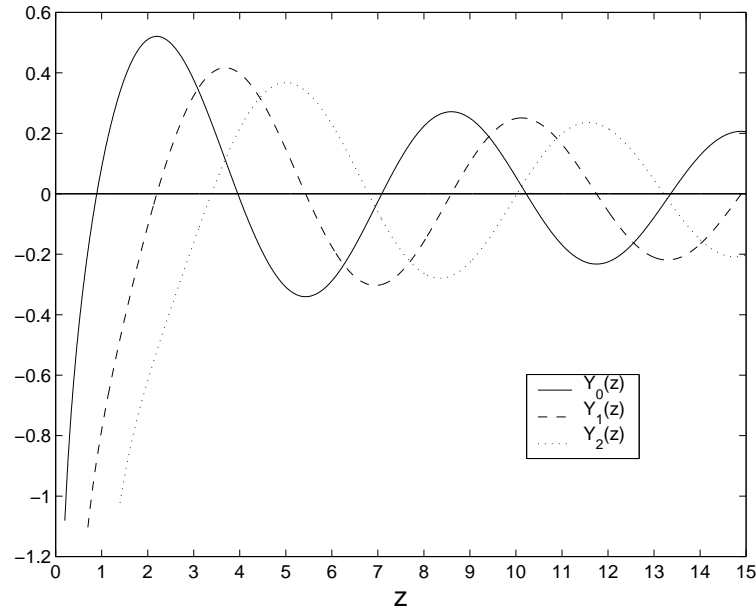


Figure A.2: Ordinary Bessel functions of the second kind, $Y_\nu(z)$ for $\nu = 0, 1, 2$

A.3 Series Expansions

Ordinary Bessel Functions of the first kind may be expressed as a series expansion in z ,

$$J_\nu(z) = \left(\frac{z}{2}\right)^\nu \sum_{n=0}^{\infty} \frac{(-1)^n (z/2)^{2n}}{\Gamma(n + \nu + 1)n!}, \quad (\text{A.5})$$

where $\Gamma(z)$ denotes the gamma function, defined by

$$\Gamma(z) = \int_0^{\infty} t^{z-1} e^{-t} dt, \quad (\text{A.6})$$

where $\Re(z) > 0$. Note that $\Gamma(n + 1) = n!$ for integer n .

A.4 Integral Expressions

For $\Re(z) > 0$ we can express the ordinary Bessel Functions through the following integral expressions:

$$J_\nu(z) = \frac{1}{\pi} \int_0^\pi \cos[\nu\theta - z \sin(\theta)] d\theta - \frac{\sin(\nu\pi)}{\pi} \int_0^\infty e^{-\nu t - z \sinh t} dt \quad (\text{A.7a})$$

$$Y_\nu(z) = \frac{1}{\pi} \int_0^\pi \sin[z \sin(\theta) - \nu\theta] d\theta - \int_0^\infty [e^{\nu t} + e^{-\nu t} \cos(\nu\pi)] e^{-z \sinh t} dt. \quad (\text{A.7b})$$

For $\nu = n$ for some integer n , we can write

$$J_n(z) = \frac{1}{\pi} \int_0^\pi \cos[n\theta - z \sin(\theta)] d\theta. \quad (\text{A.7c})$$

A.5 Recurrence Relationships

For $C_\nu(z) = J_\nu(z), Y_\nu(z), H_\nu^{(1)}(z), H_\nu^{(2)}(z)$, we have the relationships:

$$C_{\nu-1}(z) + C_{\nu+1}(z) = \frac{2\nu}{z} C_\nu(z) \quad (\text{A.8a})$$

$$C_{\nu-1}(z) - C_{\nu+1}(z) = 2 \frac{dC_\nu(z)}{dz}. \quad (\text{A.8b})$$

A.6 Bessel Functions of Large Order

In the case of large ν we may approximate the behaviour of ordinary Bessel Functions by the following expressions

$$J_\nu(z) \sim \frac{1}{\sqrt{2\pi\nu}} \left(\frac{ez}{2\nu}\right)^\nu \quad (\text{A.9a})$$

$$Y_\nu(z) \sim -\sqrt{\frac{2}{\pi\nu}} \left(\frac{ez}{2\nu}\right)^{-\nu} \quad (\text{A.9b})$$

$$(\text{A.9c})$$

A.7 Generating Function and Related Series

The generating function [65] for ordinary Bessel functions of the first kind is given by

$$e^{\frac{1}{2}z(t-\frac{1}{t})} = \sum_{k=-\infty}^{\infty} t^k J_k(z). \quad (\text{A.10})$$

The related series expansions, which are the main relations through which Bessel Functions arise in the work presented in this thesis are given by

$$\cos[z \sin(\theta)] = J_0(z) + 2 \sum_{k=1}^{\infty} J_{2k}(z) \cos(2k\theta) \quad (\text{A.11a})$$

$$\sin[z \sin(\theta)] = 2 \sum_{k=0}^{\infty} J_{2k+1}(z) \sin[(2k+1)\theta] \quad (\text{A.11b})$$

$$\cos[z \cos(\theta)] = J_0(z) + 2 \sum_{k=1}^{\infty} (-1)^k J_{2k}(z) \cos(2k\theta) \quad (\text{A.11c})$$

$$\sin[z \cos(\theta)] = 2 \sum_{k=0}^{\infty} (-1)^k J_{2k+1}(z) \cos[(2k+1)\theta]. \quad (\text{A.11d})$$

Interesting special cases of these expansions include the following expressions:

$$\cos(z) = J_0(z) + 2 \sum_{k=1}^{\infty} (-1)^k J_{2k}(z) \quad (\text{A.12a})$$

$$\sin(z) = 2 \sum_{k=0}^{\infty} (-1)^k J_{2k+1}(z) \quad (\text{A.12b})$$

$$1 = J_0(z) + 2 \sum_{k=1}^{\infty} J_{2k}(z). \quad (\text{A.12c})$$

A.8 Neumann's Addition Theorem

Neumann's Addition Theorem states that for any Bessel function $C_\nu(z)$,

$$C_\nu(u \pm v) = \sum_{k=-\infty}^{\infty} C_{\nu \mp k}(u) J_k(v), \quad (\text{A.13})$$

for any v and u such that $|v| < |u|$. This restriction is not necessary if $C_\nu(z) = J_\nu(z)$ and ν is an integer. One special case of this theorem is

$$1 = J_0^2(z) + 2 \sum_{k=1}^{\infty} J_k^2(z). \quad (\text{A.14})$$

Appendix B

Calculation of Correlations

B.1 Introduction

The computations of the classical diffusion rate (2.64) and Shepelyansky's formula (3.35) are based on the evaluation of the correlations

$$C_s(i - j) = \langle \sin(\phi_i) \sin(\phi_j) \rangle = \langle \sin(\phi_{i-j}) \sin(\phi_0) \rangle$$

for the classical and quantum kicked rotors respectively. The classical correlations were originally calculated by Rechester and White [12], while the quantum correlations were originally evaluated by Shepelyansky [25, 16]. In this appendix we present for completeness an outline of the method for evaluating these correlations in the case of the generalised standard map, which allows for amplitude noise on the kick strength, i.e.,

$$\rho_{n+1} = \rho_n + \kappa_n \sin(\phi_n), \tag{B.1a}$$

$$\phi_{n+1} = \phi_n + \rho_{n+1}. \tag{B.1b}$$

Our outline is based on a very good summary by Steck [15] of the method used by Shepelyansky to evaluate the correlations.

B.2 Classical Correlations

We want to evaluate the correlation function

$$C(n) = \langle \kappa_0 \sin(\phi_0) \kappa_n \sin(\phi_n) \rangle, \tag{B.2}$$

assuming a uniform initial position distribution. We can rewrite this correlation function in terms of complex exponentials as

$$C(n) = -\frac{\kappa_0 \kappa_n}{4} \langle e^{i\phi_0} e^{i\phi_n} - e^{i\phi_0} e^{-i\phi_n} - e^{-i\phi_0} e^{i\phi_n} + e^{-i\phi_0} e^{-i\phi_n} \rangle. \tag{B.3}$$

From (A.10), we can write

$$\exp[i\kappa \sin(\phi)] = \sum_{s=-\infty}^{\infty} J_s(\kappa) e^{is\phi}, \quad (\text{B.4})$$

so that

$$\begin{aligned} e^{i\phi_1} &= \exp[i(\phi_0 + \rho_0 + \kappa_0 \sin \phi_0)] \\ &= \sum_{s_0=-\infty}^{\infty} J_{s_0}(\kappa_0) e^{i(s_0+1)\phi_0} e^{i\rho_0}. \end{aligned} \quad (\text{B.5})$$

Through successive applications of this formula, we can obtain similar expressions for $e^{i\phi_2}$ and $e^{i\phi_3}$. Reversing the order of indices, we obtain

$$e^{i\phi_2} = \sum_{s_0, s_1=-\infty}^{\infty} J_{s_0}[\kappa_1] J_{s_1}[\kappa_0(s_0+2)] e^{i(s_1+s_0+1)\phi_0} e^{i(s_0+2)\rho_0}, \quad (\text{B.6})$$

$$e^{i\phi_3} = \sum_{s_0, s_1, s_2=-\infty}^{\infty} J_{s_0}[\kappa_2] J_{s_1}[\kappa_1(s_0+2)] J_{s_2}[\kappa_0(2s_0+s_1+3)] \quad (\text{B.7})$$

$$\times e^{i(s_2+s_1+s_0+1)\phi_0} e^{i(2s_0+s_1+3)\rho_0}. \quad (\text{B.8})$$

The pattern resulting from successive iterations is now clear. We write

$$\alpha_0 = s_0 + 1 \quad (\text{B.9a})$$

$$\alpha_{n+1} = \alpha_n + s_{n+1}, \quad (\text{B.9b})$$

and

$$\beta_0 = 1 \quad (\text{B.10a})$$

$$\beta_{n+1} = \beta_n + \alpha_n, \quad (\text{B.10b})$$

allowing us to express the exponential function of ϕ_n as

$$e^{i\phi_n} = \sum_{s_0, \dots, s_{n-1}=-\infty}^{\infty} J_{s_0}(\kappa_{n-1}\beta_0) J_{s_1}(\kappa_{n-2}\beta_1) \dots J_{s_{n-1}}(\kappa_0\beta_{n-1}) e^{i\alpha_{n-1}\phi_0} e^{i\beta_{n-1}\rho_0}. \quad (\text{B.11})$$

Noting that the average over a uniform distribution in position and momentum gives

$$\langle e^{im\phi_0} e^{in\rho_0} \rangle = \delta_{m,0} \delta_{n,0} \quad (\text{B.12})$$

for integer m and n , where $\delta_{a,b}$ is a Kronecker delta, we obtain

$$\begin{aligned} C(n) &= \frac{\kappa_0 \kappa_n}{2} \sum_{s_0, \dots, s_{n-1}=-\infty}^{\infty} J_{s_0}(\kappa_{n-1}\beta_0) J_{s_1}(\kappa_{n-2}\beta_1) \dots J_{s_{n-1}}(\kappa_0\beta_{n-1}) \\ &\quad \times (\delta_{\alpha_{n-1},1} - \delta_{\alpha_{n-1},-1}) \delta_{\beta_{n-1},0}. \end{aligned} \quad (\text{B.13})$$

The first few correlations are thus given by

$$C(0) = \frac{\kappa_0^2}{2} \quad (\text{B.14a})$$

$$C(1) = 0 \quad (\text{B.14b})$$

$$C(2) = -\frac{\kappa_0\kappa_2}{2} J_2(\kappa_1) \quad (\text{B.14c})$$

$$C(3) = \frac{\kappa_0\kappa_3}{2} [J_3(\kappa_1)J_3(\kappa_2) - J_1(\kappa_1)J_1(\kappa_2)] \quad (\text{B.14d})$$

$$C(4) = \frac{\kappa_0\kappa_4}{2} [J_2(\kappa_1)J_2(\kappa_3) + O(\kappa^{-3/2})], \quad (\text{B.14e})$$

where $O(\kappa^{-3/2})$ denotes a collection of terms of the order of $\kappa^{-3/2}$, where κ is a statistical average over the κ_n . Substituting these terms into (2.60) with $\kappa_n = \kappa$ gives the classical diffusion rate equation (2.64), and if we take a statistical average over some distribution of κ_n values, we obtain the generalised version of this with amplitude noise, (7.1).

B.3 Quantum Correlations

The equivalent calculation for the quantum correlations follows the same general pattern, but is rather more complicated due to the commutation relations involved. We want to calculate the (symmetrised) correlation function

$$C_q(n) = \frac{\kappa_0\kappa_n}{2} \langle \psi_0 | \sin \hat{\phi}_n \sin \hat{\phi}_0 + \sin \hat{\phi}_0 \sin \hat{\phi}_n | \psi_0 \rangle, \quad (\text{B.15})$$

where $\hat{\phi}_n$ and $\hat{\rho}_n$ are Heisenberg picture position and momentum operators which obey the quantum version of the generalised standard map (B.1), and $|\psi_0\rangle$ is approximately uniform over phase space, so that

$$\langle \psi_0 | e^{im\hat{\phi}_0} e^{in\hat{\rho}_0} | \psi_0 \rangle = \delta_{m,0} \delta_{n,0}. \quad (\text{B.16})$$

We begin by expanding the exponential operator

$$e^{i\hat{\phi}_1} = e^{i(\hat{\phi}_0 + \hat{\rho}_0 + \kappa_0 \sin \hat{\phi}_0)} = \exp[i\hat{\rho}_0 + i\hat{\phi}_0 + \frac{\kappa_0}{2} e^{i\hat{\phi}_0} - \frac{\kappa_0}{2} e^{-i\hat{\phi}_0}]. \quad (\text{B.17})$$

We then factorise this exponential using two special cases of the Baker-Hausdorff relation, firstly that

$$e^{\hat{A} + \hat{B}} = e^{\hat{B}} e^{\hat{A}} e^{[\hat{A}, \hat{B}]/2},$$

for \hat{A} and \hat{B} such that $[\hat{A}, [\hat{A}, \hat{B}]] = [\hat{B}, [\hat{B}, \hat{A}]] = 0$, [(9.5)], and secondly that

$$\exp(\hat{A} + \hat{B}) = \exp[\hat{B}(e^c - 1)/c] \exp(\hat{A}),$$

for \hat{A} and \hat{B} such that $[\hat{A}, \hat{B}] = c\hat{B}$ where c is a constant [(9.11)]. This proceeds similarly to the factorisation of $\exp(i\hat{\rho}_1)$ in section 9.3, and results in the expression

$$e^{i\hat{\phi}_1} = \exp \left[i \frac{2\kappa_0}{\bar{k}} \sin(\bar{k}/2) \sin(\hat{\phi}_0 + \bar{k}/2) \right] e^{i\hat{\phi}_0} e^{i\hat{\rho}_0} e^{i\bar{k}/2}. \quad (\text{B.18})$$

Making use of the Bessel function expansion (B.4) we obtain the result

$$e^{i\hat{\phi}_1} = \sum_{s_0=-\infty}^{\infty} J_{s_0}(K_{q,0}) \exp[i\bar{k}(s_0 + 1)/2] e^{i(s_0+1)\hat{\phi}_0} e^{i\hat{\rho}_0}, \quad (\text{B.19})$$

where $K_{q,i} = 2\kappa_i \sin(\bar{k}/2)/\bar{k}$. The exponential operator $\exp(i\hat{\phi}_n)$ may be found using multiple iterations of the Bessel function expansion, and normally ordering the operators. The result obtained by Shepelyansky for this is

$$e^{i\hat{\phi}_n} = \sum_{s_0, \dots, s_{n-1}=-\infty}^{\infty} J_{s_0}(K_{q,n-1}\beta_0) \dots J_{s_{n-1}}(K_{q,0}\beta_{n-1}) e^{i\gamma_{n-1}} e^{i\alpha_{n-1}\hat{\phi}_0} e^{i\beta_{n-1}\hat{\rho}_0}, \quad (\text{B.20})$$

where α and β are defined as in (B.9) and (B.10) respectively, and γ_n is given by

$$\gamma_0 = \frac{\bar{k}}{2}(s_0 + 1) \quad (\text{B.21a})$$

$$\gamma_{n+1} = \gamma_n + \frac{\bar{k}}{2}s_n(\alpha_n + \beta_n) + \frac{\bar{k}}{2}\alpha_n^2. \quad (\text{B.21b})$$

If we define the function

$$\begin{aligned} R(n, r) &= \frac{1}{2} \langle \psi_0 | [\exp(-ir\hat{\phi}_0) \exp(i\hat{\phi}_n) + \exp(i\hat{\phi}_n) \exp(-ir\hat{\phi}_0)] | \psi_0 \rangle \quad (\text{B.22}) \\ &= \sum_{s_0, \dots, s_{n-1}=-\infty}^{\infty} J_{s_0}(K_{q,n-1}\beta_0) J_{s_1}(K_{q,n-2}\beta_1) \dots J_{s_{n-1}}(K_{q,0}\beta_{n-1}) \\ &\quad \times (1 + e^{-i\beta_{n-1}\bar{k}r}) e^{i\gamma_{n-1}} \delta_{\alpha_{n-1}, r} \delta_{\beta_{n-1}, 0}, \quad (\text{B.23}) \end{aligned}$$

then we can write the correlation function $C_q(n)$ as

$$C_q(n) = \frac{\kappa_0 \kappa_n}{4} [R(n, -1) - R(n, 1)] + \text{c.c.}, \quad (\text{B.24})$$

where c.c. denotes the complex conjugate of the preceding expression.

Thus, the first few quantum correlations are given by

$$C_q(0) = \frac{\kappa_0^2}{2} \quad (\text{B.25a})$$

$$C_q(1) = 0 \quad (\text{B.25b})$$

$$C_q(2) = -\frac{\kappa_0 \kappa_2}{2} J_2(K_{q,1}) \quad (\text{B.25c})$$

$$C_q(3) = \frac{\kappa_0 \kappa_3}{2} [J_3(K_{q,1}) J_3(K_{q,2}) - J_1(K_{q,1}) J_1(K_{q,2})] \quad (\text{B.25d})$$

$$C_q(4) = \frac{\kappa_0 \kappa_4}{2} [J_2(K_{q,1}) J_2(K_{q,3}) + O(K_q^{-3/2})], \quad (\text{B.25e})$$

where $O(K_q^{-3/2})$ denotes terms of the order of $K_q^{-3/2}$, and K_q is a statistical average over possible K_q values. As an analogue to the classical case, these correlations are the origin of Shepelyansky's formula (3.35), and also the generalised version of Shepelyansky's formula which is used in the case of amplitude noise, (7.3).

Appendix C

Source Code

This appendix contains example source code for many of the simulation methods used in the work which is presented in this thesis. These methods are described in detail in chapter 5, and the main purpose of this code is to illustrate those methods.

C.1 Poincaré Sections: poin.m

This program produces Poincaré Sections for the δ -kicked rotor, evolving initial conditions in time using the classical standard map, 2.38.

```
N=20
nkicks=100
kappa=7

phis0=linspace(-pi,pi,N)';           % Set up positions for initial grid
rhos0=linspace(-2*pi,2*pi,N)';      % Set up momenta for initial grid

phis=phis0*(ones(size(phis0))');    % Create matrices representing the grid of
rhos=ones(size(rhos0))*(rhos0');    % initial positions and momenta.

phis=phis(:);                       % Create two vectors, representing a matching list
rhos=rhos(:);                       % of initial positions and momenta.

for i=1:nkicks
    i
    rhos=rhos-kappa*sin(phis);       %
    phis=phis+rhos/2;                % Evolve the positions and momenta
    phis=mod(phis+pi,2*pi)-pi;       % using the classical standard map,
    plot(phis/pi,rhos/pi, '.', 'MarkerSize',1); % and plot points on a Poincare
    hold on                          % section at appropriate times.
    phis=phis+rhos/2;                %
    phis=mod(phis+pi,2*pi)-pi;       %
end
```

```

axis equal                                %
axis([-1,1,0,2])                          % Adjust axes and add labels to graph.
xlabel('\phi/\pi', 'FontSize', 18)         %
ylabel('\rho/\pi', 'FontSize', 18)        %

```

C.2 Simulation of the Pulse - Kicked Rotor

C.2.1 Integration of Differential Equations: ckr.c

The following program, written in C, simulates the pulse-kicked rotor for arbitrary pulse shapes and determines $\langle \rho^2 \rangle$ as a function of kick number and κ . It is based on routines from *Numerical Recipes in C* [55]) which are not included here.

```

/*CKR.C Simulates the Classical Pulse Kicked Rotor for an arbitrary pulse shape.
Integrates the DEs for the motion using routines modified from
Numerical Recipes in C */

#include <stdio.h>
#define NRANSI
#include "nrajd.h"
#include "nrutil.h"
#include <math.h>
#include <time.h>

#define N 2

#define ALPHA 0.005 /* Pulse width */
#define PRECISION 1e-8 /* Numerical integration precision */
#define NKAPPA 99 /* Numer of kappa values to simulate */
#define KAPPASTART 1.0
#define KAPPAEND 50.0
#define PI 3.1415926535898
#define OUTFILENAME "ckrout.txt"

int doint(float x0, float p0, float* xvar, float* pvar);
extern float gasdev(long *idum);

float dxsav, *xp, **yp; /* defining declarations */
float kappa;

FILE *dataout;

long kmax, kount;

long nrhs; /* counts function evaluations */

float pulsefcn(float t) /*Can be used with devivs() to implement arbitrary pulse
profile */
{

```

```

    float res;
    res=1;
    return res;
}

void derivs(float x,float y[],float dydx[]) /*Function evaluating derivatives
                                           during the pulse*/
{
    nrhs++;
    dydx[1] = y[2];
    dydx[2] = (kappa/ALPHA)*sin(y[1]);
}

int main(void)
{
    float **phis;
    float **rhos;
    float **momdiff;
    int nmom=1;
    int npos=4000;
    int nkicks=50;
    float rho0=0.0;
    int i,j,k,l;
    float fnpos;
    float fj;
    float idum1=(-1);
    rhos=matrix(1,5000,1,300);
    phis=matrix(1,5000,1,300);
    momdiff=matrix(1,100,1,300);

    /* initialize random number generator */
    idum1=(long) time(NULL);

    if (idum1 > 0){
        idum1 = -idum1; }

    for(l=1;l<=NKAPPA;l++)
        {

    kappa=KAPPASTART+((float)l-1)*(KAPPAEND-KAPPASTART)/(NKAPPA-1.0);
    printf("kappa = %f\n",kappa);

    for(i=1;i<=nmom;i++)
        {
            rho0=0; /*setup initial momentum*/
            rho0=SIGMAN*gasdev(&idum); */
            /*setup momenta & postions for each run*/
            for(j=1;j<=npos;j++)

```

```

        {
        fj=j;
        fnpos=npos;
        rhos[j][0]=rho0;
        phis[j][0]=fj/fnpos*2.0*PI;
        }

    for(k=1;k<=nkicks;k++)        /*do runs for this momentum*/

        {
        printf("%d\n",k);
        for(j=1;j<=npos;j++)    /*Cycle over different positions*/
            {
            doint(phis[j][k-1],rhos[j][k-1],&phis[j][k],&rhos[j][k]);
                /*Evolution during pulse*/
            phis[j][k]+=(1.0-ALPHA)*rhos[j][k];
                /*Free Evolution after pulse*/
            momdiff[l][k]=pow(rhos[j][k],2)/((float)npos);
                /*Mean Squared Momentum*/
            }
        }
    }
}

/*
for (j=1;j<=npos;j++)
printf("%16.6f\n",phis[j][nkicks]); */
printf("\n");
for (k=1;k<=nkicks;k++)
printf("%16.6f\n",momdiff[k]);

dataout=fopen(OUTFILENAME,"w");
for(k=1;k<=nkicks;k++)
{

    for (l=1;l<=NKAPPA;l++)
    {
        fprintf(dataout,"%10.6f  ",momdiff[l][k]);
    }
    fprintf(dataout,"\n");
}
fclose(dataout);

free_matrix(phis,1,5000,1,300);
free_matrix(rhos,1,5000,1,300);
free_matrix(momdiff,1,100,1,300);

return 0;
}

int doint(float x0,float p0,float* xvar,float* pvar)

```

```

{
    int i,nbad,nok;
    float eps=PRECISION,h1=ALPHA/5,hmin=0.0,hmax=ALPHA/5,x1=0.0,x2=ALPHA,*ystart;

    ystart=vector(1,N);
    xp=vector(1,200);
    yp=matrix(1,10,1,200);
    ystart[1]=x0;
    ystart[2]=p0;
    nrhs=0;
    kmax=100;
    dxsav=(x2-x1)/60;
    odeint(ystart,N,x1,x2,eps,h1,hmin,hmax,&nok,&nbad,derivs,rkqs);
        /*Do Integration*/
    *xvar=yp[1][kount];
    *pvar=yp[2][kount];
    free_matrix(yp,1,10,1,200);
    free_vector(xp,1,200);
    free_vector(ystart,1,N);
    return 0;
}
#undef NRANSI

```

C.2.2 Use of Jacobi Elliptic Functions: pulseclass.m

The following program (in two M-files) implements a classical simulation of the rectangular pulse-kicked rotor using the analytic solutions for the classical rotor in terms of Jacobi elliptic functions. The function `ellipf()` evaluates the inverse function $\text{sn}^{-1}(x)$, and is based on code from *Numerical Recipes in C* [55]. This function was implemented as a MATLAB[®] MEX file, which was written by S. M. Tan. The function `pulseclass.m`, shown below, was also based on code originally written by S. M. Tan.

```

N = 8000;                % Number of initial conditions to evolve
kk=[9 10 11 12];        % Kappa values to cycle through

alpha=0.005;
nkicks = 50;            % Set the number of kicks that the system will evolve through.

p2=zeros(M+1,1);
meanenergy=zeros(length(kk),M+1);

for jj=1:length(kk)     % Loop through different kappa values

    kappa=kk(jj)

    xilist = 2*pi * rand(N,1) - pi; % Choose a set of random initial positions from
                                     % a uniform distribution on the interval [-pi,pi]

```

```

mulist = 4*randn(N,1);      % Choose random initial momenta from a gaussian
                             % distribution with standard deviation 4 and centre 0

p2(1)=sum(mulist.^2)/N;    % Store average initial square momentum

for l = 1:nkicks           % Cycle through kicks
    l
    [xilist,mulist] = pulsestep(xilist,mulist,alpha,kappa/alpha);
                             % Evolve the momenta and positions during the kick
    xilist = xilist + (1-alpha)*mulist;
                             % Calculate the positions after free evolution
    xilist = xilist-2*pi*floor(xilist/(2*pi)); % Ensure that the positions are
    xilist = xilist - 2*pi*(xilist>pi);      % still in the range [-pi,pi]
    p2(l+1)=sum(mulist.^2)/N; % Store average initial square momentum
end

meanenergy(jj,:)=p2'/2; % Determine mean kinetic energy after each kick

end % End of loop for particular kappa value
-----

function [phi,p] = pulsestep(phi0,p0,t,K)

TINY=1e-15;
phi0=phi0+TINY;

E = 0.5.*p0.*p0 - K*cos(phi0)+TINY;

sK = sqrt(K)+TINY;

p0pos=(p0+TINY)>0;
rotyes=E>K;

k = sqrt(0.5*(1+E/K));
k=k+(rotyes).*(-k+1./k);
k=k+TINY*((abs(k))<0.5);
m = k.^2;
t0lp = ellipfv(asin(sin(0.5*phi0)./k)+TINY,k)./sK;
[snlp,cnlp,dnlp] = ellipj(sK.*(t0lp+t),m);
philp = 2*asin(k.*snlp);
plp = 2.*sK.*k.*cnlp;

t0ln = ellipfv(-asin(sin(0.5*phi0)./k)+TINY,k)./sK;
[snln,cnln,dnln] = ellipj(sK.*(t0ln+t),m);
philn = -2*asin(k.*snln);
pln = -2.*sK.*k.*cnln;

t0rp = k.*ellipfv(0.5*phi0+TINY,k)./sK;
[snrp,cnrp,dnrp] = ellipj(sK.*(t0rp+t)./k,m);
phirp = 2*asin(snrp.*sign(cnrp));
prp = 2.*sK./k.*dnrp;

```

```

t0rn = k.*ellipfv(-0.5*phi0+TINY,k)./sK;
[snrn,cnrn,dnrn] = ellipj(sK.*(t0rn+t)./k,m);
phirn = -2*asin(snrn.*sign(cnrn));
prn = -2*sK./k.*dnrn;

phi=rotyes.*(p0pos.*phirp + (~p0pos).*phirn)...
          +(~rotyes).*(p0pos.*philp+(~p0pos).*philn);
p=rotyes.*(p0pos.*prp + (~p0pos).*prn)+(~rotyes).*(p0pos.*plp+(~p0pos).*pln);

```

C.2.3 Spontaneous Emission recoils in the CKR: spemclass.m

The code below shows the addition to the CKR simulation of random momentum recoils due to spontaneous emission events, as described in section 5.2.2.

```

clear
N = 1; % Number of atoms to trace per set of emission times
N2 = 1000; % Number of noise realisations i.e., sets of emission times

kappa=10
alpha=0.005;
etaeta=[0.1,0.3,0.2]; % Spontaneous emission probabilities per kick to simulate
nkicks = 50;

pp=zeros(length(kk),M+1);

ecount=0;
lostem=0;

rand('state',sum(100*clock))

for jj=1:length(etaeta)

    eta=etaeta(jj);
    p2=zeros(1,M+1);

    for nnn=1:N2
        nnn
        eta
        xilist = 2*pi * rand(N,1) - pi;
        mulist = 4*randn(N,1);

        p2(1)=p2(1)+sum(mulist.^2)/N/N2;

        spemtime=cumsum(-log(rand(M,1))/eta); % Choose spontaneous emission times
        spemkick=floor(spemtime); % Determine kick number
        spempart=spemtime-spemkick; % Determine fraction of kick

        for l = 1:nkicks

```

```

if ~isempty(find(spekkick==(l-1))) % Determine whether recoil occurs
                                % on this kick
    ecount=ecount+1;
    emno=find(spekkick==(l-1));

    if length(emno)==1 % Single recoil during this kick

        [xilist,mulist] = pulsestep2(xilist,mulist,alpha*spempart(emno),...
                                     kappa/alpha);
                                % Evolve up to recoil time
        mulist=mulist+(rand(N,1)-1/2);
                                % Add random recoil momentum between -1/2 and 1/2
        [xilist,mulist] = pulsestep2(xilist,mulist,...
                                     alpha*(1-spempart(emno)),kappa/alpha);
                                % Complete Evolution

    else % Account for 2 recoils during one kick
        ecount=ecount+1;
        lostem=lostem+length(emno)-2;
        [xilist,mulist] = pulsestep2(xilist,mulist,...
                                     alpha*spempart(emno(1)),kappa/alpha);
        mulist=mulist+(rand(N,1)-1/2);
        [xilist,mulist] = pulsestep2(xilist,mulist,...
                                     alpha*(spempart(emno(2))-spempart(emno(1))),kappa/alpha);
        mulist=mulist+(rand(N,1)-1/2);
        [xilist,mulist] = pulsestep2(xilist,mulist,...
                                     alpha*(1-spempart(emno(2))),kappa/alpha);

    end

else % Do evolution during kick for the case where no recoil occurs
    [xilist,mulist] = pulsestep(xilist,mulist,alpha,kappa/alpha);
end

xilist = xilist + (1-alpha)*mulist;
xilist = xilist-2*pi*floor(xilist/(2*pi));
xilist = xilist - 2*pi*(xilist>pi);
p2(l+1)=p2(l+1)+sum(mulist.^2)/N/N2;

end

end

pp(jj,:)=p2/2;

end

```

C.3 Simulation of the QKR with Decoherence: mcwfspem.m

This is an example program for the simulation of the atom optics kicked rotor using the MCWF method described in sections 5.3.1 and 5.3.2. This simulation was based on code originally written by A. C. Doherty for reference [46].

```
function kbar=mcwfspem(alpha,kappa,kbar,eta,flnme)

nsteps1=5;           % Choose the number of steps into which each kick is divided
ntraj=1000;         % Number of initial wavefunctions
sigman=8;           % Standard Deviation of initial momentum distribution
                    %           in units of kbar/2
Nkicks=200;         % Number of kicks to evolve through

N=2^11;              % Choose Momentum Basis size

drho=kbar/2;        % Evaluate Momentum Basis spacing

rhos=drho*(-N/2:N/2-1)'; % Create a vector with momentum values of
                    %           corresponding basis states

dphi=4*pi/N;        % Determine Position Basis Spacing
phis=(-N/2:N/2-1)*dphi; % Create a vector with position values of
                    %           corresponding basis states

cosphi=cos(phis);   % Create vectors corresponding to cos(phi)
cosphio2=cos(phis/2); %           and cos(phi/2)

Hlight=kappa*cosphi/alpha-i*kbar*eta*(1+cosphi)/2/alpha;
                    % Set potential due to the kicking beam
kick=exp(-i*alpha*Hlight/kbar/nsteps1); % Evolution operator due to potential alone

P2=zeros(1,Nkicks+1); % Initialise vector for storing basis state probabilities
p2store=zeros(10,Nkicks+1); % And the same, in 10 groups of trajectories

momdist0=zeros(N,1); %
momdist100=zeros(N,1); % Initialise vectors for storing momentum distributions
momdist200=zeros(N,1); %

randn('state',sum(100*clock)); % Initialize Random number generators
rand('state',sum(100*clock)); %

for m=1:ntraj        % Main loop for trajectory evolution

    p=sigman*randn; % Choose a momentum value from the initial Gaussian distribution

    n=round(p);      % Round momentum value to nearest basis state
    q=kbar/2*(p-n);  % Determine initial quasimomentum
    psi0=[zeros(N/2+n,1); 1;zeros(N/2-1-n,1)] ;
```

```

                                % Set initial vector of basis state amplitudes
                                % (momentum space wavefunction).

psi=psi0;
freeH=(rhos+q).^2/2; % Compute free evolution Hamiltonian for this quasimomentum
momdist0=momdist0+abs(psi).^2/ntraj/norm(psi)^2;
    % Add this state to the initial momentum PROBABILITY distribution
P2(1)=P2(1)+psi'*(2*freeH.*psi/kbar^2)/ntraj/norm(psi)^2;
    % Include this state's momentum in average initial rho^2 value

freeev1=exp(-i*alpha*freeH/kbar/nstps1/2);
    %Free evolution operator for during the kick (Applied twice in each step)

freeev2=exp(-i*(1-alpha)*freeH/kbar);
    % Free evolution operator for free evolution period

thresh=rand; % Choose a random quantum jump threshold
nl=1;
dt=1;

for k=1:Nkicks % Evolve this state through the prespecified number of kicks

    psi=freeev2.*psi; % Apply the free evolution operator

    for l=1:nstps1 % Consider the evolution during the kick in parts
        psi=freeev1.*psi; % Apply the Free evolution operator (for during the kick)
        phi1=fftshift(fft(fftshift(psi)))/sqrt(N);
            % Transform to position space wavefunction
        phi1=phi1.*kick; % Apply the evolution operator due to the potential
        nr=phi1'*phi1; % Calculate the norm of the wavefunction

    if nr < thresh % If the norm has dropped below the threshold, do quantum jump

        tc=max(0,log(nl/thresh)/log(nl/nr)*dt);
            % Estimate the time that the norm dropped below the threshold
        bkick=exp(i*dt*alpha*Hlight/kbar/nstps1);
        phi1=phi1.*bkick; % Reverse the evolution due to the potential
            % back to the start of the kick
        psi=sqrt(N)*fftshift(ifft(fftshift(phi1)));
            % Transform to momentum space wavefunction
        bfreeev2=exp(i*dt*alpha*freeH/kbar/nstps1/2);
        psi=bfreeev2.*psi;
            % Reverse the free evolution back to the start of the kick.
        freeev3=exp(-i*tc*alpha*freeH/kbar/nstps1/2);
        psi=freeev3.*psi; %
        phi1=fftshift(fft(fftshift(psi)))/sqrt(N); %
        kick2=exp(-i*tc*alpha*Hlight/kbar/nstps1); % Evolve forwards to tc
        phi1=phi1.*kick2; %
        psi=sqrt(N)*fftshift(ifft(fftshift(phi1))); %
        psi=freeev3.*psi; %

    phi1=fftshift(fft(fftshift(psi)))/sqrt(N);
        % Transform to position space wavefunction

```

C.3. SIMULATION OF THE QKR WITH DECOHERENCE: MCWFSPEM.M 187

```

u=2*(rand-0.5); % Randomly choose projection (in [-1,1]) of momentum
                %                               recoil onto standing wave
p=2*q/kbar -u/2; % Add the recoil (projection/2) to the quasimomentum
n=round(p);     % Determine basis state translation
q=q-u*kbar/4-kbar/2*n; % Account for rest of recoil in quasimomentum

collapse=coshio2.*exp(-i*n*phis); % Compute the collapse operator

phi1=collapse.*phi1; % Apply the collapse operator
phi1=phi1/norm(phi1); %

psi=sqrt(N)*fftshift(iff(fftshift(phi1)));
                % Transform to momentum space wavefunction

freeH=(rhos+q).^2/2; % Update
freeev1=exp(-i*alpha*freeH/kbar/nstps1/2); % quasimomentum dependent
freeev2=exp(-i*(1-alpha)*freeH/kbar); % Hamiltonians

freeev3=exp(-i*(1-tc)*alpha*freeH/kbar/nstps1/2); %
psi=freeev3.*psi; %
phi1=fftshift(fft(fftshift(psi)))/sqrt(N); %
kick2=exp(-i*(1-tc)*alpha*Hlight/kbar/nstps1); % Evolve to the end
phi1=phi1.*kick2; % of the step
psi=sqrt(N)*fftshift(iff(fftshift(phi1))); %
psi=freeev3.*psi; %

thresh=rand; % Choose new random threshold
nl=phi1'*phi1;

else %
psi=sqrt(N)*fftshift(iff(fftshift(phi1))); % Complete evolution if
psi=freeev1.*psi; % there is no quantum jump
nl=nr; %
end % End if statement

end % End of step evolution loop

% Include momentum probability distribution in the averages for after each kick
P2(k+1)=P2(k+1)+psi'*(2*freeH.*psi/kbar^2)/ntraj/norm(psi)^2;
p2store(floor((m-1)/100)+1,k+1)=p2store(floor((m-1)/100)+1,k+1)...
+psi'*(2*freeH.*psi/kbar^2)/ntraj/norm(psi)^2;

if k== Nkicks
momdist200=momdist200+abs(psi).^2/ntraj/norm(psi)^2;
end

if k== 100
momdist100=momdist100+abs(psi).^2/ntraj/norm(psi)^2;
end

```

```

end % End of evolution of a single trajectory

disp(strcat(int2str(m),'/',int2str(ntraj),' trajectories computed for kbar=',...
    num2str(kbar),' ,alpha=',num2str(alpha),' ,kappa=',num2str(kappa),' ,eta=',...
    num2str(eta)))
    % Display statistics to indicate progress of simulation

end % End of evaluation of particular trajectory

cmd4now=strcat('save ',flnme,' momdist200 momdist100 alpha kappa eta kbar N ...
    nsteps1 Nkicks sigman P2 ntraj p2store') % Save data in the specified file.
eval(cmd4now)

```

C.4 QKR with Decoherence and Amplitude Noise: ampspem.m

This program is the same as the MCWF simulation with spontaneous emission noise, except that it includes amplitude noise on the kick strength.

```

function kbar=ampspem(alpha,kappa,eta,noise,kbar,flnme)

nsteps=5;
sigman=8;
Nkicks=200;
ntraj=50; % Number of different initial momenta per noise realisation
ntraj2=20; % Number of different noise realisations (i.e., total number
           % of trajectories is given by ntraj*ntraj2).

N=2^11;
ntraj2=20; %number of different noise realisations

drho=kbar/2;
rhos=drho*(-N/2:N/2-1)';
momdist=zeros(N,ntraj2);

dphi=4*pi/N;
phis=(-N/2:N/2-1)*dphi;

cosphi=cos(phis);
cosphio2=cos(phis/2);
randn('state',sum(100*clock));
rand('state',sum(100*clock));

P2=zeros(1,Nkicks+1);
p2store=zeros(ntraj2,Nkicks+1);

for mm=1:ntraj2 % Loop for different realisations of the noise
rn=rand(1,Nkicks)-0.5; % Generate a set of random numbers in the interval [-0.5,0.5]
% for this realisation

```

C.4. QKR WITH DECOHERENCE AND AMPLITUDE NOISE: AMPSPEM.M189

```

for m=1:ntraj          % Loop to average the realisation over the initial
                      % momentum distribution

    p=sigman*randn;
    n=round(p);
    q=kbar/2*(p-n);
    psi0=[zeros(N/2+n,1); 1;zeros(N/2-1-n,1)] ; %initial state
    psi=psi0;
    freeH=(rhos+q).^2/2;

    freeev1=exp(-i*alpha*freeH/kbar/nsteps/2);
    freeev2=exp(-i*(1-alpha)*freeH/kbar);
    P2(1)=P2(1)+psi'*(2*freeH.*psi/kbar^2)/ntraj2/ntraj/norm(psi)^2;
    p2store(mm,1)=p2store(mm,1)+psi'*(2*freeH.*psi/kbar^2)/ntraj/norm(psi)^2;

    thresh=rand;
    nl=1;
    dt=1;

for k=1:Nkicks

sz=(1+noise*rn(k)); % Determine the factor which kappa will be multiplied
                    % by for this kick.

Hlight=sz*kappa*cosphi/alpha-i*kbar*eta*(1+cosphi)/2/alpha;
kick=exp(-i*alpha*Hlight/kbar/nsteps);

psi=freeev2.*psi;

    for l=1:nsteps
        psi=freeev1.*psi;
        phi1=fftshift(fft(fftshift(psi)))/sqrt(N);
        phi1=phi1.*kick;
        nr=phi1'*phi1;
        if nr < thresh
            tc=max(0,log(nl/thresh)/log(nl/nr)*dt);
            bkick=exp(i*dt*alpha*Hlight/kbar/nsteps);
            phi1=phi1.*bkick;
            psi=sqrt(N)*fftshift(ifft(fftshift(phi1)));
            bfreeev2=exp(i*dt*alpha*freeH/kbar/nsteps/2);
            psi=bfreeev2.*psi;
            freeev3=exp(-i*tc*alpha*freeH/kbar/nsteps/2);
            psi=freeev3.*psi;
            phi1=fftshift(fft(fftshift(psi)))/sqrt(N);
            kick2=exp(-i*tc*alpha*Hlight/kbar/nsteps);
            phi1=phi1.*kick2;
            psi=sqrt(N)*fftshift(ifft(fftshift(phi1)));
            psi=freeev3.*psi;
            phi1=fftshift(fft(fftshift(psi)))/sqrt(N);

            u=2*(rand-0.5);
            p=2*q/kbar -u/2;
        end
    end
end

```

```

n=round(p);
q=q-u*kbar/4-kbar/2*n;

collapse=cosphio2.*exp(-i*n*phis);
phi1=collapse.*phi1;

phi1=phi1/norm(phi1);
psi=sqrt(N)*fftshift(iff(fftshift(phi1)));

freeH=(rhos+q).^2/2;
freeev1=exp(-i*alpha*freeH/kbar/nstps/2);
freeev2=exp(-i*(1-alpha)*freeH/kbar);

freeev3=exp(-i*(1-tc)*alpha*freeH/kbar/nstps/2);
psi=freeev3.*psi;
phi1=fftshift(fft(fftshift(psi)))/sqrt(N);
kick2=exp(-i*(1-tc)*alpha*Hlight/kbar/nstps);
phi1=phi1.*kick2;
psi=sqrt(N)*fftshift(iff(fftshift(phi1)));
psi=freeev3.*psi;

thresh=rand;
nl=phi1'*phi1;

else
psi=sqrt(N)*fftshift(iff(fftshift(phi1)));
psi=freeev1.*psi;
nl=nr;
end

end % End Loop for number of steps

if k== Nkicks
momdist(:,mm)=momdist(:,mm)+abs(psi).^2/ntraj/ntraj2/norm(psi)^2;
end

P2(k+1)=P2(k+1)+psi'*(2*freeH.*psi/kbar^2)/ntraj2/ntraj/norm(psi)^2;
p2store(mm,k+1)=p2store(mm,k+1)+psi'*(2*freeH.*psi/kbar^2)/ntraj/norm(psi)^2;

end % End loop for a particular kick
disp(strcat(int2str(m+ntraj*(mm-1)),'/',int2str(ntraj*ntraj2),...
' trajectories computed for kbar=',num2str(kbar),' alpha=',num2str(alpha)...
', kappa=',num2str(kappa),' noise=',num2str(noise),' eta=',num2str(eta)))

end % End loop for a particular trajectory

end % End loop for a particular noise realisation

cmd4now=strcat('save ',flnme,...
' momdist alpha kappa noise kbar N Nkicks sigman P2 ntraj p2store')
eval(cmd4now)

```

Bibliography

- [1] T. Bhattacharya, S. Habib, K. Jacobs, and K. Shizume, *Phys. Rev. A* **65**, 032115 (2002).
- [2] A. J. Daley, A. S. Parkins, R. Leonhardt, and S. M. Tan, *Phys. Rev. E* **65**, 035201(R) (2002).
- [3] D. Cohen, *Phys. Rev. A* **44**, 2292 (1991).
- [4] A. J. Lichtenberg and M. A. Lieberman, *Regular and Chaotic Dynamics*, Second Edition (Springer-Verlag, Berlin, 1992).
- [5] L. E. Reichl, *The Transition to Chaos in Conservative Classical Systems: Quantum Manifestations* (Springer-Verlag, Berlin, 1992).
- [6] A. N. Kolmogorov, *Dokl. Akad. Nauk. SSSR* **98**, 527 (1954).
- [7] V. I. Arnol'd, *Russ. Math. Surver* **18**, 9, 95 (1963).
- [8] J. Moser, *Nachr. Akad. Wiss. Gottingen II, Math. Phys. Kd* **1**, 1 (1962).
- [9] S. M. Tan, *Linear Systems*, (Department of Physics, University of Auckland, 2000).
- [10] G. H. Ball, MSc thesis (Physics), University of Auckland, Auckland, New Zealand (1999).
- [11] B. G. Klappauf, W. H. Oskay, D. A. Steck and M. G. Raizen, *Physica D* **131** 78-89 (1999).
- [12] A. B. Rechester and R. B. White, *Phys. Rev. Lett.* **44**, 1586 (1980).
- [13] A. B. Rechester, M. N. Rosenbluth and R. B. White, *Phys. Rev. A* **23**, 2664 (1981).
- [14] H. D. I. Abarbanel and J. D. Crawford *Phys. Lett.* **82A**, 378 (1981).
- [15] D. A. Steck, PhD thesis (Physics), University of Texas at Austin, Austin, TX, USA (2001).
- [16] D. L. Shepelyanskii, *Theor. Math. Phys.* **49**, 925 (1982).

- [17] M. Berry, *Physica Scripta* **40**, 335 (1989).
- [18] T. Geisel, G. Radons and J. Rubner, *Phys. Rev. Lett.* **57**, 2883 (1986).
- [19] K. Vant, G. Ball, H. Ammann and N. Christensen, *Phys. Rev. E* **59**, 2846 (1999).
- [20] G. Casati, B. V. Chirikov, F. M. Izrailev and J. Ford, in *Stochastic Behaviour in Classical and Quantum Hamiltonian Systems*, Vol. 93 of *Lecture Notes in Physics*, edited by G. Casati and J. Ford (Springer-Verlag, Berlin, 1979).
- [21] B. V. Chirikov, F. M. Izrailev and D. L. Shepelyansky, *Sov. Sci. Rev. C* **2**, 209 (1981).
- [22] S. Fishman, D. R. Grempel and R. E. Prange, *Phys Rev. Lett.* **49**, 509(1982).
- [23] D. R. Grempel, R. E. Prange and S. Fishman, *Phys. Rev. A* **29**, 1639 (1984).
- [24] W. H. Oskay, D. A. Steck, V. Milner, B. G. Klappauf and M. G. Raizen, *Optics Communications* **179**, 137 (2000)
- [25] D. L. Shepelyansky, *Physica D* **28**, 103 (1987).
- [26] R. Graham, M. Schlautmann and P. Zoller, *Phys. Rev. A* **45**, R19 (1992).
- [27] F. L. Moore, J. C. Robinson, C. F. Bharucha, B. Sundaram, and M. G. Raizen, *Phys. Rev. Lett.* **75**, 4598 (1995)
- [28] M. G. Raizen, *Adv. At. Mol. Opt. Phys.* **41**, 43 (1999).
- [29] H. Ammann, R. Gray, N. Christensen and I. Shvarchuck, *J. Phys. B: At. Mol. Opt. Phys.* **31**, 2449 (1998).
- [30] H. Ammann, R. Gray, I. Shvarchuck and N. Christensen, *Phys. Rev. Lett.* **80**, 4111 (1998).
- [31] M. B. d’Arcy, R. M. Godun, M. K. Oberthaler, D. Cassettari and G. S. Summy, *Phys. Rev. Lett.* **87**, 074102 (2001).
- [32] M. B. d’Arcy, R. M. Godun, M. K. Oberthaler, G. S. Summy, K. Burnett and S. A. Gardiner, *Phys. Rev. E* **64**, 056233 (2001).
- [33] C. S. Adams, M. Sigel and J. Mlynek, *Phys. Rep.* **240**, 145 (1994).
- [34] D. F. Walls and G. J. Milburn, *Quantum Optics*, (Springer-Verlag, Berlin, 1994).
- [35] R. Graham and S. Miyazaki, *Phys. Rev. A* **53**, 2683 (1996).
- [36] I. Shvarchuck, MSc thesis (Physics, University of Auckland, Auckland, New Zealand (1997)).

- [37] H. J. Metcalf and P. van der Straten, *Laser Cooling and Trapping*, (Springer-Verlag, New York, 1999).
- [38] D. A. Steck, *Cesium D Line Data*, Revision 1.3, (Physics, University of Texas at Austin, Austin, TX, USA, 2001) <http://george.ph.utexas.edu/~dsteck/alkalidata>
- [39] C. E. Tanner and C. Wieman, *Phys. Rev. A* **38**, 1616 (1988).
- [40] N. Bohr, *Nature*, **121**, 580 (1928); reprinted in *Quantum Theory and Measurements*, edited by J. A. Wheeler and W. H. Zurek, (Princeton U. P., Princeton, NJ, USA, 1983).
- [41] W. H. Zurek, *Physics Today* **44**, 36 (1991).
- [42] H. Everett III, *Rev. Mod. Phys.* **29**, 454 (1957).
- [43] J. A. Wheeler, *Rev. Mod. Phys.* **29**, 463 (1957).
- [44] W. H. Zurek and J. P. Paz, *Phys. Rev. Lett.* **72**, 2508 (1994).
- [45] S. Dyrting, *Phys. Rev. A* **53**, 2522 (1996).
- [46] A. C. Doherty, K. M. D. Vant, G. H. Ball, N. Christensen and R. Leonhardt, *J. Opt. B: Quant. Semiclass. Opt.* **2**, 605 (2000).
- [47] E. Ott, T. M. Antonsen Jr., and J. D. Hanson, *Phys. Rev. Lett.* **53**, 2187 (1984).
- [48] T. Dittrich and R. Graham, *Ann. Phys.* **200**, 363 (1990).
- [49] B. G. Klappauf, W. H. Oskay, D. A. Steck, and M. G. Raizen, *Phys. Rev. Lett.* **81**, 1203 (1998).
- [50] V. Milner, D. A. Steck, W. H. Oskay, and M. G. Raizen, *Phys. Rev. E* **61**, 7223 (2000).
- [51] D. A. Steck, V. Milner, W. H. Oskay, and M. G. Raizen, *Phys. Rev. E* **62**, 3461 (2000).
- [52] K. Vant, G. Ball, and N. Christensen, *Phys. Rev. E* **61**, 5994 (2000).
- [53] P. Marte, R. Dum, R. Taïeb and P. Zoller, *Phys. Rev. A* **47**, 1378 (1993).
- [54] K. Mølmer, Y. Castin, and J. Dalibard, *J. Opt. Soc. Am. B* **10**, 524 (1993).
- [55] W. H. Press, S. A. Teukolsky, W. T. Vetterling and B. P. Flannery, *Numerical Recipes in C*, Second Edition (Cambridge University Press, 1995).
- [56] R. Dum, P. Zoller, and H. Ritsch, *Phys. Rev. A* **45**, 4879 (1992).

- [57] R. Dum, A. S. Parkins, P. Zoller, and C. W. Gardiner, *Phys. Rev. A* **46**, 4382 (1992).
- [58] H. J. Carmichael, *An Open Systems Approach to Quantum Optics*, (Springer-Verlag, Berlin, 1993).
- [59] T. Bhattacharya, S. Habib, and K. Jacobs, *Phys. Rev. Lett.* **85**, 4852 (2000).
- [60] M. P. Sadgrove, M. E. K. Williams, and R. Leonhardt (University of Auckland, unpublished). An experimental study of diffusion rate structures in the quantum kicked rotor with amplitude noise using unscaled units.
- [61] M. E. K. Williams, M. P. Sadgrove, and R. Leonhardt (University of Auckland, unpublished). An experimental study of diffusion rate structures in the quantum kicked rotor with decoherence using unscaled units.
- [62] W. K. Hensinger, H. Häffner, A. Browaeys, N. R. Heckenberg, K. Helmerson, C. McKenzie, G. J. Milburn, W. D. Phillips, S. L. Rolston, H. Rubinsztein-Dunlop, and B. Upcroft, *Nature* **412**, 52 (2001).
- [63] D. A. Steck, W. H. Oskay, and M. G. Raizen, *Science* **293**, 274 (2001).
- [64] A. S. Parkins (University of Auckland, unpublished).
- [65] M. Abramowitz and I. A. Stegun, *Handbook of Mathematical Functions* (Dover, New York, 1972).
- [66] *CRC Standard Mathematical Tables and Formulae*, 30th Edition, edited by D. Zwillinger (CRC Press, Florida, 1996).